The Cosmic Ballet: spinning in the web

Ganeshaiah Veena, Punyakoti

DOI:
10.33612/diss.134370695

rijksuniversiteit groningen

The Cosmic Ballet: spinning in the web

PhD thesis

to obtain the degree of PhD at the
University of Groningen
on the authority of the
Rector Magnificus Prof. C. Wijmenga
and in accordance with
the decision by the College of Deans.

This thesis will be defended in public on

Friday 16 October 2020 at 9:00 hours

by

Punyakoti Ganeshaiah Veena

born on 31st July 1991
in Bengaluru, India

Supervisors
Prof. M.A.M. van de Weijgaert
Prof. Elmo Tempel

Co-supervisor
Dr. Marius C. Cautun

Assessment committee
Prof. Joss Bland-Hawthorn
Prof. Nabila Aghanim
Prof. Filippo Fraternali

What the caterpillar calls the end, the rest of the world calls a butterfly.

– *Lao Tzu*

To *appaji,* who instilled in me the courage to question and to *amma,* who educated me to persevere and stay strong.

university of groningen / faculty of mathematics and natural sciences / kapteyn astronomical institute

Book cover: The background represents the cosmic web from the P-Millennium simulation (figure 4.1 from chapter 4), recreated in the impressionism style of Van Gogh, using the free online tool: http://www.picturetopeople.org/. The ballerina adorned in a galaxy was made by the artist Mr. Sunil Mishra, based in Bengaluru, India.

This work was funded by the University of Groningen and Tartu Observatory, the University of Tartu.

Contents

1 Introduction

1.1 A glimpse into the unknown

A story goes that in 327 BCE, along the river Sindhu, in India, Alexander the Great asks a gymnosophist meditating in solitude,[*]
"Why are you naked?"
"Why are you wearing clothes?"
"I am asking the questions here"
"Questions give birth to only more questions"
"What are you doing?"
"Nothing. I am mastering the art of doing nothing."
"While you have been doing nothing, I have been conquering the world"
"Without conquering the ultimate truth of our own origins (of cosmos), it is futile to believe you are conquering the world..."

A grand quest of mankind has been to unravel the origin of the Universe and our place in it. Since the gymnosophist of 300 BC to now, we have made monumental progress towards this. But, with every step towards the answer, we ended up unlocking even more secrets, hence deepening our quest for our origins. This pursuit has helped us take several giant leaps from the initial view of a geocentric finite cosmos to the current model of a dynamically evolving and unimaginably large Universe.

[*] The exact conversation between Alexander and the gymnosophist is not known, but there are several versions of it in folk tales.

1

When looking at the night-sky, we see planets, countless stars and a plethora of celestial bodies, and one cannot stop but ponder how all this began. The stars we see are a part of our own *Milky Way* galaxy. Although not visible to the naked eye, there are millions of galaxies in the Universe that are seen through large telescopes.

Numerous large-scale sky surveys starting with the early redshift surveys CfA, CfA2 (Huchra & Geller 1982; de Lapparent, Geller & Huchra 1986) and others such as the 2dFGRS (Colless et al. 2003), SDSS (Abazajian et al. 2003) and 2MASS (Huchra et al. 2005) have revealed that on large scales of millions to hundreds of millions of light years, the Universe is pervaded by a complex, intricate and intriguing web-like network, called the cosmic web, consisting of the largest known structures of the Universe.

Each dot in Figure 1.1 represents a galaxy in the SDSS survey, showing that galaxies are not randomly located in the Universe but cluster together to form a rich network of large-scale **filaments**, **sheets**, **clusters** and empty regions known as **voids**.

Dark matter and galaxies that make up the skeleton of the cosmic web are held together by gravity. Huge **clusters** of galaxies form the major hubs of the web network, akin to central stations in a busy city. These clusters are in turn connected via elongated **filaments** to other hubs, similar to train tracks diverging from and converging to major stations. There are large empty regions of space with very few galaxies called **voids** that are bordered by **sheets** or **walls**. All these together constitute the large-scale web network. Filaments also act as transport channels that channel matter from voids, walls and into the clusters.

The first structures and the largest structures that are present today all emerged out of the quantum noise present in the early Universe, as gravity started to fold the originally uniform blanket of mass and radiation. This primordial noise that seeded today's structures is the closest description we have of our origins, and without these, there would be no galaxies, no stars, hence no planets or life.

Galaxies are huge ensembles of stars, gas, and dust, and are embedded at the centre of much more massive dark matter haloes. Galaxies come in a large variety of sizes, from ultra-faint dwarfs that weigh a few hundred thousand times the mass of the Sun to truly massive objects with mass up to few orders of magnitude higher. They also have a multitude of shapes that correlate with their rotation profiles, from elliptical objects in which the stars have highly random motions (nearly zero net rotation) to spiral galaxies in which most stars rotate in a thin disc on almost circular orbits (highly ordered rotation).

The origin of rotation in galaxies remains an important question in the field of galaxy formation as it is not only linked to their morphology but also to the rotation of their host dark matter haloes. The key to answering these questions lies in studying the underlying cosmic web in which galaxies and dark matter haloes form and grow.

Within this large-scale network of matter, galaxies stand out as majestic pearls and are spinning in a specific rhythm, resembling swirling ballerinas along the long filamentary strings of matter. This is akin to performing a grand ballet on this gigantic cosmic stage, the cosmic web, making us wonder how all of this has been set into motion. The most prominent example is the disc of our own galaxy, the Milky Way, which is spinning perpendicular to the underlying local web.

In this thesis, we investigate how and why galaxies rotate from the point of the view of the large-scale cosmic web. We study how different features of the web influences properties such as spin and shape of galaxies and their dark matter haloes. We find explicit correlations between spin and the host cosmic web components in which they are growing.

Since the gravitational fields responsible for the emergence of these structures also caused galaxies to rotate, galaxy spins can also reveal the properties of the early Universe. Such studies also help with developing precise models to account for the effect of galaxy alignments on weak lensing measurements (Mandelbaum et al. 2006; Joachimi et al. 2015; Kiessling et al. 2015; Chisari et al. 2015). This will enable us to make better interpretations of the data from future weak lensing surveys such as EUCLID and LSST.

We obtain our results using large state-of-the-art cosmological simulations and advanced techniques for cosmic web characterisation. To understand the present-day universe, we perform this analysis at multiple redshifts and follow the evolution of these correlations.

1.1.1 A brief history of the Universe

Observations of the Universe have revolutionised our understanding of the cosmos and our place in it. In particular, a few key discoveries within the last century have led to the establishment of the standard model of our Universe.

Edwin Hubble discovered that galaxies further away from us are receding faster than those close by (Hubble 1929). The idea of an expanding Universe (Lemaître 1927), in which the space stretches, led us to hypothesize the occurrence of the *Big Bang*, that the whole Universe was once packed together in a hot and dense state. The discovery of the Cosmic Microwave Background (CMB) radiation (Penzias & Wilson 1965) (see Figure 1.3), which is the resid-

ual radiation emitted by this early hot period validated this theory and placed the occurrence of the Big Bang at around 13.8 billion years ago (Planck Collaboration et al. 2018).

The Universe went through a phase of very rapid expansion, also known as inflation (Guth 1981) within the first few fractions of a second. This was crucial, since it lead to a near uniform and isotropic matter distribution. Just minutes later, the first atomic nuclei were formed (Gamow 1946), and for the next 380,000 years the Universe cooled down until atomic nuclei recombined with electrons to form the first atoms, which led to the CMB. The intensity of the CMB radiation is highly isotropic across the sky and provides the strongest evidence that the early Universe was almost uniform and contained only very tiny density fluctuations. These fluctuations have since grown due to gravity and have resulted in the rich pattern of galaxies, stars, and planets that we see today.

The motion of cluster galaxies (Zwicky 1933; Einasto, Kaasik & Saar 1974) and the rotation curves of spirals (Rubin, Ford & Thonnard 1980; Bosma 1981) have indicated that the Universe is even more mysterious than we imagined, with most of the cosmic matter being made of an unknown substance, which we refer to as *dark matter*. Our best guess is that dark matter is a fundamental particle or a set of such particles that interacts with normal baryonic matter mostly through gravity (for a review, see Frenk & White 2012).

More recently, Riess et al. (1998) and Perlmutter et al. (1999) measured the recession velocities of supernovae Ia and were surprised to find that the late-time Universe is undergoing an accelerated expansion. This confirmed the suggestion that the cosmological constant, Λ is a major factor in the evolution of the Universe (see Efstathiou, Sutherland & Maddox 1990; Calder & Lahav 2010, for a brief review). One possible explanation for this is that in addition to luminous and dark matter, the cosmos contains another obscure ingredient, so called *dark energy*, which permeates empty space and affects the dynamics of our Universe on large scales of tens of Megaparsecs.

Composition of the Universe

Modern cosmology is built on the assumption that the Universe is *homogeneous* and *isotropic* on large scales and that its dynamics can be described by Einstein's General Relativity (GR). Solutions to the Einstein's field equations for such a Universe are given by the Friedmann-Lemaitre-Robertson-Walker equations (Friedmann 1922). These equations form the basis of modern cosmology and describe the dynamics of the universe consisting of radiation, baryons, dark matter and dark energy.

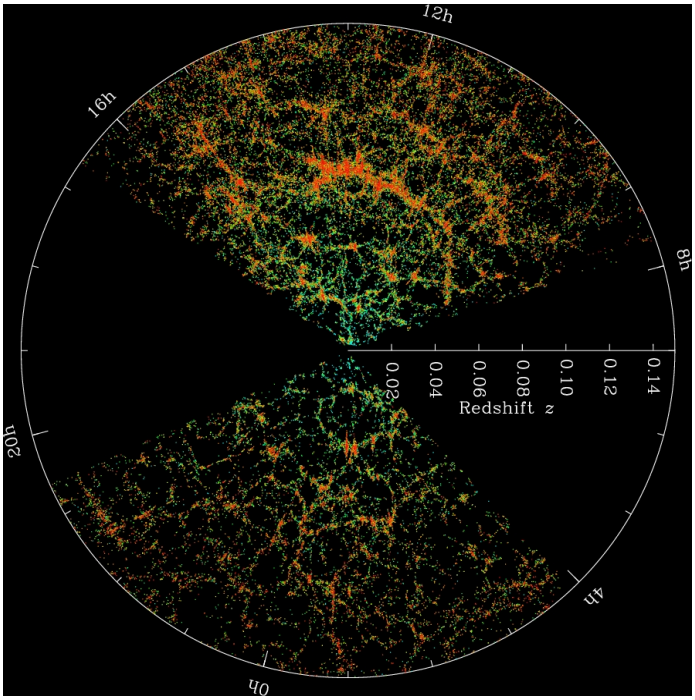

Figure 1.1 – *Sloan Digital Sky Survey [SDSS] map of the universe in which the cosmic web is clearly visible. Each dot represents a galaxy and the color scale depicts the age of their stars, with redder being older. Image credit: M. Blanton and the SDSS* `http://www.sdss.org/science/`.

The Planck Collaboration et al. (2016) have established that the Universe is geometrically flat and is dominated by dark matter and dark energy, which constitute 95% of the cosmic budget, with only the remaining 5% consisting of baryons. The relative fractions of the different constituents play a crucial role in structure formation and are usually expressed in terms of density parameters. The ΛCDM model, which is currently the prevailing model for the Universe, has the following values of density parameters for baryons (Ω_b), radiation (Ω_r), dark matter ($\Omega_{\rm DM}$) and dark energy (Ω_Λ) respectively:

$$\begin{aligned} \Omega_b &= \frac{\rho_b}{\rho_c} = 0.0486, \quad \Omega_r = \frac{\rho_r}{\rho_c} = 0.005, \quad \Omega_{\rm DM} = \frac{\rho_{\rm DM}}{\rho_c} = 0.259, \\ \Omega_\Lambda &= \frac{\Lambda}{3H_0^2} = 0.691, \quad H_0 = 67.74 \text{ km s}^{-1}\text{Mpc}^{-1}. \end{aligned}$$

These fractions are given with respect to the critical density $\rho_c = \frac{3H_0^2}{8\pi G}$, defined as the density for which the Universe is spatially flat. The Hubble parameter H is defined as $H = \frac{\dot{a}}{a}$ where a is the expansion factor and H_0 is the Hub-

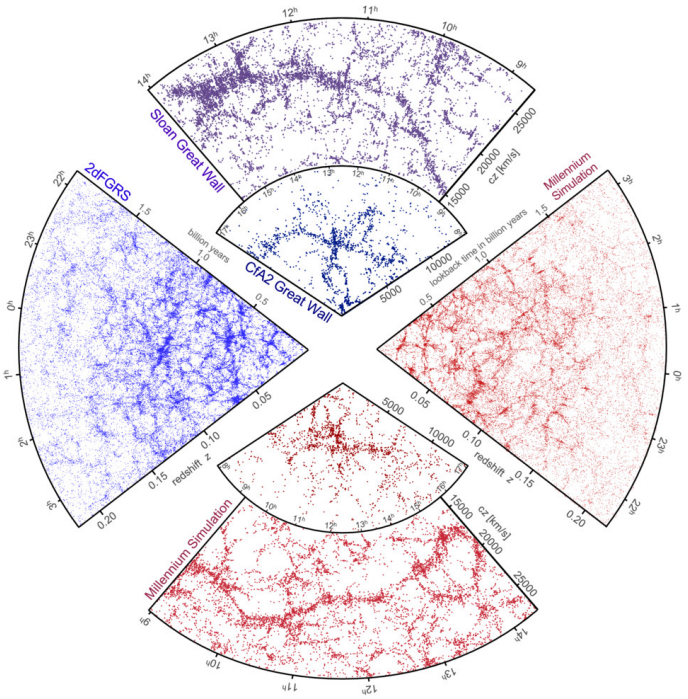

Figure 1.2 – *The cones on the top and left in blue show galaxy distributions from observational surveys, and the corresponding cones on the right and bottom in red illustrate very similar galaxy distributions from the Millennium cosmological simulation. Image from: Springel, Frenk & White (2006).*

ble parameter at present day and at redshift z, it is given by the Friedman equation,

$$H^2(z) = H_0^2(\Omega_r(1+z)^4 + \Omega_m(1+z)^3 + \Omega_k(1+z)^2 + \Omega_\Lambda). \qquad (1.1)$$

1.2 Structure Formation

Galaxies, gas and dark matter follow an intricate pattern in the Universe as we have already discussed, that raises certain obvious questions: Why this pattern? What are the main drivers behind the formation of filaments, walls and voids? Can we explain the emergence of the cosmic web based only on certain simple physical laws? These questions are essential for explaining the cosmic web and, in turn, for understanding what the web environments reveal about the Universe at large. The answers to these questions lie in tracing the gradual growth of large-scale structures, whose seeds lie in very tiny primordial fluctuations that are well described by a Gaussian random field. The earliest

window into the embryonic Universe is given by the Cosmic Microwave Background, which formed when the fluctuations in the baryonic component had an amplitude of $\sim 10^{-5}$.

1.2.1 Gravitational Instability

The theory of gravitational instability (Peebles 1980) describes the emergence of the cosmic web from the initial density and velocity perturbations. The early Universe consisted of tiny over and underdensities. Due to gravity, matter aggregates more in the over-dense regions and streams out of the underdense regions. This led to a net flow of matter towards high-density patches while the underdense regions became further devoid of matter. The matter-rich patches bound by gravity grew into virialised haloes and galaxies, while the underdense patches evolved into the voids of the cosmic web.

The density contrast $\delta(\mathbf{x}, t)$, with respect to the background density of the Universe ρ_u, at a location $\mathbf{x}$ is defined as

$$\delta(\mathbf{x}, t) = \frac{\rho(\mathbf{x}) - \rho_u(t)}{\rho_u(t)}. \tag{1.2}$$

Here, $\mathbf{x}$ denotes the comoving coordinate and $\rho(\mathbf{x})$ the density at position $\mathbf{x}$. The evolution of the density contrast and velocity of mass distribution in the Universe can be described to a good approximation by the set of three fluid equations for a continuous medium (Peebles 1980): the continuity equation (Equation 1.3) that describes the conservation of mass, the Euler equation (Equation 1.4) as equation of motion of the mass elements as a result of the exerted gravitational and pressure forces, and the Poisson equation (Equation 1.5) relating the gravitational potential to the mass distribution. For a collisional medium with pressure p these are, in comoving coordinates,

$$\frac{\partial \delta}{\partial t} + \frac{1}{a}\nabla.[(1+\delta)\mathbf{v}] = 0 \tag{1.3}$$

$$\frac{\partial v}{\partial t} + \frac{1}{a}(\mathbf{v}.\nabla)\mathbf{v} + \frac{\dot{a}}{a}\mathbf{v} = \frac{-1}{a}\nabla\phi - \frac{\nabla p}{\rho a} \tag{1.4}$$

$$\nabla^2\phi = 4\pi G\rho a^2\delta \tag{1.5}$$

Here, $\mathbf{v}$ is the peculiar velocity, which is the relative velocity of a particle with respect to the Hubble flow, and it is given as:

$$\mathbf{u} = H\mathbf{r} + \mathbf{v}, \tag{1.6}$$

where $\mathbf{u}$ is the total velocity and $\mathbf{r} = a\mathbf{x}$.

1.2.2 Linear Regime

In the early Universe, when the density perturbations are very small compared to the mean background density, we can approximate $\delta << 1$. For a pressureless medium these equations reduce to

$$\frac{\partial^2 \delta}{\partial^2 t} + 2\frac{\dot{a}}{a}\frac{\partial \delta}{\partial \delta} = 4\pi G\overline{\rho}\delta. \tag{1.7}$$

The solution involves two parts, namely a decaying mode, $D_-(t)$, and a growing mode, $D_+(t)$, with $\delta(\mathbf{x}, t) = D_-(t)\ \delta(\mathbf{x}) + D_+(t)\ \delta(\mathbf{x})$. Since the decaying mode becomes negligible with time, we consider only the growing mode solution

$$\delta(\mathbf{x}, t) = D(t)\delta(\mathbf{x}, t_o). \tag{1.8}$$

Here, $D(t)$ is the linear growth factor that captures the information regarding the evolution of the density fluctuations from time t_0 to t. Therefore, the rate of change of fluctuations is constant at all locations, and is a function only of time. The growth factor is determined by the matter and energy compositions of the Universe. Accordingly, at different epochs, the growth factor $D(t)$ assumes different forms. In an Einstein-de Sitter universe (flat, matter only), the linear growth factor $D(t) \propto t^{2/3}$, whereas for an empty universe, it is a constant, meaning that structures don't grow. For the late-time Universe, where the dominant components are matter and dark energy, the solution is

$$D(z) = \frac{5\Omega_{m,0}H_0^2}{2}H(z)\int_z^\infty \frac{1+z'}{H^3(z')}dz', \tag{1.9}$$

where $H(z)$ is the Hubble parameter at redshift z. given as

$$H^2(z) = H_0^2(\Omega_m(1+z)^3 + \Omega_k(1+z)^2 + \Omega_\Lambda). \tag{1.10}$$

The evolution of dark matter density for a cold dark matter cosmology is illustrated in Figure 1.4.

1.2.3 Hierarchical growth of structures

As the density perturbations grow, the build up of structures is by gradual merging of smaller haloes and by accretion. Growth of structures is determined by the shape of the power spectrum, which has spectral index between 1 and -3 for ΛCDM cosmology. Inflation ensures nearly scale invariant perturbations, with the spectral index being very close to one (large scales) and the growth of these fluctuations are later modulated by radiation and matter (on smaller scales). For such a spectrum, the variance at a mass scale $M = \frac{4\pi}{3}\rho_m R^3$ with the comoving radius R and mean density of matter ρ_m is

$$\sigma_M^2 \propto M^{-\left(\frac{n+3}{6}\right)}. \tag{1.11}$$

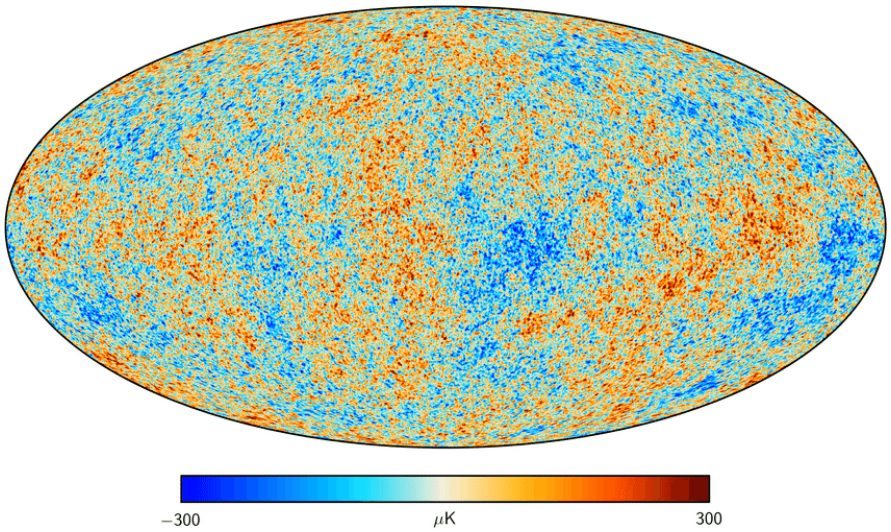

Figure 1.3 – *Temperature fluctuations map of the Cosmic Microwave Background as measured by the Planck satellite. The mean temperature is 2.7K and the fluctuations are of the order of* 10^{-5} *around the mean. These fluctuations are the seeds of structure formation.*

For any spectral index $n > -3$, lower mass scales induce higher fluctuations and higher mass scales induce lower fluctuations so matter clumps at smaller scales first and then at larger scales, so at first, low-mass haloes merge and subsequently grow into ever more massive objects. This is the hierarchical clustering scenario. Although the non-linear regime is difficult to solve analytically, there are powerful models such as the Press Schechter formalism (Press & Schechter 1974) and the ellipsoidal collapse model (Icke 1973; White & Silk 1979; Bond & Myers 1996; Sheth & Tormen 2002) that provide statistical estimates of the number and mass distributions of collapsed haloes. Using this, the mass fluctuations σ_M can be derived for several mass scales. The abundance of collapsed objects is given in the function $\sigma(M)$ which is a function of mass and redshift in the standard cosmological framework. Hierarchical growth and the evolution of structures is illustrated in Figure 1.4 where small scale clumps form first (higher redshift) which evolve into larger and dense structures with time.

1.3 Numerical simulations

At a certain stage in the structure formation process, the regions of overdensities corresponding to $\delta > 0$ overtake and matter accumulates rapidly in these regions. At this stage, the linear approximation, which is valid for $|\delta| \lesssim 1$,

1

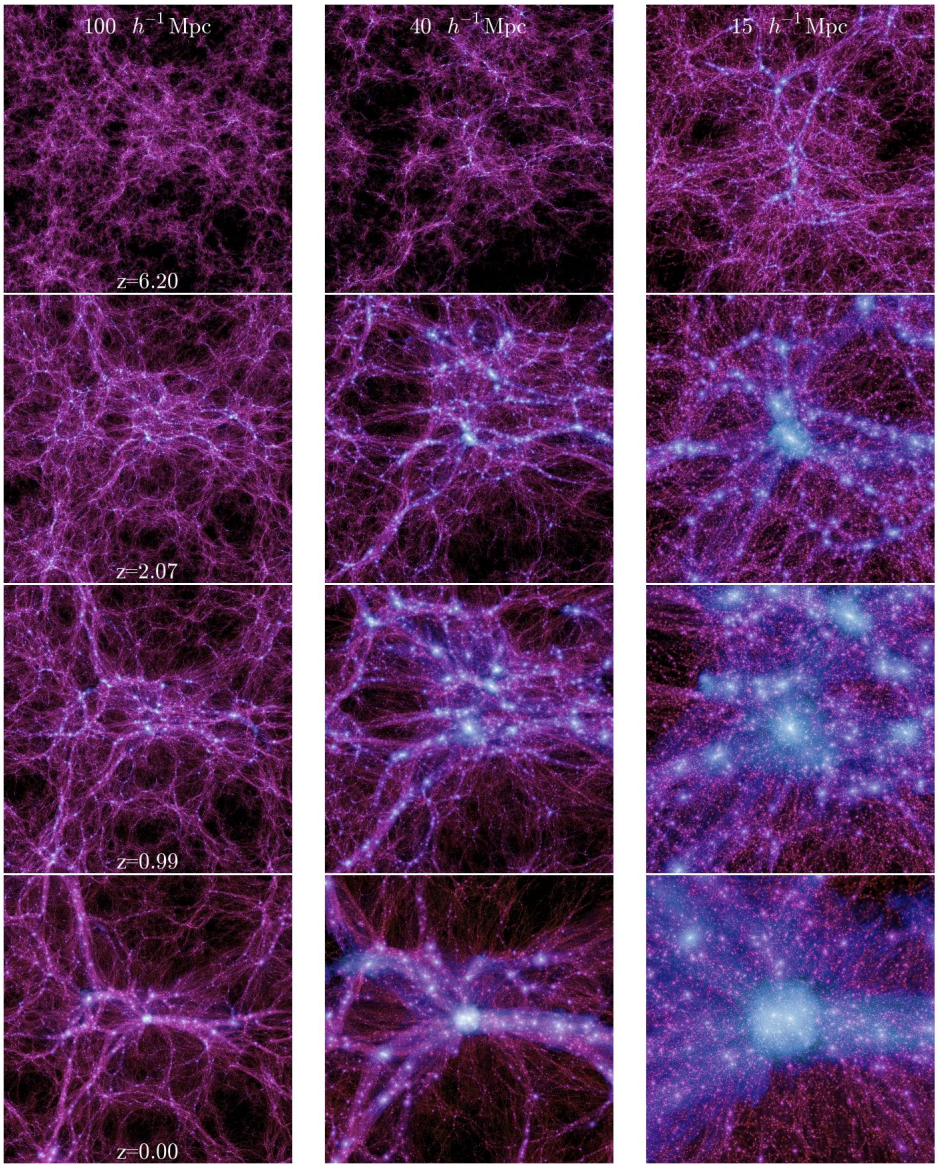

Figure 1.4 – *A slice from the Millennium-II simulation showing the growth of the cosmic web from a redshift of 6.2 to 0. It also highlights the hierarchical growth of structures with small objects forming first that merge to grow into more massive structures. Image from: Boylan-Kolchin et al. (2009)*

breaks down and we enter the nonlinear regime. The density evolution equation becomes increasingly complex and it is not possible to solve it analytically, as several fluctuation modes get coupled. Therefore, numerical simulations are our best tools to predict theoretically non-linear structure formation. Broadly, numerical simulations are of two categories: dark matter only and hydrodynamical, both of which can either be large volume or zoom simulations. The N-body codes which trace only dark matter interacting through gravity are computationally less demanding as they ignore baryons and associated gas physics. This is not necessarily a drawback as dark matter forms the skeleton of the cosmic web and lays the foundation for galaxy formation. Hydrodynamical simulations follow the joint evolution of dark matter and baryons, and, in particular, they focus on simulating many of the baryonic processes that plays an important role in the galaxy formation process. Though dark energy enjoys a major share in the cosmic budget, it does not contribute to structure formation (since the energy density of dark energy remains constant as per ΛCDM model, giving rise to negative pressure, and thus the deviations don't grow or decay), it only affects the cosmic expansion rate. Figure 1.5 shows a selection of N-body as well as hydrodynamic simulations that are currently available. This figure is from Vogelsberger et al. (2020), which also provides a thorough review of recent cosmological simulations. For this thesis, we have extensively utilised the dark matter only P-Millennium and the EAGLE hydro simulations, which we will describe in more details in upcoming chapters.

1.3.1 Simulating dark matter

A typical N-body simulation follows the motion of a large number of collisionless particles as they move in their own gravitational potential. This potential is obtained by solving the Poisson equation for the given distribution of particles. These are solved in an expanding background Universe that are described by the Friedman equations which are governed by general relativity. A majority of the simulations employ Newtonian dynamics instead of relativistic gravity. This is because the growth of structures is identical for both in the linear regime, while, in the non-linear regime, the typical velocities are much lower than the speed of light (Peebles 1980) and thus non-Newtonian corrections can be neglected.

The simulations are carried out with periodic boundary conditions to account for the cosmological principle that the Universe is homogeneous and isotropic on large scales. The power spectrum for cold dark matter is usually used to initialize a simulation. Positions and velocities are assigned to each dark matter particle and are evolved from a uniform distribution using the linear theory approximation (as described in subsection 1.4.1). This sets up the initial conditions for the simulation.

1

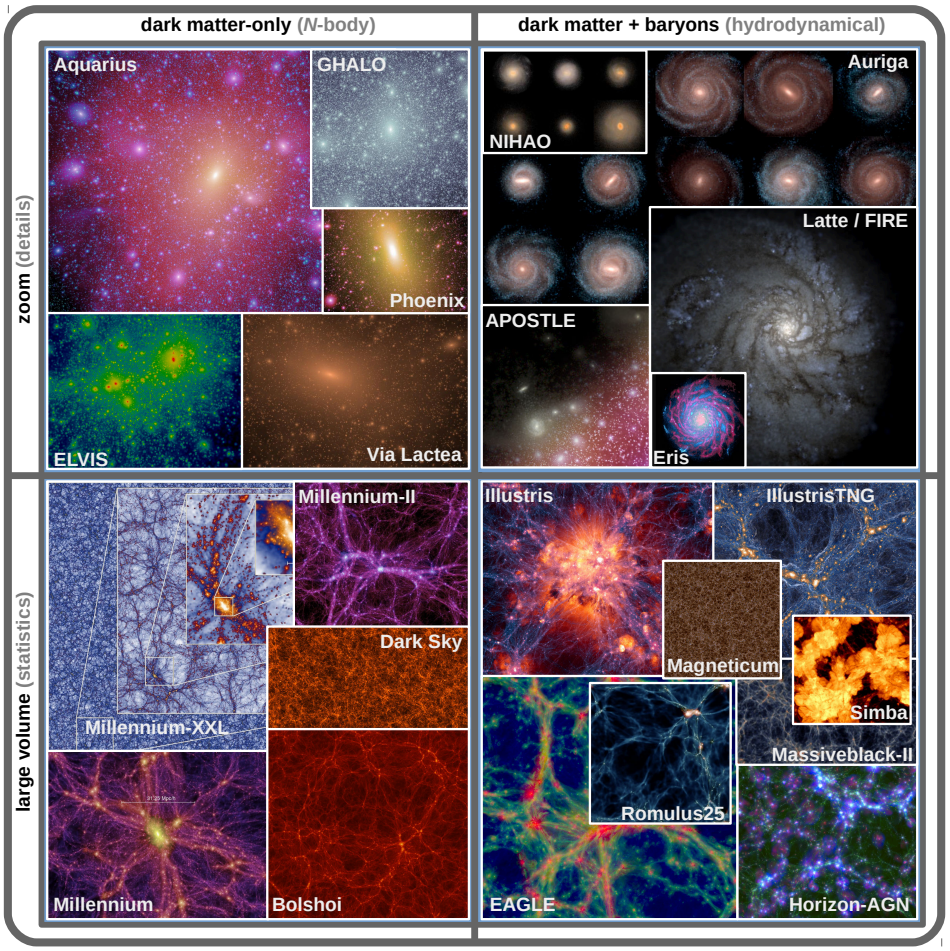

Figure 1.5 – *The figure shows representative images from various cosmological simulations segregated into four different types: N-body versus hydrodynamical (left versus right columns), and zoom versus large volume (top versus bottom rows). Image courtesy: Vogelsberger et al. (2020).*

Success of N-body codes: Cosmological N-body simulations have successfully reconstructed non-linear structure formation and have shown that dark matter on the large scales is distributed in a web-like pattern consisting of filaments, clusters, walls and voids. They also predict that the two point correlation function for dark matter is different from that of galaxies, as the brightest galaxies form in massive haloes, which are biased tracers of the matter distribution. According to the cold dark matter model, structure forms hierarchically through merging. As a result, we find that the halo mass function has a unique shape with a large number of low-mass haloes and fewer high-mass haloes. N-body codes have successfully reproduced the halo mass functions with a greater resemblance to the ellipsoidal collapse model (Sheth & Tormen 2002) compared to the spherical collapse model (Press & Schechter 1974). N-body simulations today have excellent resolutions and have revealed several internal structural features of the cold dark matter haloes. One of the prominent discoveries is that of a universal radial density profile known as the Navarro-Frenk-White profile (Navarro, Frenk & White 1997).

1.3.2 Simulating galaxies

Although dark matter and dark energy dominate the cosmic budget, to make predictions for the visible Universe, we need baryons that make up galaxies. Simulating baryons is complicated because we have to simultaneously resolve processes on the very large scales as well as processes at galactic scales such as star formation, AGN and supernovae. Most of the relevant baryonic processes take place at scales below those resolved by cosmological simulation and are included as sub-grid models, i.e. phenomenological prescriptions that try to approximate the average behaviour of processes unresolved by simulations. For example, gas particles have masses of million of solar masses and the stellar particles correspond to single stellar populations with similar total masses.

Successes of hydro simulations: The recent decade has seen several large volume simulations that can reproduce surprisingly well many global properties of galaxies, such as the stellar mass function, the bimodality of star-formation rates and colours, and galaxy morphologies. Some of the most studied and most advanced hydrodynamical simulations include: Illustris(Vogelsberger et al. 2014), EAGLE (Schaye et al. 2015), Horizon AGN (Dubois et al. 2014), Illustris TNG (Springel et al. 2018), Magneticum (Bocquet et al. 2016) and a few others have been very successful in this respect.

One of the main strengths of hydrodynamical simulations is that they make detailed predictions for the structure and dynamics of stars and that of gas, both inside and outside galaxies. For example, they can resolve the hot gaseous atmospheres around galaxies (circumgalactic medium) and between galaxies

(inter galactic medium). These are essential for studying the cosmic distribution of baryons, which currently has several unsolved questions such as the missing baryons problem, and for probing the Universe in hot ionized gas, such as the Sunyaev-Zel'dovich effect.

Limitations: Cosmological hydro simulations have offered a great platform to carry out detailed studies of the Universe, but they come with a set of caveats. Sub-grids models are unavoidable because of the multiscale nature of structure formation. The resolution scale of a simulation is limited as the scale range varies by around 12 orders of magnitude between AGN (10^{-3}pc) and large-scale structures (1 Gpc). Therefore, certain calibrations or adjustments are made in large simulations where the small scale models cannot afford to be as detailed as in zoom simulations. This means that the simulations do not follow the actual physical processes responsible for galaxy formation, but only approximate them using simplified phenomenological models. Thus, their validity is only as trustworthy as the sub-grid models they employ.

1.4 The Cosmic Web

The complex intricate large-scale structure pattern we observe emerges from seemingly simple physical laws and initial conditions. The complexity arises as gravity collapses over-dense patches and amplifies the anisotropy of the matter distribution. This gives rise to the clusters, filaments, walls and voids that together form the cosmic web.

1.4.1 Anisotropic collapse

The anisotropic collapse is a consequence of gravitational instability, in which slight asphericities are amplified due to gravity. It can be understood very well from the first order Zel'dovich approximation (Zel'Dovich 1970) but also by the fully nonlinear ellipsoidal equations (Icke 1973).

The Zel'dovich formalism

The Zel'dovich approximation (Zel'Dovich 1970) is an analytical approach that provides an intuitive way to comprehend the emergence of the cosmic web through the anisotropic collapse of matter. It is a first order lagrangian perturbation theory. It describes the trajectory of fluid elements or particles as a ballistic motion purely due to the gravitational field given by the initial fluctuations.

Consider a set of mass elements that are uniformly distributed in space. Let $\mathbf{q}$ be the initial Lagrangian coordinate (i.e. in the initial conditions) of a

particle in this space. The particles are now subjected to a displacement by only the initial gravitational potential. The Zel'dovich approximation states that the Eulerian coordinate at time t, $\mathbf{x}(t)$, of this particle, is related to its initial position, $\mathbf{q}$, through a ballistic term (i.e. depending only on the initial fluctuations) given by

$$\mathbf{x}(t) \;=\; \mathbf{q} \;+\; D(t)\,\nabla\mathbf{\Psi}(\mathbf{q}). \tag{1.12}$$

Here, $D(t)$ is the linear growth factor and $\mathbf{\Psi}(\mathbf{q})$ is a vector field related to the initial gravitational potential field ϕ, which is given as

$$\mathbf{\Psi}(q) = \frac{2}{2Da^2H^2\Omega_m}\phi(\mathbf{x},t). \tag{1.13}$$

Based on this, it is possible to infer the evolution of the density field by requiring mass conservation, that is the mass $\rho_o d^3\mathbf{q}$ within the initial volume $d^3\mathbf{q}$ will be the same after it is displaced. Therefore,

$$\rho_o\, d^3\mathbf{q} = \rho\, d^3\mathbf{x} \quad\Longrightarrow\quad \rho \;=\; \rho_o \left|\frac{\partial\mathbf{x}}{\partial\mathbf{q}}\right|^{-1}. \tag{1.14}$$

where $\left|\frac{\partial\mathbf{x}}{\partial\mathbf{q}}\right|$ is the Jacobian of the transformation from Eulerian to Lagrangian coordinates. Rewriting the above equation using Equation 1.12, we obtain

$$\rho = \frac{\rho_o}{[1-D\lambda_1][1-D\lambda_2][1-D\lambda_3]}. \tag{1.15}$$

Here $\lambda_1, \lambda_2, \lambda_3$ denote the eigenvalues of the deformation tensor,

$$\mathbf{\Psi}_{ij} = \frac{\partial^2\Psi}{\partial q_i \partial q_j}. \tag{1.16}$$

The approximation was introduced half a century ago and it still stands as a robust model to estimate the distribution of matter on large scales based purely on the initial density field. This is because it is simply a first order lagrangian perturbation. This makes the formalism very powerful for setting up the initial positions and velocities of particles in N-body simulations.

The nature of the eigenvalues of the tidal deformation tensor from Equation 1.15 provide insightful information on the processes that shape the initial matter fluctuations into pancakes, filaments and clusters. The absolute values give the lengths of the three axes of the deformation ellipsoid. A positive value implies a compression along the corresponding axis and negative value means an expansion. A positive λ blows ρ up as the term $1 - D(t)\lambda \longrightarrow 0$. A combination of positive and negative values of λ_i results in clusters, filaments, walls and voids as summarised below.

Nodes or **clusters** are formed if there is a collapse along all three axes of a similar magnitude: $\lambda_1 \approx \lambda_2 \approx \lambda_3 > 0$. This leads to a close to spherical collapse of the volume and hence an overdensity.

Filamentary structures are formed when the collapse occurs along the two longest axes, provided the magnitude or the strength of collapse is comparable: $\lambda_1 \approx \lambda_2 > 0$.

Walls or **sheets** form when the compression is along the first axis, i.e, $\lambda_1 > 0$. The density along the compressed axis is highest compared to the other two, $\lambda_1 >> \lambda_2 \approx \lambda_3$.

Voids are formed due to an expansion along all three axes with all negative eigenvalues $\lambda_1 > \lambda_2 > \lambda_3$.

Tidal shear force is driving the collapse of matter into sheets, filaments and clusters. Initially, planar sheets are formed. These sheets drain into filaments which further drain into clusters.

The Zel'dovich approximation breaks down when there is shell crossing. At this point, Zel'dovich approximation predicts that matter will continue to stream away, whereas in reality, matter binds due to gravity and forms structures. The adhesion model (Gurbatov, Saichev & Shandarin 1989; Kofman, Pogosian & Shandarin 1990; Kofman et al. 1992; Hidding et al. 2012) overcomes this drawback by introducing an additional viscosity term that ensures that particles stick together.

1.4.2 Characteristics of the cosmic web

The cosmic web consists of numerous clusters interconnected by cosmic filaments that stretch across the universe bordering diffuse sheets (walls) and huge spaces of emptiness in between, known as voids. These constituent elements exist on several spatial scales. This complex cosmic network is dynamic and constantly evolving (Cautun et al. 2014), with dark matter and galaxies flowing out of the voids and into the walls and filaments, with filaments also acting as pathways (Bond, Kofman & Pogosyan 1996; Colberg, Krughoff & Connolly 2005; van de Weygaert & Bond 2008a; Aragón-Calvo, van de Weygaert & Jones 2010a) that transport matter into clusters (van Haarlem & van de Weygaert 1993a; Knebe et al. 2004). The main features of the cosmic web are its:

- anisotropic components
- multiscale nature (as a result of hierarchical evolution)
- overdense-underdense asymmetry

- complex connectivity

The largest structures known today are the **superclusters** consisting of millions of galaxies, such as the *Great Attractor* (Lynden-Bell et al. 1988), the *Shapley* cluster (Shapley 1930; Proust et al. 2006), the *Vela* supercluster (Kraan-Korteweg et al. 2017; Bharadwaj, Bhavsar & Sheth 2004; Romano-Díaz & van de Weygaert 2007; Libeskind et al. 2015) and our own home supercluster Laniakea (Tully et al. 2014; Tempel 2014a). A catalogue for superclusters using SDSS data has been made by Liivamägi, Tempel & Saar (2012).

These clusters are connected by **filaments** which are the most prominent and defining features of the web. They contain nearly 50% of the total mass of the Universe (Cautun et al. 2014), even though their average matter density is less than clusters. The *Pisces-Pegasus* filament (Batuski & Burns 1985), which is $130h^{-1}$ Mpc and part of the *Perseus-Pisces* complex Haynes & Giovanelli (1986), is one of the largest filaments known today in the local UniverseSeveral filaments extracted from the SDSS galaxy survey of the local Universe have been catalogued by Tempel et al. (2014b). They found that the longest filament in their sample had a length of $60h^{-1}$ Mpc, illustrating the immensity of these objects. Surrounding the filaments are large planar structures known as **walls** or **sheets**. They are more diffuse and visually less prominent than filaments, but occupy large volumes, only lesser than that of voids. The largest wall structure known today is the *BOSS Great Wall*, with a volume of $2.4 \times 10^5 h^{-3} Mpc^3$ (Lietzen et al. 2016). Two other prominent specimens of walls are the *CfA Great Wall* (Geller & Huchra 1989), and the *Sloan Great Wall* (Gott et al. 2005).

Voids are empty regions of space and occupy 77% of the total volume of the Universe (Platen, van de Weygaert & Jones 2007, 2008; Cautun et al. 2014; van de Weygaert 2016), but with only 15% of the total mass, making them the most matter-poor regions of the Universe. Voids are of several sizes and multiscale in nature forming a foam like network. Their hierarchical growth is described by the extended Press-Schechter formalism (Sheth & van de Weygaert 2004). Observations of the large-scale structures serve also as testing grounds for deviations from General Relativity on scales that is difficult to probe by other means (Jain & Khoury 2010; Koyama & Sakstein 2015; Berti et al. 2015). Voids, in particular, are very good probes for dark energy (Platen, van de Weygaert & Jones 2008; Lavaux & Wandelt 2010, 2012; Bos et al. 2012; Sutter et al. 2015; Pisani et al. 2015).

1.4.3 Tracing the structural features

The evolution of large-scale structures and its properties such as size, distribution and density depend on the cosmological parameters such as matter density and dark energy. Therefore the cosmic web offers a wealth of information to constraining the underlying cosmological model and to further understand galaxy evolution physics. The structural features of the cosmic web probe a variety of scales and can shed light both on the linear and the non-linear regimes. The geometry and topology of the various web elements hold key information on the dynamical processes that shaped them. This makes it crucial to detect the structures and characterise their morphology. Detecting and characterising web elements can be a challenging process due to its complexity and multi-scale nature. Web elements vary structurally, in their densities, geometry, connectivity and galaxy mass distributions. There are currently several methods to characterise the web that account of for a few of these variations and result in a cosmic web that is specific to its definition. Depending on the science case at hand, it is ideal to choose a web extraction definition that suits the problem. There are several formalisms to extract the morphological features of the cosmic web (see e.g Libeskind et al. 2018), each with their own set of strengths and drawbacks. Those that are currently being used can be broadly categorized into the following:

1. **Graphical techniques**: This family of web extractors employs concepts derived from graph theory to detect the web. Initial attempts to formulate an algorithm that traces the filamentary network using particle distribution resulted in the minimal spanning tree (MST) method introduced by Doroshkevich in Doroshkevich (1970a); Barrow, Bhavsar & Sonoda (1985). These methods have advanced with a recently developed technique known as the Adapted Minimal Spanning Tree by Alpaslan et al. (2014a) developed for identifying filaments and voids in the GAMA survey (Alpaslan et al. 2014b) and Metric Space Technique by Wu, Batuski & Khalil (2009). More recently, *Semita* (Pereyra et al. 2019) and T-Rex (Bonnaire et al. 2019) have been developed. The major advantage is that these methods can be directly applied on a discrete distribution of galaxies and haloes with or without smoothing.

2. **Geometric techniques**: A natural approach, and indeed the most frequently employed one, to characterise the large-scale structure is based on the geometric information of the cosmic web. The key principle is to determine the morphology of a web element by computing the Hessian of either density, tidal or velocity shear fields. These can either be done on a fixed smoothing scale or on multiple scales and combined using the *Scale Space* technique. A class of web finders that use the tidal field

information are by Hahn et al. (2007b), Forero-Romero et al. (2009) and Bond, Strauss & Cen (2010a,b).

Scale space based methods:
This subclass of methods detect the structures based on the geometry of the density field and delineate the morphological elements simultaneously at several scales. The first methods to implement the *Scale Space* formalism to encapsulate the multi-scale nature of the cosmic web was the MMF technique (Aragón-Calvo et al. 2007a), NEXUS+ (Cautun, van de Weygaert & Jones 2013) and MMF2 (Aragon-Calvo & Yang 2014). They discern the morphological features at several scales makes it best to apply for scientific problems that search for influence of large scales on smaller scales. Therefore, in this thesis we mainly use NEXUS. The NEXUS suite of web classification methods also employ a scale space approach and can be applied to density, tidal and velocity shear fields.

Web extraction techniques V-web and have been developed by Hoffman et al. (2012); Libeskind et al. (2012) that use the velocity shear information to detect the web morphology.

3. **Topological techniques**: This class of web finders identifies structures based on topological properties such as genus and connectivity, that draw inspiration from algebraic topology and Morse theory (Morse 1996). They offer a powerful perspective on the connectivity and the multiscale configuration of galaxies in the Universe. Few prominent examples under this subclass are the *shape finder*, SURFGEN2 algorithms (Sahni, Sathyaprakash & Shandarin 1998; Sheth & Sahni 2005; Bag et al. 2019), the *Watershed Transform* developed as the Watershed Void Finder to detect underdense void basins in the cosmic web (WVF; Platen, van de Weygaert & Jones 2007) and ZOBOV (Neyrinck 2008). The Spineweb technique Aragón-Calvo, van de Weygaert & Jones (2010b) extended the WVF method to also detect the sheets, filaments, and nodes of the web. A similar approach, the DisPersSE formalism (Sousbie 2011; Sousbie, Pichon & Kawahara 2011) identifies filaments.saddle point and walls as regions around two minima and centred around a saddle point.

4. **Stochastic techniques**: This class of web-finders extracts the structural features by statistically analysing stochastic processes applied directly on galaxy or halo distributions. The Bisous model (Stoica et al. 2005; Tempel et al. 2014c) is developed based on an object point process with connected and well aligned cylinders. It has been used to successfully extract and catalogue the filaments from the SDSS galaxy distributions (Tempel et al. 2014b). A major advantage of this technique is that it can be directly applied in the galaxy distribution and does not need any

density field reconstructions. Few other prominent stochastic techniques are the Filament Identification using NodEs (FINE) method described in González & Padilla (2010), very recently (Burchett et al. 2020) have proposed the Monte Carlo Physarum Machine (MCPC) method which is an agent based algorithm that emulates the growth of the organism *Physarum polycephalum* also known as slime mould.

5. **Phase space techniques**: The motivation behind this class of web classifiers is the intrinsic velocity dispersion of particles in the early Universe is tiny and the mass distribution appears as a 3D sheet folding in a 6D phase space, known as the *phase space sheet* (Shandarin 2011; Abel, Hahn & Kaehler 2012; Falck, Neyrinck & Szalay 2012). The ORIGAMI technique (Falck, Neyrinck & Szalay 2012; Falck & Neyrinck 2015), the phase-space sheet formalism or the MultiStream Web Analysis (MSWA) by Shandarin (2011); Ramachandra & Shandarin (2015) and the Claxon formalism (Hidding 2017; Gurbatov, Saichev & Shandarin 1989; Hidding et al. 2012), DynamIcal Void Analysis (DIVA) (Lavaux & Wandelt 2010) fall into this category.

6. **Machine learning fromalisms**: With the advent of several deep learning methods, applying it to identify and classifying the cosmic web is a promising approach. The first attempt to characterise filaments and walls was carried out by Aragon-Calvo (2019). The classification is done using a deep convolutional neural network (CNN) with a U-Net architecture that was trained with a Voronoi model and the MMF2 geometric technique to uncover the web features. Buncher & Carrasco Kind (2019) have introduced a new way to classify particles in the cosmic web using a supervised machine learning algorithm. One of the main concerns of the deep learning approach is the possible classification of spurious features as real ones, because the framework on which they work may not always have a physical reasoning. Such drawbacks can be overcome by using a physical formalism up to a certain level of training before the neural net layers take over.

In this thesis we compare the differences between geometric and statistical techniques specifically the NEXUS+, NEXUS_VELOCITY_SHEAR (Cautun, van de Weygaert & Jones 2013) and the Bisous (Tempel et al. 2014c; Stoica et al. 2005) models for the specific case of galaxy and halo spin alignments in the cosmic web. The geometric formalism is motivated by the anisotropic collapse and the stochastic technique reconstructs the filamentary network based on the connectivity and alignment of cylinders.

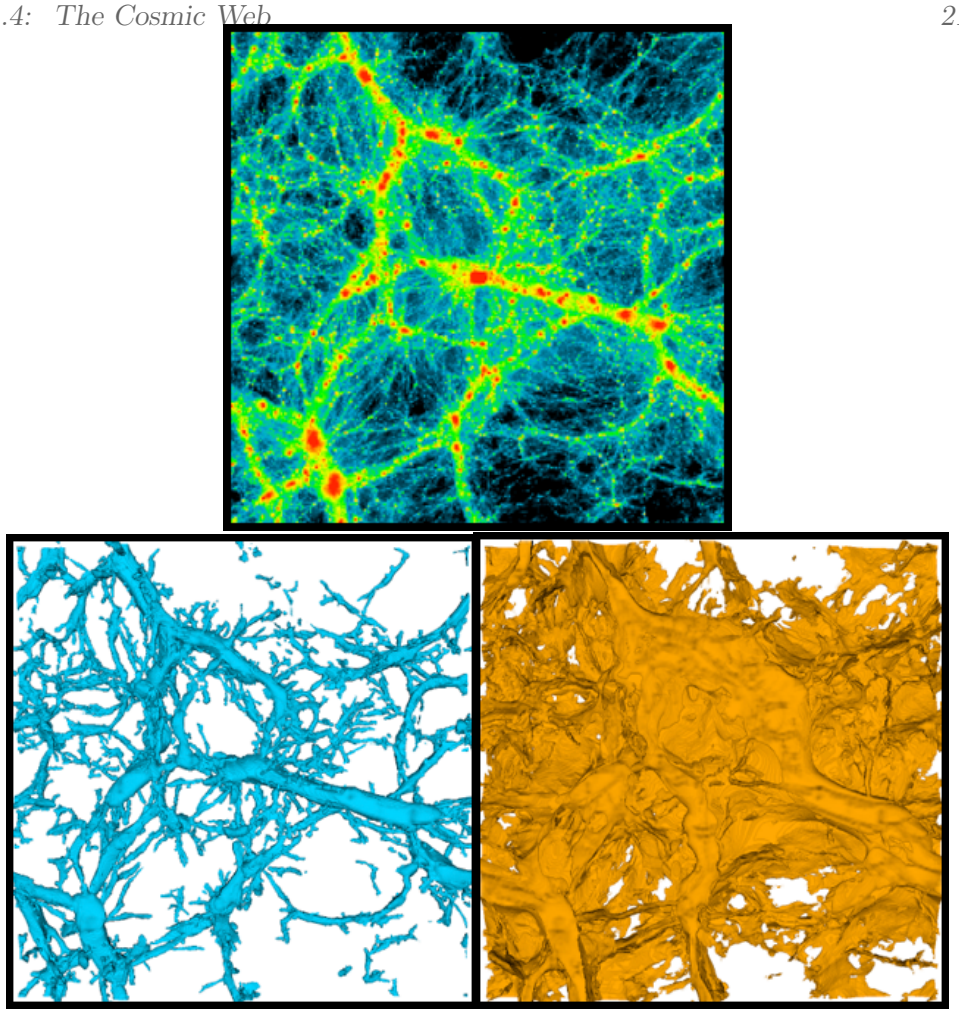

Figure 1.6 – *A* $10h^{-1}$ Mpc *slice of a simulation showing the dark matter density field on top. The multiscale filamentary network extracted from this using* NEXUS+ *is shown in the bottom-left panel and the walls in the bottom-right panel. Figure courtesy: Cautun et al. (2014).*

1.4.4 MMF/NEXUS

The NEXUS suite of cosmic web detection is a scale-space technique that captures the multiscale nature of the cosmic mass distribution. Unlike most other techniques it addresses the hierarchical growth of the cosmic web. NEXUS (Cautun, van de Weygaert & Jones 2013) represents a development of the Multiscale Morphology Filter (MMF) (Aragón-Calvo et al. 2007a) to explicitly include physical factors that are important in structure formation. The MMF itself has its roots in the field of medical imaging (Sato et al. 1998; Li, Sone & Doi 2003), where such methods are designed to detect nodes and blood vessels in medical images.

1

NEXUS extracts the geometric information of the cosmic web at several scales and classifies the morphological features based on the principle that anisotropic collapse generates various structural features. In this thesis, we compare two of the NEXUS methods, namely NEXUS+ and NEXUS_VELOCITY_SHEAR, that use logarithms of the density field and velocity shear fields respectively.

NEXUS+ looks at the local geometry as expressed in the Hessian of the density field. It recovers the morphological elements far more vividly at multiple scales compared to other techniques as it employs the scale-space technique. NEXUS+ works by calculating the eigenvalues of the Hessian of the log density field at multiple smoothing scales. Then, the sign and inequalities of these eigenvalues decide the nature of the morphological element and the associated eigenvectors represent its orientation. It is important to note that the eigenvalues obtained here are not exactly the same as the ones we saw in Zel'dovich approximation as in NEXUS+, we take the Hessian of the present day non-linear density field and not of the initial one. Also, in the Zel'dovich formalism, it was the deformation tensor, obtained by calculating the Hessian of the gravitational potential.

NEXUS_VELOCITY_SHEAR uses the velocity field information to delineate the features of the web. The divergence of the velocity flow indicates either an expansion or a contraction of a mass element. Thus, while NEXUS+ uses geometric signatures to identify the cosmic web, NEXUS_VELOCITY_SHEAR identifies it through its dynamical signatures. This is achieved by calculating the shear of the velocity flow that is induced by the underlying gravitational potential which drives the cosmic structure formation. More specifically, the velocity shear is the symmetric part of the velocity gradient*, with the ij component is:

$$\sigma_{ij}(\mathbf{x}) = \frac{1}{2H}\left(\frac{\partial v_j}{\partial x_i} + \frac{\partial v_i}{\partial x_i}\right) , \tag{1.17}$$

where v_i is the i component of the velocity. In this definition, the velocity shear is normalized by the Hubble constant, H.

Both NEXUS+ and NEXUS_VELOCITY_SHEAR basically refer to the Hessians, but of different physical quantities. Hessian of the density field gives the shape around a point and the Hessian of the velocity potential is the velocity shear. This is simply the second order term of the variation of the density and velocity potential around a point. For example, Hessian of the density field corresponds to the ellipsoidal shape around a peak or a trough, and hence captures its geometric shape. This is the main motivation to use these methods to study the shape and spin alignment of haloes with the large-scale web.

* The velocity shear is sometimes defined as the traceless symmetric part of the velocity gradient. But we use only the divergence part of the velocity flow which reflects the contraction or expansion of a mass element.

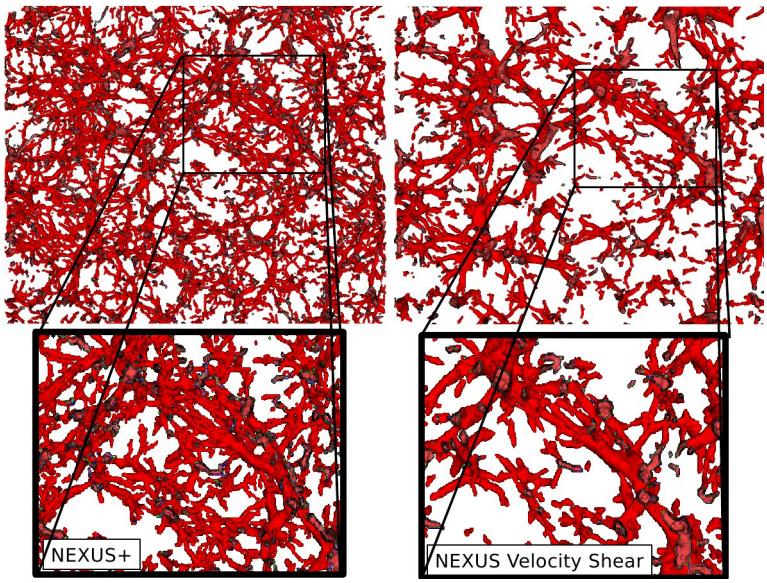

Figure 1.7 – *This image shows the filamentary network extracted from* NEXUS+ *and* NEXUS_VELOCITY_SHEAR *from the same slice of the P-Millennium N-body simulation. Image reproduced from: Ganeshaiah Veena et al. (2018).*

More details on the working and the comparison between these two formalisms are addressed in section 2.2 of the thesis. For a full description of all the associated group of NEXUS techniques, see Cautun, van de Weygaert & Jones (2013). In Figure 1.7 NEXUS+ and NEXUS_VELOCITY_SHEAR filaments extracted from the same slice of a simulation are shown for comparison.

1.4.5 Bisous model: filamentary network using marked point process

The Bisous model extracts filaments from a given galaxy distribution based on a marked point process. The model was originally designed to extract spatial patterns (Stoica et al. 2005) such as rivers and highways from a satellite image. This has been further remodelled to detect the filamentary network from a three dimensional galaxy distribution (Tempel et al. 2014c). A marked point process is a point process with a mark associated to every point. In the Bisous filament extraction technique, cylinders are randomly distributed on a given galaxy distribution. It is then estimated how likely it is that the cylinder corresponds to a cosmic filament by comparing the number of galaxies inside the cylinder with the number just outside. The centers of these cylinders are considered as points in the point process. The mark in this context is the

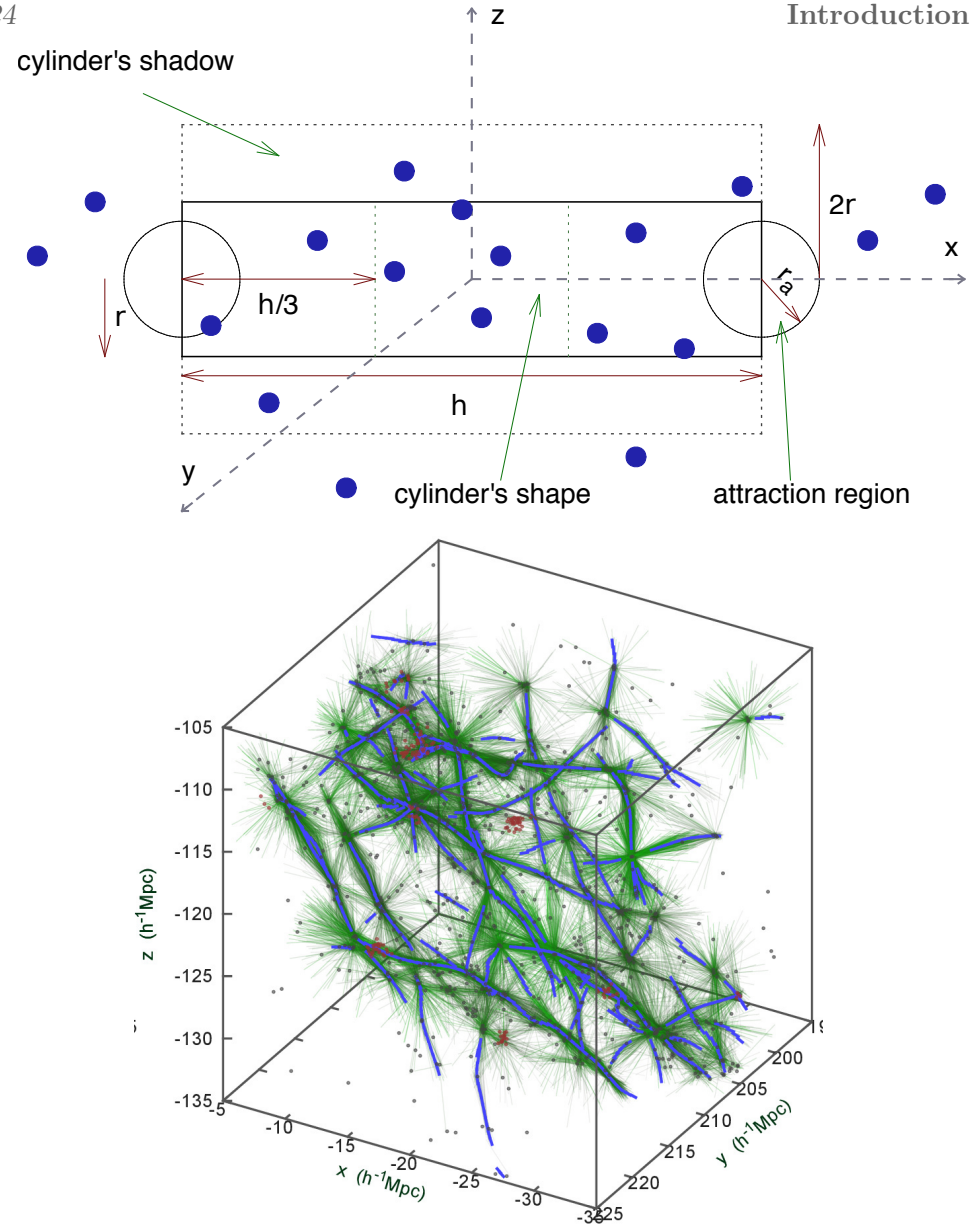

Figure 1.8 – *Top panel: The points represent galaxies and the cylinder is the object used in the marked point process. The regions that connect to neighbouring cylinders are depicted as circles. Right panel: Filamentary network reconstructed from several* MCMC *realizations. Figure adapted from Tempel et al. (2014b).*

radius, length and orientation of the cylinder. The cosmic web filamentary network is then constructed by selecting the most connected and well-aligned

cylinders. These cylinders have a fixed radius, whereas the length varies within a specified range.

A key advantage of this model over other structure identifying formalisms is that it does not require a smooth density field reconstruction but, the smoothing is implicit while defining the radius and other properties of the cylinders. The filaments are extracted directly from a galaxy distribution, proving to be very useful in observations. The model provides two important outputs - the filament detection probability field and the filament orientation field. For a detailed explanation of the mathematical framework of the Bisous model, see Tempel et al. (2014c, 2016). A catalogue of filaments identified using Bisous from the SDSS galaxy survey can be found in Tempel et al. (2014a). In this thesis, we apply the Bisous model to the spatial distribution of galaxies in the EAGLE simulation, see chapter 3 for further details.

1.5 Galaxies caught in the web

The initial density peaks in the primordial Universe grow linearly up to a certain critical density, and then collapse to form virialized structures such as dark matter haloes. The haloes represent the gravitational wells in which baryonic matter aggregates, cools, and undergoes a multitude of small-scale processes such as fragmentation and star-formation, to ultimately form galaxies. Thus, every galaxy is characterized by a surrounding dark matter halo.

Galaxies form in the highest local density peaks of the initial fluctuation field (Kaiser 1984; Bardeen et al. 1986; van de Weygaert & Bertschinger 1996a), and are embedded within a network of invisible dark matter. Therefore, exploring the links between galaxies and the cosmic web helps to shed light both on the underlying dark matter density field and also on the physics of galaxy formation.

The dependence of galaxy properties on environment has been a hotly studied topic since the pioneering work of Dressler (1980). Galaxies in high density cluster environments are usually populated by red, quiescent early-type galaxies, whereas blue star forming galaxies tend to be found in low-density regions (Dressler 1980; Kauffmann et al. 2004; Baldry et al. 2006; Bamford et al. 2009; Kreckel et al. 2011, 2012).

There has also been increasing evidence on the correlations between galaxy properties and the local cosmic web environment. Alpaslan et al. (2015, 2016) showed in the GAMA survey that the stellar mass of isolated spiral galaxies increases if they are closer to filaments, but the specific star formation rate decreases. A similar effect was reported by Malavasi et al. (2017) in the VIPERS survey. In contrast, Kuutma, Tamm & Tempel (2017) do not find an increase

in stellar mass closer to filaments. There is a general consensus on an increased fraction of star-forming galaxies in filaments compared to field regions of the Universe (Fadda et al. 2008; Darvish et al. 2014). Kuutma, Tamm & Tempel (2017) also report an increase in the ratio of the number of elliptical to spiral galaxies from voids towards filament spines. van de Weygaert (2000); van de Weygaert et al. (2011) report that void galaxies are bluer with an increased star formation rate, which is consistent with the trend that galaxies in low densities have a higher specific star formation rate.

Several studies have established links between halo/galaxy properties and their host cosmic web environment in numerical simulations. For example, Aragon Calvo, Neyrinck & Silk (2019) propose that the local web environment is a major driver of galaxy quenching. They have argued that when the galaxies detach from the cosmic web environment surrounding them, they stop accreting gas and thus undergo star-formation quenching. Hahn et al. (2007a) reported correlations between halo spin, shape and its web environments, Cautun et al. (2014) showed that halo mass function evolve distinctly depending on the web environment, (see subsection 3.3.3 for more details).

However, the most prominently studied topic that reflects the influence of the cosmic web on galaxy evolution is the spin of galaxies and its alignment observed with large-scale filaments (Jones, van de Weygaert & Aragón-Calvo 2010; Tempel, Stoica & Saar 2013; Tempel & Libeskind 2013a; Hirv et al. 2017; Welker et al. 2020; Blue Bird et al. 2020), which is also the topic of this thesis. This is discussed in much more detail in section 1.7. In the next section we will study how a galaxy acquires its angular momentum from tidal torques that results in a spin alignment with the large-scale structures.

1.6 Angular momentum

In physics, angular momentum is a conserved quantity. So, how are galaxies and haloes rotating if they started with zero angular momentum? There were two competing theories to explain the origin of rotation in galaxies, *the cosmic turbulence theory* and *the gravitational instability theory* (for a review see eg. Jones 1976). According to the turbulence theory, galactic spins are the residuals of early turbulence such as the primordial vortices. But this theory did not succeed as the initial velocity field is irrotational, and vorticity is damped due to the expansion of the Universe, as it is not amplified by gravity. The gravitational instability picture suggests that nascent clouds of matter known as protogalaxies started spinning due to the tidal interactions with the surrounding clumps of matter. Fred Hoyle pioneered in connecting galaxy spins to the large-scale tidal fields (Hoyle 1949).

> *'We now reach the important step of interpreting the external gravitational field that produces the couple acting on the condensation. Instead of regarding this field as arising from a neighbouring galaxy, we notice that there are large-scale irregularities in the distribution of the internebular material. The existence of such irregularities probably exist also among the general field nebula...'*
> –**Fred Hoyle**, in the paper submitted to the proceedings *Problems of Cosmical Aerodynamics*, **1949**.

James Peebles highlighted this idea in his paper, Peebles (1969), and computed the galaxy angular momentum using linear theory to study its growth within a comoving spherical region.

In this paper, Peebles calculates the angular momentum for two different regimes in an expanding universe. The linear phase when protogalaxies can still be regarded as density fluctuations above the mean matter density of the universe and the non-linear phase where galaxies are more compact objects.

Although Peeble's work headed in the right direction, he incorrectly assumes the Lagrangian volume of a protogalaxy is spherical. This assumption gives no angular momentum for the first order perturbations (White 1984) and so he uses second order in density perturbation. With this assumption, he shows that the spin in these regions grow as $t^{5/3}$ for an Einstein-de Sitter universe. Doroshkevich (1970b) rectified this and showed that the angular momentum, $\mathbf{J}$ grows linearly ($J(t) \propto t$) for first order perturbations in a flat universe and that Peebles' result ($J(t) \propto t^{5/3}$) is a consequence of his imposed symmetry. White (1984) expounded this theory and used N-body simulations to verify the results by Doroshkevich (1970b), thus, laying the very foundation for the currently accepted tidal torque scenario.

1.6.1 The Tidal Torque Theory

The *Tidal Torque Theory* (TTT) (Hoyle 1949; Peebles 1969; Doroshkevich 1970b; White 1984; Catelan & Theuns 1996; Porciani, Dekel & Hoffman 2002a; Schäfer 2009) is a theoretical framework explaining the origin and growth of angular momentum of haloes and galaxies in an expanding Universe. Within the TTT framework, the fluid elements (e.g. dark matter particles) associated to a halo are followed back in time to obtain the Lagrangian region that collapses to form that halo. This region is often referred to as the protohalo, and, can be followed in time to study how a given halo forms, as shown in Figure 1.9.

According TTT, a protohalo in the Gaussian inital field is not spherical, and its

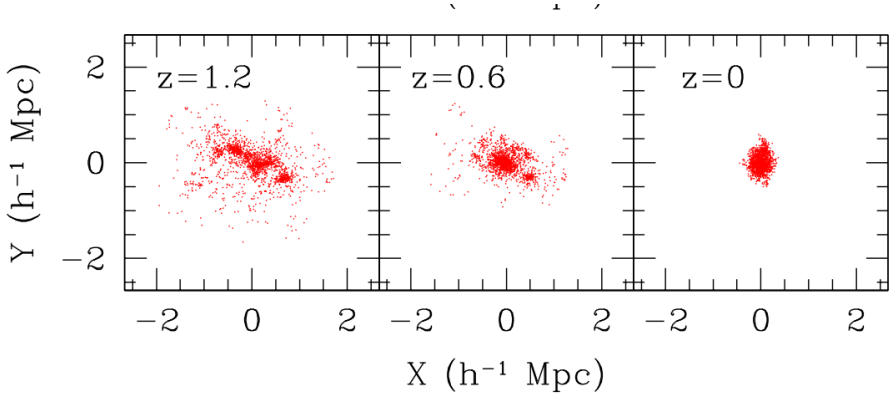

Figure 1.9 – *This figure shows the evolution of a protohalo with an irregular shape at redshift 1.2 to a collapsed halo at z=0. Figure from: Porciani, Dekel & Hoffman (2002a).*

moment of inertia is not perfectly aligned with tidal field. In such a scenario, the tidal field torques up the protohalo.

In the linear regime, as we have discussed in subsection 1.2.2, protohaloes are density perturbations above the background density of the universe. So, to follow the angular momentum growth in an expanding universe, let us first consider the growth of density perturbations. The matter overdensity at the physical coordinate $\mathbf{r}$ is defined as $1 + \delta(\mathbf{r}, t) = \rho(\mathbf{r}, t)/\rho_0(t)$ where ρ_0 is the average density of the universe. The physical coordinate $\mathbf{r}$ can be related to the comoving coordinate $\mathbf{x}$ by scaling with the expansion factor, i.e. $\mathbf{r}(\mathbf{q}, t) = a(t)\ \mathbf{x}(\mathbf{q}, \mathbf{t})$. Here, $\mathbf{q}$ is a Lagrangian coordinate defined as the position $\mathbf{x}$ of the particle as $t \longrightarrow 0$.

Now, consider all the material within a protohalo, that will eventually collapse to form a virialised halo. Let V_L be the Lagrangian volume that it occupies. Then, the angular momentum of all the material within this volume is

$$\mathbf{J}(t) = \int_{V_L} \rho_0 a^3\ [\mathbf{r}(\mathbf{q}, t) - \overline{\mathbf{r}}(t)] \times [\mathbf{v}(\mathbf{q}, t)]\ d^3\mathbf{q}. \tag{1.18}$$

Here, $\overline{\mathbf{r}}$ is the center of mass and $\rho_0 a^3$ is the mass element with a velocity $\mathbf{v}(\mathbf{q}, t)$ with respect to the center of mass of the protohalo. Re-writing this equation in comoving coordinates, we obtain

$$\mathbf{J}(t) = \rho_0 a^3 \int_{V_L} [a\mathbf{x} - a\overline{\mathbf{x}}] \times a\dot{\mathbf{x}}\ \ d^3\mathbf{q}. \tag{1.19}$$

In the linear regime, when $\delta << 1$, protohaloes can be approximated as small density perturbations above the mean and we can use the Zel'dovich formal-

ism (see subsection 1.4.1) to predict the angular momentum growth of a protohalo. Recall that the Zel'dovich approximation gives the displacement of a fluid element, $\mathbf{x} = \mathbf{q} - D(t)\nabla\phi(\mathbf{q})$ where $\phi(\mathbf{q})$ is the velocity potential but is proportional to the initial gravitational potential in the linear regime. By differentiating this with respect to time we get the term $\dot{\mathbf{x}}$. Since in the linear regime the direction of the displacement is along the direction of the velocity, the cross product of $\mathbf{x}$ with $\dot{\mathbf{x}}$ vanishes and the protohalo spin can be written as:

$$\mathbf{J}(t) = -a^2\dot{D}(t)\ \rho_0 a^3 \int_{V_L} [\mathbf{q} - \overline{\mathbf{q}}] \times \nabla\phi(q)\ \ d^3\mathbf{q}\ . \tag{1.20}$$

To garner deeper insight into the physical meaning of the above equation, we can approximate the potential with its second order Taylor series expansion around the initial protohalo centre, $\overline{\mathbf{q}}$. It has been found that the contributions from higher order terms does not significantly change the outcome (Porciani, Dekel & Hoffman 2002a). For simplicity we use the notation $\mathbf{q}' = [\mathbf{q} - \overline{\mathbf{q}}]$, to have

$$\phi(\mathbf{q}) = \phi(\overline{\mathbf{q}}) + q_i' \left.\frac{\partial\phi}{\partial q_i}\right|_{\overline{\mathbf{q}}} + \frac{1}{2} q_i' q_j' \left.\frac{\partial^2\phi}{\partial q_i \partial q_j}\right|_{\overline{\mathbf{q}}} \tag{1.21}$$

This represents the first three terms of the Taylor expansion that, when inserted into Equation 1.20 and after further algebraic manipulations, leads to

$$J_i(t) \quad = \quad a^2\dot{D}(t)\epsilon_{ijk} \left.\frac{\partial^2\phi}{\partial q_j \partial q_l}\right|_{\overline{\mathbf{q}}} \int_{V_L} q_l' q_k' \rho_0 a^3\ d^3\mathbf{q}\ , \tag{1.22}$$

where ϵ_{ijk} is the Levi-Civita or the antisymmetric symbol, $T_{jl} = \frac{\partial^2\phi(\mathbf{q})}{\partial q_j \partial q_l}$ is the tidal tensor, $I_{lk} = \int_{V_L} d^3\mathbf{q}\rho(q) q_l q_k$ is the moment of inertia tensor and summation is implied over repeated indices. The tidal tensor quantifies the deformation of a mass element and it reflects the underlying gravitational potential in the region, as the tidal field is the Hessian of the gravitational potential. Incorporating these, Equation 1.22 can be simplified and the i^{th} component of the angular momentum takes the elegant form,

$$J_i(t) = a^2\dot{D}(t)\epsilon_{ijk}\ T_{jl}\ I_{lk}\ . \tag{1.23}$$

This expression reflects that the angular momentum of a protohalo is the tensor product of the inertia tensor and the tidal tensor. The inertia tensor depends only on the shape of the material that ends up collapsing into the halo or galaxy whereas the tidal tensor depends also on the neighboring matter distribution.

The shape of the initial protohalo is jointly determined by the initial tidal field and by the non-linear tidal field at the halo position, which in turn induces correlations between I and T (Ludlow, Borzyszkowski & Porciani 2014).

Therefore, according to this framework, the spin of a halo is determined by the inertial tensor, tidal tensor and the initial misalignment between them. The growth factor for spatially flat Einstein de-Sitter universe is $D \propto a(t) \propto t^{2/3}$ and the term $a^2\dot{D}(t) \propto t$ so according to the linear TTT framework, the angular momentum grows linearly with time. The evolution of the angular momentum of protohaloes is rather accurately predicted by the linear TTT before collapse sets in (Catelan & Theuns 1996). Once the dark matter haloes collapse and detach from the expanding background, the tidal torquing continues, but at a much lower rate (Porciani, Dekel & Hoffman 2002a).

Limitations

Although TTT may be consistent with the overall growth of halo angular momentum, it cannot reliably predict the growth of individual haloes especially after collapse (Porciani, Dekel & Hoffman 2002a). This is because it is difficult to specify the Lagrangian volume that consists of all the matter that ends up in the halo. Secondly, it does not account for the effects of non-linear phases of halo evolution on its angular momentum. Even after collapsing into a bound virialised object, angular momentum of haloes evolve by merging with other haloes.

Another caveat is that the tidal field calculations depend on the scale on which it is smoothed. Tidal field and moment of inertia of a protohalo are not truly independent (Porciani, Dekel & Hoffman 2002a) so the outcomes can differ depending on their degree of alignment. Neyrinck et al. (2019) emphasize the lack of accuracy of the TTT because it rests on the assumption that an ellipsoid uniformly torques up in a non-rotating background of almost the same density as the background, which calls for questioning the effects on the boundaries. They further propose an alternative model to TTT known as the *Spin from Linearly Evolving Inner Motions* (SPIM) which predicts the angular momentum growth by following the velocity field within a protohalo.

All these studies point to the fact that TTT is a fine model and a good approximation up to the time of turn around, but it is not adequate and cannot be relied upon for more accurate growth calculations. It cannot also completely explain spin alignment trends seen with the cosmic web. Currently the best way to account for all these inadequacies is to use N-body simulations to fully capture the evolution of angular momentum into the non-linear regime.

1.6.2 Mergers and Accretion

After a halo collapses, it can acquire angular momentum via mergers, flybys, smooth accretion and accretion of satellites. During these processes, the accretion orbital angular momentum from the merger gets transformed into the total

angular momentum of the merged system. Vitvitska et al. (2002); D'Onghia & Navarro (2007); Peirani, Mohayaee & de Freitas Pacheco (2004) argue that mergers and satellite accretion cause a significant impact on angular momentum growth. D'Onghia & Navarro (2007) developed a model for the growth of halo angular momentum as a stochastic increase resulting from merger events and the model correctly reproduces the log-normal distribution of the halo spin. Bett & Frenk (2012, 2016) explicitly show that the halo spin vector can flip over its lifetime after it is collapsed, as a result of these mechanisms.

1.7 Spin and shape alignments in the cosmic web

The cosmic web is a mildly nonlinear manifestation of the large-scale tidal fields , and according to TTT, the same tidal fields also torque up protohaloes. Therefore, we expect a correlation between galaxy spins and the underlying geometry of the cosmic web.

In Equation 1.23, if we choose a reference frame where T is diagonal, we can express the components of the angular momentum in terms of the eigenvalues λ_i of T as

$$
\begin{aligned}
J_1 &\propto (\lambda_2 - \lambda_3) I_{23}, \\
J_2 &\propto (\lambda_3 - \lambda_1) I_{31}, \\
J_3 &\propto (\lambda_1 - \lambda_2) I_{12}.
\end{aligned}
$$

Since $\lambda_1 \geq \lambda_2 \geq \lambda_3$, J_2 is the largest component of $\mathbf{J}$. In an ideal situation where the inertia tensor of the Lagrangian volume and the tidal fields are *initially uncorrelated*, we would expect the angular momentum of a protohalo to be preferentially along the second eigenvector of the tidal field.

In reality, tidal fields and the inertia tensor are correlated (Lee & Pen 2000; Porciani, Dekel & Hoffman 2002a), so the dependence between the tidal field and the angular momentum evolution is more complex, with the correlation becoming weaker at lower redshifts. Therefore, we need robust statistics to detect angular momentum alignments with the cosmic web at current times.

1.7.1 Halo spin alignments

Starting with the work by Aragón-Calvo et al. (2007b). several subsequent studies have shown a mass-dependent spin alignment trend with respect to the large-scale filaments in large N-body cosmological simulations. Low-mass haloes, usually below $M < 10^{12} h^{-1} \mathrm{M}_{\odot}$, tend to spin aligned along the filament axis, while those with higher mass tend to spin perpendicular to the filament axis (Hahn et al. 2007a; Codis et al. 2012; Libeskind et al. 2013; Trowland,

Lewis & Bland-Hawthorn 2013; Dubois et al. 2014; Welker et al. 2014; Forero-Romero, Contreras & Padilla 2014; Codis, Pichon & Pogosyan 2015; Wang & Kang 2017, 2018a; Ganeshaiah Veena et al. 2018; Codis et al. 2018; Ganeshaiah Veena et al. 2019; Kraljic, Davé & Pichon 2020). Results from several studies are compared in Table 1.

The mass at which the halo population goes from a preferential parallel to perpendicular alignment is known as the transition mass and it is usually around $10^{12}h^{-1}\mathrm{M}_{\odot}$, with variations across studies. This mass-dependent trend is not predicted by the linear TTT, several ideas have been proposed to understand this.

Parametric models

To quantify the effects of the correlation between the tidal tensor and the inertia tensor on the angular momentum growth of a halo, Lee & Pen (2000, 2001) proposed a parametric model. They introduce the spin-shear correlation parameter a, and the autocorrelation function takes the form

$$\langle L_i L_j | \mathbf{T} \rangle \propto \frac{1+a}{3}\delta_{ij} - a\, T_{ij}T_{kj}\ . \tag{1.24}$$

This equation has been extensively used in the literature to study the preferential alignment of angular momentum with the underlying tidal field and the parameter a has been used to describe the probability distribution of the spin alignment angle $\cos(\theta)$. A value of $a = 0$ implies $\langle L_i L_j | \mathbf{T} \rangle = \frac{\delta_{ij}}{3}$, which means that the angular momentum of haloes is randomly oriented without any correlation with the tidal field. Linear TTT restricts a to $0 < a < \frac{3}{5}$, with a positive value implying that the halo angular momentum is aligned along the second eigenvector of the tidal fields (orthogonal to filament axis) (Trowland, Lewis & Bland-Hawthorn 2013).

The parameter should be determined empirically from numerical simulations with tidal fields measured on a smoothed scale equal to the scale on which the angular momentum is defined. Lee & Pen (2000) have found this value to be $a = 0.24$, indicating the presence of a weak but detectable correlation between galaxy spins and the tidal fields. Trowland, Lewis & Bland-Hawthorn (2013) show that it is positive at higher redshifts ($a = 1.29$ at $z = 3$) but it can also take negative values, deviating from the linear theory predictions at lower redshifts ($a = -0.035$ at z=0). This illustrates the spin alignment evolution from an orthogonal alignment with the filament axis at higher redshift to a preferential parallel alignment at lower redshifts. More recently, Lee (2019) has introduced an additional parameter to this model to account for the origin and evolution of transition mass.

Constrained tidal torques

Codis, Pichon & Pogosyan (2015) extended the linear TTT in certain constrained environments of the cosmic web to more precisely predict the angular momentum growth of haloes in these geometries. A constrained environment in this case is a saddle point of the density field corresponding to a proto-filament sitting inside a proto-wall. They show that low-mass haloes usually form close to a saddle point and acquire spin along the filaments and high-mass haloes form away from it, closer to the clusters, and acquire a spin perpendicular to the filaments.

Based on this constrained theory, they show that this dependence on halo mass is because the protohalo experiences differential torquing from the tidal tensor that arises from these anisotropic geometries. They claim that a 2D analysis of this model predicts roughly the right transition mass based on the size of the vorticity quadrants a halo is in.

This is an analytical model with several assumptions involved. They assume the Lagrangian volume of a protohalo can be approximated by an ellipsoid, like in the linear TTT, whereas in reality, the shape is irregular. In the analytical approach, it is difficult to specify the Lagrangian volume that contains all the particles of the collapsed halo. N-body simulations for more accurate computations. Another approximation in their calculation is that they use the Hessian of the density field instead of the inertia tensor.

Dynamical models and secondary processes

Several studies attribute the mass-dependent alignment to the dynamics of the large-scale flows as the preferential mass accretion onto haloes is determined by the underlying geometry of the web.

Wang & Kang (2017, 2018b) propose that **halo formation and migration** in specific web environments can explain the mass dependence. Low-mass haloes form first in sheets and then migrate into filaments, so they retain their original spin orientation gained during their growth in the sheets. This corresponds to a parallel orientation to the filament spine. High-mass haloes first migrate into filaments and then accrete most of their mass and spin in filament environment in such a way that their spin is perpendicular to the filament spine.

Welker et al. (2014) argue that **mergers** along the large-scale filaments drive the mass-dependent spin alignments. The change in the halo spin orientation is sensitive to both **smooth-accretion** and mergers. Wang & Kang (2018a) also attribute this effect to local **tidal anisotropy** at a halo's location.

Ganeshaiah Veena et al. (2018) propose that haloes at the intersection of many filaments accrete preferentially along these filaments and are expected to have spin preferentially perpendicular to the filament. Haloes that are embedded in relatively thicker filaments **anisotropically accrete** mass perpendicular to the filament spine, therefore gaining a net spin along the filament spine. This hypothesis is inspired from the *accreting* and *stalled* from the work of Borzyszkowski et al. (2017), who have shown that the preferential directions of accretion onto haloes depend strongly on the relative size of the filaments feeding them.

Table 1: Halo spin alignments in simulations

Work by	Simulation box length [h^{-1} Mpc]	Cosmic web detection	Transition mass ($\times 10^{12} h^{-1} M_\odot$)
Aragón-Calvo et al. (2007b)	150	MMF	~ 1
Hahn et al. (2007a)	180	tidal tensor	–
Codis et al. (2012)	2000	DISPERSE	~ 3.5
Libeskind et al. (2012)	64	velocity shear tensor	–
Trowland et al. (2013)	300	density Hessian	~ 1.2
Forero-Romero et al. (2014)	250	T-Web	1
		V-Web	2
Aragon-Calvo & Yang (2014)	32	MMF-2	
Wang & Kang (2018b)	200	tidal tensor	0.5 - 1.4
Ganeshaiah Veena et al. (2018)	542	NEXUS+	0.3
		NEXUS_VEL_SHEAR	0.5
Lee (2019)	400	tidal tensor	–

1.7.2 Galaxy spin alignments

Galaxy spin acquisition is much more complex compared to that of haloes due to several processes that are specific to baryons, such as gas inflows and outflows, heating due to supernova and AGN and many others Sancisi et al. (2008); Dutton & van den Bosch (2012). These processes also influence galaxy

angular momentum and hence their alignment with the cosmic web.

Alignments in simulations: The first study on galaxy spin was carried out by Hahn, Teyssier & Carollo (2010). Using around a hundred disc galaxies in a 'zoom-in' simulation, they showed that massive disc galaxies are aligned along the filament axis. Due to poor statistics, this result did not provide the entire picture.

Subsequent work by Dubois et al. (2014); Welker et al. (2014); Codis et al. (2018); Wang & Kang (2018b) showed a clear mass-dependent spin transition of galaxies from parallel to perpendicular in the Horizon AGN and Illustris hydro simulations. In contrast, Ganeshaiah Veena et al. (2019) and Krolewski et al. (2019) detected a mass dependent alignment but not a spin transition in SPH based EAGLE and Massive Black-2 simulations. Apart from galaxy stellar mass, the spin alignment trend depends on galaxy morphology (Wang & Kang 2017; Ganeshaiah Veena et al. 2019), color (Codis et al. 2018; Wang & Kang 2018b), HI content and filament density (Kraljic, Davé & Pichon 2020).

Several studies report that blue, rotation supported galaxies tend to align along the filament spine and dispersion dominated, red galaxies tend to spin perpendicular. In the Simba simulation galaxies with high-HI and high filament density were found to have parallel spins and those with low-HI and low density were found to have spin perpendicular to filament spine (Kraljic, Davé & Pichon 2020). Welker et al. (2014) also showed that massive galaxies that have undergone mergers have a spin perpendicular to the filament while low-mass galaxies are parallel. Codis et al. (2018) also reported a weak galaxy alignment in walls of the cosmic web.

Galaxies in AMR based or meshless simulations show a spin transition whereas galaxies in SPH simulations don't. This can be because of the difference in the mesh-based and SPH-based schemes for solving hydrodynamical equations. The slightly diverging results can also be due to the limited statistics in small volume hydro simulations, the sub-grid models implemented and the radius of galaxy disc used to calculate the spin.

Overall, in simulations, spin alignment is shown to be dependent on a number of factors: stellar mass, galaxy morphology, star formation rate, HI mass, filament density, galaxy merger history and galaxy color (age). Other external factors that need calibration to compare results from various studies are filament detection techniques, simulation codes with substantially larger volume hydro simulations. Galaxy alignment results from hydrodynamical simulations are summarized in Table 2.

Table 2: Galaxy spin alignments in simulations

Work by	Simulation	Code	Filament	Redshift	Transition
Hahn et al. (2010)	RAMSES, zoom-in	AMR	Tidal field	0-0.5	–
Dubois et al. (2014)	Horizon AGN	AMR	DISPERSE	1.2-1.8	Detected
Codis et al. (2018)	Horizon AGN	AMR	DISPERSE	0-2	Detected
Wang et al. (2018a)	Illustris 1	Moving mesh	Tidal fields	0	Detected
Krolewski et al. (2019)	Massive Black-2	SPH	SCMS[a]	0	Not detected
Ganeshaiah Veena et al. (2019)	EAGLE	SPH	NEXUS+ Bisous	0 0	Not detected Not detected
Kraljic et al. (2020)	Simba	Meshless	Disperse	0-2	Detected

[a] SCMS - Subspace Constrained Mean Shift (Chen et al. 2016)

Alignment results in observations: Galaxy spin alignments in observations paint a complicated picture. More statistics are required in order to draw concrete conclusions. Jones, van de Weygaert & Aragón-Calvo (2010) analysed the spin alignment of 69 edge-on galaxies with respect to the large-scale filaments of SDSS and found that the distribution deviated significantly from a random distribution.

Tempel, Stoica & Saar (2013); Tempel & Libeskind (2013a) with improved statistics found a preferential parallel orientation for spirals and perpendicular for elliptical. Few studies reported a parallel alignment for Scd galaxies (Hirv et al. 2017), blue and red galaxies (Zhang et al. 2013) and perpendicular for Sab type galaxies (Hirv et al. 2017). Several other studies find either a slight deviation from random alignment or no alignment at all (Lee & Erdogdu 2007; Pahwa et al. 2016; Krolewski et al. 2019).

While most of the studies so far used galaxy minor axis as a proxy for its spin axis, Welker et al. (2020) obtained galaxy spin for the first time based on its kinematics using IFS. They reported a clear mass-dependent spin alignment with large-scale filaments in the SAMI survey based on filaments detected in GAMA. They also report a stellar transition mass between $10^{10.4} - 10^{10.9} M_{\odot}$ and suggest that it shows a slight increase with the scale of filaments. Blue Bird et al. (2020) also found a faint mass dependence of galactic spins using HI observations from the COSMOS HI Large Extragalactic Survey (CHILES). Most of the results from observations are given in Figure 1.7.2

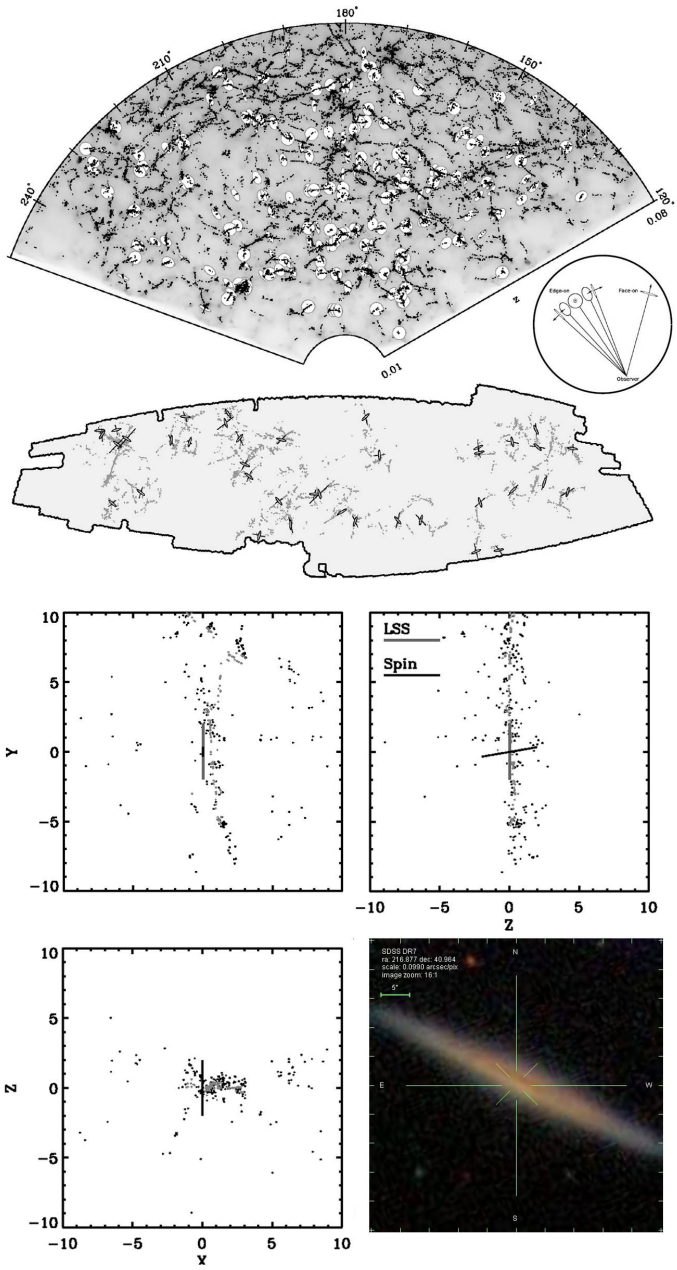

Figure 1.10 – *The top panel depicts galaxies as points and their alignments across the cosmic web in SDSS. The lower panel shows a galaxy with its spin perpendicular to the underlying large-scale structure. Figures adapted from:* Jones, van de Weygaert & Aragón-Calvo (2010).

Table 3: Galaxy spin alignments in observations

Work by	Survey	Filament detection	Galaxy spin vector	Galaxy type	Preferential alignment (e_3)
Jones et al. (2010)	SDSS	MMF	minor axis	–	not random
Tempel et al. (2013)	SDSS	Bisous	minor axis	spirals elliptical	parallel perpendicular
Pahwa et al. (2016)	2MRS	velocity shear	minor axis	spiral elliptical	random perpendicular
Hirv et al. (2017)	SDSS	Bisous	minor axis	Scd Sab	parallel perpendicular
Krolewski et al. (2019)	MANGA	SCMS	IFS[a]	-	random
Welker et al. (2020)	MANGA	Disperse on GAMA	IFS	low mass high mass	parallel perpendicular
Blue Bird et al. (2020)	CHILES	Disperse on SDSS	perp. to major axis	-	not random hint at parallel

[a] IFS - Integral Field Spectroscopy, kinematic method.

1.7.3 Shape alignments

In the initial Gaussian field, a correlation exists between shape of the peaks and the neighbouring matter distribution (van de Weygaert & Bertschinger 1996a; de Rossi et al. 2009). The gravitational collapse of the density peaks eventually form haloes and galaxies. The anisotropic nature of the collapse (see subsection 1.4.1) accentuates non-sphericity, so we expect the haloes to be aspherical and ellipsoid like. In N-body simulations, haloes are fit with ellipsoids characterized by the major, intermediate and minor axes, $a > b > c$. Most haloes are prolate ($a \approx b; c > a$) with their major axis aligned along the axis of its host filament (Hahn, Teyssier & Carollo 2010; Shao et al. 2016; Ganeshaiah Veena et al. 2018). Unfortunately, there are very few observational constraints on halo shapes, but with the advent of weak lensing surveys, these are expected to get better and reveal a better correlation with the underlying tidal fields.

1.8 This thesis in a nutshell

There are several pressing and unresolved issues related to the spin and shape alignment of haloes and galaxies with the cosmic web. Firstly, we lack a convincing model that describes the spin alignment with the web environments and how this alignment changes with time. Numerous explanations have been proposed (see discussion in section 1.7), however it is unclear which of those processes are most important. Part of the difficulty lies in the strength of the alignment signal, which is rather small, and thus it is difficult to disentangle it from other effects. Another challenge is the complexity of the problem which likely involves many physical processes whose importance might change with halo mass and redshift.

Results from several studies highlight the lack of agreement on numerous fronts. Most studies that use cosmological N-body simulations agree that the spin of low-mass haloes tends to align along the filament spine and massive haloes tend to spin perpendicular to it. But the reported mass at which this trend changes is not the same and varies over an order of magnitude (0.5 to 5) $\times 10^{12} h^{-1} \mathrm{M}_{\odot}$. The results are much more diverging in hydrodynamical simulations and observations with a need to improve both the statistics and theoretical models. The cosmic web - spin correlation is a rather small signal since it is a higher order effect and to robustly characterize it we need large samples of haloes and galaxies. Previous studies have used various simulations of different volume, resolution and cosmic web detection techniques (see Table 1 and Table 2), hence proving it difficult to pinpoint the reasons for the discrepancies detected in the alignment trends and transition mass values.

In this thesis we have successfully addressed several of these key issues by carrying out a detailed analysis of spin alignment with the cosmic web. The results presented here make use of the latest state-of-the-art cosmological simulation, such as the Planck-Millennium dark matter only simulation and the EAGLE galaxy formation simulation, and were made using very large samples of haloes and galaxies that were essential for obtaining statistically robust results.

Halo spin and shape alignments with the cosmic web: In chapter 2 we use over a million dark matter haloes from the Planck-Millennium N-body simulation to show that the spin of low-mass haloes is preferentially aligned along the large-scale filaments and massive haloes tend to spin perpendicular. To assess the effect of the web detection method, we compare two web definitions: NEXUS+, which classifies web features based on the geometric information of the density field, and NEXUS_VELOCITY_SHEAR, which classifies the web based on dynamical signature contained in the velocity shear field. We find that primarily the differences arises from that fact that each method assigns different haloes to filaments. NEXUS_VELOCITY_SHEAR only finds the

thickest filaments, while NEXUS+ also finds a large population of tenuous filaments that criss-cross the lower density regions. In particular, we show that the spin alignment shows a strong trend with filament thickness. One manifestation of this trend is the variation of the transition mass, which increases by more than one order of magnitude from the thinnest to the thickest filaments.

In order to understand what is causing the spin transition, we study the alignment of the inner fractions of haloes and show that the inner parts retain the original tidal torque orientation with the tidal field better than the outer parts, which are more influenced by later secondary processes such as accretion and mergers. We propose that the mass dependent alignment and the dependence on filament thickness is due to the accretion along directions perpendicular and parallel to their host filament depending on the mass of the halo and the relative filament diameter. In this chapter we also study the halo shape distribution and shape alignments. We show that most haloes are prolate and that the major axis of haloes is aligned along the filament axis, with the strength of alignment increasing for massive haloes.

Galaxy spin and shape alignments: In chapter 3, we carry out a detailed analysis on galaxy spin and shape alignments in the EAGLE hydrodynamical simulation. For this, we use filaments detected using two methods: NEXUS+ applied to the total matter density and Biosus applied to the galaxy distribution. We show that haloes in hydrodynamical simulations show the exact same alignment trend as haloes in the dark matter only simulations, implying that the addition of baryons does not affect the halo spin alignment. We find that EAGLE galaxies tend to have their spin perpendicular to the filament axis and that this effect is largest for the highest mass galaxies. However, in contrast to halo spin alignment, we do not find a transition from parallel to perpendicular alignment for galaxy spins. When segregating galaxies by morphology, we find that ellipticals show a stronger orthogonal filament alignment than spirals.

We also find a very interesting correlation between the orientation of galaxies, haloes and filaments. The galaxies whose minor axis is perpendicular to filaments show a a very tight alignment between their spins and the spins of their host haloes. The opposite is true for the galaxies whose minor axis is aligned with the spine of the filament . This novel result indicates that the processes responsible for the galaxy-cosmic web alignment are also responsible for the alignment between galaxies and their host haloes.

Halo spin evolution: Finally, in chapter 4 we explore the evolution of halo spin in the filaments and sheets of the cosmic web since redshift, $z = 2$, to present day. To identify the large-scale filaments and sheets we use the NEXUS+ multiscale method which takes into account the hierarchical nature of the cosmic web. We show that the spin–filament alignment varies with redshift and

halo mass. At fixed halo mass, halo populations tend to be more perpendicular to the filament spine at high redshift compared to present day. Consequently, the spin transition mass increases with time, and is highest at present day. Halo spin alignment varies with filament thickness at all the redshifts we studied, and, in each case, the transition mass increase by more than one order of magnitude from the thinnest to the thickest filaments.

We found that the magnitude of the halo spin shows a trend with environment: haloes in filaments spin faster than those in walls and voids. This correlation does not evolve with time, being roughly the same at all redshifts, $z \leq 2$, we studied. We also report for the first time that the magnitude of the halo spin correlates with the host filament thickness and the orientation of the halo spin with respect to the filament axis. Haloes whose spins are along the filament spine (also termed as *parallel haloes*) rotate more slowly than their perpendicular counterparts. This trend reverses below a certain mass, which we call the *cross-over mass*. Similarly, above this cross-over mass, haloes in thick filament usually spin faster than those in thin filaments. Surprisingly, we find a high degree of similarity between the values of transition mass and the cross-over mass, suggesting that the same processes are responsible for both phenomena. Our analysis indicates that these differences arise due to high redshift effects ($z > 2$), such as correlations between the angular momentum and tidal fields that are already present in the initial conditions.

1

2 Halo spin and shape alignments

Punyakoti Ganeshaiah Veena[a b], **Marius Cautun**[c], **Rien van de Weijgaert**[a], **Elmo Tempel**[b d], **Bernard J. T. Jones**[e], **Steven Rieder**[f] **Carlos S. Frenk**[c]

[a] Kapteyn Astronomical Institute, University of Groningen, PO box 800, 9700AV, Groningen
[b] Tartu Observatory, University of Tartu, Observatooriumi 1, 61602 Tõravere, Estonia
[c] Institute for Computational Cosmology, Department of Physics, University of Durham, South Road, Durham DH1 3LE, UK
[d] Leibniz-Institut für Astrophysik Potsdam (AIP), An der Sternwarte 16, D-14482 Potsdam, Germany
[e] Kapteyn Astronomical Institute, University of Groningen, PO box 800, 9700AV, Groningen
[f] RIKEN Center for Computational Science, 7-1-26 Minatojima-minami-machi, Chuo-ku, Kobe, 650-0047 Hyogo, Japan

Submitted 1 May 2018, Accepted 16 August 2018
Published in Monthly Notices of the Royal Astronomical Society, volume 481, pages 414–438, 2018.

Abstract

We investigate the alignment of haloes with the filaments of the cosmic web using an unprecedentedly large sample of dark matter haloes taken from the P-Millennium ΛCDM cosmological N-body simulation. We use the state-of-the-art NEXUS morphological formalism which, due to its multi-scale nature, simultaneously identifies structures at all scales. We find strong and highly significant align-

ments, with both the major axis of haloes and their peculiar velocity tending to orient along the filament. However, the spin - filament alignment displays a more complex trend changing from preferentially parallel at low masses to preferentially perpendicular at high masses. This “spin flip" occurs at an average mass of $5 \times 10^{11}\ h^{-1}M_{\odot}$. This mass increases with increasing filament diameter, varying by more than an order of magnitude between the thinnest and thickest filament samples. We also find that the inner parts of haloes have a spin flip mass that is several times smaller than that of the halo as a whole. These results confirm that recent accretion is responsible for the complex behaviour of the halo spin - filament alignment. Low-mass haloes mainly accrete mass along directions perpendicular to their host filament and thus their spins tend to be oriented along the filaments. In contrast, high-mass haloes mainly accrete along their host filaments and have their spins preferentially perpendicular to them. Furthermore, haloes located in thinner filaments are more likely to accrete along their host filaments than haloes of the same mass located in thicker filaments.

keywords: large-scale structures of the Universe - galaxies: haloes - methods: numerical

2.1 Introduction

Starting from almost uniform initial conditions, the Universe has evolved over billions of years to contain a wealth of structure, from small-scale virialized objects, such as haloes and galaxies, to tens-of-Megaparsec-sized structures, such as super-clusters and filaments (Peebles 1980; Oort 1983; Springel, Frenk & White 2006; Frenk & White 2012; Tempel 2014a; Tully et al. 2014). All these are embedded in the so-called cosmic web, a wispy weblike spatial arrangement consisting of dense compact clusters, elongated filaments, and sheetlike walls, amidst large near-empty void regions (Bond, Kofman & Pogosyan 1996; van de Weygaert & Bond 2008b). This pattern is marked by prominent anisotropic features, a distinct multiscale character, a complex spatial connectivity and a distinct asymmetry between voids and overdense regions. The large-scale web is shaped by the large-scale tidal field, which itself is generated by the inhomogeneous distribution of matter. Within this context, the cosmic web is the most salient manifestation of the anisotropic nature of gravitational collapse, and marks the transition from the primordial (Gaussian) random

field to highly nonlinear structures that have fully collapsed into haloes and galaxies.

The same tidal field that shapes the cosmic web is also the source of angular momentum build-up in collapsing haloes and galaxies. This is neatly encapsulated by Tidal Torque Theory (TTT), which explain how in the linear stages of evolution the tidal field torques the non-spherical collapsing protohaloes to generate a net rotation or spin (Hoyle 1949; Peebles 1969; Doroshkevich 1970b; White 1984). Specifically, this occurs due to a differential alignment between the inertia tensor of the protohalo and the local gravitational tidal tensor. TTT posits a direct correlation between halo properties such as angular momentum, shape and the large-scale tidal field at their location (see Schäfer 2009 for a review). For example, linear TTT predicts that the halo spin is preferentially aligned with the direction of secondary collapse (Lee & Pen (2001), but see Jones & van de Weygaert (2009)), and thus the spin is perpendicular on the direction of slowest collapse, which corresponds to the filament ridge (Efstathiou & Jones 1979; Barnes & Efstathiou 1987; Heavens & Peacock 1988; Lee & Pen 2001; Porciani, Dekel & Hoffman 2002a,b; Lee 2004). This alignment is mostly imprinted at the time of turn-around, when the protohaloes are the largest, and is expected to be preserved during the subsequent non-linear collapse of the protohaloes into virialized objects.

Large cosmological simulations have shown that the alignments of halo shape and spin with their surrounding mass distribution are not as straightforward as predicted by the simplified TTT framework described above. The correlations present in the linear phase of structure formation are preserved in the case of halo shapes, which are strongly oriented along the filament in which the haloes are embedded, with the alignment strength increasing with halo mass (Altay, Colberg & Croft 2006; Aragón-Calvo et al. 2007b; Brunino et al. 2007; Hahn et al. 2007a). In contrast, the spin of haloes shows a more complex alignment with their host filament. This was first pointed out by Aragón-Calvo et al. (2007b), and shortly thereafter by Hahn et al. (2007a), which have shown that the spin - filament alignment is mass-dependent, with low- and high-mass haloes having a preferential parallel and perpendicular alignment, respectively. This result has since been reproduced in multiple cosmological simulations with and without baryons (Hahn, Teyssier & Carollo 2010; Codis et al. 2012; Libeskind et al. 2013; Trowland, Lewis & Bland-Hawthorn 2013; Dubois et al. 2014; Forero-Romero, Contreras & Padilla 2014; Wang & Kang 2017). The alignment has been confirmed by observational studies, most outstandingly so in the finding by Tempel, Stoica & Saar (2013) that massive elliptical galaxies tend to have their spin perpendicular to their host filaments while the spin of less massive bright spirals has a tendency to lie parallel to their host filaments (see also Jones, van de Weygaert & Aragón-Calvo 2010; Tempel & Libeskind

2013a; Zhang et al. 2013, 2015; Hirv et al. 2017). The transition mass from halo spins preferentially perpendicular to preferentially parallel to their host haloes is known as the *spin flip* mass. While most studies agree on the existence of such a transition mass, they report highly disparate values for the spin flip mass that spread over more than an order of magnitude in halo mass, from $\sim$0.5 to $\sim 5 \times 10^{12}\ h^{-1}\mathrm{M}_{\odot}$. Furthermore, the spin flip mass varies with the smoothing scales used to identify the large-scale filaments, being higher for larger smoothing scales (Codis et al. 2012; Aragon-Calvo & Yang 2014; Forero-Romero, Contreras & Padilla 2014), and decreases at higher redshifts (Codis et al. 2012; Wang & Kang 2018a). It suggests that the mechanisms responsible for the tendency of low-mass haloes to have their spins oriented along their host filaments are complex, being both time and environment dependent.

Previous works have posited a diverse set of explanations for the spin flip phenomenon, with most responsible processes having to do with the nature of halo late-time mass accretion, the so-called secondary accretion (Bertschinger 1985). A theoretical solution is provided by Codis, Pichon & Pogosyan (2015), who explain the dichotomy in spin-filament alignment between low- and high-mass haloes within the TTT framework,. The key is that filaments form only in certain large scale tidal field configurations, in which the alignment between the inertia tensor and the tidal field follows a particular distribution that is different from the general expectation. Codis, Pichon & Pogosyan and Laigle et al. (2015) have suggested also that this is due to the vorticity distribution inside filaments (for galaxies, see Pichon et al. 2011). They have claimed that the filament cross-section can be split into four quadrants, each with an opposite vorticity sign. Low-mass haloes typically reside in one of the four quadrants and thus acquire a spin along the filament, while high-mass haloes overlap multiple vorticity quadrants and acquire a spin that is preferentially perpendicular on their host filament. Welker et al. (2014) have shown that massive galaxies tend to have their spin perpendicular to their filament due to an excess of mergers along the filament direction, while low-mass galaxies tend to be aligned along their filament due to having undergone none or many fewer mergers. However, Bett & Frenk (2012, 2016) have shown that more than 75% of changes in halo spins are due to accretion of small substructures or flyby encounters, and not due to major mergers.

On the other hand, Wang & Kang (2017, 2018a) have explained the spin - filament alignment in terms of the formation time of haloes and their migration time from sheets into filaments. Low-mass haloes accrete most of their mass at high redshift, while residing in sheets, while high-mass objects undergo most of their growth at low redshift, when they are embedded in filaments.

In this study, we carry out a systematic analysis of the alignment between

the spin and shape of haloes and the orientation of the filaments in which the haloes reside. We employ one of the largest cosmological simulations available, P-Millennium, which is characterized by a large volume and very high mass resolution, with the large dynamic range being critical for our goal of understanding how the large-scale cosmic web influences small-scale phenomena, such as spin and shape orientations of haloes. We identify the cosmic web using the state-of-the-art NEXUS technique, which employs a multiscale formalism to identify in one go both prominent and tenuous filaments (Cautun, van de Weygaert & Jones 2013, see Libeskind et al. 2018 for a comparison to other web detection methods). We employ two NEXUS variants, NEXUS+ and NEXUS_velshear, which identify the web on the basis of the density and the velocity shear fields, respectively. These two NEXUS variants show the largest difference between their identified filamentary network (Cautun et al. 2014) and comparing the halo - filament alignments between the two method reveals key details about the processes behind the halo - filament alignments and their dependence on halo mass.

Our analysis involves two major new themes which have not been studied in the literature and which we show to be indispensable for understanding the halo - filament alignments. First, we study the properties of the entire halo as well as those corresponding to different inner radial cuts. The latter is highly relevant since: i) galaxies are very strongly aligned with the inner region of the halo, and only poorly with the full halo (Bailin & Steinmetz 2005; Tenneti et al. 2014; Velliscig et al. 2015; Shao et al. 2016; Chisari et al. 2017) , and ii) recent accretion is mainly deposited in the outer regions of the halo (Salvador-Solé, Solanes & Manrique 1998; Wechsler et al. 2002; Tasitsiomi et al. 2004; Wang et al. 2011) and thus the alignments of the inner regions trace the alignment of the full halo at high redshift. The second novel features involves studying the halo spin - filament alignment as a function of filament properties to find that the spin flip mass shows a very strong dependence on filament thickness.

The layout of the chapter is as follows: section 2.2 introduces the cosmological simulations and the NEXUS formalism used to identify the cosmic web; section 2.3 describes the halo catalogues, how we calculate halo spins and shapes, and presents a detailed comparison of the halo population in filaments between our two web finders; section 2.4 presents the main results regarding the halo spin - filament alignment; section 2.5 studies the alignment between the shape of haloes and their host filaments; in section 2.6 we present a detailed discussion on how secondary accretion is likely to be the main process that shapes the halo spin - filament alignment; and we end with a summary and discussion of our main results in section 2.7.

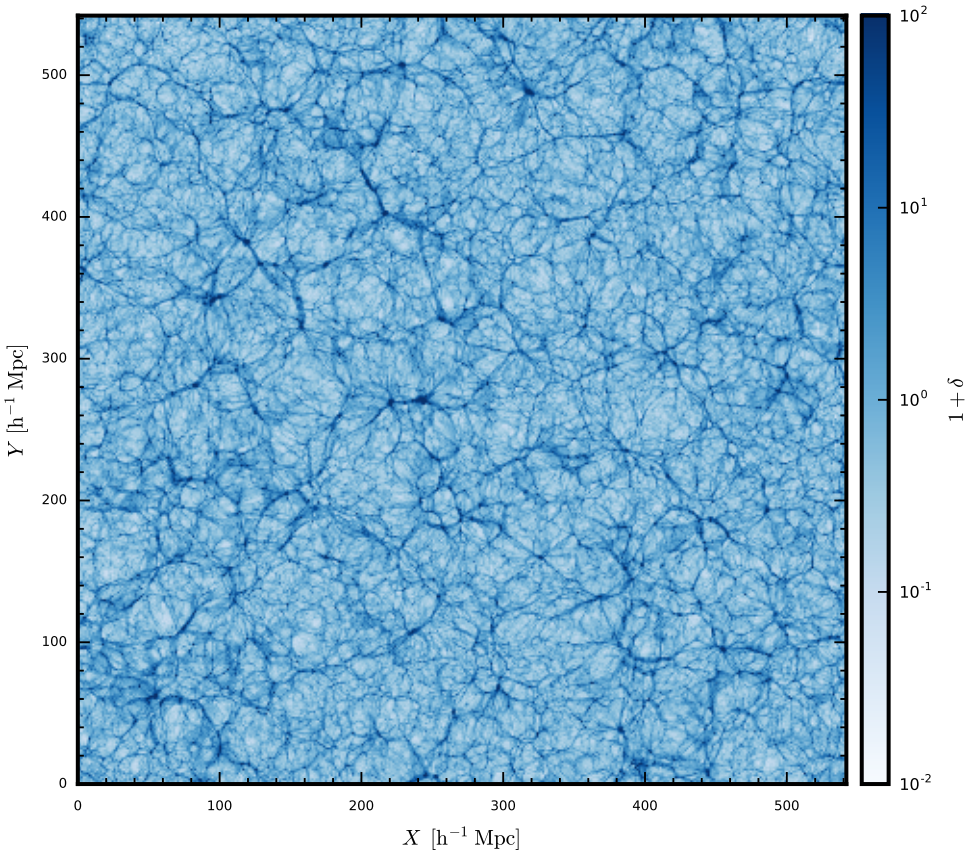

Figure 2.1 – *A 2 h^{-1}*Mpc *slice trough the $z = 0$ density field of the P-Millennium simulation. The width and height of the figure corresponds to the side length of the simulation. The colour bar indicates the density contrast, $1 + \delta$.*

2.2 Filament Population

Our analysis is based on a high resolution simulation with an unsurpassed dynamic range, Planck-Millennium, which we introduce in this section. Here, we also describe the filament identification procedure, which is based on two different versions of the MMF/NEXUS cosmic web detection algorithm: one starting from the density field and the other from the velocity shear field. By comparing the two filament populations, we hope to identify supplementary information on the processes that affect the alignment of halo angular momentum with the large scale structure.

2.2.1 Simulation

For this study we used the Planck-Millennium high resolution simulation (hereafter P-Millennium; McCullagh et al. 2017; Baugh et al. 2018), which is a dark matter only N-body simulation of a standard ΛCDM cosmology. It traces structure formation in a periodic box of 542.16 h^{-1}Mpc side length using 5040^3 dark matter particles, each having a mass of 1.061×10^8 $h^{-1}\mathrm{M}_\odot$. The cosmological parameters of the simulation are those obtained from the latest Planck survey results (Planck Collaboration et al. 2014): the density parameters are $\Omega_\Lambda = 0.693$, $\Omega_\mathrm{M} = 0.307$, the amplitude of the density fluctuations is $\sigma_8 = 0.8288$, and the Hubble parameter is $h = 0.6777$, where $h = H_0/100$ km s^{-1}Mpc^{-1} and H_0 is the Hubble's constant at present day. In the analysis presented here we limit ourselves to the mass distribution at the current epoch, $z = 0$.

Due to its large dynamic range and large volume, the P-Millennium simulation is optimally suited for investigating the issue of angular momentum acquisition and the relation between spin and web-like environment over a large range of halo masses. P-Millennium simulates the formation nearly 7.5 million well resolved haloes over three orders of magnitude in halo mass, which is critical for the success of this work. This is especially the case for the alignment between halo spin and filament orientation, which is a subtle effect (e.g. see Aragón-Calvo et al. 2007b; Libeskind et al. 2013), and for robustly characterising the dependence of this alignment on halo mass, which is one of the principal aspects addressed in this study. Besides its importance for identifying the subtle dynamical effects underlying the spin transition, the large volume of P-Millennium allows us to fully take into account the large-scale tidal forces responsible for the generation of halo angular momentum and for the formation of the cosmic web.

A visual illustration of the mass distribution in the P-Millennium simulation is shown in Figure 2.1. It shows a slice of 2 h^{-1}Mpc width through the entire simulation box, with the white-blue colour scheme representing the density contrast,

$$1 + \delta(\mathbf{x}, t) \;=\; \frac{\rho(\mathbf{x})}{\rho_u}\,, \tag{2.1}$$

where $\rho(\mathbf{x})$ and ρ_u denote the local and background mean density. Clearly visible is the intricate structure of the cosmic web, with its visual appearance dominated by elongated medium to high-density filaments and low-density voids. The image illustrates some of the characteristic properties of the cosmic web, such as the complex and pervasive connectivity of the filamentary network. We also recognize the multiscale structure of the web: the dominant thick filaments, which are often found in high-density regions bridging

the cluster mass haloes and the thin, tenuous filamentary tendrils that branch out from the thick ones. These thin filaments typically have lower densities and pervade the low-density void regions. Note that in a two-dimensional slice like the one shown in Figure 2.1, it is difficult to make a clear distinction between filaments and cross-sections through planar walls (Cautun et al. 2014). However, the more moderate density of the walls means that they would not correspond to the most prominent high-density ridges seen in the slice.

2.2.2 Filament detection

We use the MMF/NEXUS methodology for identifying filaments in the P-Millennium simulation. The MMF/NEXUS multiscale morphology technique (Aragón-Calvo et al. 2007a; Cautun, van de Weygaert & Jones 2013) performs the morphological identification of the cosmic web using a *Scale-Space formalism* that ensures the detection of structures present at all scales. The formalism consists of a fully adaptive framework for classifying the matter distribution on the basis of local variations in the density, velocity or gravity fields, which are encoded in the Hessian matrix. Subsequently, a set of morphological filters is used to classify the spatial distribution of matter into three basic components: the nodes, filaments and walls of the cosmic web. The outcome of the identification procedure is a set of diverse and complex cosmic web components, from the prominent features present in overdense regions to the tenuous networks pervading the cosmic voids.

The NEXUS version of the MMF/NEXUS formalism (Cautun, van de Weygaert & Jones 2013; Cautun et al. 2014) builds upon the original Multiscale Morphology Filter (Aragón-Calvo et al. 2007b,a) algorithm and was developed with the goal of obtaining a more robust and more physically motivated environment classification method. The full NEXUS suite of cosmic web identifiers (see Cautun, van de Weygaert & Jones 2013) includes options for a range of cosmic web tracers, such as the raw density, the logarithmic density, the velocity divergence, the velocity shear and the tidal force fields. NEXUS has incorporated these options in a versatile code for the analysis of cosmic web structure and dynamics following the realization that they represent key physical aspects that shape the cosmic mass distribution.

The goal of our analysis of halo - filaments alignments is to understand the role of large scale tidal forces in the acquisition of angular momentum in haloes. The dominant tidal field effects and the large scale peculiar velocity flows are expected to be related to the most prominent web-like structures. This motivates us to employ two methods for identifying the cosmic web filaments, on the basis of their signature in the shear or velocity fields. By contrasting the alignments of the halo spin with the two filament populations, we seek to

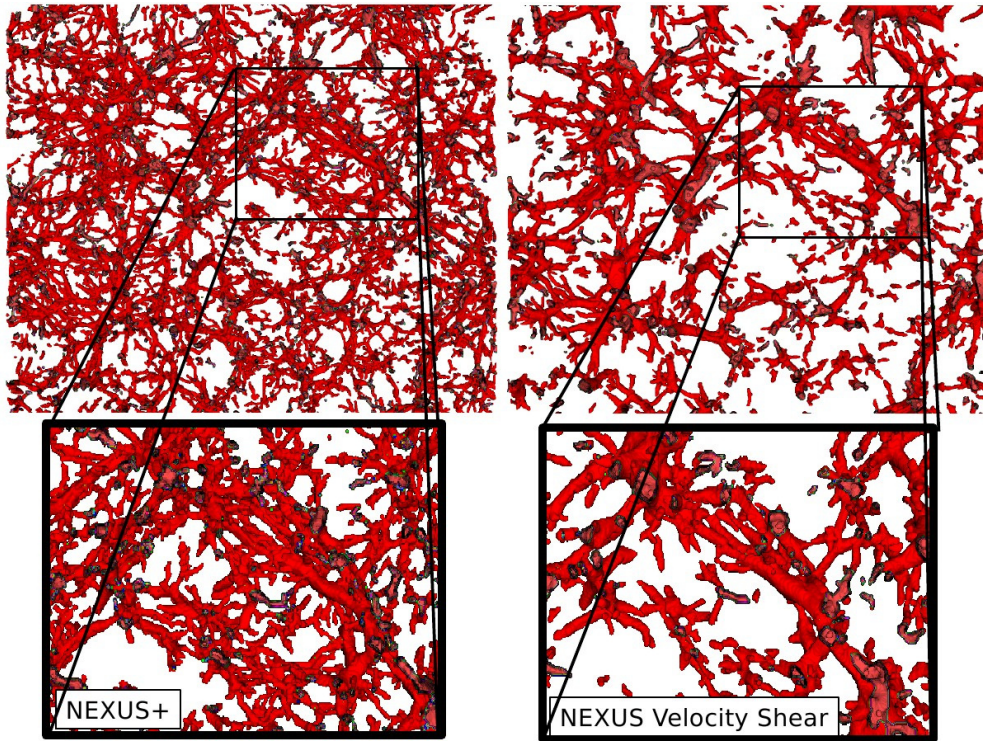

Figure 2.2 – *Left panels: Filaments detected by the* NEXUS+ *method, which identifies filaments in the density field. Right panels: For the same volume as in the left panels, filaments detected by the NEXUS_velshear method, which identifies filaments in the velocity shear field. The top row shows a* 20 h^{-1}Mpc *slice of* 300×300 $(h^{-1}\mathrm{Mpc})^2$ *size across. The bottom row shows a zoom-in into a smaller region of this slice. NEXUS_velshear identifies typically only the thick filaments, whereas* NEXUS+ *identifies even the thin and tenuous tendril like filaments in low-density regions.*

disentangle the contribution of local small-scale forces from those of larger-scale ones.

MMF/NEXUS

A major advantage of the MMF/NEXUS formalism is that it simultaneously pays heed to two crucial aspects of the web-like cosmic mass distribution: the morphological identity of structures and the multiscale character of the distribution. The first aspect is recovered by calculating the local Hessian matrix, which reveals the existence and identity of morphological web components. The second, equally important, aspect uses a scale-space analysis to uncover the multiscale nature of the web, which is a manifestation of the hierarchical

evolution of cosmic structure formation.

The scale-space representation of a data set consists of a sequence of copies of the data at different resolutions (Florack et al. 1992; Lindeberg 1998). A feature searching algorithm is applied to all of these copies, and the features are extracted in a scale independent manner by suitably combining the information from all the copies. A prominent application of scale-space analysis involves the detection of the web of blood vessels in a medical image (Sato et al. 1998; Li, Sone & Doi 2003), which bears a striking similarity to the structural patterns seen on Megaparsec scales. The MMF formalism has translated, extended and optimized the scale-space methodology to identify the principal morphological elements in the cosmic mass and galaxy distribution.

The outcome of the MMF/NEXUS procedure is a volume-filling field which specifies at each point the local morphological signature: node, filament, wall or void. The MMF/NEXUS methods perform the environment detection by applying their formalism first to nodes, then to filaments and finally to walls. Each volume element is assigned a single environment characteristic by requiring that filament regions cannot be nodes and that wall regions cannot be either nodes or filaments. The remaining regions are classified as voids.

The basic setup of MMF/NEXUS is to define a four-dimensional scale-space representation of the input tracer field $f(\mathbf{x})$. In nearly all implementations this is achieved by means of a Gaussian filtering of $f(\mathbf{x})$ over a set of scales $[R_0, R_1, ..., R_N]$.

$$f_{R_n}(\mathbf{x}) = \int \frac{\mathrm{d}^3k}{(2\pi)^3} e^{-k^2R_n^2/2} \hat{f}(\mathbf{k}) e^{i\mathbf{k}\cdot\mathbf{x}}, \tag{2.2}$$

where $\hat{f}(\mathbf{k})$ is the Fourier transform of the input field $f(\mathbf{x})$.

Subsequently, the Hessian, $H_{ij,R_n}(\mathbf{x})$, of the filtered field is calculated via

$$H_{ij,R_n}(\mathbf{x}) \quad = \quad R_n^2 \, \frac{\partial^2 f_{R_n}(\mathbf{x})}{\partial x_i \partial x_j} \,, \tag{2.3}$$

where the R_n^2 term is as a renormalization factor that has to do with the multiscale nature of the algorithm. When expressed in Fourier space, the Hessian becomes

$$\hat{H}_{ij,R_n}(\mathbf{k}) \quad = \quad -k_i k_j R_n^2 \hat{f}(\mathbf{k}) e^{-k^2R_n^2/2} \,. \tag{2.4}$$

While in principle there are an infinite number of scales in the scale-space formalism, in practice our implementation uses a finite number of filter scales, restricted to the range of $[0.5, 4.0]$ h^{-1}Mpc. This range has been predicated on the expected relevance of filaments for understanding the properties of the

haloes in our sample, which have masses in the range 5×10^{10} to $1\times10^{15}h^{-1}M_{\odot}$ (see next section). The upper filter scale of 4 h^{-1}Mpc allows the identification of the most massive filaments, while the lower filter scale allows for the detections of thin and tenuous filaments that host the occasional isolated low-mass haloes.

The morphological signature is contained in the local geometry as specified by the eigenvalues of the Hessian matrix, $h_1 \leq h_2 \leq h_3$. The eigenvalues are used to assign to every point, $\mathbf{x}$, a node, filament and wall characteristics which are determined by a set of morphology filter functions (see Aragón-Calvo et al. 2007b; Cautun, van de Weygaert & Jones 2013). The morphology filter operation consists of assigning to each volume element and at each filter scale an environment signature, $\mathcal{S}_{R_n}(\mathbf{x})$. Subsequently, for each point, the environmental signatures calculated for each filter scale are combined to obtain a scale independent signature, $\mathcal{S}(\mathbf{x})$, which is defined as the maximum signature over all scales,

$$\mathcal{S}(\mathbf{x}) = \max_{\text{levels n}} \mathcal{S}_{R_n}(\mathbf{x})\,. \tag{2.5}$$

The final step in the MMF/NEXUS procedure involves the use of criteria to find the threshold signature that identifies valid structures. Signature values larger than the threshold correspond to real structures while the rest are spurious detections. For nodes, the threshold is given by the requirement that at least half of the nodes should be virialized. For filaments and walls, the threshold is determined on the basis of the change in filament and wall mass as a function of signature. The peak of the mass variation with signature delineates the most prominent filamentary and wall features of the cosmic web (for more details and for a study of different threshold values for the environment signature see Cautun, van de Weygaert & Jones 2013).

NEXUS+ and NEXUS velocity shear

In our study, we use two NEXUS methods for identifying filament populations. The first, the NEXUS+ algorithm, is based on the local geometry of the density field. The strongly non-Gaussian nature of the non linearly evolved density field is marked by density ranges over many orders of magnitude. Simply applying a Gaussian smoothing can wash out the anisotropic nature of the matter distribution, especially close to high-density peaks. This can be alleviated by applying a Log-Gaussian filter (Cautun, van de Weygaert & Jones 2013), which consists of three steps: (1) calculate the density logarithm, $\log\left(1+\delta(\mathbf{x})\right)$, (2) apply a Gaussian smoothing to $\log\left(1+\delta(\mathbf{x})\right)$, and (3) calculate the smoothed overdensity, $\delta_{\rm smooth}(\mathbf{x})$, from the smoothed density logarithm. Subsequently, NEXUS+ calculates the Hessian matrix of the Log-Gaussian smoothed density field using Eq. (2.3). The Hessian eigenvalues, $\chi_{1,+} \leq \chi_{2,+} \leq \chi_{3,+}$, and

eigenvectors, $\mathbf{e}_{i,+}$, determine the local shape and directions of the mass distribution. For example, a filamentary feature corresponds to $\chi_{1,+} < 0$, $\chi_{2,+} < 0$ and $|\chi_{1,+}| \simeq |\chi_{2,+}| \gg |\chi_{3,+}|$. The orientation of the filament is indicated by the eigenvector $\mathbf{e}_{3,+}$, while the sectional plane is defined by the eigenvectors $\mathbf{e}_{1,+}$ and $\mathbf{e}_{2,+}$. See the top panel of Figure 2.4 for a visual illustration of the filament orientation.

The second method, NEXUS_velshear, identifies the cosmic web through its dynamical signature, that is using the shear of the velocity flow induced by the gravitational forces that drive the growth of cosmic structure. The velocity shear is the symmetric part of the velocity gradient*, with the ij component defined as:

$$\sigma_{ij}(\mathbf{x}) = \frac{1}{2H}\left(\frac{\partial v_j}{\partial x_i} + \frac{\partial v_i}{\partial x_i}\right) , \tag{2.6}$$

where v_i is the i component of the velocity. In this definition, the velocity shear is normalized by the Hubble constant, H. To keep a close parallel to the cosmic web definition based on the density field, we apply the NEXUS formalism to the negative velocity shear, i.e. to $-\sigma_{ij}(\mathbf{x})$. This is motivated by linear theory, where the velocity shear is determined by the linear velocity growth factor times the negative gravitational tidal field.

The morphological identity and the principal directions at a given location are determined by the eigenvalues, $\chi_{1,\sigma} \leq \chi_{2,\sigma} \leq \chi_{3,\sigma}$, and the eigenvectors, $\mathbf{e}_{i,\sigma}$, of the Hessian matrix calculated from the negative velocity shear. Similarly to NEXUS+, a filament is marked by $\chi_{1,\sigma} < 0$, $\chi_{2,\sigma} < 0$ and $|\chi_{1,\sigma}| \simeq |\chi_{2,\sigma}| \gg |\chi_{3,\sigma}|$, that is contraction along the first two directions and small contraction or dilation along the third direction. The filament orientation is given by the third eigenvector of the shear field, $\mathbf{e}_{3,\sigma}$.

In this sense, NEXUS_velshear follows the same cosmic web classification philosophy as the (monoscale) V-web algorithm (Hoffman et al. 2012; Libeskind et al. 2018). The crucial difference between the two is that NEXUS_velshear takes into account the multiscale nature of the velocity field.

2.2.3 Density- versus shear-based filaments

There are several intriguing differences in filament populations identified by NEXUS+ and NEXUS_velshear. Both procedures identify the most prominent and dynamically dominant arteries of the cosmic web. These massive filaments,

* Sometimes the velocity shear is defined as the traceless symmetric part of the velocity gradient. Here, we include the divergence part of the velocity flow that indicates the expansion or contraction of a mass element.

with diameters of the order of 5 h^{-1}Mpc, may extend over vast lengths, sometimes over tens of Megaparsec. They are the main transport channels in the large scale universe, along which matter, gas and galaxies flow towards higher density mass concentrations. As such, they can nearly always be identified with pairs of massive and compact clusters, whose strong tidal forces give rise to very prominent and massive filaments (Bond, Kofman & Pogosyan 1996; Colberg, Krughoff & Connolly 2005; van de Weygaert & Bond 2008b; Bos et al. 2016). They are nearly always located on the boundaries of large voids. These filaments have a dominant contribution to the large scale tidal and velocity field (Rieder et al. 2018), with their dynamical imprint being recognizable as a distinct shear pattern in the velocity flow.

The contrast between NEXUS_velshear and NEXUS+, described in detail in Cautun, van de Weygaert & Jones (2013); Cautun et al. (2014), is illustrated in Figure 2.2, which compares the two filamentary networks in a slice of 20 h^{-1}Mpc thickness and of 300×300 $(h^{-1}\text{Mpc})^2$ in area. While the prominent and massive filaments are identified by both methods, NEXUS+ manages to identify many more thin filamentary structures that illustrate the multiscale character of the cosmic filamentary network.

A second major difference between the two web finders is due to the non-linear velocity shear field having a larger scale coherence (i.e. being more non-localized) than the density field. This is due to the difference in the non-linear power spectra between velocity shear and density, with the former decreasing faster on small scales (Bertschinger & Jain 1994; Jain & Bertschinger 1994; Bond & Myers 1996; van de Weygaert 2002; Romano-Díaz & van de Weygaert 2007). Gravity, and hence tidal fields, are integrals over the density field. Hence they also manifest themselves at a distance from the source (the density fluctations) that generated them. Shear, as with the velocity field itself, is similar: it results from the action of gravity (the tidal field) over time. Hence, while you are outside the generating source, you still see the imprint of the tidal field on the velocity field. *

For tides, and shear, this means you can have the signature for a filament or a node while far removed from the object, even way into the voids. Which is indeed what you see. We need not be amazed that it is also seen in the NEXUS_velshear filament results: they are thicker than the corresponding filaments identified from the density field. Because of this, the NEXUS_velshear filaments are typically thicker than their NEXUS+ counterparts, and thus the

* It is precisely this fact which is central to using the gravitational lensing shear field as a tracer of the source. And thus we need not be amazed it is also seen in the NEXUS_velshear filament results: they are thicker than the equivalent density identified filaments.

Table 2.1 – *The population of P-Millennium haloes more massive than* $3.2 \times 10^{10}\ h^{-1}\mathrm{M}_{\odot}$ *assigned to filaments by the NEXUS+ and NEXUS_velshear web identification methods. The columns specify: (1) method name, (2) the number of haloes assigned to filaments, (3) the fraction of the total halo population, (4) the number of* common *haloes assigned to filaments by both methods, and (5) the number of* exclusive *haloes assigned to filaments by only one method.*

Method	Number [$\times 10^6$]	Fraction [%]	Common [$\times 10^6$]	Exclusive [$\times 10^6$]
NEXUS+	2.80	36.7	2.36	0.43
NEXUS_velshear	2.47	32.6		0.10

NEXUS_velshear filaments tend to include matter and haloes in the immediate vicinity that would visually be more likely to be identified as part of the wall or void regions surrounding the NEXUS+ filaments.

An even more detailed and insightful illustration of the differences between the NEXUS+ and NEXUS_velshear filamentary networks is provided by studying the halo distribution. Figure 2.3 and Figure 2.4 depict the spatial distribution of haloes assigned to filaments by the two methods. The overall impression is one of NEXUS+ identifying a sharper outline of the cosmic web, while it includes a wide spectrum of small-scale filamentary features that are not seen in the NEXUS_velshear web-like network. While NEXUS_velshear identifies the massive filamentary arteries, it does not recover the small-scale tendrils branching out from these dominant structures or the complex network of tenuous filaments in low-density regions. The large dynamic range of the NEXUS+ procedure, however, does recognize and identify these small filaments. On the other hand, the prominent NEXUS_velshear filaments have a considerable number of haloes assigned to them that lie in the dynamical influence region of the filaments but that may in fact be located in low density boundary regions. As a result, the NEXUS_velshear filaments are more massive and broader than their NEXUS+ equivalents.

2.3 Halo population

The halo catalogue has been constructed by first identifying Friends-of-Friends (FOF) groups using a linking length of 0.2 times the mean dark matter particle separation. The FOF groups were further split into bound structures using the SUBFIND algorithm (Springel et al. 2001), which first associates potential

(a) The distribution of all haloes.

(b) Haloes assigned by both NEXUS+ and NEXUS_velshear to filaments.

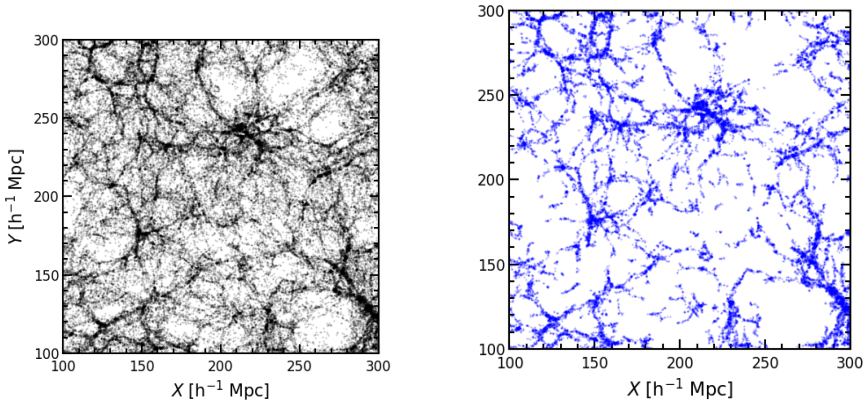

(c) Haloes assigned to filaments by NEXUS+.

(d) Haloes assigned to filaments by NEXUS_velshear.

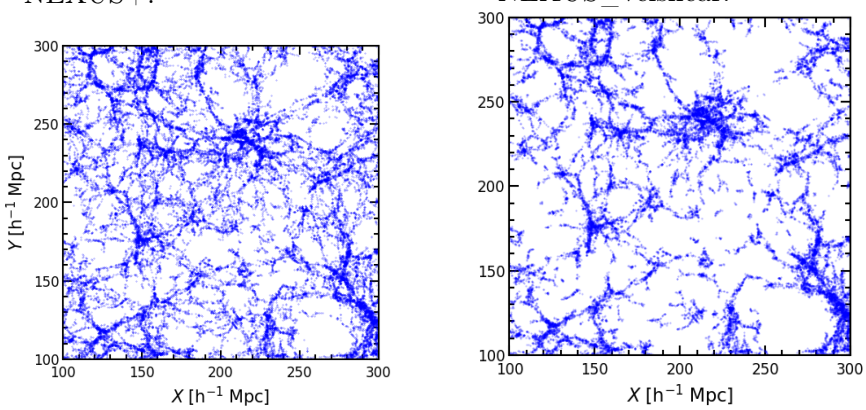

Figure 2.3 – *The distribution of haloes in a 20 h^{-1}*Mpc *slice of the P-Millennium simulation. Each dot represents a halo more massive than 3.2×10^{10} $h^{-1}\mathrm{M}_{\odot}$. It shows: all the haloes (top-left panel), the haloes residing in* NEXUS+ *filaments (bottom-left) and the haloes residing in NEXUS_velshear filaments (bottom-right). The haloes classified as residing in filaments by both methods are shown in the top-right panel.*

(a) Haloes assigned to filaments by NEXUS+.

(b) Haloes assigned to filaments by NEXUS_velshear.

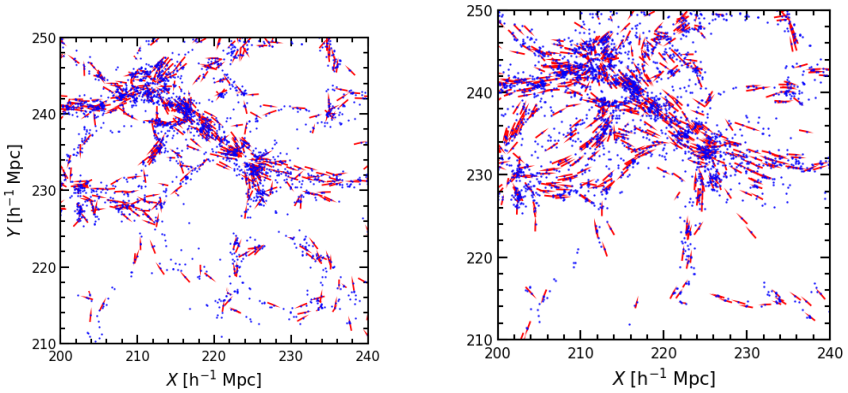

(c) Haloes assigned to filaments by NEXUS+, but not by NEXUS_velshear.

(d) Haloes assigned to filaments by NEXUS_velshear, but not by NEXUS+.

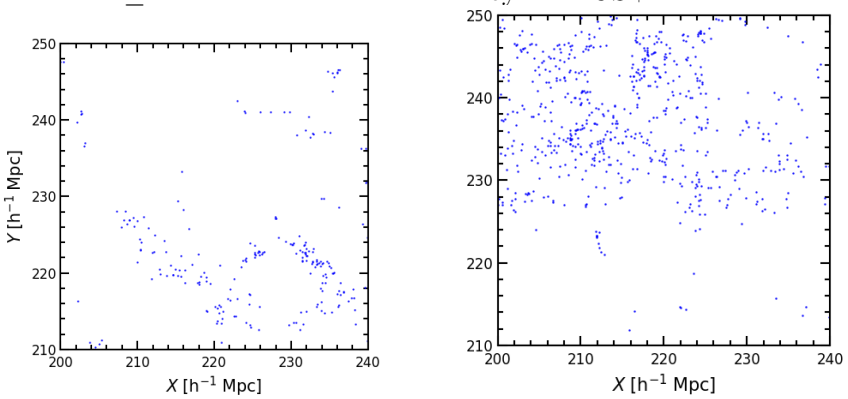

Figure 2.4 – *Comparison of haloes assigned to filaments by NEXUS+ and NEXUS_velshear. It shows a subregion of the volume shown in Figure 2.3 selected to enclose a massive filament. The thickness of the slice is 10 h^{-1}Mpc. The four panels show: all NEXUS+ filament haloes (top-left), all NEXUS_velshear filament haloes (top-right), haloes assigned to filaments only by NEXUS+ (bottom-left) and haloes assigned to filaments only by NEXUS_velshear (bottom-right). The red lines in the top two panels depict the orientation of the NEXUS+ and NEXUS_velshear filaments. The filament orientation is shown at the position of a random sample of 20% of the haloes in the slice. The contrast between both methods is substantial: NEXUS+ traces small filaments and tendrils whose minor dynamical impact eludes detection by NEXUS_velshear. Furthermore, the prominent filaments detected by NEXUS_velshear are substantially thicker than their NEXUS+ counterparts.*

subhaloes to local dark matter density peaks and then progressively discards particles that are not gravitationally bound to these substructures. For each FOF group, SUBFIND identifies the most massive subhalo as the main halo of the group. Our study uses only these main haloes. We define the halo radius, R_{200}, as the radius of a sphere located at the halo centre that encloses a mean density 200 times the critical density of the universe. Then, the halo mass, M_{200}, is the mass contained within R_{200}.

We limit our analysis to haloes more massive than $3.2 \times 10^{10}\ h^{-1}\mathrm{M}_{\odot}$, which is motivated by the condition that the structure of a halo is resolved with a sufficiently large number of particles. Following Bett et al. (2007), we select haloes resolved with at least 300 dark matter particles within R_{200}. The P-Millennium contains 3.76×10^6 such main haloes which represent a very large and statistically representative sample. This enables us to characterize the alignment between halo properties and the cosmic web directions to an unprecedented extent.

For all the haloes above our mass threshold limit, we calculate physical properties such as angular momentum and shape. Unless specified otherwise, these properties are calculated using all the gravitationally bound dark matter particles inside the halo radius, R_{200}. In order to gain deeper insight, we also calculate properties for the inner region of all haloes. We use two different radial cuts corresponding to the radii that enclose 10 and 50%, respectively, of the halo particles. We refer to these radial cuts as the inner 10% and 50% of the halo, while when describing the full halo properties we denote that as the entire halo. The inner radial cuts are motivated by the observation that recent mass accretion is mainly deposited on the outer regions of a halo (Wang et al. 2011), and thus, by studying the inner halo, we can probe how recent mass accretion, which is often anisotropic (e.g. Vera-Ciro et al. 2011; Shao et al. 2017), may be affecting halo shape and spin.

2.3.1 Cosmic web environment

We split the halo population into node, filament, wall and void samples according to the web environment identified at the location of the halo. We do so for both the NEXUS_velshear and NEXUS+ web classification schemes. In general, many of the same haloes are assigned to nodes and filaments by both methods, but there are also differences (see Table 2.1), which we discuss in more details shortly.

In the present study, we focus on main haloes residing in filaments. The statistics of filament haloes in P-Millennium are presented in Table 2.1. The filaments contain roughly 35% of the main haloes, with NEXUS+ identifying a slightly larger fraction of filament haloes. Both methods assign roughly the

same haloes to filaments, with 96% of the NEXUS_velshear filament haloes also residing in NEXUS+ filaments. For NEXUS+, 84% of its filament haloes are in common with the NEXUS_velshear ones, while the remaining 16% corresponds to haloes that populate filamentary tendrils in underdense regions.

In Figure 2.3 we illustrate the similarities and differences in the distribution of filament haloes identified by the two web finders. For this, we show the full halo distribution (top-left panel) as well as the haloes inside NEXUS_velshear and NEXUS+ filaments inside a 200×200 h^{-1}Mpc region, of 20 h^{-1}Mpc in width. Visually, we find that both methods are successful in recovering the most prominent filaments and also some of the less conspicuous ones, although it is more difficult to visually assess the latter due to the larger slice thickness. The haloes in NEXUS+ filaments (bottom-left-hand panel) trace a sharp and intricate network with prominent filamentary arteries, as well as a substantial web of thinner tenuous branches and minor filaments in low-density areas. In contrast, the NEXUS_velshear filament haloes (bottom-right-hand panel) have a rather different character, tracing mostly thick filaments.

The comparison between NEXUS+ and NEXUS_velshear filaments reveal that the latter are considerably thicker. This is a reflection of the non-local character of the velocity shear field, which, compared to NEXUS+, leads to assigning to the same filament haloes that are found at larger distances from the filament spine. The extent of this effect can be best appreciated in the top-right panel, which shows the distribution of *common* haloes, that is the ones assigned to filaments by both NEXUS+ and NEXUS_velshear. The common filament haloes have almost the same appearance, although thinner and sharper, as the ones residing in the NEXUS_velshear filaments. This clearly illustrates that NEXUS+ finds the NEXUS_velshear filaments and that it assigns them a smaller thickness.

To have a more detailed comparison between the filament haloes identified by the two web finders, Figure 2.4 zooms in on to a 40×40 h^{-1}Mpc region centred on a prominent filamentary network. The figure shows the distribution of filament haloes in and around a junction of many prominent filaments which are found around a concentration of cluster-mass haloes. This region is certainly one of the most dynamically active areas of the cosmic web and is expected to be strongly influenced by the substantial tidal forces resulting from the highly anisotropic distribution of matter in the region.

The contrast between the two web finders is substantial. NEXUS+ includes small filaments and tendrils whose minor dynamical impact on the velocity shear field eludes detection by the NEXUS_velshear method. The top row of Figure 2.4 provides a telling visualization of this effect, with NEXUS+ pointing out many thin low-density filaments around the main filamentary mass con-

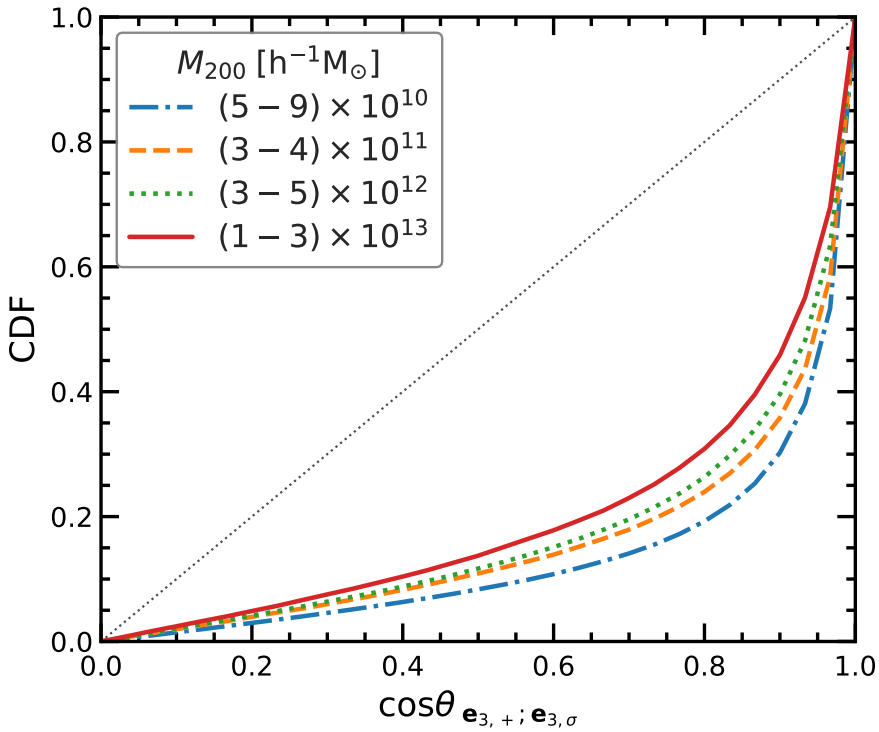

Figure 2.5 – *The CDF of the angle between the orientation of filaments identified using NEXUS+ and NEXUS_velshear. The curves correspond to the alignment of the two filament types at the positions of different mass haloes. The NEXUS+ and NEXUS_velshear filaments are mostly aligned (compare to the expectation for random alignment shown in dotted grey), with the strength of the alignment slightly decreasing for high mass haloes.*

centrations. This can also be observed in the bottom row of Figure 2.4, which shows the *exclusive* filament haloes, that is the haloes assigned to filaments by only one of the two methods. NEXUS_velshear misses the halo population of minor filaments while identifying thicker prominent filaments, which may even include haloes that NEXUS+ assigns to underdense void regions.

The directions of NEXUS+ and NEXUS_velshear filaments are illustrated in the top two panels of Figure 2.4. This shows that the orientations assigned by the two web finders match well with the visually inferred local direction of the filamentary network. The NEXUS+ and NEXUS_velshear filament orientations are nearly parallel as can be seen from Figure 2.5. The figure shows the misalignment angle between NEXUS+ and NEXUS_velshear filament axes, which was calculated at the position of each halo that is assigned to both filament types.

The NEXUS+ and NEXUS_velshear filaments are well aligned over the entire halo mass range, with a median misalignment of ∼20°. The alignment shows a small dependence on halo mass, with higher mass haloes having slightly lower alignment between the two filament types.

2.3.2 Halo mass function

A first aspect of the connection between web-like environment and the halo distribution concerns how haloes populate the different cosmic web environments. This is shown in Figure 2.6, where we present the (cumulative) mass function of haloes segregated according to the environment in which they reside. Here we show the population of main haloes with at least 100 particles, i.e. $M_{200} > 1.1 \times 10^{10}\ h^{-1}\mathrm{M}_{\odot}$, however, for the rest of the chapter, we limit the analysis to objects at least three times as massive. The halo mass function represents the number density, $n(> M)$, of haloes with a mass in excess of M,

$$n(> M) = \int_{M}^{\infty} \frac{\mathrm{d}n}{\mathrm{d}\log M} \frac{\mathrm{d}M}{M}\,, \tag{2.7}$$

where $\mathrm{d}n/\mathrm{d}\log M$ denotes the specific mass function, that is the number density of haloes of mass M per logarithmic mass bin. Figure 2.6 shows the halo mass function split according to web environments for both the NEXUS+ (top panel) and the NEXUS_velshear (middle panel) methods. We note that the identifications of node environments using the velocity shear field poses challenges (Cautun, van de Weygaert & Jones 2013), which are due to the presence of a substantial level of vorticity in these highly multi-stream regions that is not accounted by the velocity shear field. To deal with this limitation, following Cautun, van de Weygaert & Jones (2013), we augmented the NEXUS_velshear scheme such that the node identification is done using the density field, which is the procedure used by NEXUS+.

Figure 2.6 shows that the halo mass function depicts a substantial difference between environments (also see e.g. Cautun et al. 2014; Libeskind et al. 2018): the most massive haloes reside at nodes of the web while most lower mass objects are predominantly found in filaments. While there are some differences in details, in particular concerning the higher mass tails of the void and wall halo mass functions, overall the halo populations segregated by environment are very similar in both the NEXUS+ and NEXUS_velshear web finders.

Except for the most massive objects, we find that the majority of haloes are found in filaments. The exception concerns the objects with masses in excess of $M \approx 10^{13.5}\mathrm{M}_{\odot}$, which are almost exclusively found in nodes. The mass function for void haloes is strongly shifted to lower masses, and has a significantly lower amplitude than that for filament or wall haloes. This is to be expected,

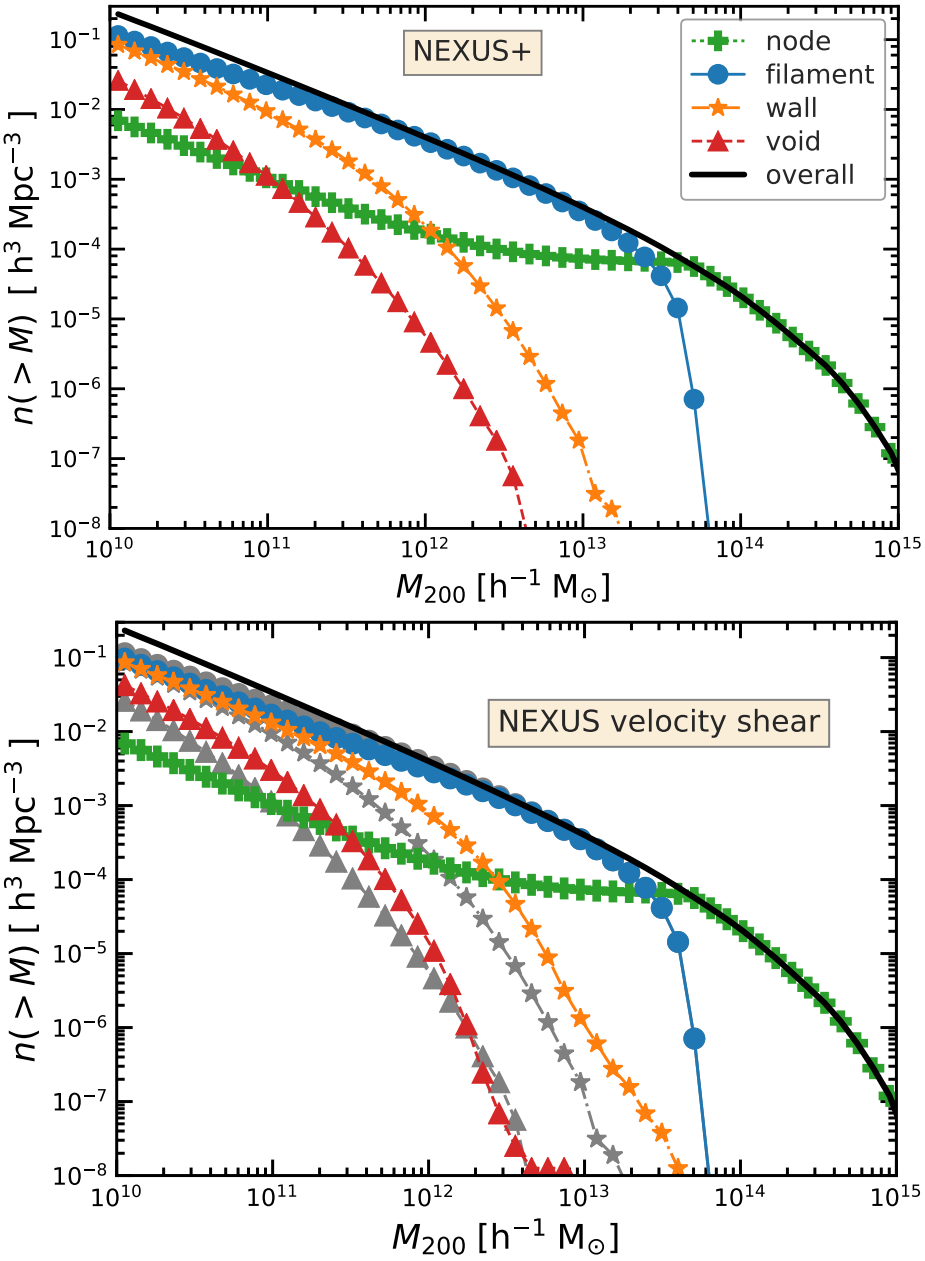

Figure 2.6 – *Cumulative halo mass function in the different cosmic web environments of the P-Millennium simulations at $z = 0$. Top panel: Environments detected using NEXUS+. Bottom panel: Environments detected using NEXUS_velshear, with the grey curves showing the NEXUS+ results from the top panel.*

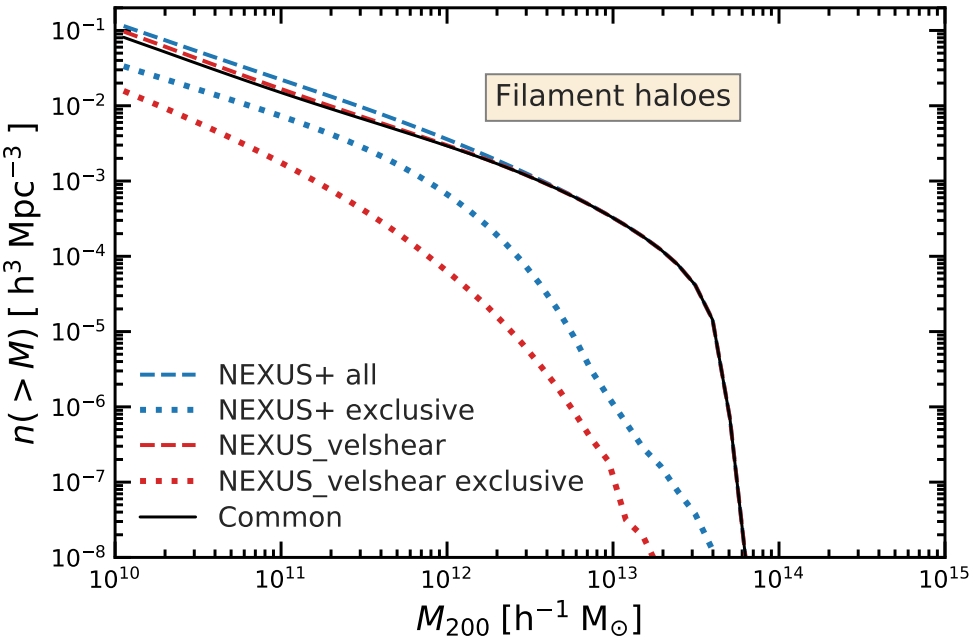

Figure 2.7 – *Cumulative halo mass function in the different cosmic web environments of the P-Millennium simulations at $z = 0$. A closer comparison of the halo mass function in NEXUS+ and NEXUS_velshear filaments. The common sample corresponds to haloes that reside in both filament types and it comprises most of the filament halo population. The exclusive sample consists of haloes assigned to only one of the two filament types.*

since voids represent the lowest density regions and are mostly populated by low mass haloes. This agrees with observations which reveal that most void galaxies are typically faint and have low stellar masses (see e.g. Kreckel et al. 2011, 2012). A similar trend is seen for haloes residing in the membranes of the cosmic web, i.e. walls, though less extreme than for void galaxies. Haloes more massive than $10^{12.0}M_\odot$ are hardly found in walls, nearly all of them residing in filaments. It explains, amongst others, why walls are so hard to trace in magnitude-limited galaxy surveys (see also Cautun et al. 2014). Overall, the halo mass functions in NEXUS+ environments are the same as in their NEXUS_velshear equivalents, with only minor differences. In the second panel of Figure 2.6, we can notice that the NEXUS_velshear allocates somewhat more haloes of all masses to voids and walls, and thus slightly fewer haloes to filaments. Figure 2.7 compares in detail the filament mass function identified by the two web finders. The common sample represents the majority of the filament halo population. This is the case in particular for NEXUS_velshear, for which the exclusive sample is nearly a factor of ten less numerous at all

masses. The NEXUS+ exclusive sample is more sizeable, consisting of ∼30% of the low mass haloes found in NEXUS+ filaments. This is a direct reflection of the fact that NEXUS+ identifies the small and tenuous filamentary tendrils, which are largely ignored by NEXUS_velshear. These less prominent features contain mostly low mass haloes (Cautun et al. 2014), which explain why the differences between NEXUS+ and NEXUS_velshear are mostly seen for low mass haloes.

2.3.3 Halo shape

We determine the shape of a halo by calculating its moment of inertia tensor, $\mathbf{I}_{ij}$ (van Haarlem & van de Weygaert 1993b; Bett et al. 2007; Araya-Melo 2008). For a halo that contains N particles, the moment of inertia with respect to the centre of mass is defined as

$$\mathbf{I}_{ij} = \sum_{k=1}^{N} m_k r_{k,i} r_{k,j} \,, \tag{2.8}$$

where m_k is the mass of the k-th particle, and $r_{k,i}$ is the particle position along the i-th coordinate axis with respect to the halo centre of mass. The inertia tensor is a 3×3 symmetric matrix that can be diagonalised to calculate its eigenvalues, $s_a \geq s_b \geq s_c$, and eigenvectors, $\mathbf{v}_a$, $\mathbf{v}_b$ and $\mathbf{v}_c$. The shape of the halo is commonly described in terms of the axes ratios b/a and c/a, where $a = \sqrt{s_a}$, $b = \sqrt{s_b}$ and $c = \sqrt{s_c}$ denote the major, intermediate and minor halo axes, respectively. A perfectly spherical halo has $b/a = c/a = 1$, a prolate one has a major axis significantly longer than the intermediate and minor axis, $c \approx b << a$, while an oblate one has a much smaller minor axis than the other two, $c << b \approx a$. The orientation of the halo is specified by the corresponding eigenvector, with $\mathbf{v}_a$, $\mathbf{v}_b$ and $\mathbf{v}_c$ pointing along the major, intermediate and minor axes, respectively.

Figure 2.8 shows the halo shape distribution in P-Millennium, which is in good agreement with previous studies (e.g. Bett et al. 2007). Overall, the haloes are triaxial, with a clear trend towards a roundish - but never perfectly spherical - shape. Most haloes have $c/a > 0.8$ and $b/a > 0.9$. They also have a slight tendency towards a prolate shape. The halo shapes show a small, but statistically significant, variation with the web environment in which a halo resides. This is clearly in indicated in the two panels of Figure 2.9, which shows the median halo shape axis ratios, b/a and c/a, as a function of halo mass and environment. Haloes in nodes and voids are more flattened than haloes residing in filaments and walls (Hahn et al. 2007a; Forero-Romero, Contreras & Padilla 2014).

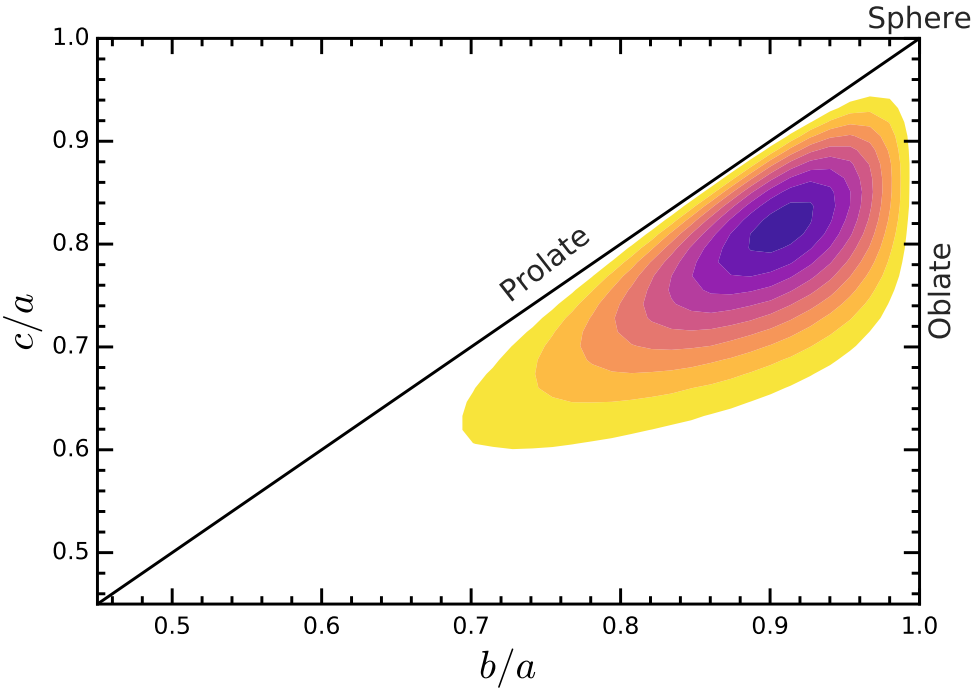

Figure 2.8 – *The distribution of halo shapes in P-Millennium in terms of the axes ratios c/a versus b/a, where a, b and c are the major, intermediate and minor axes. The coloured regions represent contour lines of the density of points, with darker colours corresponding to higher densities. We also show the point of perfect sphericity, $b/a = c/a = 1$, and the two axes corresponding to purely oblate (flattened) and prolate (elongated) haloes.*

2.3.4 Halo angular momentum

The angular momentum – or spin – of the halo is defined as the sum over the angular momentum of the individual particles that constitute the halo,

$$\mathbf{J} = \sum_{k=1}^{N} m_k \left(\mathbf{r}_k \times \mathbf{v}_k \right), \tag{2.9}$$

where $\mathbf{r}_k$ and $\mathbf{v}_k$ are the position and velocity of the k-th particle with respect to the halo centre of mass.

For each halo, we calculate the angular momentum for the entire virialized halo, as well as for inner halo regions consisting of the inner 10% and 50% of the halo particles. This yields 3 angular momenta, $\mathbf{J}_{100}$, $\mathbf{J}_{50}$ and $\mathbf{J}_{10}$ for each halo. We are interested in two aspects of the halo angular momenta: its amplitude and its orientation (i.e. the spin direction).

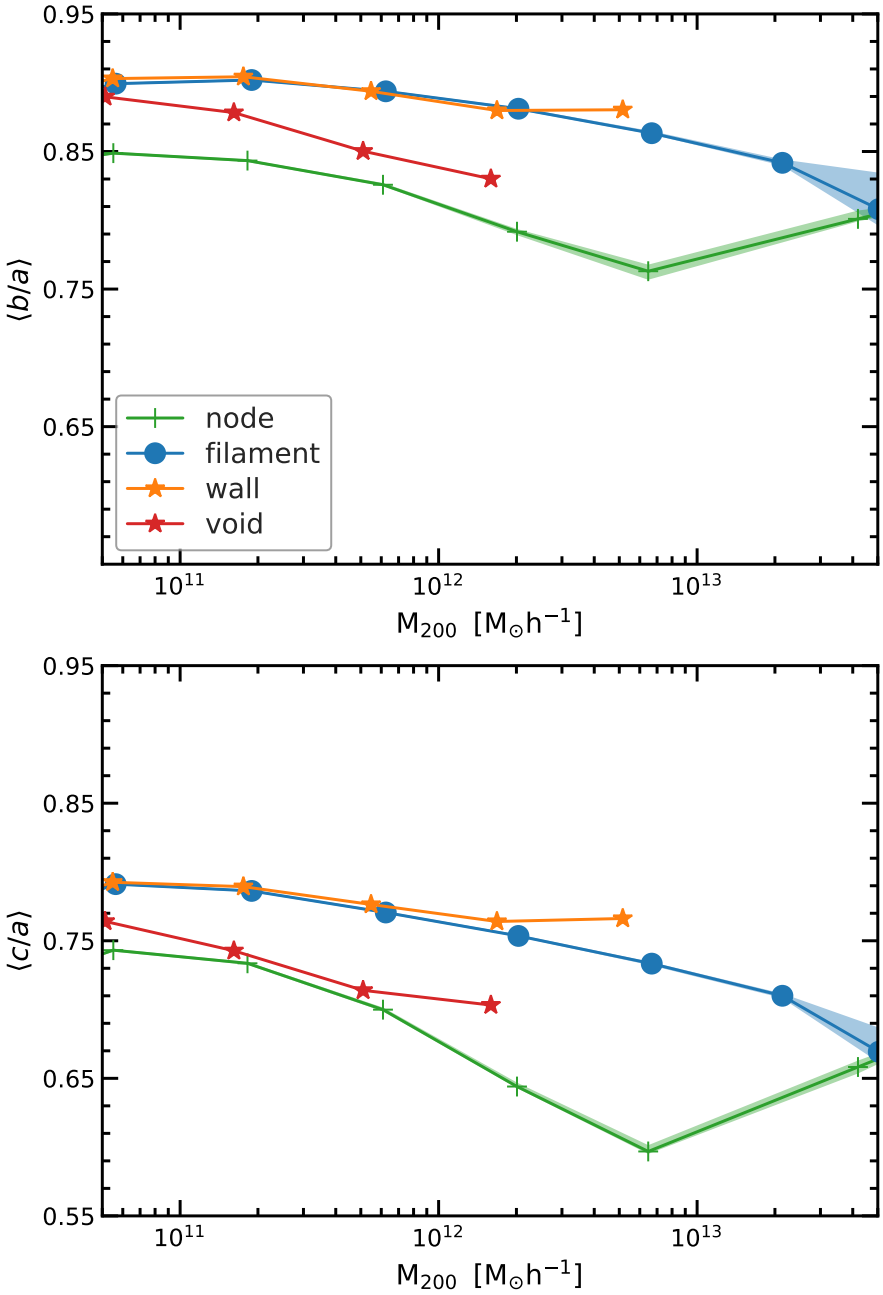

Figure 2.9 – *The median axis ratios, $\langle b/a \rangle$ and $\langle c/a \rangle$, as a function of halo mass for haloes in different cosmic web environments. The shaded region indicate the 1σ error. Both axis ratios shows a weak dependence on halo mass and a stronger variation with web environment.*

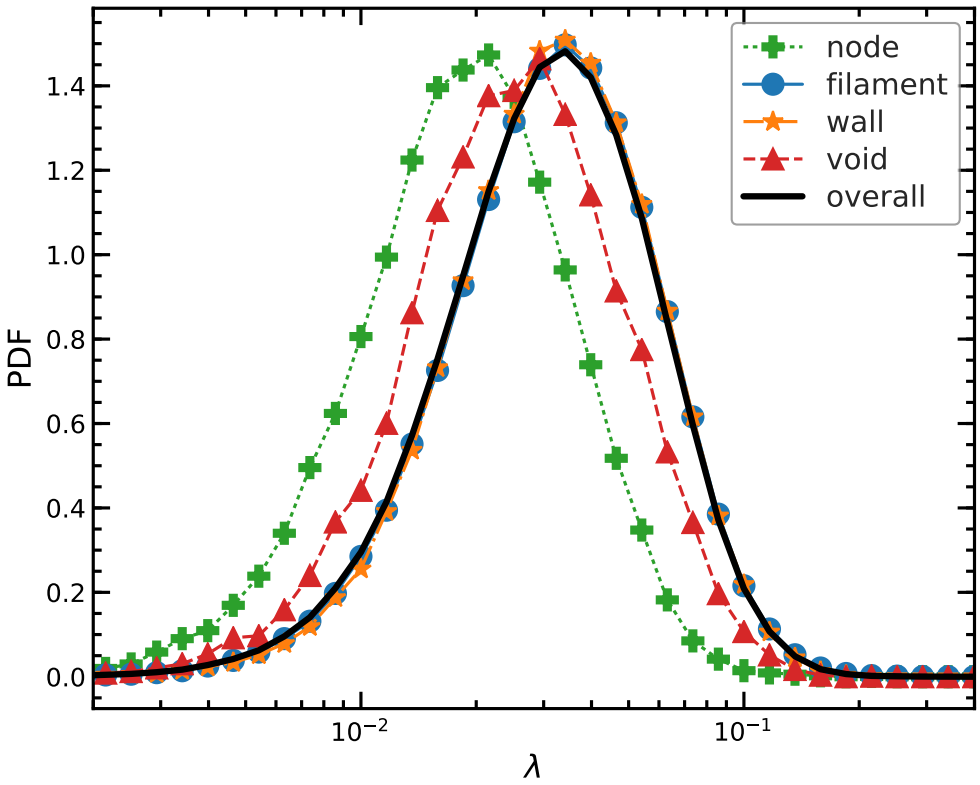

Figure 2.10 – *The distribution of halo spins segregated according to the NEXUS+ environment in which a halo resides: nodes or clusters (solid line with crosses), filaments (dotted line with dots), walls or sheets (solid line with star symbol) and voids (dashed line with triangles). The results are calculated using haloes in the mass range* $[3, 5] \times 10^{11}\ h^{-1}\mathrm{M}_{\odot}$.

Spin parameter λ

The angular momentum amplitude, $J = |\mathbf{J}|$, is usually expressed in terms of a dimensionless spin parameter, λ_P, introduced by Peebles (1969),

$$\lambda_P = \frac{J|E|^{1/2}}{GM^{5/2}}\,, \tag{2.10}$$

where J, E and M are the total angular momentum, energy and mass of the halo, and G is Newton's constant. The spin parameter λ_P quantifies the extent of coherent rotation of a halo (or any self-gravitating system). A value of unity of the parameter means that a self gravitating system is supported by rotation (Padmanabhan 1993), a value closer to zero would imply that it hardly has coherent rotation and that the system is dispersion-supported.

We use an alternative definition of the spin parameter introduced by Bullock et al. (2001). The Bullock spin parameter λ has a more practical definition, in particular when considering a subvolume of a virialized sphere, and it is also easier to calculate. For a region enclosed within a sphere of radius R, this spin parameter is defined as

$$\lambda = \frac{J}{\sqrt{2}MVR}, \tag{2.11}$$

where V is the halo circular velocity at radius R and J the angular momentum within this radius. This spin parameter definition reduces to the standard Peebles parameter λ_P when measured at the virial radius of a truncated isothermal halo. The spin parameters λ_P and λ are in fact very similar for typical NFW haloes (Navarro, Frenk & White 1997; Bullock et al. 2001), having a roughly lognormal distribution with a median value of $\lambda \approx 0.05$ (Efstathiou & Jones 1979; Barnes & Efstathiou 1987).

In order to determine if halo spin amplitude is correlated to the web environment in which a halo resides, Figure 2.10 shows the probability distribution functions (PDF) of the Bullock spin parameter for halo samples split according to the NEXUS+ environment in which a halo is located. We observe a clear segregation between the rotation properties of haloes in different web environments, with filament and wall haloes having on average the largest spin, while node haloes are the slowest rotation objects. For all environments, the PDF is close to a lognormal distribution, but with its peak value slightly shifted, from $\lambda = 0.035$ for filaments and walls, to $\lambda = 0.030$ for voids and $\lambda = 0.020$ for node haloes.

Figure 2.10 clearly reveals the influence of cosmic environment on the spin parameters of haloes, with filament and wall haloes showing a significantly stronger coherent rotation than their counterparts residing in nodes, which have a more prominent dispersion-supported character. Interestingly, this is similar with the morphology-density relation (Dressler 1980) found in observations, with early type galaxies dominating the galaxy population of clusters while the late-type spirals dominating the filamentary and wall-like "field" regions.

Spin orientation

When calculating the alignment of halo spin with the web directions, we make use of the spin direction of each halo, which is defined as

$$\mathbf{e}_J = \frac{\mathbf{J}}{|J|}\,. \tag{2.12}$$

We apply this relation for each of the three radial cuts for the radial extent, i.e. for the radii including 10%, 50% and 100% of the mass of the halo.

2.4 Spin Alignment Analysis

Here we study the alignment between the halo spins and the orientation of the filaments in which the haloes are embedded. The filament orientation corresponds to the direction along the filament spine, which is given by the $\mathbf{e}_{3,+}$ and $\mathbf{e}_{3,\sigma}$ eigenvectors for the NEXUS+ and NEXUS_velshear methods, respectively (for details see subsubsection 2.2.2 and Figure 2.11). Furthermore, we limit our analysis to filament haloes, which are the dominant population of objects.

2.4.1 Alignment analysis: definitions

We define the alignment angle as the angle between the direction of a halo property, which can be spin, shape or velocity, and the orientation of the filament at the position of the halo. A diagrammatic illustration of the alignment angle θ is shown in Figure 2.11, with the ellipse representing a halo and the cylinder the local stretch of the filament. For a given halo vector property $\mathbf{h}$, the halo-filament alignment angle is

$$\mu_{hf} \equiv \cos\theta_{\mathbf{h},\mathbf{e}_3} = \left| \frac{\mathbf{h}\cdot\mathbf{e}_3}{|\mathbf{h}||\mathbf{e}_3|} \right| , \tag{2.13}$$

which is the normalized scalar product between the halo and filament orientations. We take the absolute value of the scalar product since filaments have an orientation and not a direction, that is both $\mathbf{e}_3$ and $-\mathbf{e}_3$ correspond to a valid filament orientation. Note that the symbol, $\mu_{hf} \equiv \cos\theta_{\mathbf{h},\mathbf{e}_3}$, denotes the cosine of the alignment angle, however, for simplicity, we refer to it both as the alignment parameter and as the alignment angle.

A halo property that is parallel to the filament orientation corresponds to $\mu_{hf} = 1$, while a property that is perpendicular to the filament orientation corresponds to $\mu_{hf} = 0$. A random or isotropic distribution of alignment angles corresponds to a uniform distribution of μ_{hf} between 0 and 1, which provides a useful reference line for evaluating deviations from isotropy. In the case of a distribution of alignment angles for a halo population, we refer to that sample as being *preferentially parallel* if the median alignment angle is larger than 0.5. Conversely, that sample is *preferentially perpendicular* if the median alignment angle is lower than 0.5. Following this, and somewhat arbitrary, we consider that $\mu_{hf} = 0.5$ marks the transition between a preferentially parallel, median $\mu_{hf} > 0.5$, and a preferentially perpendicular, median $\mu_{hf} < 0.5$, alignment.

We use bootstrapping to estimate the uncertainty in the distribution of align-

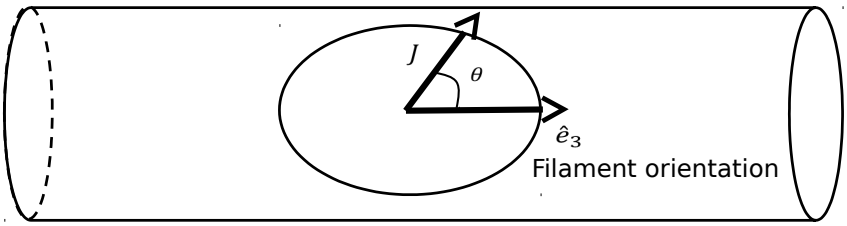

Figure 2.11 – *Schematic representation of the alignment angle θ between the angular momentum of a halo, $\mathbf{J}$, and the filament orientation, $\mathbf{e}_3$. The cylinder represents the filament and the ellipse depicts the halo residing in it. A value of $\cos\theta \sim 1$ corresponds to the halo spin direction being parallel with the filament, while $\cos\theta \sim 0$ corresponds to a perpendicular configuration.*

ment angles. For each distribution, we generate 1000 bootstrap realizations and compute the distribution and median values for each realizations. These are then used to estimate 1 and 2σ uncertainty intervals. We apply this procedure for estimating PDF uncertainties (e.g. see Figure 2.12) as well as for calculating the error in the determination of the median value (e.g. see Figure 2.13).

2.4.2 Halo spin alignment: statistical trends

Figure 2.12 gives the distribution of the halo spin alignment angle, i.e. of $\mu_{Jf} = \cos(\theta_{\mathbf{J};\mathbf{e}_3})$, between the halo spin directions and the filament orientation at the position of the haloes. The panels of the figure correspond to haloes of different masses. The figure shows the alignment only for NEXUS_velshear filaments, but a nearly identical result is found for NEXUS+ filaments. We study the alignment of the entire halo, as well as for inner radial cuts that contain 50% and 10% of the halo mass. In each case, we require at least 300 particles to determine the halo spin, which is why the spin for the 50% and 10% inner radial cuts is shown only for haloes more massive than 1 and $3 \times 10^{11}\ h^{-1}\mathrm{M}_\odot$, respectively.

For haloes in each mass range, we find that the alignment angle has a wide distribution, taking values over the full allowed range from $\cos\theta = 0$ up to $\cos\theta = 1$ (note that the y-axis only goes from 0.8 to 1.2). Nonetheless, the distribution is clearly different from an isotropic one, which is the case even when accounting for uncertainties due to the finite size of the sample, which are shown as the grey shaded region around the isotropic expectation value. The spin directions of low-mass haloes show an excess probability to have $\cos\theta_{\mathbf{J};\mathbf{e}_3} \simeq 1$, which indicates a tendency to be preferentially parallel to the filament spine. In contrast, high-mass haloes show an opposite trend, with an excess of objects

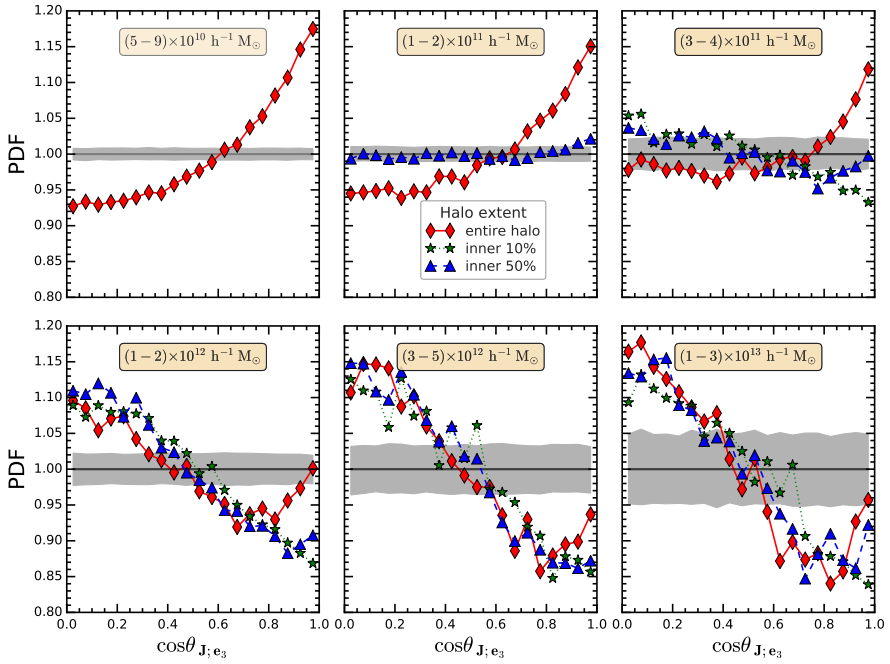

Figure 2.12 – *The distribution of alignment angles, $\cos\theta_{\mathbf{J};\mathbf{e}_3}$, between the halo angular momentum, $\mathbf{J}$, and the filament orientation, $\mathbf{e}_3$, for haloes residing in filaments identified using the NEXUS velocity shear method. Each panel shows the PDF for a different range in halo mass, M_{200}. Each panel (except the two for the lowest halo mass) shows the alignment between the filament orientation and the angular momentum calculated using different radial cuts: entire halo (red rhombus symbols), and the inner regions that contain 50% (blue triangles) and 10% (green stars) of the particles. The horizontal line shows the mean expectation in the absence of an alignment signal and the grey shaded region shows the 1-sigma uncertainty region given the sample size. The alignment distribution depends on halo mass, with the spin of massive haloes being preferentially perpendicular and that of low mass haloes being preferentially parallel to the filament orientation. Furthermore, at low masses the alignment depends on the inner radial cut used for calculating the halo spin.*

with $\cos\theta_{\mathbf{J};\mathbf{e}_3} \simeq 0$, i.e. tendency to be preferentially perpendicular to the filament axis. To summarize, while we find a wide distribution of halo spin - filament orientations, there is a statistically significant excess of haloes that, depending on mass, have their spin preferentially parallel or perpendicular to their host filaments.

The nature of the spin - filament alignment depends on halo mass. Many low-mass haloes, with masses in the range $M_{200} = (5-9) \times 10^{10} h^{-1}\mathrm{M}_\odot$ (top left-hand panel of Figure 2.12) have alignment angles, $\cos\theta \gtrsim 0.8$, which indicates their tendency to orient parallel to the filament spine. On the other hand, evaluating the alignment in the subsequent panels, which correspond to increasing halo mass, we observe a systematic shift from preferentially parallel to preferentially perpendicular configurations. For example, haloes with masses of $(3-4) \times 10^{11}\ h^{-1}\mathrm{M}_\odot$ show a considerably weaker parallel alignment excess, while for halo masses of $(1-2) \times 10^{12}\ h^{-1}\mathrm{M}_\odot$ and higher, most haloes have an alignment angle $\cos\theta \lesssim 0.3$.

The spin - filament alignment depends not only on halo mass, but also on the radial extent in which the halo spin direction is calculated. This is illustrated in Figure 2.12, which shows the spin-filament alignment calculated using the inner most 10% and 50% of the halo mass. While for high halo masses, $M_{200} > 1 \times 10^{12}\ h^{-1}\mathrm{M}_\odot$, the inner and the entire halo spins are aligned to the same degree with their host filament, at lower masses, $M_{200} < 5 \times 10^{11}\ h^{-1}\mathrm{M}_\odot$, the inner halo spin shows no preferential alignment. This is in contrast to the entire halo spin, which is preferentially parallel to the filament spine. The most remarkable contrast between the inner and outer halo spin orientations is found for objects in the mass range $(3-4) \times 10^{11}\ h^{-1}\mathrm{M}_\odot$ (third panel of Figure 2.12). While the inner halo spin has a slight tendency for a perpendicular alignment, the entire halo spin is oriented preferentially along the filament spine.

In summary, the halo spin - filament alignment is mass dependent: low-mass haloes have a preferentially parallel alignment, while haloes of Milky Way mass and more massive have a preferentially perpendicular alignment. The latter fits with the tidal torque theory (TTT) which predicts that halo spin directions are perpendicular on the filament in which the haloes reside (Lee & Pen 2000). However, the spin - filament alignment of low mass haloes is opposite to the predictions of TTT. The picture is further complicated since the alignment of low-mass haloes depends on the radial extent used for calculating their spin, with the alignment changing from preferentially perpendicular in the inner region, which agrees with TTT predictions, to preferentially parallel in the outer region. The inner region consists of mostly early accreted mass while the converse is true for the outer region. This suggests that the initially induced halo spin during the linear evolution phase (Peebles 1969) is substantially modified

by subsequent mass accretion stages. Particularly outstanding in this respect is the contrast between low- versus high-mass haloes, with the spin - filament alignment of the latter being less disturbed by recent accretion.

2.4.3 The spin flip

We now proceed to study in more detail the dependence on halo mass of the halo spin - filament alignment. This is shown in Figure 2.13, where we plot the median spin - filament alignment angle, $\langle \mu_{Jf} \rangle = \langle \cos \theta_{\mathbf{J};\mathbf{e}_3} \rangle$, calculated using narrow ranges in halo mass. To assess the statistical robustness of the median alignment angle, we show the 2σ uncertainty in the median value, which is calculated using bootstrap sampling. The uncertainty range is small, especially at low masses, which is due to the large number of haloes in each mass range. For clarity, we only show the uncertainty in the alignment with NEXUS_velshear filaments, but roughly equal uncertainties are present in the alignment with NEXUS+ filaments. The threshold between preferentially parallel and perpendicular alignments corresponds to $\langle \cos \theta_{\mathbf{J};\mathbf{e}_3} \rangle = 0.5$ and is shown with a horizontal solid line in Figure 2.13.

Figure 2.13 shows a clear and systematic trend between halo mass and the median spin - filament alignment angle: the alignment angle, $\langle \cos \theta_{\mathbf{J};\mathbf{e}_3} \rangle$ increases with decreasing halo mass. This trend is visible for both NEXUS+ and NEXUS_velshear filaments, although the exact median angles vary slightly between the two methods. Especially telling is the transition from preferentially perpendicular alignment at high masses to a preferentially parallel alignment at low masses, which takes place at $M_{200} = 5.6$ and $3.8 \times 10^{11}\ h^{-1}\mathrm{M}_{\odot}$ for NEXUS_velshear and NEXUS+ filaments, respectively. This transition is known as *spin flip* and has been the subject of intense study (Aragón-Calvo et al. 2007b; Hahn, Teyssier & Carollo 2010; Codis et al. 2012; Trowland, Lewis & Bland-Hawthorn 2013). The exact value of the spin flip halo mass varies between studies, and, as we found here, it varies between the two web finders employed here. In the next subsection we investigate this difference in more detail.

Figure 2.13 also shows the spin - filament alignment for the inner halo, whose strength and mass dependence is different from that of the entire halo. The difference between the inner and entire halo spin alignment is most pronounced for low mass haloes, in line with the conclusions of Figure 2.12. For example, the spin of the inner 10% of the halo mass shows little mass dependence for high masses, after which it slowly increases from preferentially perpendicular towards preferentially parallel alignment with the filament spin. However, due to the limited resolution of the simulation (we need at least 300 particles in the inner 10% region of the halo), we cannot probe if there is a spin flip and

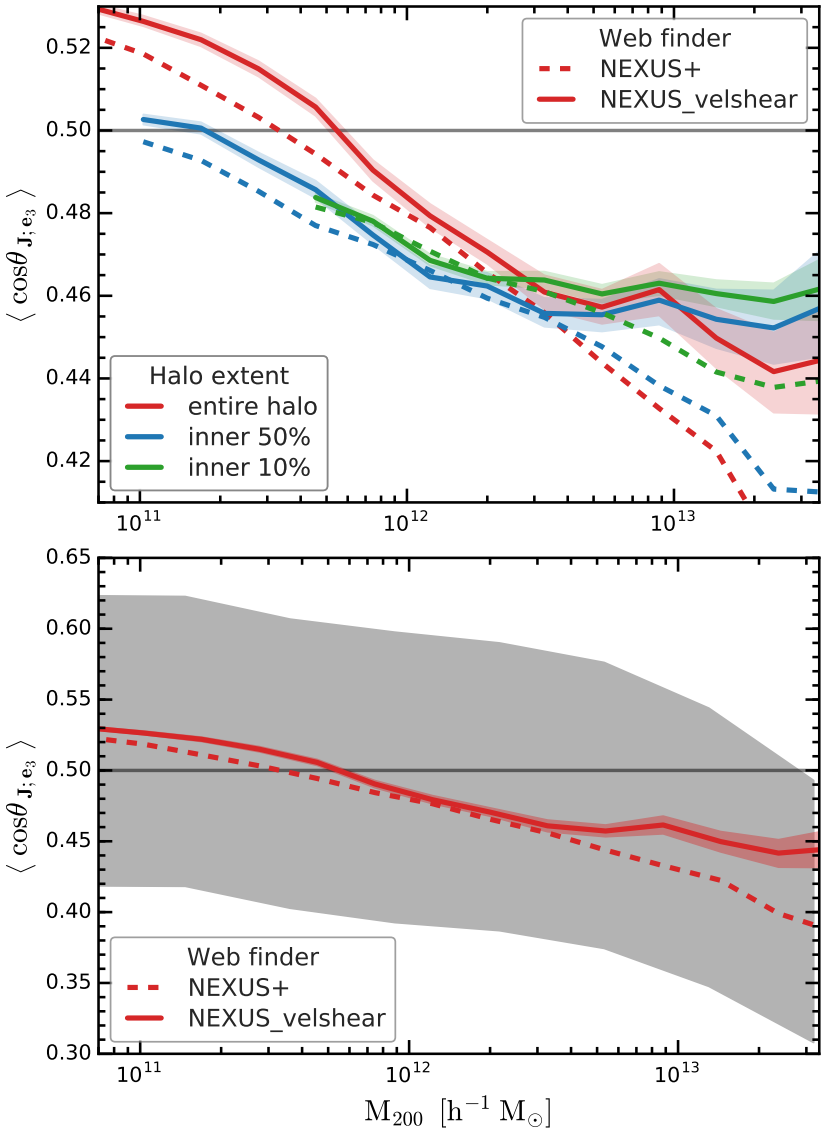

Figure 2.13 – *Median alignment angle, $\langle \cos\theta_{\mathbf{J};\mathbf{e_3}} \rangle$, between the angular momentum and filament orientation as a function of halo mass. It shows the alignment with the filament orientation identified by NEXUS+ (dotted line) and NEXUS velocity shear (solid line). The various colours correspond to different angular momentum definitions using the entire halo and using the innermost 50% and 10% of the particles. The coloured shaded region around each lines gives the 2-sigma bootstrap uncertainty in determining the median, which we only show for solid lines. The bottom panel (note the different y-axis) shows the 40 to 60 percentiles of the $\cos\theta_{\mathbf{J};\mathbf{e_3}}$ distribution, which is indicated via the grey shaded region.*

at what halo mass it takes place. However, for the spin - filament alignment of the inner 50% of the halo mass, we just resolve the spin flip, which takes place at masses a factor of ∼3 times lower than the spin flip of the entire halo.

The systematic nature of the *spin flip* is a clear indication of the significant role played by additional physical processes not captured by TTT in determining the final angular momentum of haloes. The spin - filament alignment of high-mass haloes is, at least qualitatively, in agreement with TTT, so it is unclear what is the effect, if any, of additional processes not included in TTT. In contrast, the alignment of low-mass haloes is contrary to TTT predictions, suggesting that the spin acquired during the linear evolution phase, which is well described by TTT, gets modified by additional phenomena that result in a gradual transition towards spins aligned with the filament spine. The major keys to the dynamics of this process are to be found in the contrast between the spin of the inner and outer halo regions, as well as in the variation of the alignment strength between different regions of the filamentary network, which is the topic of the next subsection.

2.4.4 Spin alignment and the nature of filaments

Here we investigate how the spin - filament alignment varies with the filament properties, focusing on two crucial aspects. First, we study what explain the small, but statistically significant, variation in *spin flip* mass between the NEXUS+ and NEXUS_velshear filaments (see Figure 2.13). Secondly, we study if the halo spin - filament alignment is sensitive to the filament type in which a halo is located, focusing on prominent versus tenuous filaments.

NEXUS+ vs. NEXUS_velshear filaments.

There are two sources of difference between the two filament populations. First, even if a NEXUS+ filament overlaps with a NEXUS_velshear one, they do not necessarily have the same orientation, since the filament orientation is given by the eigenvectors of the density gradient and velocity shear fields, respectively. However, the density gradient and velocity shear are reasonably well aligned, with a median alignment angle of ∼22 degrees (Tempel et al. 2014a). Secondly, the two filaments contain different halo populations. As we discussed in subsection 2.3.1, NEXUS+ filaments include many thin filamentary tendrils, either branching off from more prominent filaments or residing in low density regions. These tenuous structures, which are mostly populated by low-mass haloes, are not identified by NEXUS_velshear. In contrast, the NEXUS_velshear formalism includes a fair number of haloes far from the ridge of prominent filaments (see Cautun et al. 2014); these haloes would typically be assigned by NEXUS+ to neighbouring low-density areas (see Figure 2.4).

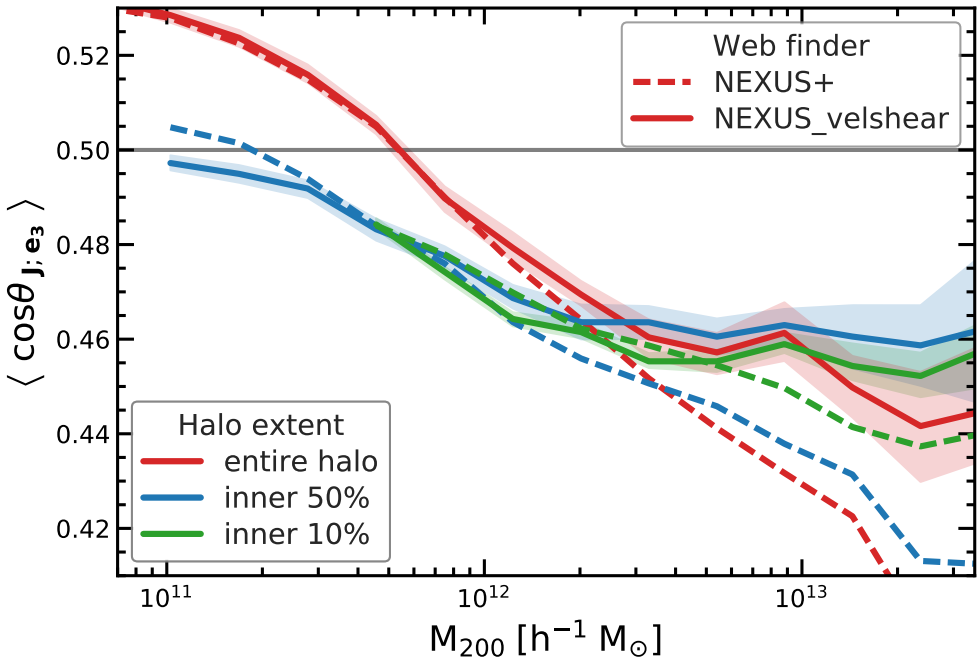

Figure 2.14 – *Median alignment angle, $\langle \cos\theta_{\mathbf{J};\mathbf{e_3}} \rangle$, between halo spin and filament orientation for common haloes found to reside in both NEXUS+ and NEXUS velocity shear filaments. Note that for $M_{200} < 10^{12}$ $h^{-1}\mathrm{M}_\odot$ the alignment strength of the entire halo (solid and dashed red curves) is independent of the filament identification method implying that the differences seen in Figure 2.13 are due to the two web finders assigning somewhat different haloes to filaments.*

Figure 2.14 studies the impact of halo population on the spin - filament alignment. It shows the halo mass dependence of the spin - filament alignment for *common* haloes, which are haloes that are assigned to both NEXUS+ and NEXUS_velshear filaments (see Figure 2.3 for an illustration of the spatial distribution of these haloes). For masses, $M_{200} \leq 10^{12}$ $h^{-1}\mathrm{M}_\odot$, the common haloes have the same median spin - filament alignment angle for both web finders, to the extent that the curves almost perfectly overlap with each other. This translates into an agreement on the spin flip transition mass, at $M_{200} = 5 \times 10^{11}$ $h^{-1}\mathrm{M}_\odot$. This result demonstrates that there are no fundamental differences between the spin - filament alignment of low-mass common haloes, whether the filaments are identified by NEXUS+ or NEXUS_velshear methods.

The story is different for haloes more massive than 10^{12} $h^{-1}\mathrm{M}_\odot$, where the

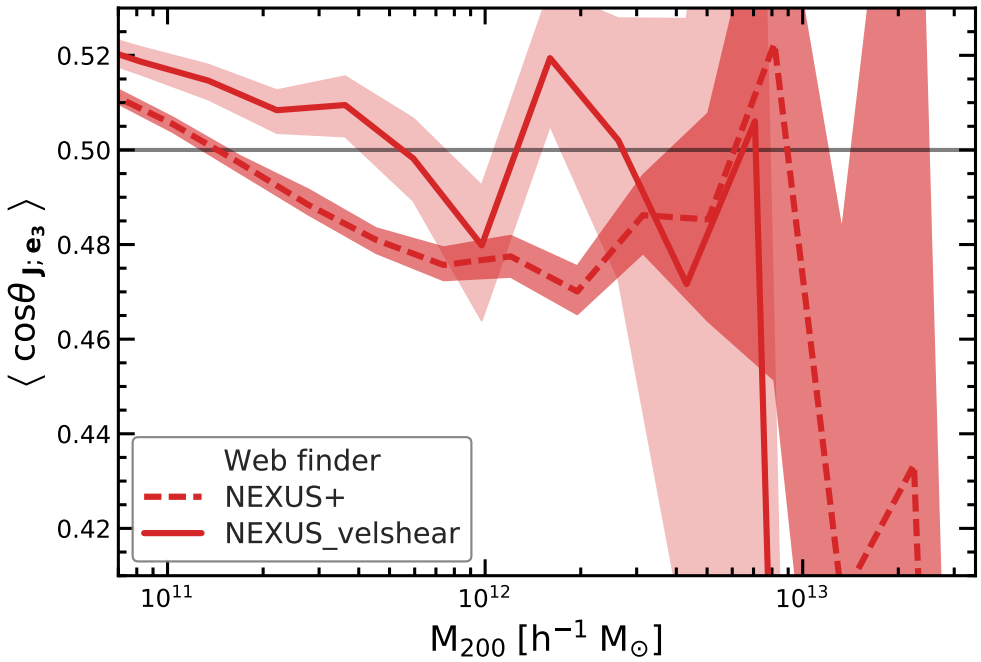

Figure 2.15 – *Median alignment angle, $\langle \cos\theta_{\mathbf{J};\mathbf{e_3}} \rangle$, between halo spin and filament orientation for exclusive haloes, that is haloes that reside only in NEXUS+ (dashed line) or only in NEXUS_velshear (solid line) filaments. For clarity, we only show the alignment of the entire halo spin. For NEXUS_velshear, the exclusive haloes have roughly the same spin flip mass as the total population of filament haloes. In contrast, for* NEXUS+*, the exclusive haloes have a ∼4 times smaller spin flip mass than the total population of filament haloes.*

spin - filament alignment of common haloes is the same as that of the full filament population. In particular, while both web finders find that halo spins are preferentially perpendicular on their host filaments, the spin - filament alignment using NEXUS+ orientations is stronger (i.e. more perpendicular) than that using NEXUS_velshear orientations, and this discrepancy increases at higher halo masses. This is a manifestation of the differences in orientations between NEXUS+ and NEXUS_velshear filaments (see Figure 2.5), with NEXUS+ being able to recover better the orientation of filaments around massive haloes. These haloes, due to their high mass, affect the mass flow around themselves and thus locally change the large-scale velocity shear field. In turn, this diminishes the ability of the NEXUS_velshear web finder to recover the orientation of the large-scale filaments. More massive haloes change the velocity flow to a larger extent and to larger distances, which explains why the

Table 2.2 – *The values of the spin flip mass which determines the transition of the halo spin - filament alignment from preferentially parallel at low halo masses to preferentially perpendicular at high halo masses. We specify the spin flip masses for the two filament population studied here as well as for various halo sub-samples. We also give the spin flip mass for NEXUS+ filaments of different thickness.*

Web finder	Halo subsample	Spin flip mass $[\times 10^{11} \mathrm{M}_\odot]$
NEXUS+	all	3.3
	common	5.4
	exclusive	1.4
NEXUS_velshear	all	5.4
	common	5.4
	exclusive	5.6
	$[h^{-1}\mathrm{Mpc}]$	
NEXUS+ filament thickness	$(0-2)$	1.8
	$(2-4)$	5.2
	(>4)	18

difference between the two filament finders increases at higher halo masses.

Figure 2.15 studies the mass-dependence of the spin - filament alignment of *exclusive* haloes, i.e., haloes assigned exclusively to the filaments of NEXUS+ or NEXUS_velshear. We focus our discussion on haloes with $M_{200} \leq 2 \times 10^{12}\ h^{-1}\mathrm{M}_\odot$ since the exclusive halo sample contains a small number of higher mass objects, which is a consequence of the fact that most massive haloes are assigned to filaments by both methods. In contrast to common haloes, which reside typically in the central region of prominent filaments, the exclusive halo population is very different between the two web finders.

The NEXUS+ exclusive sample, which consists of haloes in tenuous filamentary tendrils, shows preferentially perpendicular alignments down to very low masses, with the spin flip mass being $\sim 1 \times 10^{11}\ h^{-1}\mathrm{M}_\odot$. This transition mass is much lower than the corresponding mass of all the NEXUS+ filament haloes, which is $\sim 3 \times 10^{11}\ h^{-1}\mathrm{M}_\odot$. The spin flip mass for haloes in different filament populations is presented in Table 2.2. Thus, the spin - filament alignment depends on filament properties, with same mass haloes being more likely to have a preferentially perpendicular configuration if they reside in a thinner filament (the next sub-section discusses this trend in more detail).

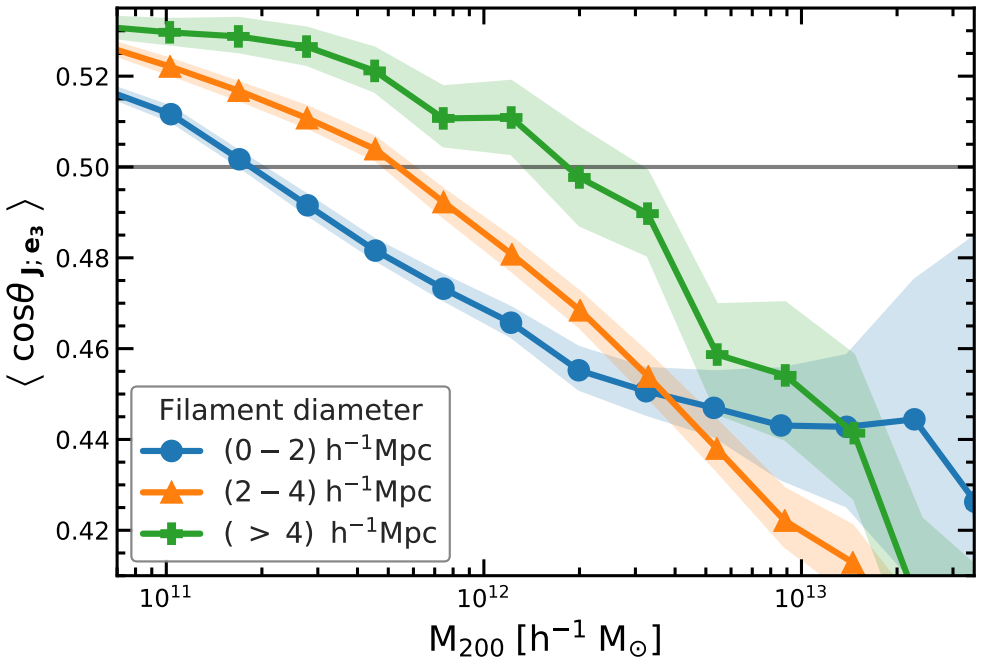

Figure 2.16 – *Median alignment angle, $\langle \cos\theta_{\mathbf{J};\mathbf{e_3}} \rangle$, between halo spin and filament orientation when splitting the sample according to the filament diameter. The three curves show the alignment signal for haloes in filaments with diameters: (0 - 2) h^{-1}Mpc (solid line with circles), (2 - 4) h^{-1}Mpc (solid line with triangle symbols) and more than 4 h^{-1}Mpc (solid line with crosses). The transition halo mass from preferentially parallel to preferential perpendicular alignment increases with increasing filament diameter.*

The NEXUS_velshear exclusive sample, consisting mostly of haloes found at the outskirts of prominent filaments, shows a spin flip mass of $\sim 6 \times 10^{11}$ $h^{-1}\mathrm{M}_\odot$. This spin flip mass is a factor of 6 times higher than that of NEXUS+ exclusive haloes, and thus substantiates the hypothesis that the spin alignment depends on the nature of filaments. Furthermore, the spin flip of the NEXUS_velshear exclusive sample has the same value as that of the NEXUS_velshear common sample (see Figure 2.14). Both samples reside in the same filaments, but the former is typically found in the outskirts, that is farther from the filament spine. Thus, comparing the two suggests that the spin flip mass does not vary strongly with the distance from the filament spine.

Alignment & filament thickness

We now carry out a detailed investigation of the hypothesis proposed in the previous sub-section that the spin - filament alignment depends on the nature

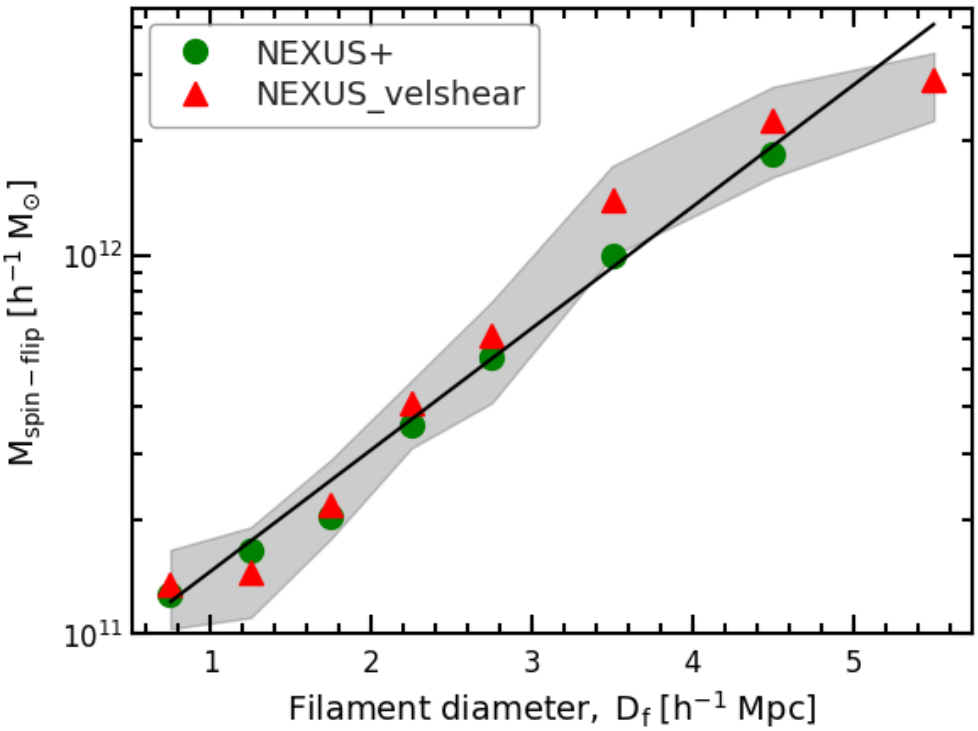

Figure 2.17 – *The dependence of the spin flip mass, $M_{\rm spin-flip}$, on the filament diameter, $D_{\rm f}$, in which the haloes reside. The two symbols correspond to NEXUS+ (circles) and NEXUS_velshear (triangles) filaments. The grey shaded region shows the 2σ error in the determination of $M_{\rm spin-flip}$ for NEXUS_velshear filaments. The spin flip mass dependence on D_f is well fitted by Equation 2.14, with the solid line showing the best fit.*

of filaments. In particular, we study if the alignment of same mass haloes depends on the thickness of the filament in which the haloes are embedded. This is shown in Figure 2.16, where we present the mass-dependence of the spin - filament alignment for halo subsamples split according to the diameter of their host filament. The filament diameter was determined following the Cautun et al. (2014) prescription. In a first step, we compress the filaments to their central spine. This involves an iterative procedure where for each iteration step all filament voxels are shifted closer to the filament centre until resulting into a very thin curve, which is the filament spine. In a second step, for each voxel along the filament spine we find the number of neighbouring voxels within a radius of $R = 2\ h^{-1}$Mpc. Then, the filament diameter, $D_{\rm f}$, at that point is given by the diameter of a cylinder of length, $2R$, that has the same volume as the total volume of the neighbouring voxels. The filament

diameter associated to each halo is the one corresponding to the voxel in which the halo is located. For simplicity, we focus the analysis on the alignment of the entire halo spin.

Figure 2.16 shows an immediately obvious trend: over nearly the entire mass range, the spin - filament alignment angle, $\langle \cos \theta_{\mathbf{J};\mathbf{e_3}} \rangle$, is systematically lower for haloes in thin filaments than for those in thick filaments. Thus, same mass haloes tend to have their spin more perpendicular to the filament spine if they reside in a thinner filament. In particular, it is striking the systematic variation in the spin flip transition mass, which varies by an order of magnitude between different filaments: from $1.8 \times 10^{11}\ h^{-1} M_{\odot}$ for the thinnest filaments to $1.8 \times 10^{12}\ h^{-1} M_{\odot}$ for the thickest filaments (see Table 2.2). This is clearly shown in Figure 2.17 where we show the dependence of the spin-flip mass, $M_{\rm spin-flip}$, on filament diameter. We find that both NEXUS+ and NEXUS_velshear filaments of the same thickness have approximatively the same spin flip mass. This mass increases systematically with filament diameter, $D_{\rm f}$, and is well described by the linear functional form

$$\log_{10} M_{\rm spin-flip}/(h^{-1} M_{\odot}) = m D_{\rm f} + c, \tag{2.14}$$

with the best fitting parameters having the values $m = 0.32$ h Mpc^{-1} and $c = 10.8$.

Thicker filaments are more massive since they typically contain a higher mass per unit length (Cautun et al. 2014), and we expect that they form in regions with a strong tidal field. Thus, we would expect that thicker filaments would host halo spins that are more perpendicular on their filament spine than in the case of thinner filaments. This is opposite to the results of Figure 2.16 and suggests that additional processes, like mergers and secondary or late mass accretion, have a substantial impact on the orientation of halo spins.

2.5 Halo shape alignment

The alignment of the halo shape with the large-scale mass distribution represents a complementary aspect to the spin - filament alignment. Here, we focus on two aspects related to the orientation of haloes:

- the halo shape - filament alignment, and
- the halo shape - halo spin alignment.

The shape and orientation of a halo is specified in terms of its three principal axes a, b and c, and the corresponding eigenvectors (see subsection 2.3.3). Of particular interest are the longest and the shortest axes. The longest axis,

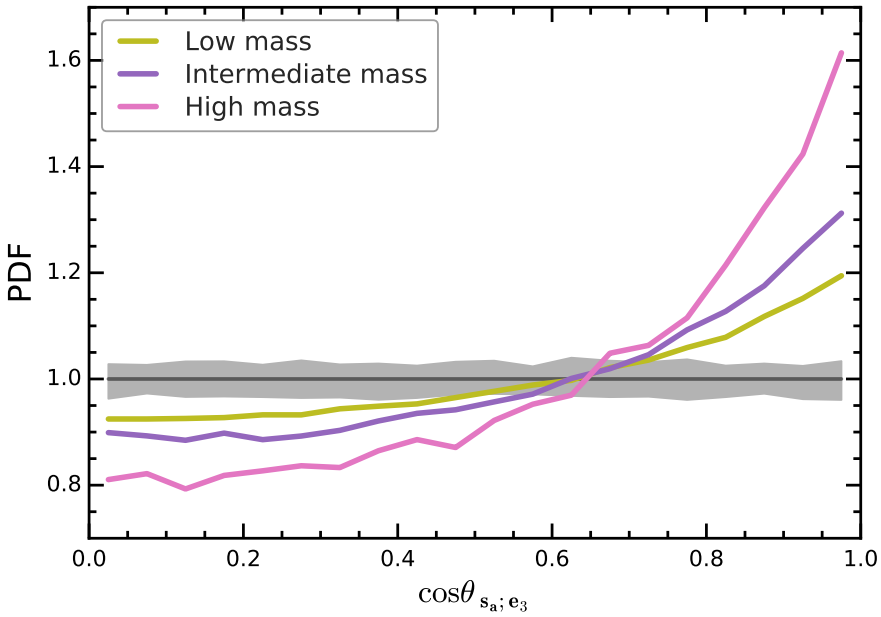

Figure 2.18 – *The alignment of halo shape with the filament orientation: distribution of alignment angle,* $\cos\theta_{\mathbf{s_a};\mathbf{e_3}}$*, between the halo long axis and the* NEXUS+ *filament orientation for haloes in three mass ranges: low mass,* $M_{200} = (5-9)\times10^{10}\ h^{-1}\mathrm{M}_\odot$*, intermediate mass,* $(3-5)\times10^{11}\ h^{-1}\mathrm{M}_\odot$*, and high mass,* $(3-5)\times10^{12}\ h^{-1}\mathrm{M}_\odot$*.*

a, is the one that specifies the orientation along which the main body of the halo is pointing. The shortest axis, c, is preferentially oriented in the same direction as the halo spin and their mutual misalignment reflects the history of the angular momentum acquisition by the halo. It is also of interest to see in how far the shortest halo axis emulates the halo spin - filament alignment.

2.5.1 Halo shape - filament alignment

Already in the initial Gaussian field there is a strong correlation between the shape of peaks and the surrounding cosmic matter distribution (van de Weygaert & Bertschinger 1996b; de Rossi et al. 2009). For example, an emerging filament is defined by a primordial configuration of the tidal or velocity shear fields with one expanding and two contracting directions, with the former corresponding to the filament axis (see van de Weygaert & Bertschinger 1996b; de Rossi et al. 2009). As pointed out by Bond, Kofman & Pogosyan (1996), this identification is the principal reason why prominent filaments form between and connect pairs of massive clusters (see van de Weygaert & Bond 2008b, for an extensive theoretical description).

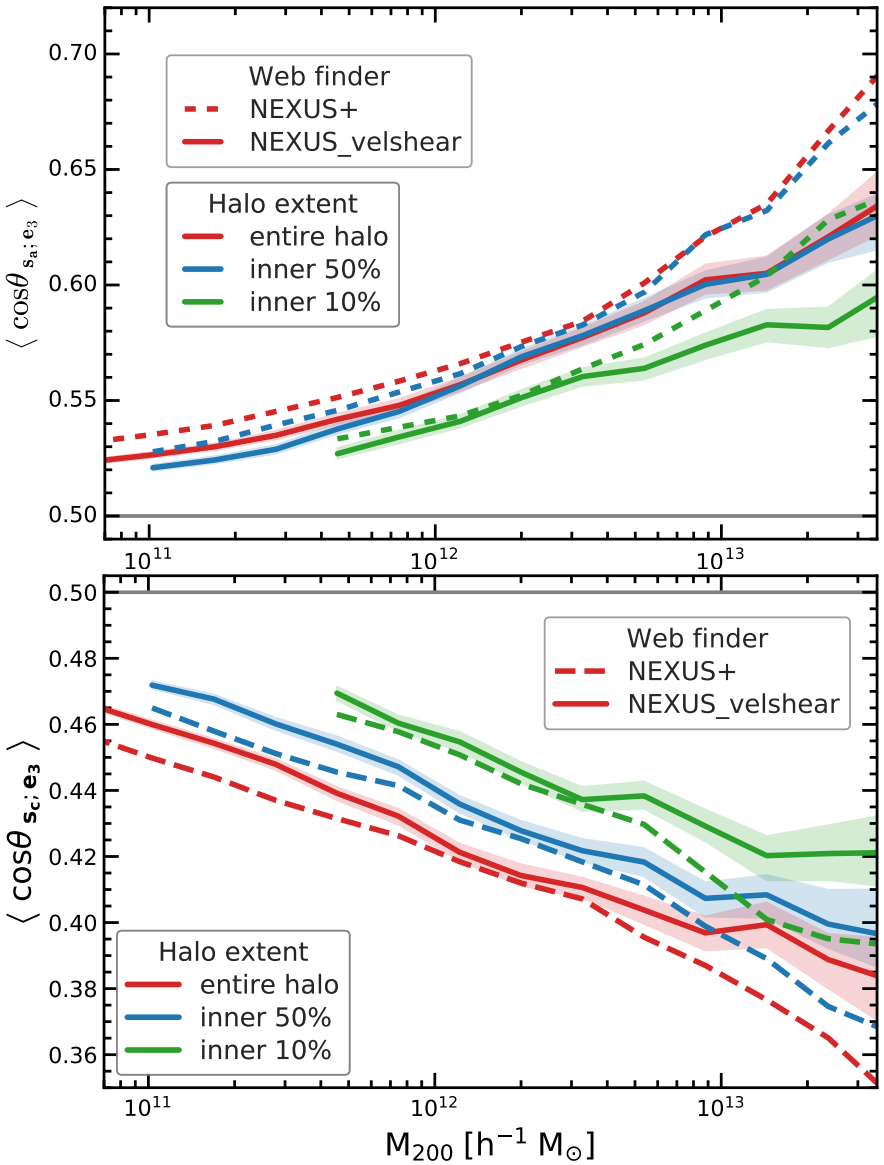

Figure 2.19 – *The alignment of halo shape with the filament orientation. Top panel: median alignment angle, $\langle \cos\theta_{\mathbf{s_a};\mathbf{e_3}} \rangle$, between halo long axis and filament orientation as a function of halo mass. It gives the median for both* NEXUS+ *and* NEXUS_*velshear filaments as well as for different radial extents of the halo. It shows the strong tendency of haloes to have their long axis oriented along that of filaments and that the alignment becomes larger for higher halo masses. The trends are similar for the entire halo, as well as for the inner parts of the haloes. Bottom panel: same as centre panel, but for the median alignment angle, $\langle \cos\theta_{\mathbf{s_c};\mathbf{e_3}} \rangle$, between halo short axis and filament orientation.*

Following the non-linear collapse and build-up of haloes, we wish to see in how far the alignment between the shape of haloes and the filaments in which they reside still reflects the primordial alignment. To this end, we evaluate the angle between the principal axes of haloes, $\mathbf{v_a}$, $\mathbf{v_b}$, and $\mathbf{v_c}$ (see section 2.3.3), and the filament orientation, $\mathbf{e_3}$, which specifies the direction along the ridge of the filament (see section 2.2.2). Similar to the spin - filament alignment, we characterize the shape - filament alignment in terms of the cosine of the angle between halo shape principal axes and the filament orientation (see eq. 2.13).

Figure 2.19 reveals the tendency of the halo shape to be aligned with the filament ridge. The top panel of the figure shows the distribution of alignment angles, $\cos\theta_{\mathbf{s}_a;\mathbf{e}_3}$, between the halo major axis and the filament orientation. For all halo mass bins, the alignment angle distribution is broad, reflecting the wide range of halo - filament orientations. At the same time, the plot shows an excess of objects with $\cos\theta_{\mathbf{s}_a;\mathbf{e}_3} \simeq 1$, which reveals the tendency of the major axis of haloes to be aligned preferentially parallel to their host filaments (Hahn et al. 2007a; Shao et al. 2016). The alignment is mass dependent, being most pronounced for high-mass haloes. We further investigate the mass dependence in the middle panel of Figure 2.19, where we show the median alignment angle, $\langle\cos\theta_{\mathbf{s_a};\mathbf{e_3}}\rangle$, as a function of halo mass. It shows how high-mass haloes are strongly aligned with their host filaments, while the lowest mass ones show a much weaker, almost random, alignment with their host filament. The major axis - filament alignment is the largest for the entire halo, and becomes weaker when considering inner halo radial cuts. This is expected, since the outer region of the halo consists of mostly recently accreted mass, which fall in preferentially along the filaments in which a halo is embedded (Aubert, Pichon & Colombi 2004; Libeskind et al. 2005; Rieder et al. 2013). Late time accretion is most anisotropic in higher mass haloes, which explain the mass dependence of the major axis - filament alignment (Kang & Wang 2015; Wang & Kang 2018a). Figure 2.19 also shows that the haloes are aligned to almost identical degrees to both NEXUS_velshear and NEXUS+ filaments, with the shape - filament alignment being slightly stronger in the latter case, especially at high halo masses.

The bottom panel of Figure 2.19 illustrates the alignment between the halo minor axis and the filament ridge. Unsurprisingly, the minor axis of haloes is preferentially perpendicular on their host filament, with the alignment being the strongest for the highest mass objects.

The plots of Figure 2.19 show that the level of alignment of halo shapes with the tidal field has increased considerably with respect to that present in the primordial Gaussian field. This is due to non-linear evolution, which has lead to substantial changes in the orientation of haloes (see van Haarlem & van

de Weygaert 1993b). There is also a rather strong and systematic increase in alignment as a function of halo mass: more massive haloes are more strongly oriented along the filaments in which they reside. This may be partially a reflection of primordial conditions, in which the tidal shear at a given location is more strongly correlated with the orientation of more substantial peaks (Bardeen et al. 1986; van de Weygaert & Bertschinger 1996b). More important, however, may be the subsequent anisotropic nature of the accretion of mass and substructure (van Haarlem & van de Weygaert 1993b; Shao et al. 2017), which, since it takes places mostly along filaments, amplifies the halo shape - filament alignment.

2.5.2 Halo shape - halo spin alignment

Several physical effects contribute to a preference of haloes to rotate along an axis that is close to their minor axis. First, the strong correlation between inertia tensor of a peak and the tidal field implies a spin direction that is closely aligned to the peak's minor axis (see Lee & Pen 2000). Secondly, the peak collapses fastest along its shortest axis (Icke 1973), and, moreover, a rotating self-gravitating isolated object is expected to contract to a larger extent along its rotation axis.

Figure 2.20 shows that there is indeed a preference for the minor axis of a halo to be oriented along the spin axis. Nonetheless, this tendency is rather weak (Bailin & Steinmetz 2005; Bett et al. 2007). The distribution of alignment angles between rotation axis and the minor axis is very broad and, although it shows some dependence on halo mass, this variation is neither substantial nor systematic. Furthermore, the strength of the spin - minor axis alignment depends weakly on the radial extent of the halo: the inner 50% of the halo is characterized by a stronger alignment than the inner 10%, while, in the outer regions, the trend reverses, with the entire halo having a lower spin - minor axis alignment (see Bailin & Steinmetz 2005).

2.6 Filamentary Accretion Flows & Spin Flips

Numerical simulations reveal a complex mass dependence of the halo spin-filament alignment, with the spin of high-mass haloes close to perpendicular to their host filament, while the spin of low-mass haloes showing the opposite result, being preferentially parallel to their host filament. The transition halo mass between the two configurations, i.e. preferentially perpendicular at high masses to preferentially parallel at low masses, is known as the spin flip mass. We found that the spin flip mass depends strongly on the nature of filaments, showing more than an order of magnitude variation between the thinnest and

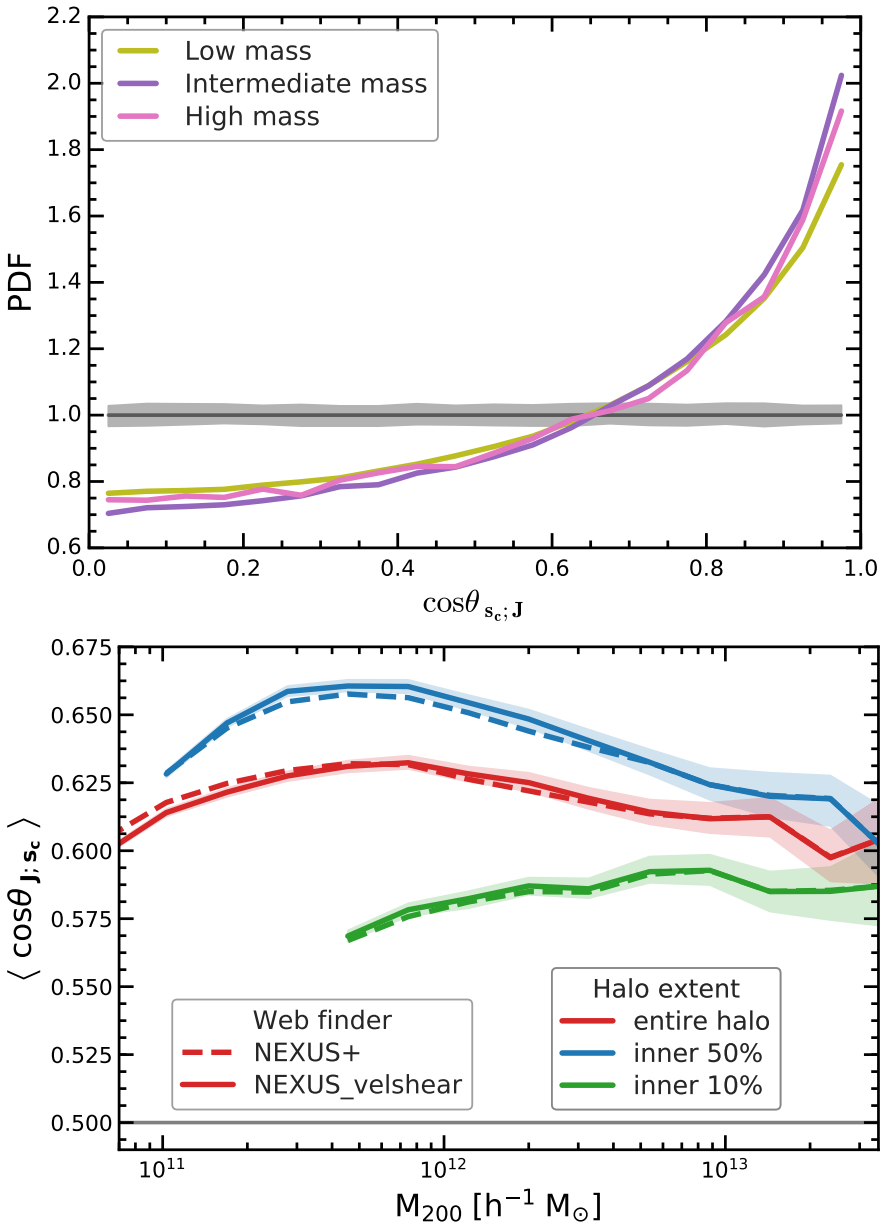

Figure 2.20 – *The alignment between the shape and spin of haloes. Top panel: the distribution of the alignment angle, $\cos\theta_{\mathbf{s_c;J}}$, between halo short axis and halo spin for haloes of three different masses: low mass, $M_{200} = (5-9) \times 10^{10}$ $h^{-1}\mathrm{M}_\odot$, intermediate mass, $(3-5) \times 10^{11}$ $h^{-1}\mathrm{M}_\odot$, and high mass, $M_{200} = (3-5) \times 10^{12}$ $h^{-1}\mathrm{M}_\odot$. Bottom panel: the median alignment angle, $\langle\cos\theta_{\mathbf{s_c;J}}\rangle$, between halo minor axis and halo spin as a function of halo mass. In both panels we show only filament haloes, which are the subject of this study.*

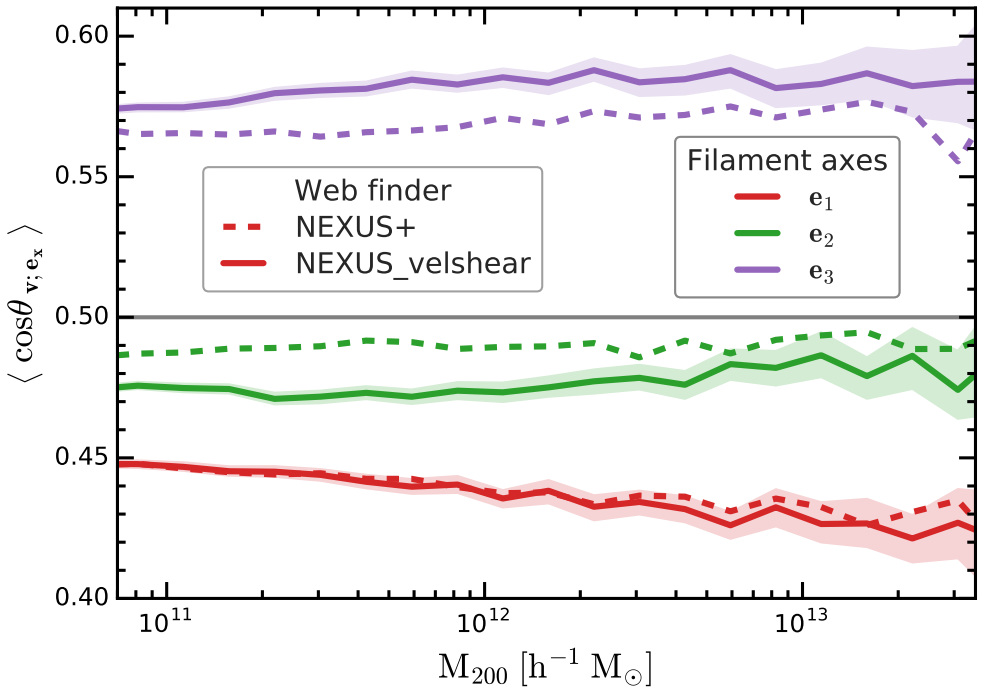

Figure 2.21 – *The median alignment angle, $\langle \cos\theta_{v;e_x} \rangle$, between the halo bulk velocity and the preferential axes of filaments. It shows the alignment with the filament orientation, e_3 (purple lines), and with the principal directions perpendicular to the filament, e_1 and e_2 (red and green lines, respectively). All haloes irrespective of their mass move preferentially along the direction of the filament and they show a coherent accretion inflow along the cross-sectional plane of filaments.*

thickest filaments (see section 2.4.4). In other words, same mass haloes are more likely to have perpendicular spin orientations with respect to their host filament if they are embedded in thinner filaments. The conventional TTT (however see the latest predictions of Codis, Pichon & Pogosyan 2015) does not explain this trend, and previous works have argued that the key element for understanding the spin flip phenomenon is the anisotropic accretion of mass and substructures along filaments (see also Libeskind et al. 2013; Welker et al. 2014; Wang & Kang 2017, 2018a). Our analysis agrees with this interpretation and, as we discuss shortly, provides additional evidence to support it.

To obtain a detailed picture of the level of mass flow anisotropy in and around filaments, we use haloes as flow tracers and investigate the orientation of halo velocities with respect to the filaments in which they reside. To this end, we calculate the alignment angles between the halo bulk velocity and the three

orthogonal directions that determine the principal axes of filaments: $\mathbf{e}_3$, which is the orientation of the filament ridge, and $\mathbf{e}_1$ and $\mathbf{e}_2$, which give the principal directions perpendicular to the filament.

Figure 2.21 shows the median of the alignment angle between halo velocity and the three principal axes of filaments, as a function of halo mass. Overall, we find that the haloes flow preferentially parallel along the filament (Forero-Romero, Contreras & Padilla 2014). While the velocity component along the filament represents the major share of the flow, the perpendicular components are a combination of the substantial level of mass accretion on to the filament and the velocity dispersion in the filament cross-sectional plane. Also, no bias is seen in flow properties between high-mass and low-mass haloes. The slight differences between NEXUS+ and NEXUS_velshear results may be ascribed to the fact that the NEXUS+ filament population also includes dynamically weaker tendrils, with the haloes inside the tenuous filaments being slightly less likely to flow parallel to the filaments.

Secondary accretion (Bertschinger 1985) is the key for understanding how the anisotropic filamentary shear inflow is responsible for the observed spin flip of low mass galaxies (see eg. van Haarlem & van de Weygaert 1993b). Figure 2.22 provides an impression of the typical flow patterns along and perpendicular to a filament. It shows the flow-lines in two perpendicular planes centred on a galaxy-sized halo in the COSMOGRID simulation (Ishiyama et al. 2013). Compared to Figure 2.21, which describe the flows of individual tracers, the flow lines characterize the mean flow at each point. The flow in and around the filaments is a combination of shear and divergent flow, which are themselves due to a combination of the outflow from neighbouring voids and the flow along the filament. In general, haloes accreted mass both along the filaments (e.g. see the top panel in Figure 2.22) and also perpendicular to their host filament. The former tends to preferentially increase the halo spin component that is perpendicular on the filament, while the latter increase the spin component parallel to the filament. Which of the two dominates depends on the balance between accretion along and perpendicular to the host filament. As we will discuss shortly, this balance depends on a combination of the mass and the local neighbourhood of a halo.

The acquisition of halo angular momentum through secondary accretion results from the transfer of orbital angular momentum, which yields a non-zero residual spin for the halo. It is due to anisotropies in the distribution of accreted mass, such as spatial inhomogeneities (e.g. filamentary infall) as well as mergers with matter clumps. The majority of large and rapid changes in halo spin are caused by mass changes, minor mergers and flyby encounters, and not by major mergers (Bett & Frenk 2012, 2016; Contreras, Padilla & Lagos 2017).

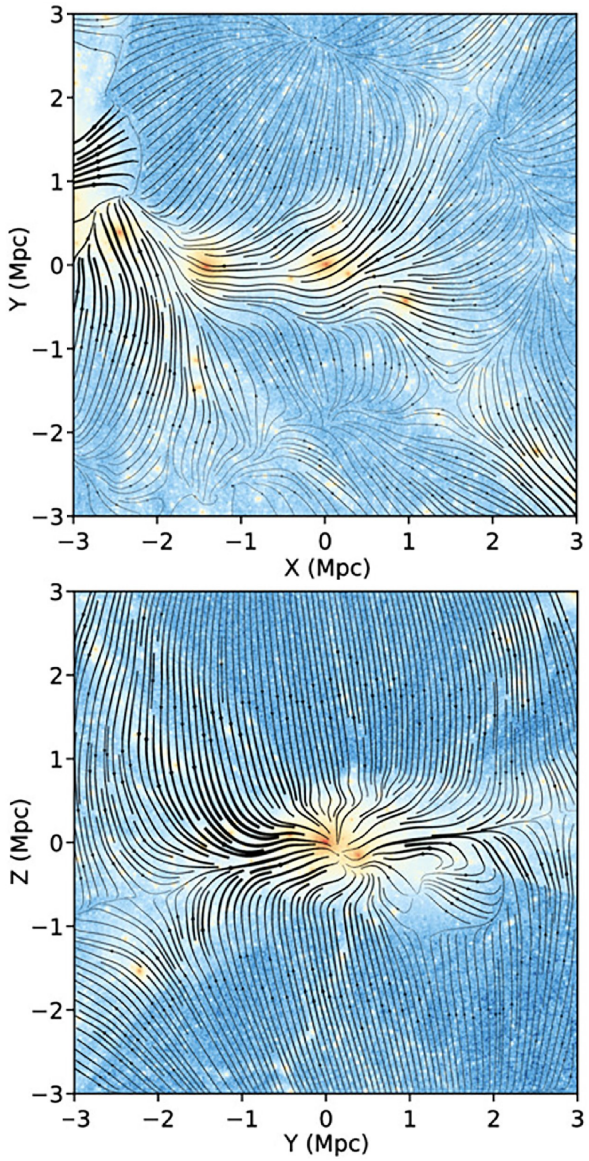

Figure 2.22 – *Flow pattern along a filament in the cosmic web. The image shows the flow-lines in two mutually perpendicular planes centred on a galaxy sized halo in the* COSMOGRID *simulation (see e.g. Ishiyama et al. 2013). The planes are defined by the eigenvectors of the inertia tensor of the mass distribution on a 2 Mpc scale. The first panel show the flow along the filament in which the halo is embedded, while the second panel offers a cross-section view, showing the accretion flow onto the filament.*

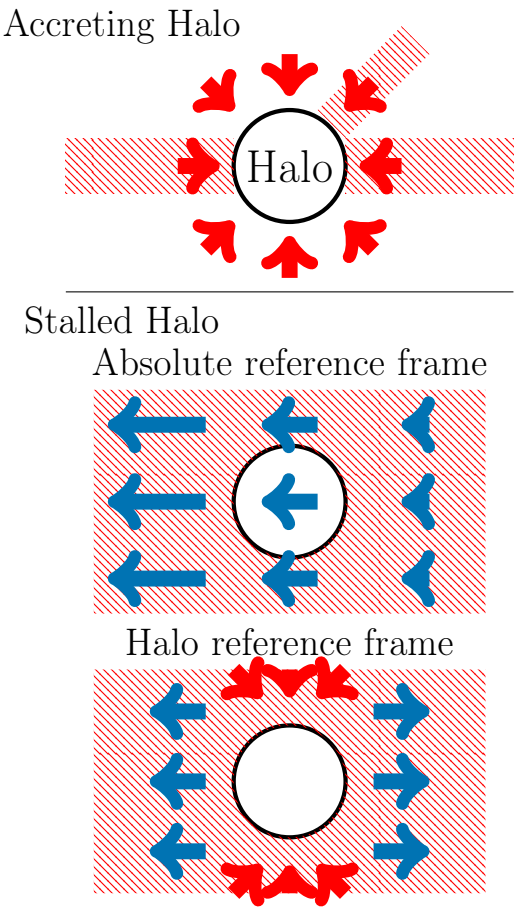

Figure 2.23 – *A schematic representation of the mass distribution around and the infall patterns of accreting and stalled haloes. In each panel, the circle represents the halo, the raster pattern indicates the position and extent of filaments, and the red and blue arrows show the direction and magnitude of the average velocity flow. Accreting haloes (top panel) are embedded in filaments that are thin compared to their radius and accrete matter from all directions. Due to the higher density of filaments, the majority of mass growth is due to infall along filaments and leads to a net increase in halo spin perpendicular to the filament. Stalled haloes typically reside in thick filaments with large velocity gradients (centre panel), which are indicated by longer arrows on the left-hand side of the panel than on the right-hand side. When viewed in the reference frame of the stalled halo (bottom panel), the surrounding matter flows away along the filament and infall can only take place from directions perpendicular to the filament. The inhomogeneities in the distribution of accreted mass impart a net spin that points preferentially along the filament.*

Borzyszkowski et al. (2017, see also Romano-Díaz et al. 2017; Garaldi et al. 2018) describes how haloes can be divided in two groups: haloes that are still accreting and those that have stopped most of their mass accretion, so called stalled haloes. The large-scale mass distribution and velocity flow patterns around these two halo types are illustrated in Figure 2.23. Accreting haloes typically consists of haloes that are the main perturber in their neighbourhood, they sit at the intersection of several filaments and accrete preferentially along these filaments. Thus, accreting haloes are expected to have their spin preferentially perpendicular on their host filament. The latter group of stalled haloes are found in regions of strong external tidal field, for example they are embedded in filaments much thicker than the halo size, and mostly accrete from directions perpendicular on their host filament orientation (see Figure 10 of Borzyszkowski et al. for a visualization of the striking contrast between accreting and stalled haloes). Thus, the stalled haloes have spins mostly parallel to their host filament. The fraction of accreting versus stalled haloes is mass dependent, with the fraction of accreting haloes increasing rapidly with halo mass.

The dichotomy in terms of spin - filament alignment between accreting and stalled haloes provides a natural explanation for the trends we found in this work. While accreting haloes dominate the population of high-mass haloes, the converse is true for low-mass haloes. This suggests that the spin - filament alignment should vary smoothly from being preferentially perpendicular at high masses to preferentially parallel at low masses, which is exactly the trend we measure in Figure 2.13.

The fraction of accreting haloes varies with redshift and, at fixed halo mass, it was larger at higher redshift. It suggest that the spin flip mass should decrease with redshift, which is in very good agreement with previous studies (Codis et al. 2012; Wang & Kang 2018a). Furthermore, most of the recently accreted mass settles in the outer regions of the halo (Wang et al. 2011), with the inner regions mostly maintaining the spin of the halo when they were assembled. Thus, the spin of the inner halo regions should be perpendicular to the host filament to a larger degree than the outer halo, which is what we observe in Figures 2.12 and 2.13.

The fraction of accreting haloes depends on environment and at fixed halo mass is smaller in regions with strong external tidal fields, such as inside and around massive filaments (the tidal field is what leads to the formation of these filaments). Thus, same mass haloes should have a higher degree of parallel spin - filament configurations if the haloes are embedded in thicker filaments, which is what we find in Figure 2.16. This trend also leads to the spin flip mass varying with filament thickness, with the transition mass being higher in

thicker filaments.

2.7 Conclusions & Discussion

In this study we have carried out a systematic investigation of the orientation of the spin, shape and peculiar velocity of haloes relative to the filaments in which they are embedded. Our goal has been to elucidate one of the most outstanding manifestations of environmental influences on halo and galaxy formation, by specifically focussing on the connection between the generation of angular momentum on galactic scales (Lee & Pen 2000; Porciani, Dekel & Hoffman 2002a; Aragón-Calvo et al. 2007b; Aragón Calvo 2007; Jones, van de Weygaert & Aragón-Calvo 2010; Schäfer 2009) and the dynamics of the large-scale cosmic web (Bond, Kofman & Pogosyan 1996; van de Weygaert & Bond 2008b; Cautun et al. 2014). Previous works, starting with Aragón-Calvo et al. (2007b) and Hahn et al. (2007a), have shown how cosmological simulations show a complex halo spin - filament alignment, with the mean orientation of halo spin changing from largely perpendicular for high-mass haloes to preferentially parallel for low-mass haloes, with the transition mass, typically $\sim 10^{12} h^{-1} \mathrm{M}_{\odot}$, known as the *spin flip* mass.

To study halo - filament alignments, we have used one of the largest cosmological N-body simulations available, P-Millennium. It has an impressive dynamic range, combining a large volume with a very high mass resolution, which makes it ideally suited for investigating the connection between halo formation and the large-scale structure. The halo - filament alignment can be a subtle and mass-dependent effect, even more so for the halo spin - filament alignment, and studying it needs a large number of haloes spanning a wide mass range. P-Millennium fulfils both requirements, having no less than 7.5 million well resolved haloes that span more than three orders of magnitude in halo mass. The large volume of P-Millennium is also critical, since it contains both the large-scale tidal forces responsible for the generation of halo spin and the diversity of environments in which haloes reside.

We have identified the filamentary network using the NEXUS multiscale morphology filter (Aragón-Calvo et al. 2007a; Cautun, van de Weygaert & Jones 2013; Cautun et al. 2014). To obtain further insight into the dynamical factors affecting the halo - filament alignments, we have studied the filament populations selected by two different versions of the NEXUS formalism. The first, NEXUS+, extracts filaments on the basis of the density field and identifies a broad range of the filament spectrum, from prominent arteries, which dominate the dynamics of the cosmic web, to tenuous tendrils, which branch off major arteries and reside in underdense regions. The second formalism, NEXUS_velshear, is based on the velocity shear field; it mostly identifies the

dynamically dominant filaments and typically assigns them a larger width than NEXUS+. As we discuss shortly, the contrast between NEXUS+ and NEXUS_velshear reveals key information about the processes behind the spin - filament alignment and its dependence on local environment.

In the current study we focus on the orientation of the spin, the shape and the peculiar velocities of the dark matter haloes relative to the filament in which they are embedded at the present epoch, $z = 0$. The properties of the dark component have the advantage of being mostly determined purely by gravitational effects rather than the complex physical processes affecting the baryonic component. In subsequent studies, we will perform a detailed comparison of halo-by-halo evolution as a function of cosmic web environment, and we will investigate the alignments of the stellar and gas components of galaxies in the EAGLE project (Schaye et al. 2015).

The following points summarize the main results of this study concerning the alignments of halo spins and shape with their host large-scale filament:

1. Halo spin orientation

In this study we have characterized how the spin of haloes is oriented with respect to their host filament to an unprecedented precision and over three orders of magnitude in halo mass. Overall, the orientation of the halo spin follows a wide distribution with a small, but statistically significant, preferential alignment with the direction of the filament (see Figures 2.12 & 2.13). There is a clearly discernible systematic trend in the median of the spin orientation: high-mass haloes tend to have their spin perpendicular to their host filament, while low-mass haloes tend to have their spin parallel to their host filament (Aragón-Calvo et al. 2007b; Hahn et al. 2007a; Hahn, Teyssier & Carollo 2010; Codis et al. 2012; Trowland, Lewis & Bland-Hawthorn 2013; Forero-Romero, Contreras & Padilla 2014). We have found a transition mass of $\sim 5 \times 10^{11}\ h^{-1}\mathrm{M}_{\odot}$ between perpendicular and parallel alignments, which is in good agreement with the wide range of "spin flip" masses, around 0.5 to $5 \times 10^{12}\ h^{-1}M_{\odot}$, reported by previous studies.

1.1 Dependence on web finder

Both the spin - filament alignment as well as the spin flip mass show a small, but systematic dependence on the method used to identify the cosmic web. For same mass haloes, the halo spin tends to be closer to perpendicular on NEXUS+ filaments than on the NEXUS_velshear ones. This is manifested as slightly different values for the spin flip mass, which we have found to be 4 and

$6 \times 10^{11}\ h^{-1}M_{\odot}$ for NEXUS+ and NEXUS_velshear filaments, respectively. At high mass, the discrepancy is explained by the haloes themselves influencing the surrounding velocity shear field and thus limiting the extent to which NEXUS_velshear can recover the direction of large-scale filaments. For masses lower than $10^{12}\ h^{-1}M_{\odot}$, the discrepancy between the two web finders is mostly due to NEXUS+ identifying a population of haloes associated to filamentary tendrils in low-density regions, which tend to have more perpendicular spin orientations.

Interestingly, for haloes with $M_{200} < 10^{12}\ h^{-1}M_{\odot}$, the differences in alignment between haloes in the NEXUS+ and NEXUS_velshear filament populations disappear when we study the common haloes identified by both web finders as residing in filaments (see Figure 2.14). This implies that the discrepancy is due to differences in the halo population associated to filaments. Two outstanding differences are that the NEXUS+ population contains a significant fraction of thin filaments that are either branches of major filaments or tenuous tendrils inside underdense regions. In contrast, the NEXUS_velshear filaments consists of mostly the dynamically dominant arteries. As we discuss shortly, the variation between the two filament populations is mostly due to the dependence of the spin - filament alignment on filament properties. In short, the careful comparison of halo alignments with both filament populations, in relation with the major visual differences between the populations, casts a new light on the processes involved in the evolution of halo angular momentum and its environmental dependence.

1.2 Dependence on filament properties

We have also shown that the spin - filament alignment displays a strong systematic variation with the properties of filaments, in particular on the filament thickness. We have found that haloes of the same mass show a stronger trend to have their spin oriented perpendicular to their host filament if they are embedded in thinner filaments (see Figure 2.16 and 2.17, and Aragon-Calvo & Yang 2014). The trend is strong enough to result in more than an order of magnitude variation in spin flip mass, from $0.1 \times 10^{12}\ h^{-1}M_{\odot}$ for the thinnest filaments, with diameters below $1\ h^{-1}$Mpc, to $3.0 \times 10^{12}\ h^{-1}M_{\odot}$ for the thickest filaments. The mass density and diameter of filaments shows a tight correlation (Cautun et al. 2014) and thus we expect that a similar trend would be visible as a function of filament mass density. We note that the multiscale character of NEXUS has been instrumental in identifying this trend, since the multiscale approach allows for the simultaneous identification of both thin and thick filaments.

The strong variation with filament properties explains many puzzling results

of previous studies. For example, the discrepancy between alignment strengths and the spin flip values reported by previous studies is due to the variation in the characteristics of filaments identified by different web finders (for a comparison of many web finders see Libeskind et al. 2018). The same holds for the differences between the NEXUS+ and NEXUS_velshear methods which we have studied here. The dependence of spin orientation on filament thickness also explains the variation of spin - filament alignment on the smoothing scales used to identify filaments. For single scale web finders (which is not the case for the NEXUS formalism) increasing the smoothing scale leads to identifying mostly thicker filaments (see e.g. Cautun, van de Weygaert & Jones 2013), and thus results in halo spins that tend to be closer to perpendicular to their host filament, explaining the results of Codis et al. (2012) and Wang & Kang (2018a).

1.3 Dependence on halo radial extent

We have studied for the first time how the spin - filament alignment depends on the radial position within the halo. For Milky Way mass haloes and below, the inner halo spin is more likely to be oriented perpendicular to filaments than the spin of the entire halo (see Figure 2.13). The galaxies are more strongly aligned with the inner halo and thus, when compared to their entire host halo, we expect that galaxy spins are more likely to orient perpendicularly on their host filaments. This hypothesis is in good agreement with an upcoming analysis of galaxy spin - filament alignments in the EAGLE galaxy formation simulation (Ganeshaiah Veena et al., in prep.). For haloes more massive than $\sim 5 \times 10^{12}\ h^{-1} M_{\odot}$, the converse is true and the inner halo spin is less aligned with the host filament than the whole halo spin.

Most of the recent mass accretion of a halo, especially if it is due to smooth accretion and minor mergers, is deposited in the outer regions and leaves the inner halo structure mainly intact (Wang et al. 2011). Thus, by calculating the spin of different inner halo regions we have a window into the time evolution of halo spin. This suggests that the progenitors of haloes with present day mass, $M_{200} < 2 \times 10^{12}\ h^{-1} M_{\odot}$, had spins which were oriented perpendicular to filaments to a larger extent than their present day descendants. Thus, in low-mass haloes, recent accretion leads to a reorientation of halo spins to point preferentially along the filament. This trend is reversed for haloes more massive than $\sim 5 \times 10^{12}\ h^{-1} M_{\odot}$, whose progenitors spins were less likely to be oriented perpendicular to filaments than their present day descendants. Thus, in high-mass haloes, recent accretion leads to an increase in the halo spin tendency to be perpendicular on the host filament.

2. Halo shape orientation

When considering the orientation of the halo's shape, i.e. of the inertia tensor, we find similar alignment results as for the halo spin. While the distribution of orientation angles is broad, we have found clear systematic alignment trends that are stronger than in the case of the halo spin - filament alignment (see Figure 2.19). For all mass ranges, the major axis of the halo points preferentially along its host filament ridge. On the other hand, the minor axis tends towards a perpendicular orientation with respect to the host filament. The alignment of both major and minor axes is larger for more massive haloes, which is most likely a manifestation of recent accretion processes that vary with halo mass. When analysing different halo radial ranges, we have found that the shape of the inner halo is less well aligned with the host filament than the shape of the full halo. The different behaviour of the spin - filament and shape - filament alignments is due to the weak alignment between halo spin and halo shape, with the spin showing a surprisingly wide range of orientations with respect to the shape minor axis (see Figure 2.20).

3. Secondary accretion and filament flows

The results we have presented here reinforce and provide additional evidence that secondary anisotropic accretion is a major driver for the late time acquisition of halo spin and its orientation with respect to the large-scale filaments in which the haloes are embedded (Libeskind et al. 2013; Welker et al. 2014; Codis, Pichon & Pogosyan 2015; Laigle et al. 2015; Wang & Kang 2018a). The change in halo spin is a residual effect due to the transfer of orbital angular momentum from accreted clumps and from anisotropies in the smoothly accreted component. Low-mass haloes are more likely to accrete mass along directions perpendicular to their host filament, which results in their spins orienting preferentially along the filament spine. In contrast, high-mass haloes are more likely to accrete mass along their host filament, which ends up enhancing the tendency of their spin to be perpendicular to the host filament. Furthermore, haloes of the same mass are more likely to accrete mass along their host filament if they are embedded in thinner filaments.

This hypothesis is supported by the work of Borzyszkowski et al. (2017) which demonstrated a strong correlation between large-scale environment and the preferential directions of accretion. This is best understood in terms of halo types at opposite sides of the formation path spectrum: accreting versus stalled haloes. The typical mass distribution and velocity flow patterns around these two halo types are illustrated in Figure 2.23. Accreting haloes represent the dominant mass concentration in their neighbourhood, are found at the intersection of several filaments, whose diameters are typically smaller than the

halo size, and accrete most of their mass along these filaments. This represents the typical filamentary accretion picture, where filaments transport mass to the haloes at their endpoints. Borzyszkowski et al. refer to these objects as accreting haloes since they have a large growth rate.

Stalled haloes, on the other hand, are embedded in a strong external tidal field, such as inside a massive filament between two clusters, and, as their name suggests, have low growth rates. The growth of these haloes takes place through accretion mainly from directions perpendicular to their host filament, and thus their spin becomes more parallel to the filament as time goes by. To understand this, lets consider a low-mass halo embedded in a prominent filament between two massive clusters. Since the filament acts as a highway for channelling mass into the clusters at its endpoints, it is characterized by a large velocity gradient along its spine. This inhibits the growth of low-mass haloes embedded in the filament since, in the halo reference frame, the velocity gradient manifests itself as mass flowing away from the halo in both directions along the filament. If the halo has a low mass, it cannot overcome the velocity gradient and thus cannot accrete significantly along the filament direction, and can grow only by accreting mass from directions perpendicular to the filament.

This hypothesis matches the results presented in this work as well as those of previous literature. The formation time of haloes depends on their mass, with massive haloes having formed only recently (see e.g. Davis et al. 1985; Hellwing et al. 2016). Thus, the fraction of accreting haloes increases with halo mass: from low-mass haloes that are mostly of the stalled type to high-mass haloes that are mostly of the accreting type (e.g. Ludlow et al. 2013). This explains why the spin - filament alignment changes from preferentially parallel at low masses to preferentially perpendicular at high masses. The fraction of accreting haloes varies with redshift, with haloes of a given mass being more likely to be of the accreting type at high redshift. This describes why the spin - filament alignment changes with redshift, with the spin flip taking place at lower halo masses at high redshift. Furthermore, the fraction of accreting haloes is larger in thin filaments, like filamentary tendrils in underdense regions, since those filaments form in regions without massive haloes (Cautun et al. 2014). This observation reveals why haloes of the same mass are more likely to have their spins oriented perpendicularly when embedded in thinner filaments.

While the present study has concentrated on the present epoch, in an accompanying study we will investigate in detail the build-up of halo angular momentum as haloes form and evolve during their complex hierarchical growth. We will investigate the processes that accompany the accretion on to and along filaments and in how far they augment the angular momentum imparted by tidal torquing during the early phases of structure formation. The redshift evo-

lution will elucidate other aspects likely to affect the spin - filament alignment, such as the impact of the birth location of haloes (e.g. proto-haloes formed in voids versus filaments) and the role of their migration path. Tracing the detailed halo history will also reveal any differences in the evolution of haloes in various filament types, e.g. prominent versus minor filaments.

For a full understanding of the impact of the cosmic web on the formation and evolution of galaxies, dark matter only simulations as the one studied here are not sufficient. Gas, radiation and stellar (evolution) processes determine to a large extent the outcome and morphology of the emerging galaxies, and the rotation properties of their gas and stellar content. For example, some models suggest that a significant fraction of the angular momentum of low mass galaxies is due to the accretion of cold gas streams, which can penetrate deeper in the halo than dark matter filaments (Dekel & Birnboim 2006; Pichon et al. 2011; Danovich et al. 2015; Stewart et al. 2017). Before infall into the halo, gas and dark matter acquire angular momentum through the same processes, such as torquing due to the surrounding matter distribution. However, once the gas streams enters the inner fractions of the haloes, their angular momentum can change due to non-linear torques, dissipation, disc instabilities and feedback processes (e.g. see Danovich et al. 2015). Such processes might lead to a different galaxy spin - filament alignment than the one found for the inner region of haloes in dark matter only simulations. In order to assess how far the spin properties of the dark matter haloes are transferred to the gas and stars of the galaxy, we need to analyse galaxy formation simulations. In the next chapter, we will study spin - filament alignments in the EAGLE project (Schaye et al. 2015). It will be a step towards understanding how the angular momentum of gas and stars in galaxies is related to that of the parent dark halo, seeking to extend earlier studies along these lines (eg. Hahn, Teyssier & Carollo 2010; Dubois et al. 2014; Welker et al. 2014; Zavala et al. 2016).

Acknowledgements

We are very grateful to the referee(s) for their constructive inputs, which helped us improve the paper substantially. PGV thanks the Institute for Computational Cosmology (ICC) in Durham for their support and hospitality during 2 long work visits during which the major share of the work for this study was carried out. Also RvdW thanks the ICC for its hospitality and support during 2 short work visits. MC and CSF were supported by Science and Technology Facilities Council (STFC) [ST/P000541/1]. ET acknowledges the support by the ETAg grants IUT26-2, IUT40-2, and by the European Regional Development Fund (TK133, MOBTP86). This work used the DiRAC Data Centric system at Durham University, operated by the Institute for Computational Cosmology on

behalf of the STFC DiRAC HPC Facility (www.dirac.ac.uk). This equipment was funded by BIS National E-infrastructure capital grant ST/K00042X/1, STFC capital grants ST/H008539/1 and ST/K00087X/1, STFC DiRAC Operations grant ST/K003267/1 and Durham University. DiRAC is part of the National E-Infrastructure.

3

Galaxy spin alignments

Punyakoti Ganeshaiah Veena[a b], Marius Cautun[c], Elmo Tempel[b d], Rien van de Weijgaert[a], Carlos S. Frenk[c]

[a] Kapteyn Astronomical Institute, University of Groningen, PO box 800, 9700AV, Groningen
[b] Tartu Observatory, University of Tartu, Observatooriumi 1, 61602 Tõravere, Estonia
[c] Department of Physics, Institute for Computational Cosmology, University of Durham, South Road, Durham, DH1 3LE, UK
[d] Leibniz-Institut für Astrophysik Potsdam (AIP), An der Sternwarte 16, 14482 Potsdam, Germany

Submitted 15 March 2019, Accepted 3 May 2019
Published in Monthly Notices of the Royal Astronomical Society, volume 487, pages 1607–1625, 2019.

Abstract

We investigate the alignment of galaxies and haloes relative to cosmic web filaments using the EAGLE hydrodynamical simulation. We identify filaments by applying the NEXUS+ method to the mass distribution and the Bisous formalism to the galaxy distribution. Both web finders return similar filamentary structures that are well aligned and that contain comparable galaxy populations. EAGLE haloes have an identical spin alignment with filaments as their counterparts in dark matter only simulations: a complex mass dependent trend with low mass haloes spinning preferentially parallel to and high mass haloes spinning preferentially perpendicular to filaments. In contrast, galaxy spins do not show such a spin transition and have a propensity for perpendic-

ular alignments at all masses, with the degree of alignment being largest for massive galaxies. This result is valid for both NEXUS+ and Bisous filaments. When splitting by morphology, we find that elliptical galaxies show a stronger orthogonal spin–filament alignment than spiral galaxies of similar mass. The same is true of their haloes, with the host haloes of elliptical galaxies having a larger degree of orthogonal alignment than the host haloes of spirals. Due to the misalignment between galaxy shape and spin, galaxy minor axes are oriented differently with filaments than galaxy spins. We find that the galaxies whose minor axis is perpendicular to a filament are much better aligned with their host haloes. This suggests that many of the same physical processes determine both the galaxy–filament and the galaxy–halo alignments. The volume of the EAGLE simulation is relatively small and many of the alignments we have found are weak; validation of our conclusions will require cosmological hydrodynamical simulations of significantly larger volumes. Keywords: large-scale structure of Universe - galaxies: haloes - methods: numerical

3.1 Introduction

The present study extends the analysis of Ganeshaiah Veena et al. (2018) of the alignment of haloes with respect to cosmic web filaments. To this end, we explore whether the systematic alignment between the dark halo spins and their host filaments found in that study is preserved when studying the alignments of galaxy spins, and, in particular, we assess which factors may introduce differences in the spin–filament alignment of haloes and galaxies. Using the state-of-the-art EAGLE hydrodynamical simulation, we investigate in parallel both the galaxy spin–filament and the halo spin–filament alignments as a function of galaxy mass and morphology. Furthermore, to avoid an explicit dependence on the compare the differences and similarities of filament classifying methods, we analyse the alignment of haloes and galaxies relative to filaments identified by two web finders: Nexus+ and Bisous (Cautun, van de Weygaert & Jones 2013; Tempel, Stoica & Saar 2013). Galaxies in the Universe cluster together to form a web-like configuration known as the Cosmic Web. This large scale web is built up of dense superclusters connected by elongated filaments and sheet-like walls which surround underdense void regions (Zeldovich, Einasto & Shandarin 1982; Geller & Huchra 1983; Davis et al. 1985; de Lapparent, Geller & Huchra 1986; Shandarin & Zeldovich 1989; Bond, Kofman & Pogosyan 1996; Einasto et al. 2002; van de Weygaert & Bond 2008b; Aragón-Calvo, van de Weygaert & Jones 2010b; Frenk & White 2012; Liivamägi, Tempel & Saar 2012; Huchra et al. 2012; Tempel 2014b; Cautun et al. 2014; Pomarède et al. 2017). The cosmic web arises from the anisotropic gravitational collapse of primordial Gaussian density fluctuations, which evolve over billion of years into

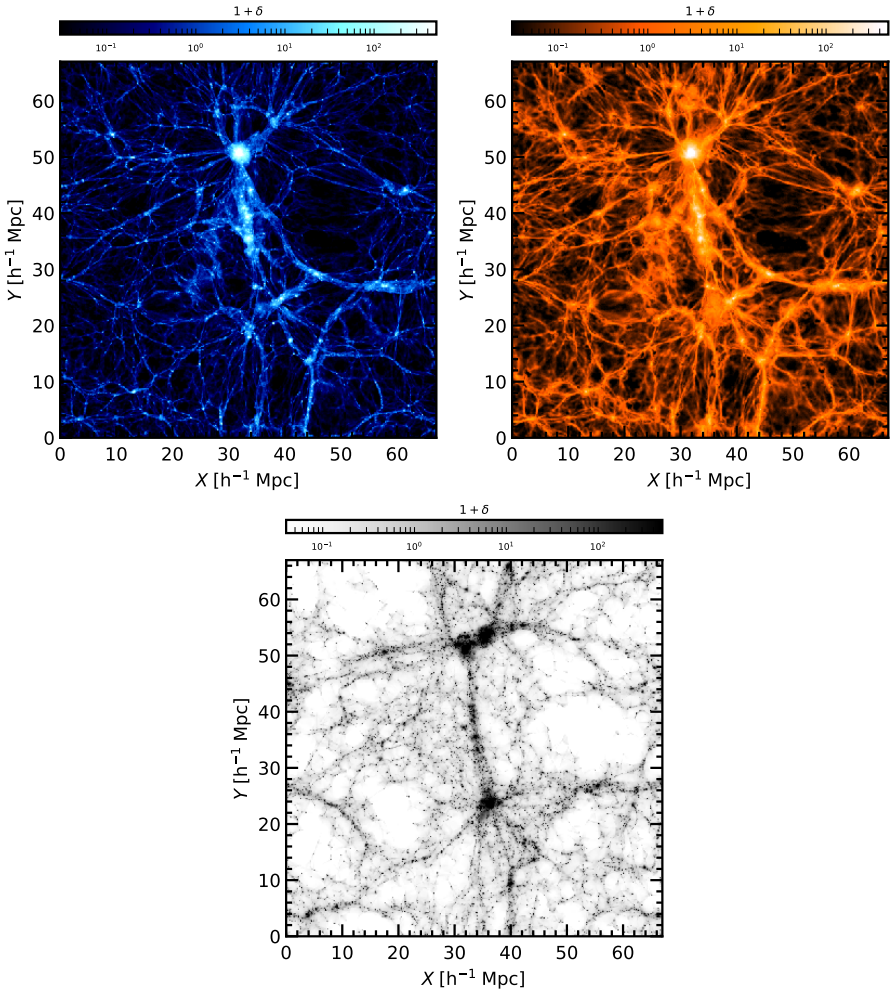

Figure 3.1 – ***Dark matter, gas and stellar density fields.*** *Dark matter (top-left) and gas (top-right) density distributions in a thin slice (*132 h^{-1} kpc*) of the* EAGLE *simulation. Lower Panel: Stellar density field in a thick slice (*10 h^{-1} Mpc*) centred on the thin slice shown in the top panels. The logarithmically scaled colour bar represents the density contrast,* $1 + \delta$*.*

the highly complex and non-linear structures we observe today (Doroshkevich 1970b; Zel'Dovich 1970; Shandarin & Zeldovich 1989; van Haarlem & van de Weygaert 1993a; Bond & Myers 1996; Bond, Kofman & Pogosyan 1996; Sathyaprakash, Sahni & Shandarin 1996; van de Weygaert & Bond 2008b; Shandarin & Sunyaev 2009).

The cosmic web is shaped by the gravitational tidal field, which determines the directions of anisotropic mass collapse. The same tidal field is also responsible for spinning up haloes and galaxies. For example, during the linear phase of structure formation, the Tidal Torque Theory [TTT] (Hoyle 1949; Peebles 1969; Doroshkevich 1970b; White 1984), describes how the angular momentum of a protohalo is generated by the gravitational shear of the surrounding matter distribution. Specifically, the misalignment between the inertia tensor of the protogalaxy and the tidal tensor at that position generates a net spin (see Schäfer 2009 for a review). Therefore, haloes and galaxies residing in different cosmic web environments acquire different spins. Gradually, the angular momentum evolves until the time of turn around as the protohaloes and protogalaxies collapse and decouple from cosmic expansion. The spin thus acquired is mostly preserved even during the later stages of nonlinear evolution as the haloes develop into fully virialised entities.

The TTT and its extensions predict a direct correlation between the spin of haloes and the large-scale structure, such as an alignment of halo spin with the local directions of anisotropic collapse (e.g. Efstathiou & Jones 1979; Barnes & Efstathiou 1987; Heavens & Peacock 1988; Lee & Pen 2001; Porciani, Dekel & Hoffman 2002a,b; Jones & van de Weygaert 2009). Using cosmological N-body simulations, Aragón-Calvo et al. (2007b), and shortly after Hahn et al. (2007a), have confirmed that halo spins are preferentially aligned with the orientation of the cosmic filaments and walls in which they are located and they has been confirmed by numerous follow-up studies (e.g. Codis et al. 2012; Libeskind et al. 2013; Trowland, Lewis & Bland-Hawthorn 2013; Forero-Romero, Contreras & Padilla 2014; Wang & Kang 2017; Lee 2019).

Of particular interest is the halo spin–filament alignment that shows a complex mass dependence, with high mass haloes having spins preferentially perpendicular to filaments while low mass haloes show the opposite trend, with their spins being preferentially parallel to filaments. The halo mass at which this transition happens is known as the *spin-flip transition mass*, or, in short, spin-flip mass. This transition mass increases with decreasing redshift (e.g. see Codis et al. 2012; Wang & Kang 2018a) and is $\sim 1 \times 10^{12}\ h^{-1}\mathrm{M}_{\odot}$ at present day, with the exact value differing by up to a factor of several between different studies. Furthermore, the spin-flip mass is highest for haloes in thick filaments and is up to an order of magnitude lower for haloes in thin and tenu-

ous filaments (Ganeshaiah Veena et al. 2018). The dichotomy in spin–filament alignment between low- and high-mass haloes has been attributed to various processes related to late-time accretion (e.g. Welker et al. 2014; Codis, Pichon & Pogosyan 2015; Laigle et al. 2015; Wang & Kang 2017; Ganeshaiah Veena et al. 2018). High-mass haloes form recently and accrete most of their mass along the filaments they reside in, which results in a net spin gain that is preferentially perpendicular on the filament axis. In contrast, low-mass haloes accumulated most of their mass at higher redshift when they might have been found in cosmic sheets and any present day mass accretion imparts a net spin along their host filament.

Extending the halo spin–filament alignment results to galaxies is not trivial since the spin of many galaxies is poorly aligned with that of their host halo (e.g. Velliscig et al. 2015; Tenneti et al. 2014; Shao et al. 2016; Chisari et al. 2017). As gas streams enter the inner regions of the halo, they gain most of their angular momentum through non-linear torques and dissipation and galaxy spin is affected by disc instabilities and feedback, such as gas outflows due to supernovae (Danovich et al. 2015). Therefore, though galaxies and haloes were subjected to the same tidal fields that generated the initial angular momentum, we expect galaxy spins to deviate from the their host halo spins. Hahn, Teyssier & Carollo (2010) found that in an AMR hydrodynamical simulation, massive discs have spins aligned along the filaments. Codis et al. (2012); Dubois et al. (2014); Welker et al. (2014) study spin–filament alignment for galaxies between redshift 1.2 and 1.8 using the Horizon AGN simulation. They report a galaxy spin transition from parallel to perpendicular at a stellar mass of $\sim 3 \times 10^{10} h^{-1} \mathrm{M}_{\odot}$ and find that the spin of blue galaxies is preferentially parallel to the nearest filament whereas the spin of red galaxies shows a preferential perpendicular alignment. Codis et al. (2018) find that the parallel alignment signal for low mass galaxies is weak and decreases with time whereas the strength of the orthogonal alignment of high mass galaxies increases with time. Wang & Kang (2018a) show that the spin of low mass, blue galaxies in the Illustris-1 hydrodynamical simulation are preferentially along the filament axis whereas the massive, red galaxies have spins preferentially perpendicular. This trend was also confirmed observationally by Tempel, Stoica & Saar (2013), who found that the spins of high mass ellipticals are preferentially perpendicular while those of bright spiral galaxies are preferentially parallel to their host filaments (see also Cervantes-Sodi, Hernandez & Park 2010; Jones, van de Weygaert & Aragón-Calvo 2010; Tempel & Libeskind 2013a; Zhang et al. 2013, 2015; Pahwa et al. 2016; Hirv et al. 2017). In this chapter we address how secondary baryonic processes alter the spin of galaxies, initially imparted by tidal torques, and hence its alignment with the cosmic filaments in which the galaxies reside. Mainly, we address the following questions:

- Do galaxies exhibit a mass dependent spin alignment in hydrodynamical simulations?
- How does the addition of baryons alter the transition mass of the halo spin-filament alignment?
- Does the galaxy spin–filament alignment signal depend on the filament identification method?
- If a galaxy orientation with respect to its parent filament is known, is it possible to infer the orientation of its host halo?

In this study we carry out a detailed analysis of galaxy and halo spin–filament alignments in the EAGLE hydrodynamical simulation (Schaye et al. 2015; Crain et al. 2015). We employ two methods to identify the filamentary pattern: NEXUS+ (Cautun, van de Weygaert & Jones 2013), which uses the total matter density field, and Bisous (Tempel et al. 2014c), which uses the the galaxy distribution. It is essential to compare the two cosmic web tracers, because while the matter distribution generates the tidal field, observational surveys trace only the galaxy distribution, which is a sparse and biased tracer of the total matter distribution. Therefore, we compare the spin alignments with respect to filaments detected in both matter and galaxy distributions. Further, we investigate the correlation between galaxy spin–filament alignment and galaxy morphology, and, whenever possible, compare against observations.

The structure of the chapter is as follows. In Section 2, we describe the EAGLE hydrodynamical simulation and the galaxy and halo samples used in our analysis, and give a short overview of the cosmic web extraction algorithms we employ. In Section 3 we compare the NEXUS and Bisous filament populations and their corresponding haloes and galaxies. Section 4 presents the main results on alignments of haloes and galaxies with the orientation of their host filament. Finally, in Section 5 we give a brief summary of our study and discuss its implications.

3.2 Data

In this section, we first describe the EAGLE simulation and the procedure used to extract the galaxy and halo samples. Then, we give a short overview of the two web identification methods, NEXUS+ and Bisous.

3.2.1 EAGLE simulation

Our analysis makes use of the largest box (Ref-L0100N1504) of the EAGLE cosmological simulation of galaxy formation. EAGLE follows the baryonic processes that shape galaxy formation and evolution and thus allows us to study

the influence of the large scale tidal fields on the underlying physics of galaxy formation and galaxy properties such as spin, shape and morphology. The simulation follows the evolution of 1504^3 dark matter particles and an initial equal number of gas particles in a periodic box of 67.7 h^{-1} Mpc side length, which is large enough to resolve a multitude of large scale environments. Each dark matter particle has a mass of 6.57×10^6 $h^{-1}\mathrm{M}_\odot$ and each gas particle has an initial mass of 1.2×10^6 $h^{-1}\mathrm{M}_\odot$.

The simulation is based on the ΛCDM cosmology and assumes the Planck Collaboration et al. (2016) cosmological parameters, which take the following values: $\Omega_\Lambda = 0.693$, $\Omega_\mathrm{M} = 0.307$ and $\Omega_\mathrm{b} = 0.0455$, $\sigma_8 = 0.8288$ and $h = 0.6777$, where $H_0 = 100\ h$ km s^{-1}Mpc^{-1} is the Hubble's constant at present day. The EAGLE project was run using a modified version of the GADGET code (Springel 2005) and it includes numerous baryonic processes relevant for galaxy formation that have been calibrated to match: (a) the observed galaxy stellar mass function, (b) the distribution of galaxy sizes, and (c) the observed relation between galaxy and central black hole mass (for details see Schaye et al. 2015; Crain et al. 2015). Besides the above properties, the EAGLE simulation reproduces a number of other observables: galaxy colour bimodality with roughly the correct fraction of galaxies in each population (Trayford et al. 2015), the Hubble sequence (Trayford et al. 2017), the correlation with stellar mass of galaxy colour, kinematics and morphology (Correa et al. 2017), and the content of neutral and molecular hydrogen of galaxies (Lagos et al. 2015; Rahmati et al. 2015).

A visualisation of the dark matter, gas and density fields in the EAGLE simulation can be seen in Figure 3.1. This has been obtained by applying the Delaunay Tessellation Field Estimator software (Schaap & van de Weygaert 2000; Cautun & van de Weygaert 2011) to the dark matter, gas and star particle distribution to interpolate their respective density fields to a regular grid. While dark matter and gas trace the same structures on very large scales, gas is more diffused compared to dark matter (DM), especially in the high-density regions. This is due to processes such as supernovae and AGN feedback which heat up the gas and make it less dense. In contrast, dark matter is not directly affected by such processes and can therefore form denser and more compact structures. See Haider et al. (2016) for a more detailed discussion of the effects of feedback on the general properties of large-scale structures.

The bottom panel of Figure 3.1 shows the stellar density field in a 10 h^{-1} Mpc thick slice. The stars are mostly found in the very centre of haloes and taking a thin slice through their distribution results in predominantly empty space. Thus, to appreciate the outline of the cosmic web, we show the galaxies in a much thicker slice than the one used to show the DM or gas distributions in

the top row of Figure 3.1. The stars are predominantly found in regions with high DM and gas densities, which is where haloes are mostly found.

Figure 3.2 compares the volume and mass fraction in different components of the cosmic web as identified by NEXUS+. We find that 76% of the volume in the universe is occupied by voids followed by walls (18%), filaments (6%) and clusters (0.02%) which is in good agreement with the Cautun et al. (2014) results based on DM-only cosmological simulations. In terms of mass, filaments contain most of the mass distribution of the universe: around 50% of the DM and gas, and 82% of stars. The high mass fraction of stars is a consequence of the fact that most haloes more massive than a few $\times 10^{11}\ h^{-1}\mathrm{M}_{\odot}$ are found in filaments. We also notice that compared to DM mass fraction there is slightly less gas in nodes and filaments, for example filaments contain roughly 52% of the DM and 47% of the gas budget. While initially gas follows the DM distribution, winds and feedback processes during galaxy formation heat up, push and disperse the gas from nodes and filaments into adjacent walls and voids (Haider et al. 2016; Martizzi et al. 2018).

In Table 3.1 we tabulate mass and volume fractions of DM, gas and stars in different cosmic web environments. The DM represents the vast majority of the cosmic mass budget, however it cannot be observed directly. To study the extent to which the gas distribution traces the same cosmic web as the DM, we applied the NEXUS+ method separately to the DM and gas density fields. In general, we find good agreement between the mass and volume fraction in the two web types indicating that the gas distribution is a good tracer on large scales of the total density. The only large difference is for nodes, where nodes identified in the gas distribution contain ∼10% less DM, gas and stars than nodes identified in the DM distribution. For the other web environments, the differences between the DM and gaseous cosmic web are much smaller.

3.2.2 Filament population

To detect large scale filaments in the EAGLE simulation, we use two different web identification algorithms: NEXUS+ (Cautun, van de Weygaert & Jones 2013) and Bisous (Tempel et al. 2014c, 2016). These algorithms detect the filamentary network based on two fundamentally different approaches. NEXUS+ is a geometric technique that detects filaments based on the morphology of the density field. Bisous is a statistical technique that extracts the filamentary network by applying a statistical model directly on the distribution of galaxies.

We wish to probe how the differences in these two filament populations influence the results on galaxy spin and shape alignments. Below we describe briefly the working and the implementation of the two formalisms.

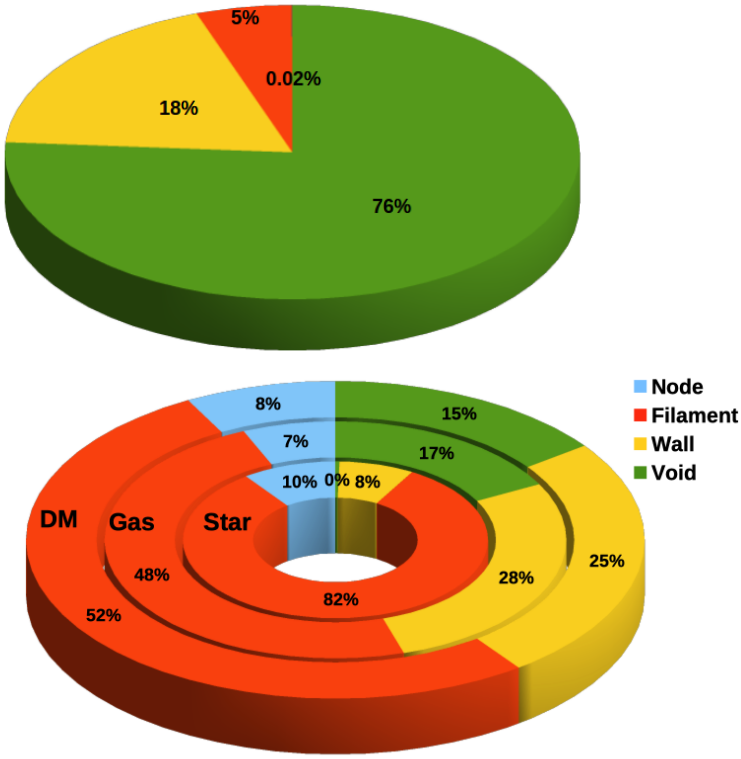

Figure 3.2 – ***Volume and mass fractions of the cosmic web.*** *The results are for web environments identified by applying the NEXUS+ method to the DM density field. The top panel shows the volume fraction occupied by each web environment. The bottom panel shows the mass fraction of DM, gas and stars in each environment. The exact values are given in Table 3.1.*

Filament detection using NEXUS+

The MMF/NEXUS (Aragón-Calvo et al. 2007a; Cautun, van de Weygaert & Jones 2013) technique uses the geometry of the matter distribution to identify the cosmic web environments. Among its most defining features, NEXUS uses the *Scale-Space formalism* to identify web environments at several scales. The method has its roots in the field of medical imaging (see e.g. Sato et al. 1998; Li, Sone & Doi 2003) and has been adapted to astronomy by Aragón-Calvo et al. (2007a) under the name the Multiscale Morphology Filter (MMF). The variant that we use in this sudy, the NEXUS+ method, is an advanced version of the MMF technique and has been developed to better account for the many orders of magnitude variation in the large-scale density field.

The main advantage of the NEXUS+ formalism is that it simultaneously iden-

Table 3.1 – ***Mass and volume fractions of the cosmic web.*** *The web environments were identified using the NEXUS+ method applied to the DM (first 4 rows) and to the gas (rows 5 to 8) distributions. The last row corresponds to Bisous filaments identified using the galaxy distribution.*

Environment	Volume [%]	Mass [%]		
		[DM]	[Gas]	[Stars]
NEXUS+ applied to the DM density				
Node	0.02	7.9	7.1	10
Filament	5.4	52	47	82
Wall	19	25	28	8.0
Void	76	15	17	0.43
NEXUS+ applied to the gas density				
Node	0.02	7.2	6.5	8.7
Filament	5.9	53	48	82
Wall	18	25	28	8.8
Void	76	15	17	0.43
Bisous applied to the galaxy distribution				
Filament	5.1	45	41	70

tifies cosmic web morphology at several spatial scales. Thus, it deals with the multiscale nature of the cosmic web, which is a consequence of hierarchical structure formation and which represents a crucial aspect of the connection between the cosmic web and halo/galaxy properties. The NEXUS+ method is based on using the eigenvalues and eigenvectors of the local Hessian matrix for a range of smoothing scales, which are then used to identify the web environments.

The steps involved in the NEXUS+ formalism are as follows (for more details see Cautun, van de Weygaert & Jones 2013):

Step 1: Apply a Log-Gaussian filter of width R_n to the cosmic density contrast field, $\delta = \frac{\varrho}{\bar{\rho}} - 1$, where ρ and $\bar{\rho}$ denote the local and mean background density, respectively. The Log-Gaussian filter consists of calculating the density logarithm, $\log(1+\delta)$, smoothing the logarithm with a Gaussian filter of size R_n and then calculating the smoothed density, δ_{R_n}, from the smoothed density logarithm.

Step 2: Next, the Hessian matrix at each position, $H_{ij,R_n}(\mathbf{x})$, is calculated using:

$$H_{ij,R_n} = R_n^2 \frac{\partial^2 \delta_{R_n}(\mathbf{x})}{\partial x_i \partial x_j} \tag{3.1}$$

Here, the re-normalization by R_n^2 ensures that the Hessian is weighted identically at different scales. In this work, we implement filter scales in the range 0.5 to 4.0 h^{-1} Mpc We go from the smallest relevant scale to the upper limit of $4h^{-1}$ Mpc which allows us to identify large filaments.

Step 3: A node, filament and wall characteristic is assigned at each point $\mathbf{x}$ based on the nature of the Hessian matrix eigenvalues, $\lambda_1 \leq \lambda_2 \leq \lambda_3$. These are used to define the web environment signature, $S_{R_n}(\mathbf{x})$. The exact equation for defining environments is complex, but, qualitatively, nodes corresponds to regions with $\lambda_1 \approx \lambda_2 \approx \lambda_3 < 0$, filaments to regions with $\lambda_1 \approx \lambda_2 < 0$ and $\lambda_2 \ll \lambda_3$, and walls to $\lambda_1 < 0$ and $\lambda_1 \ll \lambda_2$. In particular, orientation of filaments corresponds to the eigenvector, $\mathbf{e_{n3}}$, along the slowest direction of collapse.

Step 4: Subsequently, steps 1 to 3 are repeated for a set of scales $[R_0, R_1, ...R_N]$ and at each scale the environment signature, $S_{R_n}(\mathbf{x})$, is computed.

Step 5: The environmental signature for the various filter scales is combined together to obtain a scale independent signature, $S(\mathbf{x})$. This is defined as the maximum value of all the scales:

$$\mathcal{S}(\mathbf{x}) = \max_{\text{levels n}} \mathcal{S}_{R_n}(\mathbf{x})\,. \tag{3.2}$$

Step 6: Finally, a threshold signature is used to determine the validity of an identified morphology. Signatures greater than the threshold are considered valid structures and rest are discarded.

From this method, we find a total of 6394 galaxies in NEXUS+ filaments which is $\sim 67\%$ of the total galaxy sample.

Filament detection using Bisous

The Bisous filament finding algorithm (Tempel et al. 2014c) works by randomly distributing a large number of fixed radius cylinders onto a galaxy distribution, and estimating how likely it is that each cylinder corresponds to a cosmic filament. This is achieved by comparing the number of galaxies inside the cylinder with the number just outside the cylinder, with filaments corresponding to a large galaxy density contrast inside a cylinder. The Bisous method is based on

a marked point process which was originally designed to extract spatial patterns (Stoica et al. 2005). A marked point process is a point process with an additional parameter or a mark associated with every point. In the context of the Bisous formalism, centers of cylinders outlining the galaxy distribution are treated as points whose mark is related to the length, radius and orientation of the cylinder. The cosmic web filamentary network is then constructed by selecting the most connected and well aligned cylinders. Briefly, the following steps are involved in determining the Bisous filamentary network from the galaxy distribution:

Step 1: Multiple Markov-Chain Monte-Carlo (MCMC) simulations are performed to obtain the cylinder configurations that outline the filamentary network based on the distribution of galaxies. These cylinders, which eventually make up the filamentary network, have a fixed radius, varying length and orientation. The probability that a cylinder should be retained in the filamentary network is determined by the distribution of the galaxies within each cylinder and its connectivity and alignment to its neighbouring cylinders.

Step 2: Using the MCMC simulations, a visit map is then determined, which gives the probability that a certain region or galaxy belongs to the filamentary network.

Step 3: The ridges of the visit map are considered as filament spines and a filamentary network for the given galaxy distribution is constructed*. Galaxies with high visit map values and those which are also placed within a certain fixed distance from the filament spine are identified as galaxies in Bisous filaments.

For a detailed explanation of the mathematical framework of the Bisous model, we refer to Tempel et al. (2014c, 2016).

In the current study, we apply the Bisous model to the spatial distribution of all EAGLE galaxies with stellar masses above $1 \times 10^8\ h^{-1}\mathrm{M}_\odot$. We define Bisous filament galaxies as all the galaxies that are within a distance of 1 Mpc from the filament spine using only locations with a visit map value larger than 0.05. In total we find that there are 5988 such central galaxies, which is ∼63% of the total sample. The algorithm also computes the orientation of the filaments, denoted as $\mathbf{e_{b3}}$, as the unit vector along the filament spine.

* A visualisation of the steps 1 to 3 can be seen here: http://www.aai.ee/~elmo/sdss-filaments/sdss_filaments.mp4

The Bisous methodology has been successfully applied to SDSS to look for galaxy-filament alignments (Tempel & Libeskind 2013a; Tempel & Tamm 2015) and satellite alignments (Tempel et al. 2015). Applying Bisous to a Λ CDM hydrodynamical simulation represents the next step towards comparing the galaxy spin–filament alignment between theory and observations.

3.2.3 Halo and galaxy populations

Haloes and galaxies are extracted from the EAGLE simulation using the Friends-of- Friends and SUBFIND algorithms (Springel et al. 2001) as described in McAlpine et al. (2016). Initially, DM clumps are identified using the FoF method by adopting a linking length of 0.2 times the average separation of DM particles. Every baryonic particle is then allotted to the FoF group to which its nearest DM particle belongs. The SUBFIND algorithm then identifies gravitationally bound substructures within these FoF groups. Therefore, every FoF group may have more than one substructure and the most gravitationally bound (least gravitational potential) substructure is labelled as the central galaxy and the rest are labelled as satellites.

For our analysis we use only the central galaxies above a stellar mass of $5 \times 10^8 \ h^{-1} \ M_\odot$ and their corresponding DM subhaloes (hereafter haloes). We choose this mass limit to ensure we have at least 300 stellar particles, enough to resolve the inner stellar and gas distributions of a galaxy and also to achieve convergence for properties such as angular momentum, shape and morphology (see e.g. Bett et al. 2007).

Halo and galaxy masses

The radius of a DM halo, R_{200} is defined as the radius from the halo centre within which the average halo density is 200 times the critical density of the universe. The mass of a halo, M_{200}, is calculated as the total mass inside the R_{200} radius. For the galaxies, in order to avoid baryonic particles that may belong to the intra cluster region, an aperture mass is computed. The stellar mass, $M_{\rm star}$, corresponds to the stellar mass within an aperture of 10 kpc while the gas mass, $M_{\rm gas}$, corresponds to the gas mass within an aperture of 30 kpc. We choose these definitions as they are similar to the observational measurements of stellar and gas disc components of galaxies.

Halo and galaxy spin

The angular momentum or spin of a halo or galaxy is calculated by summing over the angular momentum of all the particles in it. The spin, $\mathbf{J}$, of an object

Figure 3.3 – ***Disc dominated and bulge dominated galaxies in*** EAGLE**.** *The top panel shows face-on and edge-on images of a typical spiral galaxy and the bottom panel shows the same for a typical spheroidal galaxy. The stellar mass of the two galaxies are* 15 *and* $5.5 \times 10^{10}\ h^{-1}\mathrm{M}_{\odot}$*, respectively. The images were taken from the Eagle Public database RefL0100N1504.*

with N particles is given by

$$\mathbf{J} = \sum_{k=1}^{N} m_k \left(\mathbf{r}_k \times \mathbf{v_k}\right) \ , \tag{3.3}$$

where $\mathbf{r}_k$, $\mathbf{v}_k$ and m_k denote the position, velocity and mass of the $k-$th particle. The position is measured with respect to the object's centre, which is given by the most gravitationally bound particle, and the velocity is measured with respect to the centre of mass.

The DM halo spin is denoted as $\mathbf{J}_{\mathrm{dm}}$ and is calculated using all the DM particles within the R_{200} halo radius. For galaxies we determine separately the spin of the stellar component, $\mathbf{J}_{\mathrm{star}}$, and of the gas disc, $\mathbf{J}_{\mathrm{gas}}$. The stellar spin is calculated using all the star particles within a distance of 10 kpc from the

galaxy centre while the spin of the gaseous component uses all the cold (temperature below 10^5K) gas particles within a distance of 30 kpc. In all three cases, we use only galaxies and haloes with at least 300 particles of each type.

Halo and galaxy shape

The shape of galaxies and haloes is usually described in terms of the ratios of the major, minor and intermediate axes. We obtain this by calculating the eigenvalues and eigenvectors of the moment of inertia tensor,

$$\mathbf{I}_{ij} = \sum_{k=1}^{N} m_k r_{k,i} r_{k,j} \ , \tag{3.4}$$

where $r_{k,i}$ is the position of the k-th particle along the i-th coordinate axis. The principal axes of the object are given by the eigenvectors of the $\mathbf{I}_{ij}$ tensor, $\mathbf{s}_a$, $\mathbf{s}_b$ and $\mathbf{s}_c$, which are the directions corresponding to the major, intermediate and minor axes, respectively.

The eigenvalues of the inertia tensor, $s_a \geq s_b \geq s_c$ are used to obtain the axis ratios b/a and c/a, where $a = \sqrt{s_a}$, $b = \sqrt{s_b}$ and $c = \sqrt{s_c}$. The axes ratios describe the shape of a halo. If the halo is spherical then $b/a = c/a = 1$, whereas prolate haloes have the major axis longer ($c \approx b \ll a$) and oblate haloes have the minor axis shorter ($c \gg b \approx a$) than the other two.

Galaxy morphology

We classify galaxies as spheroids or discs by computing the bulge fraction B/T, where B is the bulge mass and T is the total stellar mass. The bulge mass is calculated as twice the mass of all counter-rotating stars. Specifically, if the dot product of the orbital angular momentum of a star with the total angular momentum of the galaxy is negative, then that star is considered to be counter-rotating. A galaxy which is mostly dispersion dominated will have a large fraction of counter-rotating stars, so that the value of B/T will be close to unity. If the galaxy is rotation supported B/T is closer to zero. For our galaxy sample, over the entire galaxy mass range the median value of B/T, computed using star particles within 10 kpc, is 0.76.

The third of the galaxy sample population with the lowest B/T ratio, ie. $B/T < 0.58$, are designated as disc galaxies. The third of the galaxies with the highest B/T ratio, ie. $B/T > 0.82$, are classified as spheroid galaxies. Following this classification scheme, the sample contains 2074 disc galaxies, and an equal number of spheroid galaxies. In Figure 3.3 we show representative examples of a spiral and an elliptical galaxy in the EAGLE simulation. These

images were obtained from the EAGLE database and were created using the technique described in Trayford et al. (2017).

3.3 Filament and Galaxy populations: Nexus+ and Bisous

The Bisous algorithm uses galaxies as tracers to detect the underlying filamentary network whereas NEXUS+ uses the matter density field to identify the cosmic web. Despite this crucial difference in the tracers, the filament populations detected by both methods are almost identical with a few interesting differences that will be addressed in this section. A visual representation of the structural features and as well as of the filament galaxy distribution is shown in Figure 3.4.

3.3.1 Structural similarities and differences

The top two panels of Figure 3.4 show the filamentary network detected by NEXUS+ and Bisous in a 10 h^{-1} Mpc thick slice. They show that both methods identify the same overall pattern of prominent filaments that span the weblike network pervading the simulation box and they suggest that we should expect similar halo and galaxy alignments with the two populations of filaments.

We also observe interesting differences between the NEXUS+ and Bisous filaments related to the thickness of individual structures. NEXUS+ filaments have a range of thicknesses, while all Bisous objects have roughly the same thickness. This contrast is related to differences in the formalism underlying the methods. NEXUS+ is an explicit multiscale method and belongs to the Multiscale Morphology Filter/Nexus family of cosmic web classification tools (Aragón-Calvo et al. 2007a; Cautun, van de Weygaert & Jones 2013). In the implementation for the present study we used smoothing scales ranging from 0.5 to 4 h^{-1} Mpc. The panels in Figure 3.4 reflect this: the NEXUS+ filaments vary in thickness, ranging from very thin to very thick.

In contrast, the Bisous formalism identifies filaments using a fixed transverse filament scale of 1Mpc ($0.68h^{-1}$ Mpc), which translates into cylindrically shaped filaments with a radius of 1Mpc. As a result, we see a few heavy and thick NEXUS+ filaments that correspond to a configuration of parallel cylindrical Bisous filaments. Note that the orientation of the thick NEXUS+ and the Bisous filaments will be largely similar. Also, we see a substantial difference in the identification and classification of small scale tenuous filaments, in particular in moderate and lower density regions. Several of the smaller Bisous filaments located in these regions are embedded in regions that NEXUS+ assigns to walls and voids. We see this illustrated in the central region and the

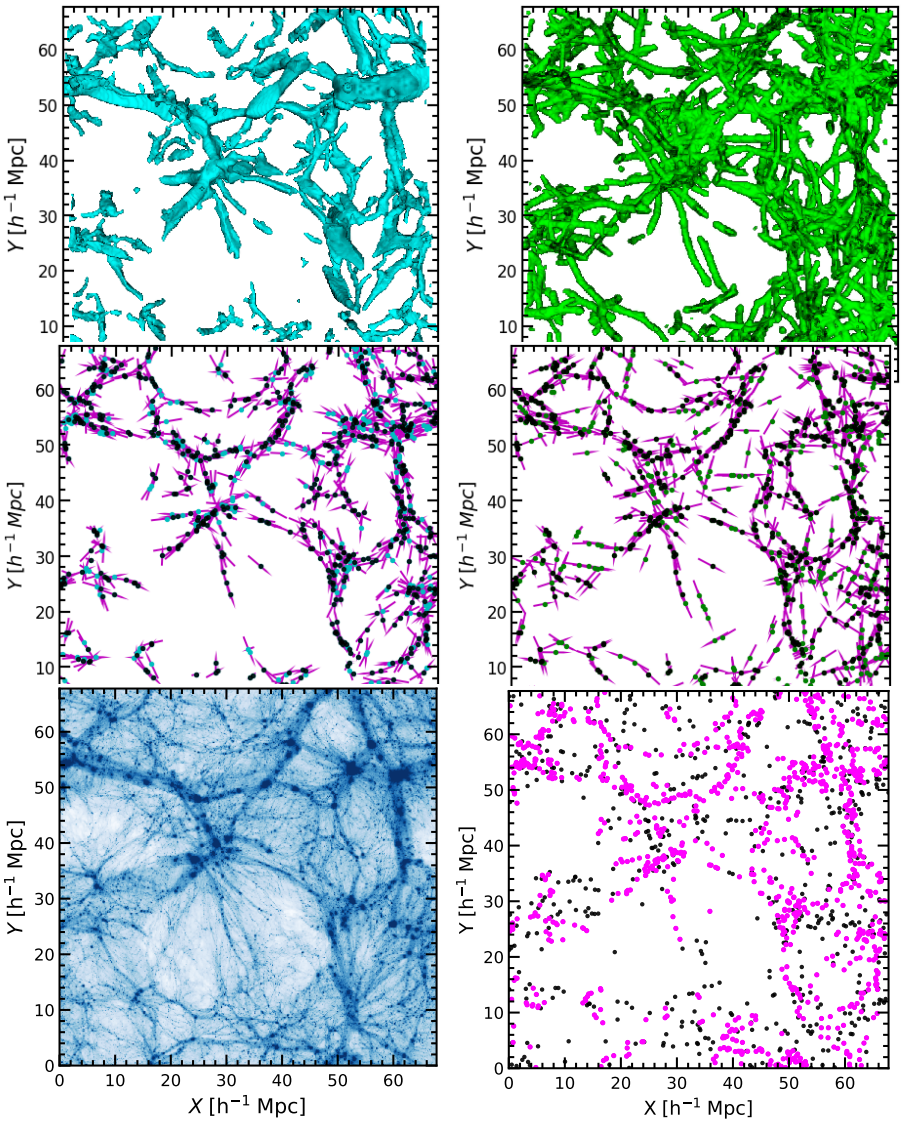

Figure 3.4 – ***Filaments and filament galaxies in a*** $10h^{-1}$ Mpc ***slice.*** *Top row: the spatial distribution of the NEXUS+ (left-hand panel) and Bisous (right-hand panel) filaments. Middle row: galaxies (shown as symbols) in the NEXUS+ (left-hand panel) and Bisous (right-hand panel) filaments; the lines give the filament orientation at each galaxy position. Black dots represent galaxies common to both NEXUS+ and Bisous while blue are only in NEXUS+ and green are only in Bisous. For clarity, we show only central galaxies with stellar mass,* $M_{\rm star} \geq 5 \times 10^8\ h^{-1}{\rm M}_\odot$. *Bottom-left panel: the DM density in the slice. Bottom-right panel: all galaxies in the slice. The magenta symbols show galaxies in NEXUS+ filaments, the black symbols depict the rest of the galaxies.*

bottom righthand corner of the panel showing the Bisous filamentary network in Figure 3.4, where many Bisous filaments crisscross to form sheet-like structures. This is a consequence of the focus of the Bisous formalism on fixed radius and elongated cylindrical features.

The structural differences between the NEXUS+ and Bisous filaments are also reflected in a quantitive comparison of the mass and volume filling fractions of their DM, gas, and galaxy content. For this complete inventory we refer to Table 3.1. The fractions were calculated by splitting the EAGLE box into a 256^3 grid (grid spacing of 0.26 h^{-1} Mpc) and counting the number of grid cells associated to each cosmic web component. We find a reasonable agreement between the two filament populations, with some modest differences. The NEXUS+ filaments contain a slightly higher DM, gas and stellar mass fractions than Bisous filaments. This result, which is consistent with the one reported in Libeskind et al. (2018), is probably a reflection of the fact that prominent NEXUS+ filaments are substantially thicker than their Bisous counterparts and thus contain more of the cosmic mass budget.

Given the focus of our study on the alignment of haloes and galaxies with their host filaments, it is crucial to compare the orientations of the Bisous and of the NEXUS+ filaments. To this end, in Figure 3.5 we plot the cumulative distribution of the cosine of the angle between the third eigenvector of Bisous ($\mathbf{e_{b3}}$) and of NEXUS+ ($\mathbf{e_{n3}}$) filaments. For an objective comparison, we assess the mutual orientation of the filaments at the locations of common galaxies that are assigned to filaments by both the Bisous and the NEXUS+ methods. Overall, we find a high degree of alignment between the two filament populations with a median alignment angle of $\sim 21°$. There is also no noticeable dependence of the alignment angle on galaxy mass, with the alignment distribution for high and low mass galaxies being practically indistinguishable.

In summary, the NEXUS+ and the Bisous web finders both detect the major prominent filamentary arteries of the cosmic web, however, there are substantial differences between the methods in the population of small-scale filaments. The multiscale nature of NEXUS+ allows it to detect filaments of different widths, while Bisous concentrates on filaments of a particular specified scale. Of considerable importance for this study is that the common Bisous and NEXUS+ filaments are well aligned with respect to each other.

3.3.2 Galaxy distribution in filaments: NEXUS+ vs. Bisous

In addition to the structural characteristics discussed above, an important aspect of filament properties concern their galaxy population. Here we compare the galaxy populations in NEXUS+ and Bisous filaments, with Table 3.2 giving

Table 3.2 – ***Number of* EAGLE *galaxies found in filaments.*** *The table gives the galaxy counts with stellar mass, $M_{\rm star} \geq 5 \times 10^8\ h^{-1}{\rm M}_\odot$ residing in NEXUS+ and Bisous filaments. In total, the* EAGLE *simulation contains 9563 galaxies more massive than the above stellar mass cut. The third column shows the fraction of galaxies found in the two filament populations. The fourth columns gives the number of galaxies in common to both NEXUS+ and Bisous filaments, while the last columns gives the number of exclusive filament galaxies, that is those assigned to filaments by one method but not by the other one.*

Filaments	Total	Fraction [%]	Overlap	Exclusive
NEXUS+	6394	66.9	4277	2117
Bisous	5988	62.6		1711

an overview of the number and fraction of EAGLE galaxies located in filaments. We limit the analysis to galaxies with a stellar mass in excess of $M_{\rm star} \geq 5 \times 10^8\ h^{-1}{\rm M}_\odot$, which are the ones resolved with enough particles to have robust spin and shape measurements.

NEXUS+ filaments contain 67% of the total number of (central) galaxies, while Bisous identifies a slightly lower fraction of filament galaxies, 63%. As we discuss in subsection 3.3.3, an important difference between the two web finders is that Bisous assigns a considerably lower fraction of massive galaxies (that is those with $M_{\rm star} \geq 10^{11}\ h^{-1}{\rm M}_\odot$) to filaments than NEXUS+. These massive galaxies are usually located in the nodes of the cosmic web and in their immediate neighbourhoods, which are regions that Bisous does not classify as filaments (see the discussion in subsection 3.3.3).

Of the entire NEXUS+ population of filament galaxies, 67% of them are residing in Bisous filaments. Meanwhile, some 71% of Bisous filament galaxies are also found in NEXUS+ filaments. The rest of the Bisous galaxies are in regions classified as walls (27.5%), voids (0.85%) and clusters (0.16%) by NEXUS+. In short, the majority of Bisous filament galaxies are also located in NEXUS+ filaments, although a considerable fraction appears to be located in regions identified as walls by NEXUS+.

A visual appreciation of the spatial distribution of galaxies in the cosmic web can be obtained from the two central row panels in Figure 3.4. They show the filament galaxy population of the two web finders, with common galaxies associated to both NEXUS+ and Bisous filaments shown as black symbols. The most outstanding difference concerns the galaxies populating the thin filaments, which are typically low mass galaxies. While the number of low mass

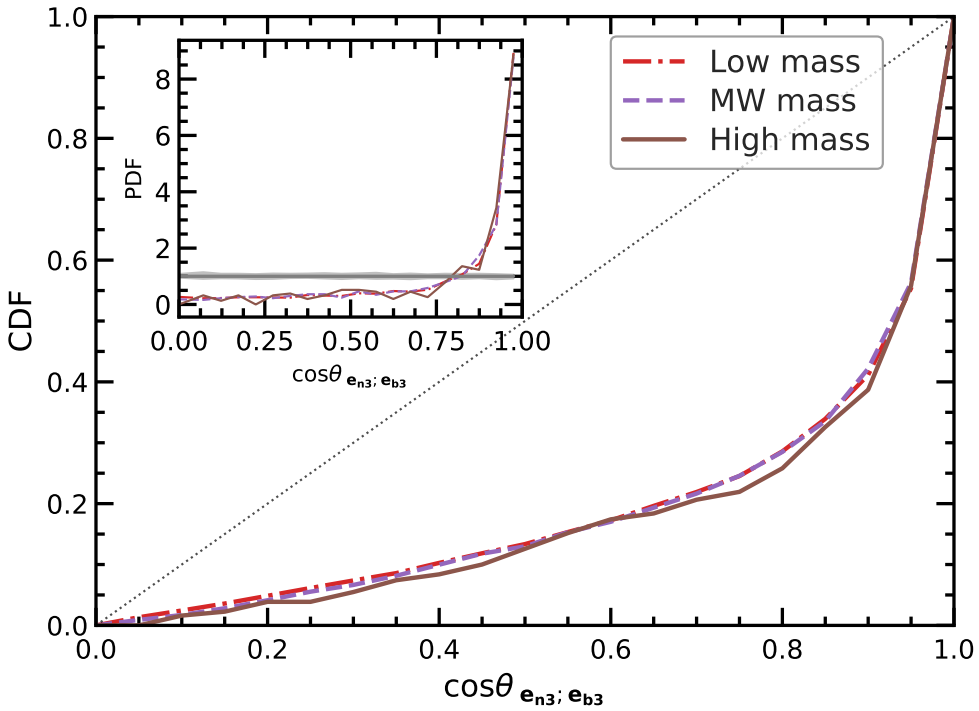

Figure 3.5 – ***Alignment between NEXUS+ and Bisous filaments.*** *The graph shows the CDF and PDF (inset) of the alignment angle between the orientation of NEXUS+ ($\mathbf{e}_{n3}$) and Bisous ($\mathbf{e}_{b3}$) filaments. The alignment is measured at the position of common filament galaxies. The various coloured lines correspond to galaxies of different stellar masses: low mass, $\leq 1 \times 10^{10}$ $h^{-1}\mathrm{M}_{\odot}$, intermediate mass, $(1-5) \times 10^{10}$ $h^{-1}\mathrm{M}_{\odot}$, and high mass, $\geq 5 \times 10^{10}$ $h^{-1}\mathrm{M}_{\odot}$. Irrespective of the galaxy mass range, NEXUS+ and Bisous filaments are well aligned with each other.*

filament galaxies is comparable, the low mass galaxies that are not shared by Bisous and NEXUS+ often concern the ones that have been classified as wall galaxies by NEXUS+.

3.3.3 Halo & galaxy mass functions

Figure 3.6 plots the halo and galaxy stellar mass functions of the EAGLE simulation as a function of the cosmic web environment, i.e. the mass functions of dark haloes and galaxies in the nodes, filaments, walls and voids of the cosmic web. To this end, we plot the number density of haloes and galaxies per logarithmic mass bin. The top panel shows the halo mass function split into web environments as determined by NEXUS+. The corresponding galaxy

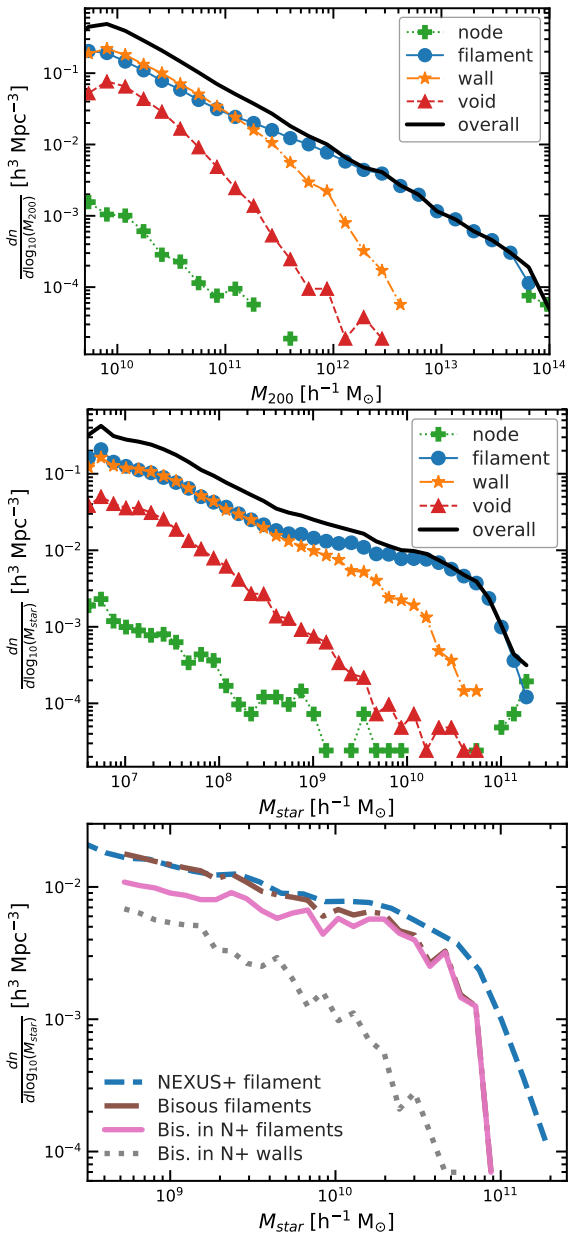

Figure 3.6 – ***Halo and galaxy stellar mass functions segregated by web environment.*** *The top panel shows the halo mass function in NEXUS+ environments. The centre panel shows the galaxy mass function in NEXUS+ environments. The bottom panel compares the galaxy mass function in NEXUS+ (dashed line) and Bisous (dashed-dotted line) filaments. The Bisous filament galaxies are mostly found in NEXUS+ filaments (solid line) and, a small fraction of them, in NEXUS+ walls (dotted line).*

stellar mass function is given in the central panel. The bottom panel compares the galaxy stellar mass function identified in Bisous filaments and with that assigned to the NEXUS+ filaments. We mostly limit our analysis to galaxies with $M_{\rm star} \geq 5 \times 10^8\ h^{-1} M_\odot$, which represents the population of objects whose spin–filament is the topic of this chapter. However, for completeness, in the case of NEXUS+ environments we show the galaxy mass function down to much fainter central galaxies with $M_{\rm star} \geq 5 \times 10^6\ h^{-1} M_\odot$ (corresponding to roughly 3 or more star particles).

The first two panels of Figure 3.6 show that a majority of haloes with a mass, $M_{200} \geq 5 \times 10^{11}\ h^{-1}{\rm M}_\odot$, and galaxies with a stellar mass, $M_{\rm star} \geq 5 \times 10^9\ h^{-1}{\rm M}_\odot$, are located in the filaments of the cosmic web (Cautun et al. 2014; Libeskind et al. 2018). In this mass range, walls, and even more so voids, represent considerably more desolate environments. These results are in good agreement with observational studies, such as Tempel et al. (2011) and Eardley et al. (2015), which show that the galaxy luminosity function varies between different environments. More specifically, Eardley et al.; Chira, Plionis & Corasaniti find that the number density of galaxies/haloes as well as the knee of the Schechter function used to fit the luminosity function (Schechter 1976) are the highest for nodes and decreases going from filament, to wall and to void environments.

We find a similar trend for galaxies in filaments, walls and voids but not for nodes. Due to its small box size, which is only 100 Mpc on a side, the EAGLE simulations is not able to produce a representative population of massive cluster sized haloes. For a structure to be identified as a node by the NEXUS+ algorithm, we use a mass threshold of $5 \times 10^{13} h^{-1}{\rm M}_\odot$. Owing to the truncated power spectrum due to the small box size, such massive structures are not formed in the EAGLE simulation. It translates into a substantial suppression of the halo and galaxy mass function in the cosmic web nodes, in line with the finding of eg. Bagla & Ray (2005). They already showed that the high mass end of the halo mass function is significantly reduced in a ΛCDM simulation volume with a side length less than 100 h^{-1} Mpc.

The differences between the NEXUS+ and the Bisous filaments are also reflected in the corresponding filament galaxy mass functions. This are illustrated in the bottom panel of Figure 3.6 which compares the galaxy mass function of Bisous and NEXUS+ filaments. At the low mass of the mass function, both web finders assign a similar number of galaxies to filaments. At the high mass end, we see a marked difference. While NEXUS+ assigns a range of massive galaxies to filaments, the Bisous formalism yields a sharp cutoff at $M_{star} \sim 10^{11}\ h^{-1}{\rm M}_\odot$. Such differences are not uncommon, as we may infer from the detailed comparison in Libeskind et al. (2018), so actually the agree-

ment between the galaxy mass function in NEXUS+ and Bisous filaments is rather good. One factor that might lead to enhanced differences between the two web finders is the very low number of massive clusters in the EAGLE simulation. On one hand, this results in NEXUS+ assigning more massive galaxies to filaments. On the other hand, the Bisous selection criteria related to the strength and orientation of valid filaments refrain the Bisous filaments from extending close to the high-density nodes. Filaments detected next to cosmic web nodes have a lower orientation strength and therefore galaxies surrounding the nodes, which are predominantly more massive, might not be part of the Bisous filamentary network (Bonamente et al. 2016). The orientation strength depends on how the majority of Bisous cylinders are aligned at a certain location (Tempel et al. 2014c). Close to a cluster, this orientation will be weak as the cylinders do not align well (Bonamente et al. 2016).

Regardless of the differences discussed above, we find that the majority of Bisous filament galaxies are also identified as filament galaxies by NEXUS+. This can be inferred from the solid line in the bottom panel of Figure 3.6, which shows the galaxies common to both Bisous and NEXUS+ filaments. A small fraction of Bisous galaxies turn out to be associated with NEXUS+ walls, while a minute number is found in either nodes or voids.

3.4 Alignment analysis and results

The present section presents our results on the alignment of the spin and shape of haloes and galaxies with respect to the orientation of the large-scale filaments in which they reside. We assess the cosmic web alignment on the basis of four different aspects:

- the alignment of the spin of haloes and the spin of galaxies with respect to the filament to which they are bound (sect. 3.4.2).
- the differences between the alignment of late-type disc galaxies to the filament in which they reside and that of early-type galaxies (sect. 3.4.3).
- the observationally more accessible alignment of galaxy and halo shape, in terms of their minor axis, with respect to the embedding filament (sect. 3.4.4).
- the alignment between the spins of galaxies and their filaments, as well as that between the minor axis of galaxies and their haloes (sect. 3.4.5).

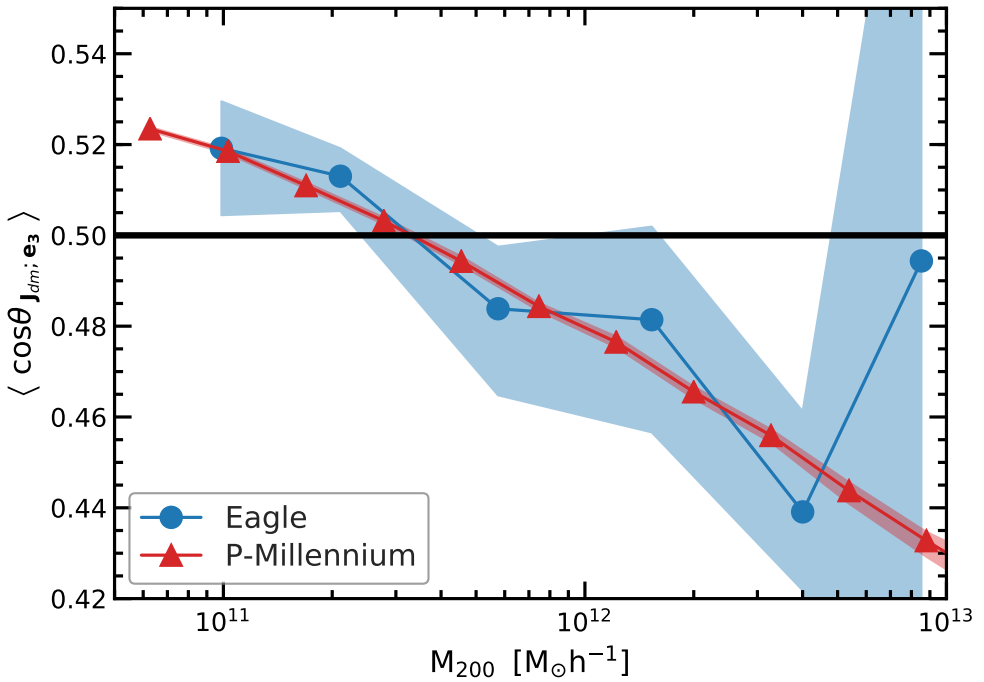

Figure 3.7 – ***Halo spin – filament alignment.*** *The dependence on halo mass of the median alignment angle between the spin of DM haloes and the orientation of NEXUS+ filaments. The plot compares the alignment in the* EAGLE *hydrodynamical simulation with the one in the P-Millennium DM-only simulation.*

3.4.1 Spin and shape alignment analysis

In order to quantify the alignment between galaxies and haloes on the one hand and the filaments in which they reside, on the other hand, we define the misalignment angle, θ, as the angle between two vectors, one of which corresponds to the property of a halo or galaxy ($\mathbf{h}$), and the other corresponds to filament orientation ($\mathbf{e_3}$), which is the slowest collapse direction. The alignment parameter, or simply the alignment angle, is given by

$$\mu_{hf} \equiv \cos\theta_{\mathbf{h},\mathbf{e}_3} = \left| \frac{\mathbf{h}\cdot\mathbf{e}_3}{|\mathbf{h}||\mathbf{e}_3|} \right| , \tag{3.5}$$

where we take the absolute value of the scalar product since filaments have an orientation, but not a direction. That is, both $\mathbf{e}_3$ or $-\mathbf{e}_3$ point along the filament axis. A vector quantity that is parallel to the filament axis (either to $\mathbf{e}_3$ or $-\mathbf{e}_3$), corresponds to $\mu_{hf} = 1$. When the galaxy spin, or shape, is directed perpendicular to filaments, it yields an alignment parameter, $\mu_{hf} = 0$.

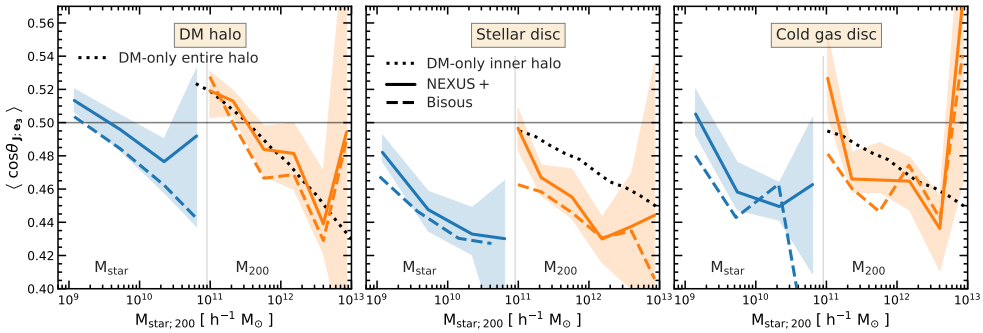

Figure 3.8 – ***Spin–filament alignment for haloes and galaxies***. *The alignment is plotted as a function of halo mass (orange) and stellar mass (blue) for central galaxies and their host haloes. The left panel is for host haloes, the central panel is for the stellar disc and the right panel for the cold gas disc. In all the panels the solid line shows the alignment with NEXUS+ filaments and the dashed line the alignment with Bisous filaments. The black dotted line shows the alignment of the entire halo in the left panel and the inner halo in the centre and right panels measured in the P-Millennium DM-only simulation. The shaded region represents the 2σ uncertainty and is plotted only for NEXUS+ filaments for clarity. The error range for Bisous is very similar.*

In general, the halo/galaxy vector properties have a distribution of alignment angles with respect to the filament axis. We can quantify this using the probability distribution function (PDF) of the alignment angle. Furthermore, the PDF can vary according to halo/galaxy mass (see e.g. Figure 10 in Ganeshaiah Veena et al. 2018), and thus different mass sample can have different PDF distributions. To quantify this mass dependence, we calculate the median alignment parameter, $\langle \mu_{hf} \rangle$, as a function of halo and galaxy mass. In the absence of any alignment, that is in the case of an isotropic distribution of alignment angles, the PDF of μ_{hf} is an uniform distribution between 0 and 1, and has a median value, $\langle \mu_{hf} \rangle = 0.5$. To calculate the alignment angle uncertainties, we generate many bootstrap realizations for each mass bin. From these, we estimate the 1σ and 2σ uncertainty intervals for both the PDF and the median alignment angle (see e.g. Figure 3.7).

We characterise a population to be preferentially parallel if the median alignment is $\langle \mu_{hf} \rangle > 0.5$. Conversely, $\langle \mu_{hf} \rangle < 0.5$ corresponds to a preferentially perpendicularly aligned population. The alignment parameter $\mu_{hf} = 0.5$ marks the transition between preferentially parallel and perpendicular and it corresponds to an angle, $\theta_{h,f} = 60°$.

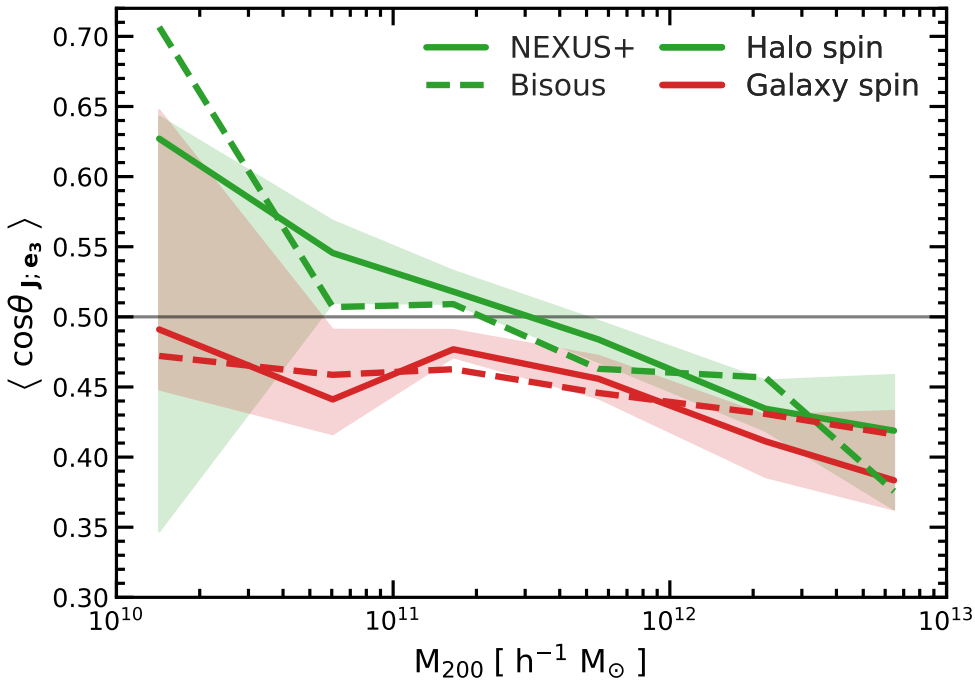

Figure 3.9 – ***Median spin alignment of common galaxies.*** *The plot shows the spin–filament alignment only for the galaxies and the haloes common to both NEXUS+ and Bisous filaments. The consistent difference seen in Figure 3.8 between spin alignments with NEXUS+ and Bisous filaments does not exist when we choose galaxies that are common to both type of filaments.*

3.4.2 Halo and galaxy spin–filament alignment

We first study the alignments between the DM halo spin and its host filament. This has been extensively studied in DM-only simulations (see discussion in the introduction section) and we want to assess if the inclusion of baryonic physics affects this alignment. Figure 3.7 compares the median halo spin–filament alignment angle as a function of halo mass in two simulations: EAGLE, which includes galaxy formation processes, and the P-Millennium DM-only simulation. The latter is a very high resolution, 5040^3 DM particles each of mass $1.061 \times 10^8\ h^{-1}\mathrm{M}_\odot$, and large volume, a 800 Mpc periodic box, simulation (McCullagh et al. 2017; Baugh et al. 2018) of structure formation in a ΛCDM universe with the same cosmological parameters as the EAGLE simulation. Ganeshaiah Veena et al. (2018) have used the very large sample of P-Millennium haloes to characterize the halo spin–filament alignment over a wide range of halo masses; their result is the one shown in Figure 3.7. Note that for both the EAGLE and the P-Millennium simulations we use the same fil-

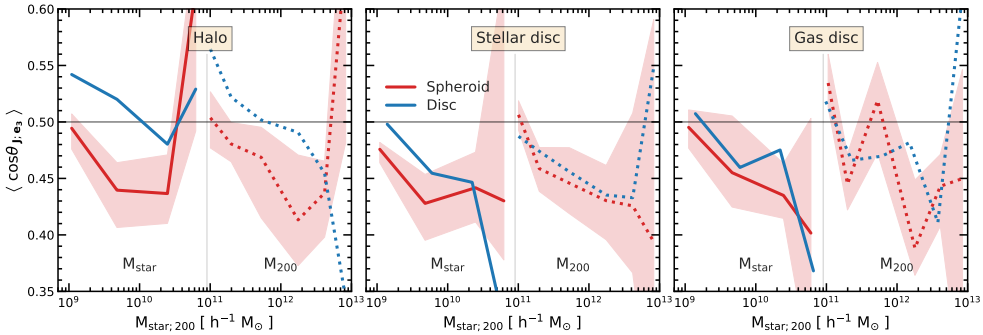

Figure 3.10 – ***Spin–filament alignment for discs and spheroids.*** *The plot shows the alignment as a function of both stellar mass (solid line) and halo mass (dotted line) for disc ($B/T < 0.58$, shown in blue) and spheroid ($B/T > 0.82$, shown in red) galaxies. The disc and spheroid samples were selected to contain a third of the galaxy population with respectively the lowest and highest bulge to total ratio. We only show the alignment with NEXUS+ filaments; however this is very similar for Bisous filaments. The shaded region shows the uncertainty, as in Figure 3.8.*

ament finding algorithm, NEXUS+, in order to eliminate discrepancies arising from the use of different web finders.

Despite differences in the initial conditions, box size and the nature of the simulations, the halo spin–filament alignments in P-Millennium and EAGLE are statistically identical. In both simulations, the spin of less massive haloes shows a preferential parallel alignment with the filaments whereas the spin of massive haloes shows a preferential perpendicular alignment. The mass where this transition happens is known as the spin-flip mass and is identical in both simulations. Thus, the inclusion of baryons does not alter (at least given the statistics of the EAGLE sample) the mean alignment between halo spins and their host filaments.

Next, we study the galaxy spin–filament alignment and compare it to the mass dependent alignment trend seen for haloes. In Figure 3.8 we show the median alignment of haloes and stellar and gaseous components of galaxies. The left-hand panel shows the halo spin–filament alignment: haloes show a clear spin transition from preferentially parallel to perpendicular with respect to both halo mass and the stellar mass of their central galaxies. The stellar (centre panel) and gas (right-hand panel) components also show a strong mass dependent alignment, with high mass galaxies showing a stronger perpendicular alignment than low mass galaxies. The spin alignment of the stellar and gas distributions are very similar, although the gas spin is slightly less perpendic-

ular to filaments than the stellar component. However, neither the stars nor the gas components exhibit a spin transition as in the case of their host haloes.

This discrepancy could be due to differences in angular momentum acquisition between haloes and galaxies. For example, Ganeshaiah Veena et al. (2018) have pointed out that the halo spin–filament alignment varies between the inner and full halo. At fixed halo mass, the spin of the inner halo is more orthogonal to the filament spine than that of the full halo. Galaxies are likely to be better aligned with the inner regions of their host haloes (e.g. Bailin & Steinmetz 2005; Velliscig et al. 2015; Shao et al. 2016), which motivates us to compare with the spin–filament alignment of the inner regions of haloes in DM-only simulations. For this, we use the Ganeshaiah Veena et al. results for the spin–filament alignment of the inner 10% of the DM halo mass, which are shown as a dotted line in the centre panel of Figure 3.8. It shows a closer match to the galaxy spin–filament alignment, although there are still discrepancies: the galaxy spin in EAGLE is systematically more orthogonal to the host filament axis than the spin of the inner halo in DM-only simulations. Because of feedback and dissipation processes the angular momentum build-up in galaxies can be different from that of the inner halo regions and thus stellar spin can deviate somewhat from that of the inner halo.

We also investigate whether the alignment trend is sensitive to the tracers and techniques used for filament detection. Figure 3.8 also compares the median spin–filament alignment for two different filament populations identified using the NEXUS+ (solid lines) and Bisous (dashed lines) methods. Despite the various differences listed in section 3.3, the alignment trend is robust and consistent irrespective of the filament type. However, we find that galaxies and haloes in Bisous show a consistently stronger orthogonal signal than NEXUS+ filaments.

Previous studies have shown that the alignment varies strongly with the properties of filaments, with haloes found in thinner filaments having their spin more perpendicular on the filament axis than equal mass haloes in thicker filaments (Aragon-Calvo & Yang 2014; Ganeshaiah Veena et al. 2018). Could the same phenomenon explain the differences in halo and spin alignment between NEXUS+ and Bisous filaments? We investigate this in Figure 3.9, where we plot the median alignment using only the sample of haloes and galaxies common to both Bisous and NEXUS+ filaments. The figure shows that the alignment of the common sample with the two filament types is statistically indistinguishable and that there is no systematic discrepancy. It is interesting to note that most of the common galaxies are the ones located in prominent and dynamically active filaments (see black symbols in the central row of panels in Figure 3.4). Thus, the differences seen in Figure 3.8 are mostly due to

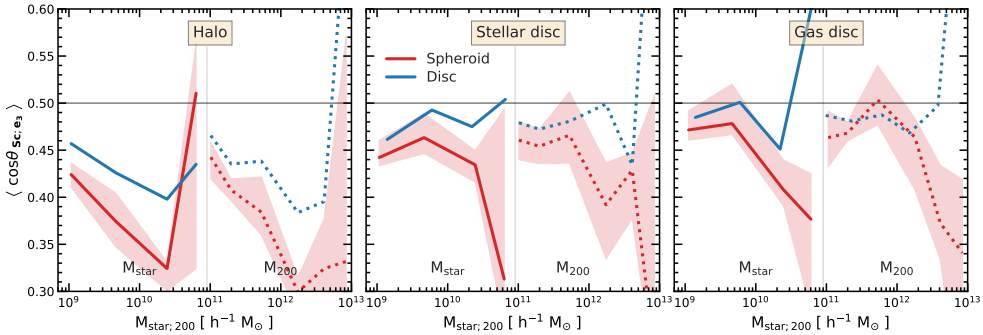

Figure 3.11 – ***Galaxy shape–filament alignment.*** *Same as Figure 3.10 but for the median alignment angle between the filament orientation and the minor axis of the halo (left panel), stellar (centre panel) and gas (right panel) components. The sample is divided into systems for which the central galaxy is either disc- (blue) or bulge-dominated (red).*

non-overlapping galaxies found either in the peripheral regions of filaments or in tenuous filaments. Motivated by this find, we checked if the galaxy spin–filament alignment varies with filament properties, such as thickness, and, while we found a hint of such a trend, the EAGLE simulation does not have a large enough sample of galaxies to robustly claim such a dependence.

3.4.3 Spin alignment and galaxy morphology

It has been shown observationally that spirals and spheroids show different alignments with their host filaments. Spirals are typically less perpendicular to the filament axis than spheroidal galaxies (e.g. see Tempel, Stoica & Saar 2013). This motivated us to study how the galaxy spin–filament alignment in EAGLE varies with galaxy morphology. EAGLE is well suited for this task since it reproduces rather well the observed galaxy colour bimodality (Trayford et al. 2015) as well as the correlation between galaxy morphology, colour and stellar mass (Correa et al. 2017). In particular, central galaxies that have red colours are mostly elliptical while blue centrals consist of mostly disc galaxies (see Fig. 3 in Correa et al. 2017). To study the dependence of spin–filament alignment on galaxy morphology, we divide the population into disc- and bulge-dominated galaxies based on the bulge to total ratio (for details and exact definition see section 3.2.3).

Figure 3.10 shows the median spin–filament alignment split according to the morphology of the central galaxy. Similar to Figure 3.8, we show the alignments of the halo, stellar and gaseous components as a function of both halo and stellar mass. Figure 3.10 shows a clear variation of the alignment signal with

galaxy morphology. This trend is the largest for the left-hand panel, indicating that host haloes of spheroids tend to have their spins more perpendicular to the filament axis than equal mass host haloes of disc galaxies. The same trend is also seen in the stellar/gas spin-filament alignment, although the trend is not as substantial as for the host haloes. Thus, in EAGLE, elliptical galaxies show a propensity towards a stronger orthogonal alignment than spirals, in qualitative agreement with observations.

Although this result indicates that the halo spin orientation with respect to the large-scale structure affects the galaxy morphology, we found no significant evidence for this hypothesis. The fraction of spheroid central galaxies is roughly the same independent of the host halo spin–filament alignment. Thus, a more likely explanation for the variation of the halo spin–filament alignment with galaxy morphology is that they are both affected by a third physical process. For example, Welker et al. (2014) have shown that galaxy mergers, which typically take place along the filament in which the galaxies are embedded, can lead to an increase both in the fraction of spheroids and in the fraction of haloes and galaxies with spins perpendicular to their filaments. Our results qualitatively match observational trends, in the sense that spheroids have an excess of perpendicular spin–filament alignments compared to disc galaxies, however they do not do so quantitatively.

For example, Tempel, Stoica & Saar (2013) have found that in observations spiral galaxies show a small, but statistically significant, preference to have their spins parallel to their host filament axis. However, in EAGLE we find that at all masses the spins of disc galaxies are preferentially perpendicular to their filaments. The discrepancy could be due to the difference in the mass range and environment of spiral galaxies between the EAGLE simulation and observations. Due to magnitude limits, most observational analyses focus on generally bright and massive spirals. However, due to the small box size, EAGLE contains only a small number of such high mass spirals. Generally, such massive spirals are residing in thick filaments and it has been shown that haloes populating thicker filaments are more likely to have their spin aligned along the filament than equal mass haloes in thinner filaments (Ganeshaiah Veena et al. 2018). Due to the limited size of the EAGLE simulation, there are only a few massive filaments and most spiral galaxies are found in thin filaments, which could explain the systematic difference between the EAGLE results and observations. We note that there are additional differences between observations and our EAGLE results that could also add to the discrepancy. Such as the different definitions of galaxy morphology and also that observational results are based on the alignment between the minor axis of galaxies and not their spin per-se.

3.4.4 Galaxy shape alignments

Observationally, it is very difficult to determine the spin of galaxies and we can only infer their shapes. In general, disc galaxies have their spin well aligned with their minor axis, however spheroid galaxies can have their spin and minor axis highly misaligned. For example, our sample of EAGLE spheroids have a median misalignment angle of 45°. Furthermore, even some spiral galaxies, e.g. those with a dominant bulge component, can have some degree of misalignment between their spin and minor axis.

In Figure 3.11 we show the alignment of halo/galaxy minor axis with the orientation of their host filaments. Similar to spheroid galaxies, haloes are mostly dispersion supported and can have a large degree of misalignment between their spin and minor axis (e.g. see Bett et al. 2007). The left-hand panel of Figure 3.11 shows that the halo minor axis is preferentially perpendicular to the filament axis for objects of all masses. This is in contrast to the halo spin which shows a transition from preferentially perpendicular at high mass to preferentially parallel at low masses (see Figure 3.10). The halo minor axis–filament alignment is the largest for haloes hosting spheroid galaxies and shows a mass dependence, being largest for high mass haloes (notwithstanding the highest mass bin which is affected by poor statistics due to the low number of objects). This is in agreement with the results of DM-only simulations, which also find that the halo shape–filament alignment is the largest for high mass haloes (e.g. see Aragón-Calvo et al. 2007b; Hahn et al. 2007a; Ganeshaiah Veena et al. 2018).

The central panel of Figure 3.11 shows that the galaxy minor axis–filament alignment is different from the galaxy spin–filament alignment. For example, within our limited statistics we find that the galaxy minor axis–filament alignment in EAGLE is independent of galaxy mass. Furthermore, while spheroid galaxies have their minor axis preferentially perpendicular to the filament axis, spiral galaxies show no preferential alignment, that is their median alignment angle is consistent with 60°, which is the expectation for the no alignment case. The largest difference between spin and shape alignments of spiral galaxies is at the high mass end, $M_{\rm star} \geq 5 \times 10^{10}\ h^{-1}{\rm M}_{\odot}$, where spirals have their spin preferentially perpendicular to the filament spine (see Figure 3.10) but show no significant alignment in terms of their minor axis. The discrepancy could be due to many massive spirals having a significant bulge component whose spin, at least in EAGLE, is not within the plane of disc.

In summary, due to the degree of misalignment between galaxy spin and shape, the galaxy spin and galaxy minor axis show different alignments with their host filaments. This needs to be accounted for when comparing against observations, which can only measure galaxy shapes. Furthermore, we note that in

most cases the 3D orientation of a galaxy is inferred from its projected 2D image and this can, in turn, affect the alignment signal; however we leave this for further study. A more firm determination would be possible from velocity field maps, which can be obtained from 21cm radio observations or from integral field spectrographs. While new generation instruments like the VLT MUSE facility and the wide-field APERTIF array on the WSRT radio interferometer will be powerful resources, as yet the amount of available data for such large-scale alignment studies is still rather limited.

3.4.5 The halo–galaxy connection

Galaxies and their host haloes form within the same large-scale environment, however, as we have shown in this section, haloes and galaxies are characterized by different spin–filament alignment trends. As discussed in the introduction, these differences are mostly due to the complex gas inflow and outflow physics which drives the formation of the stellar and gaseous components of a galaxy. Here, we study in more detail the spin and shape alignment of galaxies and their haloes, and how it relates to their host filament.

Figure 3.12 shows the spin and shape alignment between central galaxies and their host haloes. These are plotted as a function of both galaxy and halo mass and are also split according to the morphology of the central galaxy. In general, the galaxy spin shows a 45° median misalignment angle with respect to the host halo spin (see top panel of Figure 3.12). At low galaxy masses, this misalignment angle varies with galaxy morphology, with a median misalignment angle of 37° and 49° for disc and spheroids, respectively.

Even though the spin of spheroid galaxies is the least well aligned with that of their host haloes, the spin–filament alignment of spheroid galaxies traces very well the spin–filament alignment of their host haloes (compare red curves between the left-hand and central panels of Figure 3.10). Disc galaxies, in contrast, have a different spin–filament alignment than that of their host haloes: the spirals have a larger tendency to have their spins perpendicular to the filament axis than their host haloes. This difference is likely due to the dichotomy in the formation of disc and spheroid galaxies (e.g. Sales et al. 2012; Rodriguez-Gomez et al. 2017; Clauwens et al. 2018; Lagos et al. 2018). The growth of spirals is thought to occur mostly through the accretion of gas with a coherently aligned angular momentum over a long period of time. Most spirals experience only uneventful minor mergers and their disc orientations vary slowly in time (although there are exceptions, e.g. see Bett & Frenk 2012, 2016). Such mergers are unlikely to misalign the spins of the central galaxy and the host halo. In contrast, a significant fraction of spheroids forms through major mergers, with the merger taking place preferentially along the filament

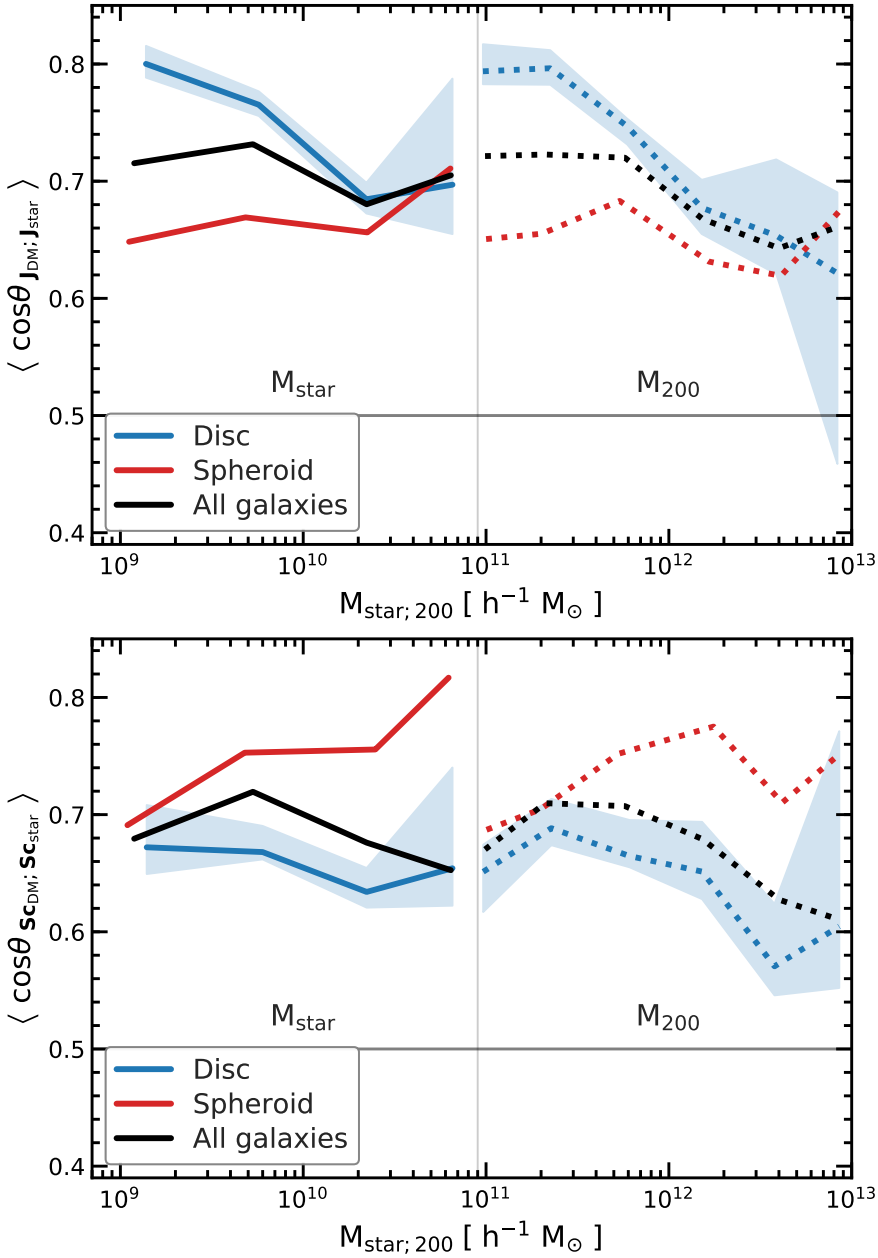

Figure 3.12 – ***Galaxy–halo spin and shape alignment.*** *The plot shows the median alignment angle of the spin (top panel) and of the minor axis (bottom panel) between haloes and their central galaxies. The alignment is show as a function of both halo and stellar mass corresponds to all galaxies (black) as well as to two morphology selected subsamples: discs (blue) and spheroids (red).*

in which the galaxies are found (e.g. Libeskind et al. 2014; Welker et al. 2014; Shao et al. 2017). In this case, the mergers would preferentially orient the spin of both the galaxy and the halo perpendicular to the filament axis.

The minor axis of galaxies and their host haloes shows a modest degree of alignment, with a median misalignment angle of 47° that is roughly galaxy and halo mass independent, as can be appreciated from the bottom panel of Figure 3.12. When splitting the sample according to galaxy morphology, we find a better alignment for spheroids than for spirals. This difference is the largest at the high mass end. The variation with galaxy morphology is opposite to the one found for galaxy–halo spin alignment, which shows a higher degree of alignment for disc galaxies.

Halo-galaxy alignments: the filament connection

The misalignment between galaxy and halo shapes explains why galaxy shapes are more poorly aligned with the filament axis than their host haloes. This is true for both disc and spheroid galaxies. In particular, the shape of haloes is aligned with their host filaments since it is mostly determined by recent accretion that takes place preferentially along the filament in which the halo is currently embedded (see e.g. Ganeshaiah Veena et al. 2018, and discussion therein). In contrast, the shape of galaxies should be best aligned with the filament orientation when the galaxies formed most of their stellar mass, which took place at a redshift, $z \sim 1-2$. The orientation of the host filament can change over time, due to either filament mergers or galaxies moving across the cosmic web (van Haarlem & van de Weygaert 1993b; Aragón-Calvo et al. 2007b; Cautun et al. 2014; Wang & Kang 2017), and thus should decrease in time.

To better understand the processes affecting the galaxy–filament alignment, we proceed by selecting two galaxy subsamples: one composed of galaxies that have their minor axis parallel to the filament and a second one composed of galaxies with minor axis perpendicular to the filament. For clarity, we refer to the two subsamples as parallel and perpendicular galaxies. To have a large enough sample, we define the galaxies with parallel minor axis–filament orientations as those with small misalignment angles, that is those with $\cos\theta_{\mathbf{Sc}_{\rm star},\mathbf{e}_3} \geq 0.8$. Similarly, we define the galaxies with perpendicular minor axis–filament orientations as those with a misalignment angle close to 90°, that is those with $\cos\theta_{\mathbf{Sc}_{\rm star},\mathbf{e}_3} \leq 0.2$. Each of the two subsamples consist of roughly 20% of the total galaxy population.

Galaxy and halo shapes are moderately aligned (see e.g. Figure 3.12) and thus it should not be surprising that parallel galaxies reside in haloes whose minor axis is also predominately parallel to the filament axis. Similarly, perpendicular

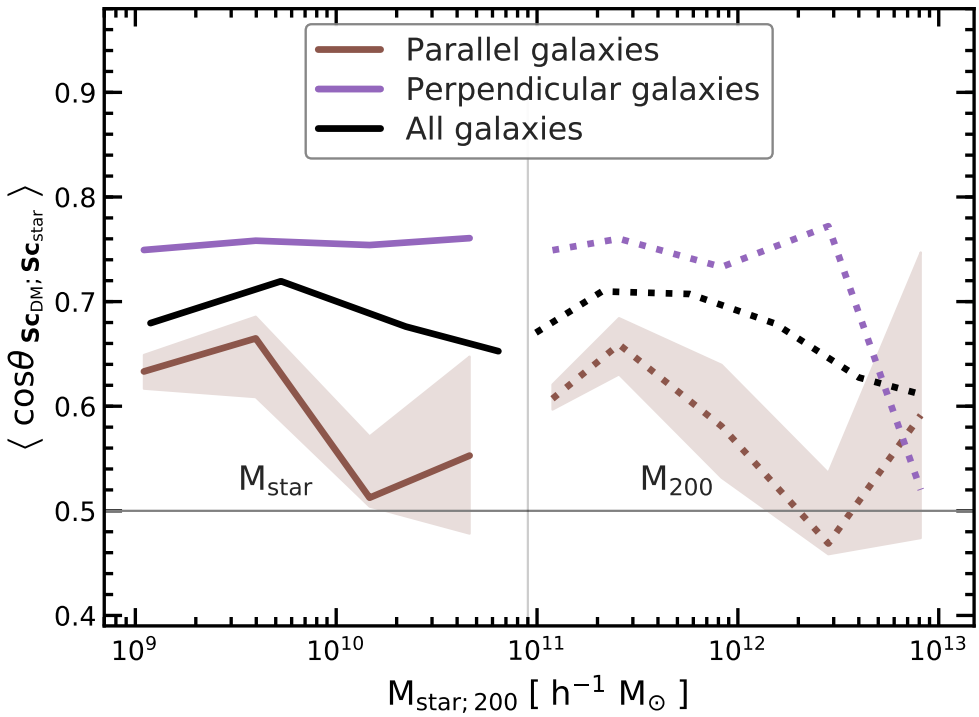

Figure 3.13 – ***Galaxy–halo minor axis alignment for galaxy subsamples selected according to the galaxy minor axis–filament alignment angle.*** *The plot shows the median alignment angle between the minor axis of central galaxies and that of their host haloes. We show results for all galaxies (black) as well as for two galaxy samples selected to have their minor axis along the filament (so called parallel galaxies shown in purple) or perpendicular to the filament (so called perpendicular galaxies shown in brown). Galaxies perpendicular to filaments show a larger alignment with their host haloes.*

galaxies are found in haloes whose minor axis is predominately perpendicular to the filament axis. More interestingly is to study how the galaxy–halo shape alignment varies between perpendicular and parallel galaxies. This is because the galaxy minor axis–filament alignment is weak and should not affect noticeably the galaxy–halo alignment.

Figure 3.13 shows the median galaxy–halo minor axis alignment angle for the two sub-samples of parallel and perpendicular galaxies. It clearly highlights that galaxies perpendicular to their filaments have a larger degree of alignment with their host haloes. In contrast, galaxies oriented along their filament axis have poorer alignments with their haloes. It suggest that the same processes that affect the galaxy shape–filament alignment play an important role for

the galaxy–halo alignment too. For example, galaxies and haloes embedded in filaments that remain stable over long periods of time are more likely to experience anisotropic infall along the same time-independent directions. This would lead to a stronger alignment between the galaxy and its halo (van Haarlem & van de Weygaert 1993b). Furthermore, this would also lead to a preferentially perpendicular alignment of galaxy and halo minor axes with the host filament since accretion preferentially takes place along the filament direction. On the other hand, objects whose cosmic web environment changes rapidly with time experience different anisotropic infall directions at various times. Most of the galaxy stellar mass is acquired at early times, while haloes are still assembling at late times. Thus, on average, such galaxies are more poorly aligned with their haloes.

A similar dichotomy in galaxy–halo alignment is present when selecting parallel and perpendicular galaxies subsamples according to the galaxy spin–filament alignment. In this case, we also find that galaxies with spins perpendicular to their filaments are better aligned with their host haloes. While the effect is about half the size of the one seen in Figure 3.13 and given the similarity, for brevity we do not include a diagram to illustrate it.

Implications: satellite planes, halo shapes

The results illustrated in Figure 3.13, which are that galaxies whose minor axis is perpendicular to their host filament are more likely to be aligned with their host haloes, have two important implications. Shao et al. (2016) have found a similar result when studying the alignment between central galaxies and their satellite galaxies: systems where most satellites are in the plane of the baryonic disc have a much higher galaxy–halo alignment. Thus, combining our results and those of Shao et al., we predict that galaxies perpendicular to filaments should have most of their satellites in the plane of the galaxy disc. This prediction of the EAGLE simulation can be checked observationally and represents one avenue for constraining the processes that affect the alignment of galaxies and haloes with their host filaments.

Furthermore, our results can be used to test a fundamental prediction of the standard cosmological model: that galaxies are embedded in flattened dark matter haloes. A possible test of this prediction would involve stacking weak lensing maps of multiple galaxies and measuring the average flattening of their DM halo (see e.g. van Uitert et al. 2017). To do so, one needs to know the orientation of the DM halo. Using galaxy orientations does not work due to galaxy–halo misalignment and makes it very challenging to measure halo shapes (see e.g. Bett & Frenk 2012, and references therein). Selecting a subset of galaxies perpendicular on their filament improves the galaxy–halo alignment

and could represent an improved approach for measuring halo shapes.

3.5 Conclusions and Discussions

The principal purpose of this study is to investigate how far secondary processes alter the original spin of haloes and galaxies. While the spin of haloes and galaxies is initially generated by tidal torques (Hoyle 1949; Peebles 1969; Doroshkevich 1970b; White 1984), a range of nonlinear and baryonic processes are likely to alter the evolution of this fundamental property of galaxies. Because the large-scale tidal field is the agent behind the contraction of mass into elongated filaments, the tidal torque theory leads to the expectation that halo and galaxy spins should tend to be oriented perpendicular to the filaments in which they are embedded (see e.g. Lee & Pen 2000; Jones & van de Weygaert 2009). Hence, by relating the spin of haloes and galaxies to their cosmic web environment we seek to identify the processes which affect the rotation of haloes and galaxies.

The simulation-based studies of Aragón-Calvo et al. (2007b) and Hahn et al. (2007a) were the first to reveal that the halo spin–filament alignment shows a complex mass dependence, with high mass haloes having their spins preferentially perpendicular to filaments while low mass haloes show the opposite trend. The transition between the two regimes today takes place at a halo mass of $\sim 10^{12}\ h^{-1}\mathrm{M}_{\odot}$, which is known as the spin-flip transition mass. In Ganeshaiah Veena et al. (2018) we performed a detailed and systematic analysis of halo spin–filament alignments to reveal a strong dependence of the alignment on the nature of filaments. In particular, the spin-flip transition mass is highest for haloes in dynamically dominant and thick filaments, while it is an order of magnitude lower for haloes in thin and tenuous filaments. This trend represents a clear indication of the impact of late-time halo evolution processes on the spin–filament alignment.

The present study extends our investigation from DM haloes to the galaxies they harbour. For this, we employ the EAGLE hydrodynamical simulation, which follows the formation and evolution of galaxies in a cosmological volume. Our goal is to address the question in how far the alignment of haloes with respect to the filaments in which they reside is reflected in an alignment of galaxies with respect to the large scale cosmic web. To this end, we investigate whether the mass dependent alignment exhibited by haloes is also exhibited by galaxies. In particular, we wish to assess the relation between the spin orientations of galaxies and their host haloes, and establish to what extent the halo spin orientation can be inferred from that of their central galaxies. In this context, we also investigate if the presence of baryons alters the halo spin–filament alignment found in DM-only simulations.

Filament population

We predominantly focus on cosmic filaments. We have identified the filament population with two different cosmic web finders (see e.g. Libeskind et al. 2018) in order to assess which results are dependent on the filament identification method. Firstly, we applied the NEXUS+ multiscale formalism to the matter distribution to identify the cosmic web nodes, filaments, sheets and voids. Secondly, we applied the Bisous method to the galaxy distribution to select galaxy filaments. In general, we find good agreement between the filament populations identified by the two methods, although some differences exist (see section 3.3 for a detailed analysis). In particular, we find a large overlap between the populations of filament galaxies in the two methods and good alignment between the orientations of the NEXUS+ and Bisous filaments. These are the two aspects that are most important for this study.

We find that most of the matter content of the $z = 0$ universe is found in filaments, in good agreement with cosmic web studies based on DM-only simulations (e.g. Cautun et al. 2014; Libeskind et al. 2018). More specifically, 52% of the DM is found in filaments, but only 47% of the total gas content. The difference is due to baryonic processes that heat up the gas in filaments and disperse it to surrounding walls and voids (Haider et al. 2016). Accordingly, we find that walls and voids contain slightly higher mass fractions of gas than of DM.

The majority of the stellar mass – 82% for NEXUS+ and 70% for Bisous – is located in filaments. The remaining stellar mass is found in nodes and sheets, each containing roughly 10% of the stars, while voids contain less than 0.5% of the total stellar mass. The filaments also contain the largest number of galaxies with stellar masses higher than $10^9\ h^{-1}\mathrm{M}_\odot$, and a dominant fraction of lower mass galaxies. In particular, most of the galaxies at the knee of the stellar mass function are found in filaments, while the very massive galaxies are found mostly in the cosmic web nodes. On the other hand, voids are mostly populated by faint dwarf galaxies.

Halo and galaxy alignments with filaments

We have investigated four different, but intimately related, aspect of the alignment between galaxies, haloes and filaments. These are the alignments of

- the spin of haloes and the spin of galaxies with respect to the embedding filament,
- the spin of late-type and early-type galaxies relative to the filament direction,

- the shape of haloes and galaxies, characterised by their minor axis, with respect to the filament in which they reside, and
- the spins of haloes with respect to the galaxies they host, as well as the orientation of the minor axis of galaxies with respect to that of their haloes.

Halo and galaxy spin alignment with filaments

We find that haloes in the DM-only P-Millennium simulation and the EAGLE hydrodynamical simulation show statistically similar distributions of spin–filament alignments: low mass haloes have their spins preferentially along the filament while high mass haloes have their spin preferentially perpendicular to the filament. The halo transition mass between the two regimes is the same for both DM-only and baryonic physics simulations. Thus, the addition of baryons does not affect the distribution of halo spins with respect to the large-scale filaments.

Galaxies, just as their host haloes, show a mass dependent spin–filament alignment: massive galaxies have their spin preferentially perpendicular to the filament to a larger extent than lower mass objects. However, we do not detect a clear transition from parallel to perpendicular alignment as we see in the case of haloes. This is in contrast to the results of Wang & Kang (2018a) who, using the Illustris simulation, found a transition in the galaxy spin–filament alignment that takes place at a stellar mass of $2.5 \times 10^9\ h^{-1}\mathrm{M}_\odot$. However, our results agree better with the Codis et al. (2018) study based on the Horizon-AGN simulation, which shows that $z = 0$ galaxies with stellar masses below $10^{10}\ h^{-1}\mathrm{M}_\odot$ have no preferential spin alignment with their host filament.

The discrepancy with the studies of Wang & Kang (2018b) and Codis et al. (2018) could be due to difference in hydrodynamic simulations. In particular, many of the subgrid implementations of baryonic physics vary from simulation to simulation and this can lead to different galaxy growth histories and thus to different galaxy spins orientations. However, we suspect that at least part of the discrepancy is a manifestation of the dependence of the galaxy spin–filament alignment on the nature of filaments. For example, this trend has been robustly established by Ganeshaiah Veena et al. (2018) for the halo spin–filament alignment, with equal mass haloes having a larger propensity for perpendicular spin–filament alignments when they are found in thinner filaments. This trend is strong enough to result in more than one order of magnitude variation in the halo spin-flip mass between the thinnest and thickest filaments. We also find tentative evidence for a dependence between the alignment of galaxy spins and filament properties; however the EAGLE volume is too small to robustly characterise such a trend.

We note that a systematic trend in which galaxies in thinner filaments are more likely to have their spins perpendicular to the filament axis than similar mass galaxies in thicker filaments is consistent with the differences between our alignment results and those of Wang & Kang (2018b) and Codis et al. (2018). The Wang & Kang method identifies mostly thick filaments, while both the NEXUS+ and Bisous algorithms detect a large population of very thin filaments. The DISPERSE method employed by Codis et al. is somewhere in between the other two studies (for a detailed comparison, see Libeskind et al. 2018).

Dependence on galaxy morphology

We find a strong dependence of the halo and galaxy spin–filament alignment on galaxy morphology. Distinguishing between disc and spheroid galaxy populations, we find that the host haloes of spheroidal galaxies show a larger tendency to have perpendicular spin–filament alignments than the host haloes of disc galaxies. Similarly, spheroid galaxies show a stronger propensity for an orthogonal spin-filament alignment than spirals. This agrees with observations which find that ellipticals are more likely to be orthogonal to filaments than spirals (Tempel, Stoica & Saar 2013; Zhang et al. 2013, 2015; Pahwa et al. 2016), although we do not detect a distinct parallel alignment of disc galaxies as detected in the SDSS.

The discrepancy could be due to the small volume of the EAGLE simulation. Due to a lack of very large modes, the simulation does not contain many objects similar to those typically present in observations: bright spiral galaxies as well as the thick filaments which host them.

Shape alignment with filaments

We find that many galaxies show a misalignment between their minor axis and their spin. The misalignment is largest for elliptical galaxies. However, even disc-dominated objects which have a massive bulge fraction can show some degree of misalignment. This results in a difference between the alignments of galaxy spin and minor axis with the filament.

Interestingly, we do find that the galaxy minor axis–filament alignment is largely mass independent. We also find that ellipticals show a larger degree of orthogonal alignment than spirals. On the other hand, there is no significant evidence for a preferential alignment of the minor axis of spiral galaxies with the spine of filaments.

Perpendicular versus parallel filament galaxies

To study the processes responsible for the galaxy–filament alignment, we split our sample according to the galaxy minor axis–filament misalignment angle. We have selected the 20% of the population with the closest to perpendicular orientations as well as an equal fraction with the closest to parallel orientations. We find that galaxies with a perpendicular orientation relative to their filament are much better aligned with their host halo than the population as a whole. In contrast, galaxies parallel to their filament are poorly aligned with their halo.

This suggests that the same processes that affect the galaxy–filament alignment are at least partially responsible for the galaxy–halo alignment too. One such factor could be the coherence over long periods of time of the cosmic web around a halo/galaxy. Objects embedded in such filaments experience anisotropic infall along the same time-independent directions (van Haarlem & van de Weygaert 1993b). Such objects are expected to have a better alignment between haloes and the galaxies they harbour, as well as with their host filaments. On the other hand, in a rapidly changing environment objects experience anisotropic infall directions that vary with time, implying a higher degree of misalignment (see e.g. van Haarlem & van de Weygaert 1993b).

Summary

To summarise, we have studied the present day alignments of the shapes and spins of haloes and galaxies with their host filament in the EAGLE simulation. This represents a first step towards understanding the processes that determine these alignments with the large-scale cosmic web.

The alignments we have studied are weak and to properly characterize them we need a large sample of galaxies. This is difficult with current hydrodynamics simulations, which typically follow relatively small cosmological volumes. Thus, it is critical to expand the study to larger simulations, such as Illustris300 which has a 27 times larger volume than EAGLE (Pillepich et al. 2018), and to robustly quantify secondary trends, such as the dependence of the alignment signal on filament properties. In parallel with this approach, we also need to understand how the alignments vary in time. In particular, it is critical to follow the evolution of individual haloes and galaxies and understand what factors affect their alignment with the filament axis. This is the subject of the next chapter.

Acknowledgements

We are grateful to Bernard Jones, Enn Saar and Noam Libeskind for many encouraging and insightful discussions, several of which formed the inspiration for the present study. We also thank the anonymous referee for their astute comments and suggestions. PGV thanks the Institute of Computational Cosmology (ICC) in Durham and the Leibniz Institute for Astrophysics in Potsdam for their support and hospitality during several long work visits during which a major share of the work for this study was carried out. Also, RvdW thanks the ICC for its hospitality and support during several short work visits. MC and CSF were supported by the Science and Technology Facilities Council (STFC) [grant number ST/I00162X/1, ST/P000541/1] and by the ERC Advanced Investigator grant, DMIDAS [GA 786910]. ET acknowledges the support of the ETAg grants IUT26-2, IUT40-2, and of the European Regional Development Fund (TK133, MOBTP86). This work used the DiRAC@Durham facility managed by the Institute for Computational Cosmology on behalf of the STFC DiRAC HPC Facility (www.dirac.ac.uk). The equipment was funded by BEIS capital funding via STFC capital grants ST/K00042X/1, ST/P002293/1, ST/R002371/1 and ST/S002502/1, Durham University and STFC operations grant ST/R000832/1. DiRAC is part of the National e-Infrastructure.

4

Halo spin evolution

Punyakoti Ganeshaiah Veena[ab], Marius Cautun[cd], Rien van de Weygaert[a], Elmo Tempel[b] and Carlos S. Frenk[c]

[a] Kapteyn Astronomical Institute, University of Groningen, PO box 800, 9700AV, Groningen
[b] Tartu Observatory, University of Tartu, Observatooriumi 1, 61602 Tõravere Estonia
[c] Institute for Computational Cosmology, Department of Physics, University of Durham, South Road, Durham DH1 3LE, UK
[d] Leiden Observatory, Leiden University, PO Box 9513, NL-2300 RA Leiden, the Netherlands

Submitted to the MNRAS journal on July 18th 2020.

Abstract

We explore the evolution of halo spins in the cosmic web using a very large sample of dark matter haloes in the ΛCDM Planck-Millennium N-body simulation. We use the NEXUS+ multiscale formalism to identify the hierarchy of filaments and sheets of the cosmic web at several redshifts. We find that at all times the magnitude of halo spins correlates with the web environment, being largest in filaments, and, for the first time, we show that it also correlates with filament thickness as well as the angle between spin-orientation and the spine of the host filament. For example, massive haloes in thick filaments spin faster than their counterparts in thin filaments, while for low-mass haloes

the reverse is true. We also have studied the evolution of alignment between halo spin orientations and the preferential axes of filaments and sheets. The alignment varies with halo mass, with the spins of low-mass haloes being predominantly along the filament spine, while those of high-mass haloes being predominantly perpendicular to the filament spine. On average, for all halo masses, halo spins become more perpendicular to the filament spine at later times. At all redshifts, the spin alignment shows a considerable variation with filament thickness, with the halo mass corresponding to the transition from parallel to perpendicular alignment varying by more than one order of magnitude. The environmental dependence of halo spin magnitude shows little evolution for $z \leq 2$ and is likely a consequence of the correlations in the initial conditions or high redshift effects.

keywords: large-scale structure of Universe - galaxies: halos - methods: numerical

4.1 Introduction

Understanding the effects of the large-scale cosmic web on small-scale phenomena such as the growth of haloes and galaxies still remains an important open question in cosmology and galaxy formation. Besides small-scale processes such as AGN and supernovae, which have the largest impact on galaxy evolution, there is increasing evidence that processes on larger scales also play a role (e.g. Dressler 1980; Ball, Loveday & Brunner 2008; Lewis et al. 2002; van de Weygaert et al. 2011; Beygu et al. 2016; Pandey & Sarkar 2017). Although the imprint of large scale on galaxy growth can be subtle, it needs to be studied such that we obtain a comprehensive understanding of galaxy formation and cosmology. One of the prominent manifestations is the spin acquisition of haloes and galaxies and its connection to the cosmic web, which is yet to be completely understood. This represents the subject of this work.

According to the classical Tidal Torque Theory (TTT), angular momentum growth of a proto-halo is due to the large-scale tidal field. When the moment of inertia tensor of a proto-halo is misaligned with the surrounding tidal field, it experiences a torque and hence starts spinning. This was first suggested by Hoyle (1949) and later studied in detail by Peebles (1969); Doroshkevich (1970b); White (1984). The same tidal field is responsible for the anisotropic gravitational collapse of density fluctuations (Peebles 1980; Zel'Dovich 1970; Icke 1973; van de Weygaert & Bond 2008b; Desjacques 2008) that result in the large-scale structure of the Universe, known as the cosmic web (e.g. Bond,

Kofman & Pogosyan 1996; van de Weygaert & Bertschinger 1996a; van de Weygaert & Bond 2008b). The web represents the complex and hierarchical pattern seen in the large-scale distribution of matter, haloes, and galaxies, and consists of an intricate cellular structure composed of clusters, filaments, sheets and voids. The hierarchical nature of structure formation leads to numerous correlations between the spins of dark matter (DM) haloes and the cosmic web the haloes reside in. If the moment of inertia of a proto-halo and the surrounding tidal field are independent, then TTT predicts that the angular momentum of a halo is on average largest along the axis of second collapse (Lee & Pen 2001; Jones & van de Weygaert 2009), which is perpendicular to the filament spine and within the plane of the wall in which the halo is embedded. However, within the standard cosmological model the moment of inertia of a protohalo and the surrounding tidal field are in-fact correlated (Lee & Pen 2000; Porciani, Dekel & Hoffman 2002a,b) and this, in turn, affects the orientation of halo spins. Porciani, Dekel & Hoffman (2002a) have shown that when accounting for the correlation between the inertia tensor and the initial tidal field, TTT predicts roughly equal alignment of the halo spin with the second and third eigenvectors of the initial tidal field.

One manifestation of the effect of tidal fields on halo and galaxy spins is the alignment of the spin with the orientations of the cosmic web component in which the galaxies and haloes reside. This correlation has been detected in both cosmological simulations and observations and it is a subject of active research in recent times due to a surge of available data. For example, cosmological simulations have found that there is a mass dependent alignment trend between halo spin and filament axis, with low-mass haloes having a propensity for parallel alignment with the filament axis and massive haloes spinning preferentially perpendicular to the filament axis (e.g. Aragón-Calvo et al. 2007b; Aragón Calvo 2007; Hahn et al. 2007a; Trowland, Lewis & Bland-Hawthorn 2013; Codis et al. 2012; Codis, Pichon & Pogosyan 2015; Libeskind et al. 2012; Forero-Romero, Contreras & Padilla 2014; Wang et al. 2011; Wang & Kang 2017, 2018b; Codis et al. 2018; Welker et al. 2014; Ganeshaiah Veena et al. 2018, 2019). This mass dependent alignment is well described by the Lee (2019) phenomenological model. The mass at which the halo spin alignment changes from preferentially parallel to preferentially perpendicular is known as the transition mass. While most studies have reported this transition in spin alignments, the value of the transition mass can vary by more than an order of magnitude between different studies. This is because the transition mass depends on the nature of filaments, with the transition mass being higher in thicker filaments (this has been explicitly shown in Ganeshaiah Veena et al. 2018). The filamentary network can vary between different web finders and this will be manifest as a different transition mass for the spin–filament alignment

(e.g. see Ganeshaiah Veena et al. 2018, 2019). The same effect is responsible for the transition mass varying with the smoothing scale used to identify the cosmic web (e.g. Codis et al. 2012; Aragon-Calvo & Yang 2014; Forero-Romero, Contreras & Padilla 2014).

Similar to haloes, the galaxies also show a mass dependent alignment between their spins and their host filaments. This has been shown in hydrodynamical simulation (e.g. Dubois et al. 2014; Welker et al. 2014; Wang et al. 2018b; Ganeshaiah Veena et al. 2019; Kraljic, Davé & Pichon 2020) and also in observations. The first robust observational evidence was provided by the Tempel, Stoica & Saar (2013) and Tempel & Libeskind (2013b) who have shown that the spins of spiral galaxies are preferentially aligned with the filament axis while the minor axis of elliptical galaxies, which are typically higher mass, is preferentially perpendicular to the filaments axis (see also Jones, van de Weygaert & Aragón-Calvo 2010; Hirv et al. 2017). The same trend, although at a lower statistical significance due to the smaller sample, is seen when inferring the spin from the stellar or gaseous velocity maps, such as those obtained using SAMI or MaNGA (Krolewski et al. 2019; Welker et al. 2020; Blue Bird et al. 2020)

The present day alignment between halo and galaxy spin and their filaments is different from that predicted by TTT. For example, as we just discussed, the high-mass haloes have a propensity for perpendicular spin while TTT predicts a parallel alignment. This can be seen also when studying the spin–filament alignment at different redshifts, which changes in time (e.g. Codis et al. 2012; Wang & Kang 2017; Wang et al. 2018b). It indicates that the spin orientation is affected by non-linear processes (TTT is valid in the linear regime) and that one of the manifestation of these processes is reflected in the spin–filament alignment and how it depends on halo, galaxy, and filament properties. This represents one of the key questions in the field, and multiple ideas have been put-forth to explain it, such as: major merger events, vorticity generation inside filaments, formation and eventual migration of the halo into filaments and sheets, anisotropic accretion, and the connectivity of filaments (Codis et al. 2012; Libeskind et al. 2013; Wang & Kang 2018b; Welker et al. 2014; Laigle et al. 2015; Forero-Romero, Contreras & Padilla 2014; Ganeshaiah Veena et al. 2018, 2019). Besides being essential for understanding halo and galaxy formation, the spin–filament alignment can be used to test cosmology, such as constraining the neutrino mass (Lee, Libeskind & Ryu 2020).

In this work, we build upon the Ganeshaiah Veena et al. (2018) results, which investigated the halo spin–filament connection at $z = 0$, and study as a function redshift the properties of DM halo spins and how they relate to the web component in which the halo resides. The goal is to determine the signatures

of the non-linear processes that affect the halo spin growth and how these processes vary with the properties of the cosmic web. We do so by addressing the following questions:

1. Does the halo spin magnitude depend on the cosmic web environment in which the halo is located?

2. How does the halo spin–cosmic web alignment vary with cosmic time?

3. How does the spin–filament alignment vary with filament properties at different cosmic times?

4. Is the magnitude of the halo spin correlated to the spin–filament alignment angle?

To address these questions, we make use of a high resolution and large volume DM-only cosmological simulation, which allows us to identify the cosmic web in a representative region of the universe while also having resolved DM haloes over a wide range of masses. For each redshift of the simulation, we identify the population of haloes, defined as virialized collapsed regions, and the cosmic web. For the latter task, we use the NEXUS+ method (Aragón-Calvo et al. 2007a; Cautun, van de Weygaert & Jones 2013); this is a multiscale approach that returns a hierarchy of filaments and sheets: from thick structures connecting the nodes of the web to tenuous ones in mostly underdense regions. Then, at each redshift we associate to a halo the web morphology and the web orientation identified at the halo's location. We then proceed to study correlations in the magnitude and direction of the DM halo spins with a halo's web morphology.

In our previous work, Ganeshaiah Veena et al. (2018), we have studied the halo spin–filament alignment at z=0 and its dependence on filament properties, such as filament thickness. In this paper, we study the evolution of the spin alignment of halo populations at different redshifts and explore to what extent this evolution varies for haloes residing in different filamentary environments, as quantified in terms of filament width.

The layout of the paper is as follows: section 4.2 contains the details of the simulation, halo population and selection criteria used for the study; in section 4.3 we describe how the spin alignment analysis is carried out; section 4.4 studies the evolution of the halo spin alignment with filaments and walls; in section 4.5 we investigate the spin alignment in filaments of different thickness and how it varies with redshift; and finally, section 4.6 presents a short discussion and conclusions.

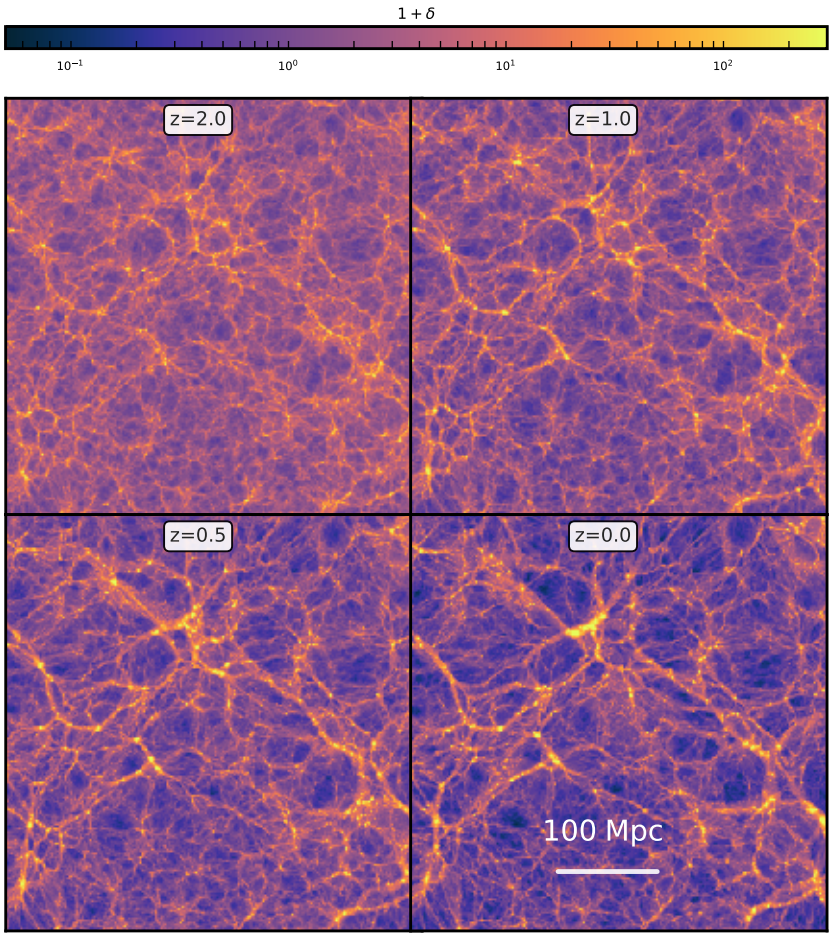

Figure 4.1 – ***Density field evolution:*** *The four panels show the density field of the P-Millennium simulation at different redshifts. Each plot is made using a slice of* $2.3h^{-1}$ Mpc. *The emergence of the cosmic web is clearly visible from these plots.*

4.2 Filament and halo population

In order to address the question we mentioned above, we require an N-body simulation with a large number of well-resolved haloes and a large box size that is representative of the universe. For these reasons, we use the Planck-Millennium simulation of structure formation in a ΛCDM cosmology.

4.2.1 P-Millennium simulation

The Planck-Millennium (or P-Millennium; McCullagh et al. 2017; Baugh et al. 2019) is a DM-only simulation of structure formation in a ΛCDM cosmology. It follows the evolution of 128 billion (5040^3) DM particles inside a 800 Mpc (542.16 h^{-1} Mpc) box. The large box size combined with the high resolution makes it ideal to explore the evolution of halo properties in the cosmic web. The simulation employs the Planck Collaboration et al. (2014) cosmological parameters and has a volume similar to the ground breaking Millennium simulation (Springel et al. 2005), hence the name Planck-Millennium. The cosmological parameters used by the simulation are as follows: density parameters, $\Omega_\Lambda = 0.693$ and $\Omega_\mathrm{M} = 0.307$, amplitude of the density fluctuations, $\sigma_8 = 0.8288$, and the Hubble parameter, $h = 0.6777$, where $h = H_0/100$ km s^{-1}Mpc^{-1} and H_0 is the Hubble's constant at present day.

The simulation was run from $z = 127$ to present day, $z = 0$. The initial conditions were generated using second order Lagrangian perturbation theory as described in Jenkins (2010). A total of 272 outputs or snapshots were generated, of which we have used four snapshots corresponding to $z = 2, 1, 0.5$ and 0.

Figure 4.1 is an illustration of the evolution of dark matter distribution from a redshift of 2 to 0 in the P-Millennium simulation. In this figure we plot the over-density given by

$$1 + \delta(\mathbf{x}, t) = \frac{\rho(\mathbf{x})}{\rho_u}, \tag{4.1}$$

where $\rho(\mathbf{x})$ and ρ_u denote the local and mean background density, respectively. We plot this to show the formation and evolution of the cosmic web. At $z = 2$, the web is in a nascent phase, with some filaments and sheets clearly visible, but in general with a low contrast between high and low density regions. With time, the majority of web elements collapse and form highly dense nodes, elongated filaments and sheets, and large underdense volumes, i.e. voids. In each stage of evolution, matter flows from low to high density regions, which increases the density contrast. Filaments act as rivulets that transport matter from walls and voids into the high density cluster regions (Aragón-Calvo, van de Weygaert & Jones 2010b; Cautun et al. 2014; Buehlmann & Hahn 2019).

The smaller filaments at high redshift coalesce to form a more prominent filamentary network at later times. This is very neatly captured by the NEXUS+ method (see Figure 21 in Cautun et al. 2014).

4.2.2 Halo population

Haloes are found by first identifying Friends-of-Friends (FoF) groups (Davis et al. 1985) using a linking length of 0.2 times the mean separation of dark matter particles (∼0.16 Mpc). Subsequently, the gravitationally bound haloes are identified using the SUBFIND algorithm (Springel et al. 2001). It first detects the subhaloes associated to the local dark matter density peaks and then discards the particles that are not gravitationally bound to these substructures. SUBFIND finds a hierarchy of subhaloes, with some being substructures of more massive subhaloes. For each FoF groups, the most massive object is defined as the main halo, and here we study only the main halos. The halo centre is given as the DM particle with the lowest binding energy.

In this paper, we present the results using only the main SUBFIND haloes and not the FoF groups. Since the FoF groups have multiple substructures linked together, the measurement of halo intrinsic spin may not be very meaningful in our context. In fact, we found that the spin distribution for FoF groups has a long tail of high values and that the spin distribution does not follow a log-normal distribution, especially at higher redshifts.

We define the halo mass, M_{200}, as the mass of all DM particles enclosed within the radius R_{200}. The R_{200} radius is that of a sphere centered at halo center whose mean enclosed density is 200 times the critical density of the universe. For the halo spin, we use the values calculated by SUBFIND, which consists of the angular momentum of all DM particles that are gravitationally bound to the halo. We use haloes with at least 300 DM particles, which are haloes with mass greater than $3.2 \times 10^{10} h^{-1} \mathrm{M}_{\odot}$. With this criteria we have about 1.13×10^7 haloes at $z = 0$ in the P-Millennium simulation. Out of this, the majority (51%) of haloes are in filaments.

4.2.3 Cosmic Web classification

To characterise the morphological elements of the cosmic web in the simulation, we apply the MMF/NEXUS+ (Aragón-Calvo et al. 2007a; Cautun, van de Weygaert & Jones 2013) method. The main feature of the method is that it identifies structures at all scales simultaneously based on the scale-space formalism. The multi-scale nature of the cosmic web is a consequence of the hierarchical structure formation and thus, to robustly identify all web elements, we need a multi-scale approach such as the one implemented within NEXUS+.

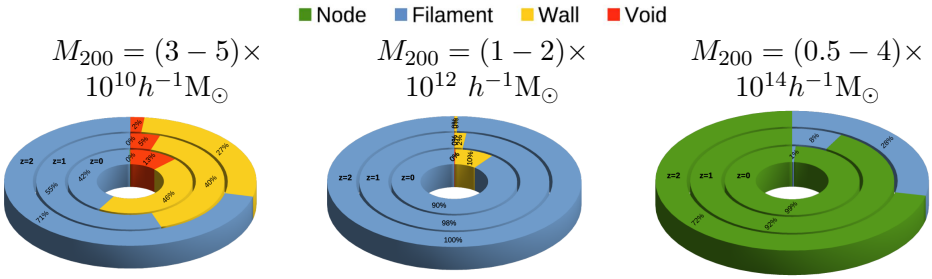

Figure 4.2 – ***Number fraction of haloes****: The panels show the fraction of main haloes in the different web environments. The outermost ring of the pie plot is for redshift $z = 2$, the middle and inner rings are for $z = 1$ and 0, respectively. The three panels show haloes of different masses: $(3.2-5)\times 10^{10}h^{-1}\mathrm{M}_\odot$ (left panel), $(1-2)\times 10^{12}h^{-1}\mathrm{M}_\odot$ (middle panel) and $(0.5-4)\times 10^{14}h^{-1}\mathrm{M}_\odot$ (right panel). The halo fraction in the various web environments varies rapidly with halo mass, with low-mass haloes residing mostly in filaments and walls, while high-mass ones are found mostly in nodes.*

The NEXUS+ method takes as input a density field on a regular grid; for this we use a 1024^3 grid (cell spacing of $0.53h^{-1}$ Mpc) and we calculate the density in each cell from the DM particle distribution using a nearest-grid-point assignment scheme. Then, the NEXUS+ algorithm consists primarily of four steps or stages. In the first stage, it calculates the logarithm of the input DM density field and smooths it with a Gaussian filter of different sizes. For implementing NEXUS+ on P-Millennium, we have used a series of filter scales, where each scale is a factor of $\sqrt{2}$ larger than the previous one. The smallest scale we consider is 0.5 h^{-1} Mpc (roughly the spacing of our grid cells), and the largest is 4.0 h^{-1} Mpc, which is the typical radius of the thickest filaments and walls (Aragón-Calvo, van de Weygaert & Jones 2010b; Cautun et al. 2014). Cautun et al. (2014) have shown that going to smaller smoothing scales does affect the properties of filaments for $z \leq 2$. This is the crux of the scale-space approach where the data is represented at different filtering scales in order to capture the strongest features at each scale.

In the second stage, the algorithm calculates the Hessian of the log-Gaussian filtered density field and obtains the eigenvalues of the Hessian matrix at every point. In the next stage, the eigenvalues ($\lambda_1 \leq \lambda_2 \leq \lambda_3$) and eigenvectors ($\mathbf{e_1}, \mathbf{e_2}$ and $\mathbf{e_3}$) are used to describe the local web morphology and orientation. The eigenvalues are used to calculate an environmental signature at each location. The exact calculation is a bit involved (see Eqs. 6 and 7 in Cautun, van de Weygaert & Jones 2013), but qualitatively NEXUS+ defines the environments as follows. Filamentary structure is characterised by the condition that

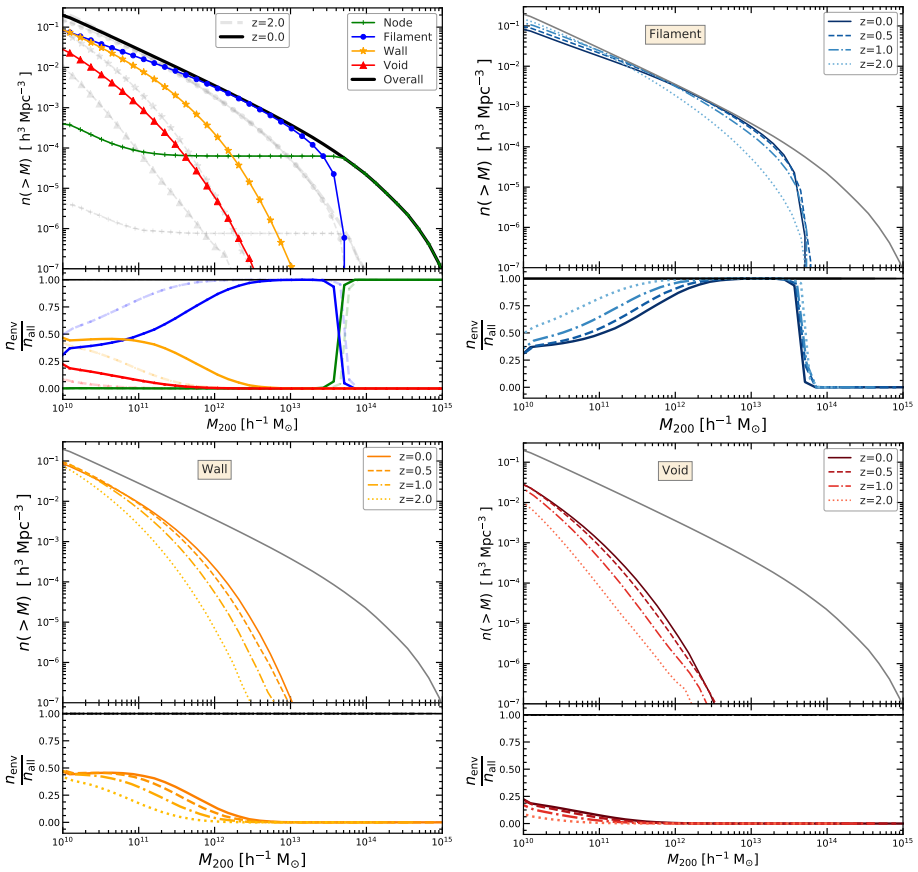

Figure 4.3 – ***Evolution of the halo mass function in the different web types:*** *The top-left panel shows the cumulative halo mass function in the different web environments for redshifts, $z = 0$ (coloured lines) and $z = 2$ (light grey lines). The various colours are for haloes in different cosmic web environments at $z = 0$. The differences of how haloes populate the various web environments are better captured in the bottom sub-panel, which shows the fraction of haloes in each web environment. The remaining panels show the halo mass function in filaments (top-right), sheets (bottom-left) and voids (bottom-right) at four redshifts: $z = 2, 1, 0.5$ and 0. For a sense of scale, the thin black line in each panel show the halo mass function for the full halo population at $z = 0$. Each panel has a bottom sub-panel that shows the fraction of haloes in that web type for the four redshifts.*

$\lambda_1 \simeq \lambda_2 < 0$ (matter is collapsing along two directions) and $|\lambda_2| \gg |\lambda_3|$ (the change in density along the third direction is small compared to the change along the other two directions). The filament spine is given by the eigenvector $\mathbf{e_3}$, as shown in Figure 4.4. A wall or sheet on the other-hand is characterised by $\lambda_1 < 0$ (collapse along one direction) and $|\lambda_1| \gg |\lambda_2| \simeq |\lambda_3|$ (the density hardly changes along the second and third directions). The eigenvector $\mathbf{e_{W1}}$ is the vector perpendicular to the plane of the wall as illustrated in the lower panel of Figure 4.4.

A web environment of a given thickness shows the largest signature when filtering the density on the same scale as the width of the structure. This motivates the third step of NEXUS+, which consists of combining at each position the environmental signature of all smoothing scales and keeping only the largest value.

The final step of the NEXUS+ method consists of identifying the regions that robustly can be characterized as being part of nodes, filaments, and walls. It consists of determining a threshold value for the environmental signature. For example, all regions with filament signatures larger than the threshold are identified as filaments. For nodes, the threshold is determined by requiring that at least half of the nodes are virialised, that is their mean density is at least the virial value (see Bryan & Norman 1998). For filaments and walls the detection threshold is decided automatically from the variation in the properties of the filamentary and wall network with environment signature (see appendix A in Cautun, van de Weygaert & Jones 2013). The regions that are not classified as nodes, filaments, or walls, are defined as voids.

Here we study the cosmic web from redshift, $z = 2$, to present-day. To do so we analyze one at a time the snapshots of the P-Millennium simulation corresponding to $z = 2, 1, 0.5$ and 0, i.e. we apply NEXUS+ and cross-correlate with the halo catalogue separately for each snapshot. In principle, we may extend our study to even higher redshifts, however doing so comes with practical difficulties. The typical width of filaments and sheets decreases rapidly with redshift (Cautun et al. 2014) and to robustly trace them at higher redshifts we need to calculate the cosmic web using a finer grid. Currently, we use a 1024^3 grid with a grid spacing of $0.53h^{-1}$ Mpc; further increasing the number of grid cells leads to a higher computational cost and especially RAM requirement.

4.2.4 Evolution of halo mass function

A simple way to quantify the effect of the cosmic web onto the halo population is to study how the halo mass function varies with web environment. Figure 4.2 shows the evolution of number fraction of haloes in different web environments for three halo mass ranges. The fraction of low-mass haloes in filaments is

high at $z = 2$ and decreases towards the present day, with the remaining haloes being mostly located in sheets and, a small fraction, in voids. A similar trend is observed for the intermediate mass haloes, $M_{200} \sim 1 \times 10^{12} h^{-1}\mathrm{M}_{\odot}$, but in this case only a small fraction ($< 10\%$) is found in sheets and hardly any inside voids or nodes. At even higher masses, most haloes are found in nodes and only a small fraction in filaments.

The fraction of haloes in different web environments varies strongly with halo mass, as illustrated in Figure 4.2. To have a comprehensive view of this dependence, in the top-right panel of Figure 4.3 we show the cumulative number density of haloes, $n(> M_{200})$, as a function of halo mass, M_{200}, segregated by cosmic web type. To help with the interpretation of the plot, the bottom sub-panel shows the fraction of haloes in each web type. At present time, which is shown by the coloured lines, most haloes with $M_{200} > 5 \times 10^{13} h^{-1}\mathrm{M}_{\odot}$ represent the nodes of the web, while most of the lower mass haloes are found in filaments. Sheet haloes become an appreciable fraction of the population for $M_{200} < 1 \times 10^{12} h^{-1}\mathrm{M}_{\odot}$ and void haloes become important at even lower masses, $M_{200} < 1 \times 10^{11} h^{-1}\mathrm{M}_{\odot}$ (Cautun et al. 2014). Qualitatively, the picture is similar at $z = 2$ (light grey lines), but with fewer haloes for a given mass especially in sheets and walls.

To better quantify the change in halo population with redshift, the remaining panels of Figure 4.3 show the halo mass function in filaments, sheets and voids for the four redshifts we analyze in this paper. We typically find that at fixed halo mass we have more haloes in a given environment at $z = 0$ than at $z = 2$. This is the case for all web environments, except for filament haloes with $M_{200} < 1 \times 10^{12} h^{-1}\mathrm{M}_{\odot}$, in which case we observe the opposite trend. We also find that the halo mass function in sheets and voids increases the most towards present day, while for filaments the change is more modest. This makes sense, with filament haloes having formed earlier, and thus changing less, than their equal mass counterparts in sheets and voids.

In terms of halo fraction, we observe the following (see the bottom sub-panels for each panel in Figure 4.3). At the low-mass end, $M_{200} \leq 1 \times 10^{12} h^{-1}\mathrm{M}_{\odot}$, we find that at $z = 2$, more than 50% of the haloes are in filaments, followed by walls and voids regions. At the current time, this fraction is reduced in filaments and there is accordingly an increase in the wall and void fractions. The decrease in the number of low-mass filament haloes is because some objects merge to form more massive haloes at later times, hence we see a reduction in the low-mass end and increase in the high-mass end.

4.2.5 Characteristic halo mass

Structure formation in ΛCDM cosmologies proceeds hierarchically. Haloes build up by gradual merging of smaller haloes and the accretion of mass. The first object to emerge are low-mass haloes, which subsequently grow into ever more massive structures. When comparing the halo populations at different cosmic epochs, we need to take this process into account: an individual halo at a given redshift z is the product of the growth of a lower mass halo at higher redshift through merging and accretion. While in the present study we investigate the evolution of the entire halo population, we incorporate the hierarchical growth of individual haloes by means of a characteristic halo mass at each redshift.

A reasonable definition for the characteristic halo mass, $M^*(z)$, follows from the analytical description of the hierarchical process in terms of the Press-Schechter formalism (Press & Schechter 1974; Bond et al. 1991; Lacey & Cole 1993). It infers the expected number density, $n(M, z)$, of haloes of mass, M, at a redshift, z, assuming that structure emerges from an initial Gaussian density field and that mass clumps on a mass scale M would collapse if their linear extrapolated overdensity would surpass the threshold level for gravitational collapse (Gunn & Gott 1972). In most practical circumstances, the collapse threshold is taken as $\delta_c = 1.686$, which is the critical collapse overdensity of a spherical peak in an Einstein-de Sitter Universe (see eg. Sheth, Mo & Tormen 2001, for more realistic estimates).

The Press-Schechter mass function typically consists of a power-law low-mass wing that diverges to low masses, with an exponential cutoff that reflects the Gaussian nature of the initial fluctuations. The characteristics halo mass, $M^*(z)$, for this hierarchically evolving halo population is the exponential cutoff mass. It is the scale at which the field variance $\sigma(M)$ on mass scale M is equal to the critical linear over-density of gravitational collapse,

$$\sigma(M^*) \sim \delta_c \approx 1.686\,. \tag{4.2}$$

In a sense, it is the mass scale at which the average density peak in the primordial mass distribution undergoes gravitational collapse.

For a given (linearly extrpolated) power spectrum, $P(k, z)$, the mass variance $\sigma(M, z)$ is

$$\sigma^2(M, z) = \int_0^\infty \frac{dk}{2\pi^2}\, P(k, z)\, \tilde{W}_{TH}^2(\mathbf{k}R)\, k^2, \tag{4.3}$$

Table 4.1 – ***Characteristic halo mass,*** $M^*(z)$.

Redshift	$M^*(z)$ [$h^{-1}\mathrm{M}_\odot$]
0.0	4.3×10^{13}
0.5	1.4×10^{12}
1.0	6.0×10^{12}
2.0	5.9×10^{11}

where $\tilde{W}_{TH}(\mathbf{k}R)$ is the Fourier transform of the (tophat) window function of radius R. This is the radius of the sphere that encloses the mass, $M = 4\pi/3\ \rho_u(z)R^3$, where $\rho_u(z)$ is the mean density of the Universe at epoch z.

The evolution of the characteristic mass is indicative of the hierarchical buildup of nonlinear structures. The increase of M^* with time reflects the buildup and emergence of more and more massive haloes in the evolving universe. We use the values of this characteristic "collapse mass", $M^*(z)$, as a means to assess in how far observed trends in the various processes may be ascribed to the hierarchical growth of individual halo masses with time and, hence, in how far additional processes may be involved. The typical values of $M^*(z)$ for 4 different redshifts, for the Planck Collaboration et al. (2014) power spectrum parameters, are listed in Table 4.1.

4.3 Analysis

4.3.1 Halo angular momentum

The angular momentum, $\mathbf{J}$, of a halo with N particles, is calculated as

$$\mathbf{J} = \sum_{k=1}^{N} m_k \left(\mathbf{r}_k \times \mathbf{v}_k\right), \tag{4.4}$$

where m_k, $\mathbf{r}_k$ and $\mathbf{v}_k$ are respectively the mass, position and velocity of the k^{th} particle with respect to the centre of the halo. We sum all the DM particles that are gravitationally bound to the SUBFIND main halo.

Spin parameter

Physically, it is more useful the express the amplitude of the angular momentum, $J = |\mathbf{J}|$, in terms of the spin parameter, λ. The λ parameter gives the

degree of coherent rotation of any self-gravitating system, in our case a DM halo. A value closer to unity implies that the halo is mostly supported by rotation while a low value means that the halo is dispersion supported.

The spin parameter was first introduced by Peebles (1969) and involves quantities, such as the energy of the system, that are rather involved to calculate. An alternative simpler version was introduced by Bullock et al. (2001, see Mo, van den Bosch & White 2010 for how this compares to Peebles' definition) and it is given by

$$\lambda = \frac{J}{\sqrt{2}MV_hR_h}, \tag{4.5}$$

where V_h is the circular velocity at the halo radius, R_h.

At $z = 0$ the spin parameter follows a log-normal distribution with a median value, $\langle\lambda\rangle \simeq 0.04$, and it hardly varies with halo mass (Bett et al. 2007); the same holds true also for the haloes in the P-Millennium simulation (Ganeshaiah Veena et al. 2018). This low value indicates that DM haloes are mostly dispersion supported rather than rotation supported. To compare, for disk dominated galaxies in hydrodynamical simulations that are supported by rotation, the median spin parameter is an order of magnitude higher (Ganeshaiah Veena et al. 2019).

4.3.2 Alignment analysis

We characterise the alignment between the halo angular momentum, $\mathbf{J}$, and its host environment orientation, $\mathbf{e_n}$, by the angle, $\theta_{\mathbf{J},\mathbf{e_n}}$, between the two vectors. Physically, it is better to express the alignment in terms of the cosine of the alignment angle, i.e. $\cos\theta_{\mathbf{J},\mathbf{e_n}}$, since in three dimensions the distribution of $\cos\theta$ between two randomly oriented vectors is uniform. We calculate the alignment as

$$\cos\theta_{\mathbf{J},\mathbf{e_n}} = \left|\frac{\mathbf{J}\cdot\mathbf{e_n}}{|\mathbf{J}||\mathbf{e_n}|}\right| . \tag{4.6}$$

We take the absolute value of the dot product since filaments have an orientation and both $\mathbf{e_3}$ and $-\mathbf{e_3}$ are valid and equivalent for our case. If a halo spin points along the direction of the cosmic web, then the cosine value is close to one whereas if the halo spin is nearly perpendicular then the value of the cosine is close to zero. If there is no alignment, i.e. the two vectors are randomly oriented, then the distribution of $\cos\theta_{\mathbf{J};\mathbf{e_n}}$ is uniform between 0 and 1. Any deviation from this expectation reflects the deviation from isotropic distribution or random alignment.

We are calculating alignment angles with respect to all the three preferential axes of the cosmic web. For filaments, we denote the three orientations with

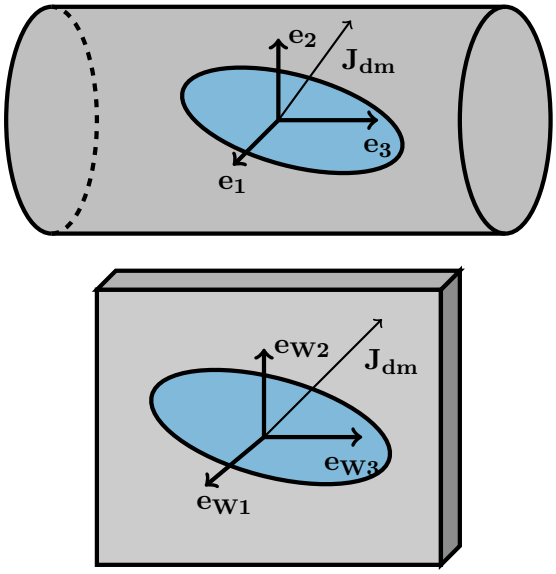

Figure 4.4 – ***Schematic of filament, wall and halo:*** *Top panel: the cylinder represents a typical cosmic filament whose principal axes are given by the* $\mathbf{e_1}$, $\mathbf{e_2}$, *and* $\mathbf{e_3}$ *orthogonal vectors, which correspond respectively to the axes of first, intermediate and last collapse. In particular,* $\mathbf{e_3}$ *gives the filament spine. The blue ellipse represents a halo embedded in the filament whose spin points along,* $\mathbf{J_{dm}}$. *Bottom panel: shows a similar schematic but for walls. The rectangular cuboid with one edge much smaller than the other two represents a cosmic wall whose preferential axes are given by* $\mathbf{e_{W1}}$ *(perpendicular to the wall),* $\mathbf{e_{W2}}$ *and* $\mathbf{e_{W3}}$ *(within the plane of the wall).*

$\mathbf{e_1}$, $\mathbf{e_2}$, and $\mathbf{e_3}$. These are given by the eigenvectors of the Hessian matrix of the density field at that location and correspond to the direction of first, intermediate and last collapse, respectively. The principal axes and their configuration with respect to the mass distribution along the filament are highlighted in the top panel of Figure 4.4. Similarly for walls, we calculate the alignment with $\mathbf{e_{W1}}$, $\mathbf{e_{W2}}$ and $\mathbf{e_{W3}}$ (we use an additional W subscript to distinguish the walls from filaments). The wall principal axes also correspond to the three collapse direction, first, intermediate, and last, respectively, and are illustrated in the bottom panel of Figure 4.4.

4.4 Spin alignment evolution

We first present an overview of the distribution of halo spins at several redshifts, which is shown in the left-hand panel of Figure 4.5. At a each redshift, there is a distribution of halo spins that is well described by a log-normal distribution

(not shown here, e.g. see Bullock et al. 2001; Bett et al. 2007). The distribution of halo spins shows very small variations between different redshifts indicating that the average halo spin does not vary much with time. In the right-hand panel of Figure 4.5, we plot the time evolution of the median spin parameter for haloes segregated into filaments, walls and voids. Haloes residing in filaments consistently have a higher spin at all redshifts, followed closely by wall haloes, while voids have systematically lower rotation support. This is in accordance with the results in Ganeshaiah Veena et al. (2018) for redshift 0. This is also in agreement with the findings of Hahn et al. (2007b) who also have shown, using a different web finder, that filament haloes have a higher median spin at all times.

The dependence of halo spin on environment is the result of two processes. Firstly, within the TTT framework, the halo spin arises from the misalignment between the initial tidal field and the proto-halo mass distribution (e.g. White 1984; Lee & Pen 2000; Porciani, Dekel & Hoffman 2002a,b). The misalignment angle, the strength and anisotropy of the tidal field, and the ellipticity of the initial proto-halo can depend on environment (e.g. Codis, Pichon & Pogosyan 2015) and would naturally lead to a variation of the halo spin with the web environment. This potentially explains why haloes in filaments, which mostly correspond to the regions with strong tidal fields (van Haarlem & van de Weygaert 1993a), have higher spins than their void counterparts. Secondly, the deviations of halo spin growth from the TTT predictions depend on the environment, with haloes in higher density regions experiencing a lower growth than those in less overcrowded environments (López, Merchán & Paz 2019), and could explain why we find only a modest difference in median spin between filaments and wall environments.

4.4.1 Evolution of spin alignments in filaments

In Figure 4.6, we show the time evolution of the angle between halo angular momentum and filament axis. We plot its probability distribution function (PDF) for four mass bins (each shown in a different panel) and for the four redshifts studied here. Although the alignment angle has a wide distribution of all possible $\cos\theta$ values, i.e. from 0 to 1 (which corresponds to $\theta = 0$ to 90), it is significantly different from what is expected for a random or isotropic distribution. For example, the haloes in the lowest-mass bin show a preferential parallel alignment, that is an excess of spins with $\cos\theta \simeq 1$, which is very low at high redshift and increases towards present day. The second panel, for haloes in the mass range $(1-4) \times 10^{11} h^{-1}\mathrm{M}_{\odot}$, neatly illustrates the time evolution of the spin–filament alignment: a propensity for perpendicular configurations at $z = 2$ that transforms to an excess of parallel configurations at $z = 0$. The highest-mass haloes, shown in the two right-most panels, have preferentially

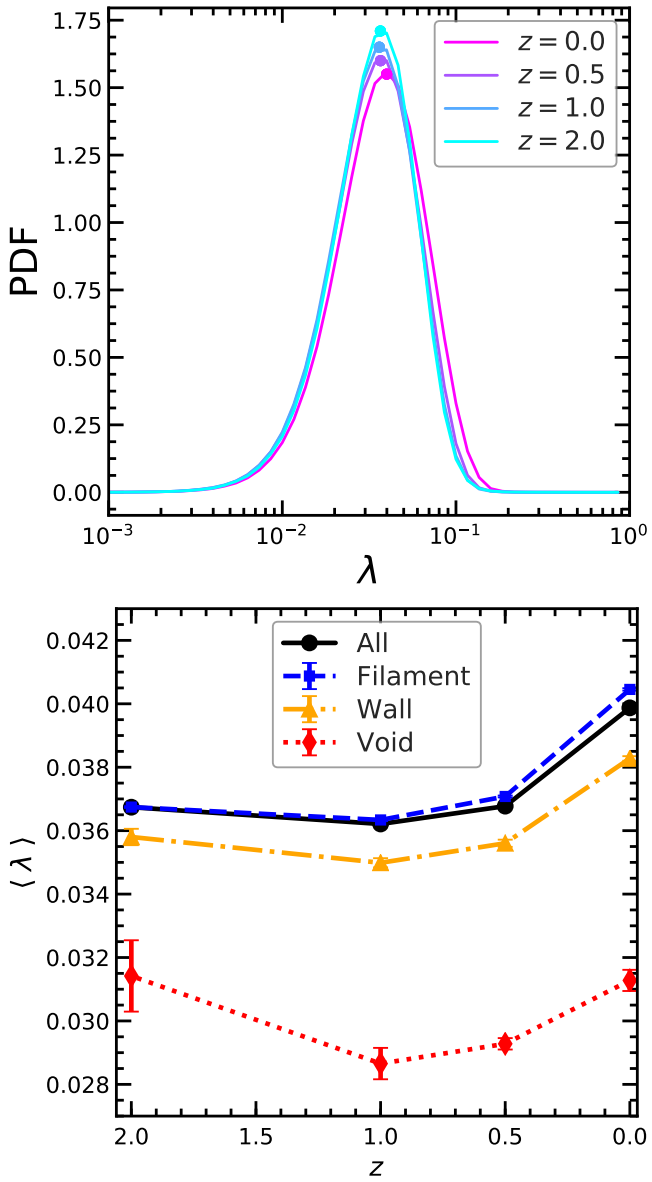

Figure 4.5 – ***The distribution of halo spins.*** *Top panel: shows the distribution of Bullock spin parameter for all haloes in the mass range* 3×10^{11} *to* $5 \times 10^{12} h^{-1} \mathrm{M}_{\odot}$ *at different redshifts. Bottom panel: shows the median spin parameter for the same haloes as a function of redshift (black solid line). The coloured lines show the median spin for haloes segregated according to their web environment. It shows that halo spin acquisition depends on the environment where a halo is located, with haloes spinning the fastest in filaments and walls.*

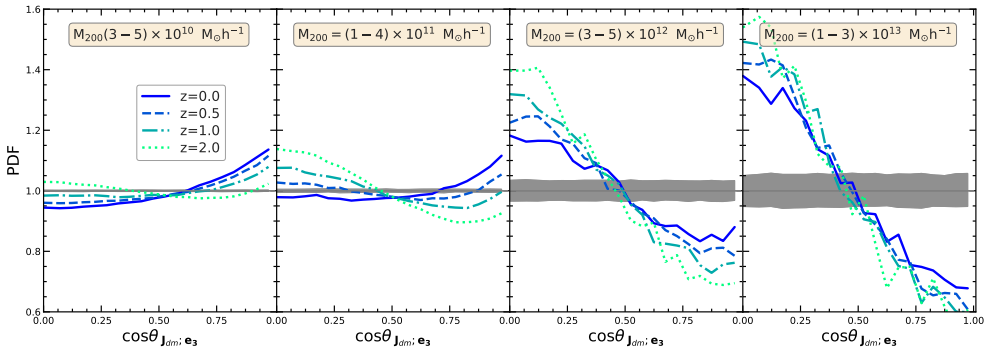

Figure 4.6 – ***PDF of the halo spin–filament alignment angle:*** *Each panel shows the distribution of the spin–filament alignment angle for haloes in different mass bins, with halo mass increasing from left to right (see upper text label in each panel). Coloured lines correspond to different redshifts (see the legend in the left-most panel). The grey horizontal line and its associated shaded region show respectively the mean expectation and the 68 percentile confidence interval when no alignment is expected. Low-mass haloes have an excess of parallel orientations (i.e. PDF is highest at* $\cos\theta = 1$*), while high-mass ones have a propensity for perpendicular orientations (i.e. the PDF is highest at* $\cos\theta = 0$*). The transition halo mass between the two regimes varies with redshift.*

perpendicular spins at all times, although this excess decreases slightly with time.

The large number of haloes in our sample allows us to measure very precisely the PDF of the halo spin alignment. This reveals a very interesting find, that is most easily visible in the $z \geq 0.5$ curves shown in the second panel of Figure 4.6. Those PDF show a weak, but statistically robust, bi-modality: there is an excess of haloes with $\cos\theta < 0.2$ and also an excess of haloes with $\cos\theta > 0.8$ (at least compared to haloes with $\cos\theta \sim 0.7$). To our knowledge, this is the first time a bi-modality in the alignment angle has been detected. It suggests that there are at least two processes (or classes of processes) that affect the evolution of the halo spin–filament alignment. The first class of phenomena generates preferentially perpendicular alignment, i.e. $\cos\theta \sim 0$, while the second one produces mainly parallel alignments. In general, one of the two effects is dominant, such as for low-mass haloes at $z \leq 1$ (left-most panel in Figure 4.6) or for high-mass haloes at all redshifts (right-most panel in Figure 4.6), and no obvious bi-modality can be observed. However, this bi-modality is easily seen for the halo sample that is in the process of changing alignment from preferentially perpendicular to preferentially parallel, when the

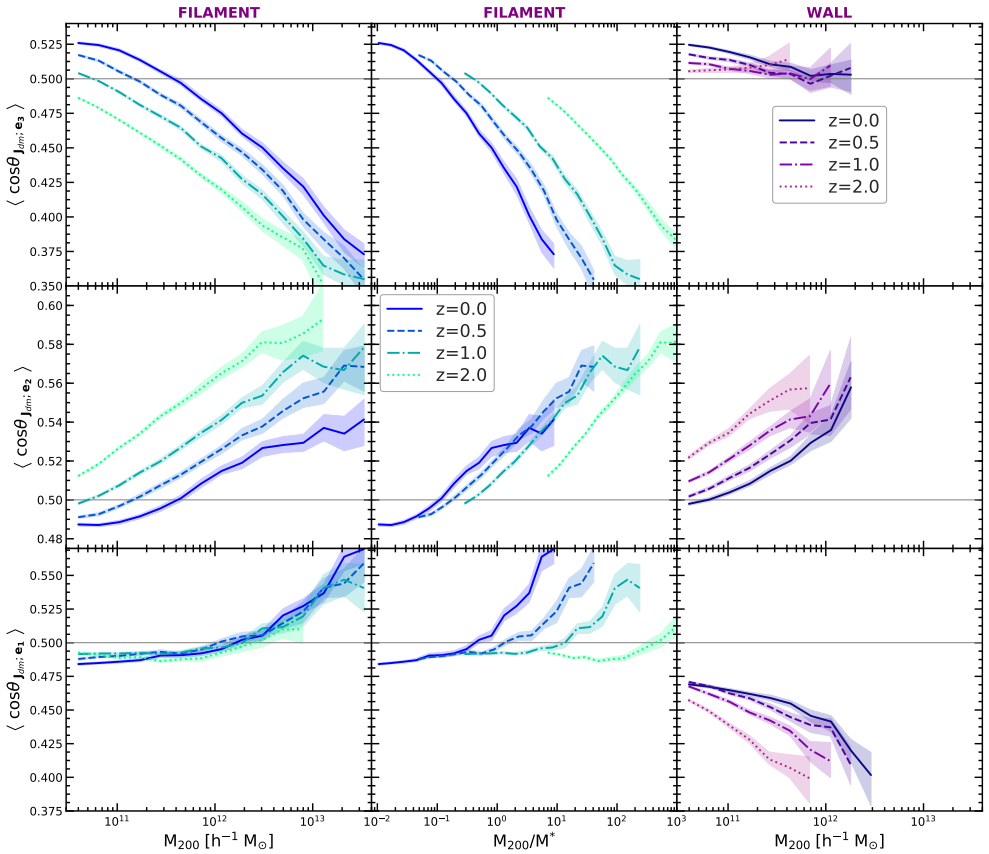

Figure 4.7 – ***The evolution of halo spin alignment in filaments and walls:*** *It shows the median alignment angle, $\cos\theta$, between the spins of haloes and the principal axes of their environment. The median angle is plotted as a function of halo mass (left- and right-hand columns) and halo mass normalised by the characteristic mass, $M^\star$, at each redshift (middle column). The first two columns are for filament haloes and the right-hand column is for wall haloes. The rows correspond to three environment principal axes: :* $\mathbf{e_3}$ *is the axis of last collapse (top row),* $\mathbf{e_2}$ *is the axis of second collapse (middle row), and* $\mathbf{e_1}$ *is the axis of first collapse (bottom row). The various colors and linestyles represent haloes at different redshifts, and the shaded region indicates the 1σ uncertainty when determining the median alignment angle.*

two classes have a roughly equal impact on the alignment of halo spins.

As we have seen in Figure 4.6, the spin–filament alignment varies with halo mass. To more clearly illustrate this dependence, we study in the left-hand panels of Figure 4.7 the median alignment angle and its time evolution. We study the spin alignment not only with the filament spine, denoted with $\mathbf{e_3}$, but also with the other two principal axes: $\mathbf{e_2}$ and $\mathbf{e_1}$.

The top-left panel of the figure shows the alignment with the filament spine, $\mathbf{e_3}$, and clearly illustrates that this alignment varies with both redshift and halo mass. A higher fraction of haloes have perpendicular spin orientations at: i) high redshift when comparing equal mass objects, or ii) at higher halo masses when comparing objects at the same redshift. In particular, for most redshifts we find a transition from an excess of perpendicular alignments for massive haloes to a propensity for parallel alignments at low halo masses. The mass at which this transition takes place decreases with redshift. For $z = 2$, this transition probably takes places at halo masses below $3 \times 10^{10} h^{-1} \mathrm{M}_{\odot}$, which is the lowest halo mass well resolved by our simulation.

The middle-left panel of Figure 4.7 shows the spin alignment with the axis of second collapse, $\mathbf{e_2}$, for filament haloes. Here we find an excess of parallel spin alignments, that increases with halo mass. In particular, we find a transition from parallel alignment at high masses to perpendicular alignment at low masses, with the transition mass being very close to the transition mass found for the alignment with the $\mathbf{e_3}$ filament axis. The bottom-left panel of Figure 4.7 shows the alignment with $\mathbf{e_1}$, which is the direction of first collapse. This is rather interesting since it shows hardly any evolution with redshift, although we do find a trend with halo mass that is weaker than the one found for $\mathbf{e_3}$ or $\mathbf{e_2}$.

Thus, at fixed mass, the angular momentum of haloes is changing only in the $\mathbf{e_3} - \mathbf{e_2}$ plane and stays roughly at the same angle with respect to $\mathbf{e_1}$, which corresponds to a precession of the spin around the $\mathbf{e_1}$ axis. However, we note that the mass of a halo increases with time, so when comparing equal mass haloes at different redshifts we are not comparing the same objects at different epochs. This observation suggests that the spin–$\mathbf{e_1}$ alignment varies as the halo grows but in such a way that the spin alignment of the resulting halo is on average the same as for an equal mass halo at an earlier redshift.

The halo mass growth with redshift can be accounted for by normalizing the halo masses by the characteristic mass, $M^{\star}$, at each redshift. In a certain sense, this is equivalent to following the growth of individual haloes back in time. In the middle column of Figure 4.7, we show the evolution of the median alignment after this scaling. If the spin alignment evolution was purely a consequence of

the halo mass growth, this should have shifted the curves at different redshifts to overlap each other, however this is not the case. At fixed $M_{200}/M^{\star}$ values, we find that the halo spin evolves towards a more perpendicular alignment with the $\mathbf{e_3}$ axis at late times (see also Trowland, Lewis & Bland-Hawthorn 2013; Wang & Kang 2018b). This is to be expected since at early times proto-halo spins are predominantly aligned with the $\mathbf{e_3}$ principal axis of the tidal field (Porciani, Dekel & Hoffman 2002a; López & et al. 2020), and thus nonlinear spin acquisition (i.e. that is not captured by TTT) leads to the halo spins reorienting themselves such that they are more likely to be perpendicular to the filament spine, $\mathbf{e_3}$. Interestingly, at fixed $M_{200}/M^{\star}$ values, the spin alignment with the $\mathbf{e_2}$ axis hardly changes with time, especially for $z \leq 1.0$. This suggests that at late times the spin reorientation proceeds on average as a precession around the $\mathbf{e_2}$ filament axis.

4.4.2 Evolution of spin alignments for wall haloes

We now study the evolution of halo spin alignments with the walls of the cosmic web. The anisotropy and strength of tidal fields in walls are different from those in filaments and we expect deviations from what we have found for filaments. The right-hand column of Figure 4.7 shows the median spin alignment for haloes in walls, where the rows correspond to the alignment with the wall principal axes: $\mathbf{e_{W3}}$, $\mathbf{e_{W2}}$, and $\mathbf{e_{W1}}$. The schematic of the three preferential axes of walls is given in Figure 4.4, where $\mathbf{e_{W1}}$ is the axis perpendicular to the plane of the wall, and $\mathbf{e_{W2}}$ and $\mathbf{e_{W3}}$ are along the plane of the wall.

The spin alignment of wall haloes is different from that of filament haloes, especially for the $\mathbf{e_{W3}}$ and $\mathbf{e_{W1}}$ axes. With respect to $\mathbf{e_{W3}}$, we find that the alignment is only weakly varying with halo mass and that haloes of all masses and at all redshifts are oriented preferentially along $\mathbf{e_{W3}}$. In particular, we do not find the transition from parallel to perpendicular alignment seen for filaments. In contrast, the alignment with $\mathbf{e_{W2}}$ depends on both halo mass and redshift, and it is nearly identical to that observed for filaments, except that the median $\cos\theta$ is slightly larger for walls than for filaments when compared at equal halo mass and redshift.

The spin alignment with $\mathbf{e_{W1}}$, which is the normal to the plane of the walls, is the most interesting and the one that shows the largest contrast with respect to the filament haloes. On average, wall haloes of all masses have their spin perpendicular to $\mathbf{e_{W1}}$, i.e. the spin is oriented predominantly within the wall plane. The excess of perpendicular configurations is largest at early times and more so for massive haloes. In contrast, most filament haloes have their spins along $\mathbf{e_1}$, especially for higher mass haloes.

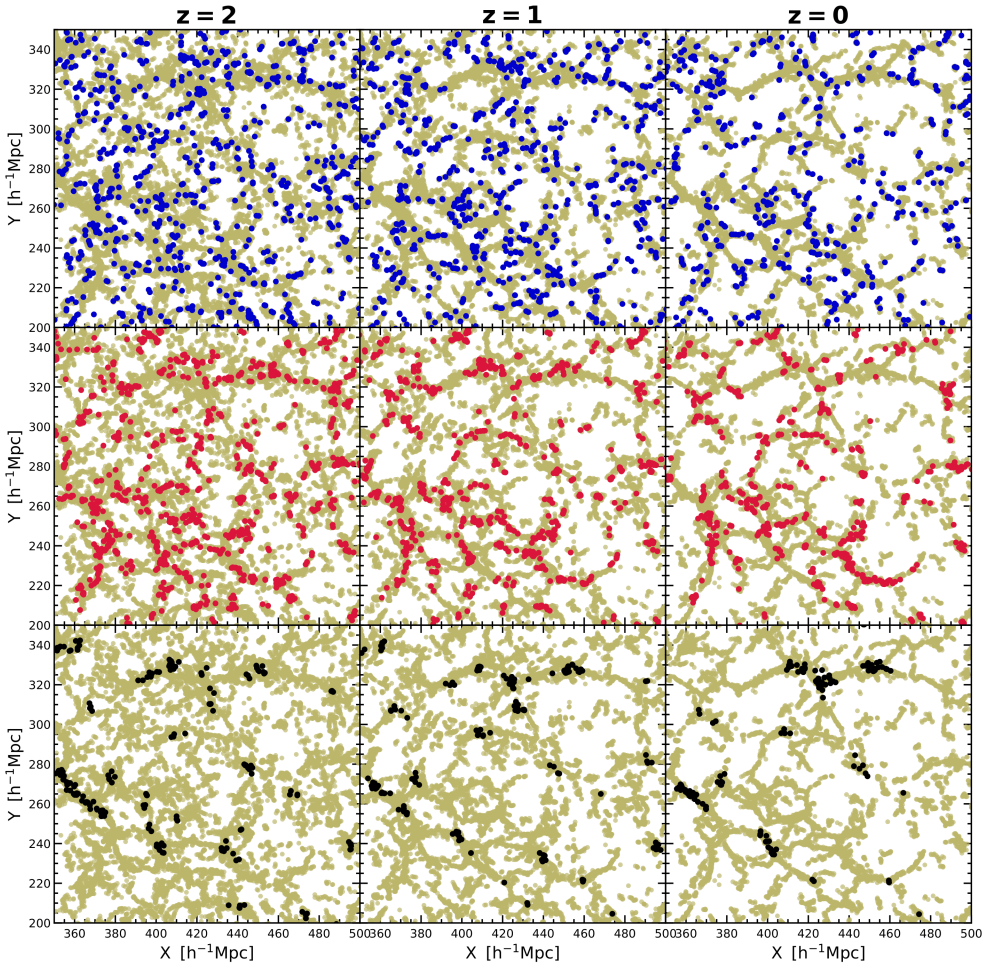

Figure 4.8 – ***Haloes in thin, medium, and thick filaments:*** *The top row: shows haloes in thin filaments ($D_{\rm filament} < 2\ h^{-1}$ Mpc) as blue dots and all the filament haloes in that slice as light green dots. From left to right, the panels show the same slice at $z = 2$, 1 and 0, respectively. The center row: shows the haloes in medium thickness filaments ($D_{\rm filament} \in [2, 4]\ h^{-1}$ Mpc) as red dots. The bottom row shows haloes in thick filaments ($D_{\rm filament} > 4\ h^{-1}$ Mpc) as black dots. On average, haloes in thin filaments (top row) are at the periphery of the filamentary network bordering the void regions, whereas haloes in thick filaments (bottom row) are mostly at the intersections of massive filaments. All panels show the same slice (at different redshifts) which has a comoving thickness of 4.5 h^{-1} Mpc. The x- and y-coordinates are also given in comoving units.*

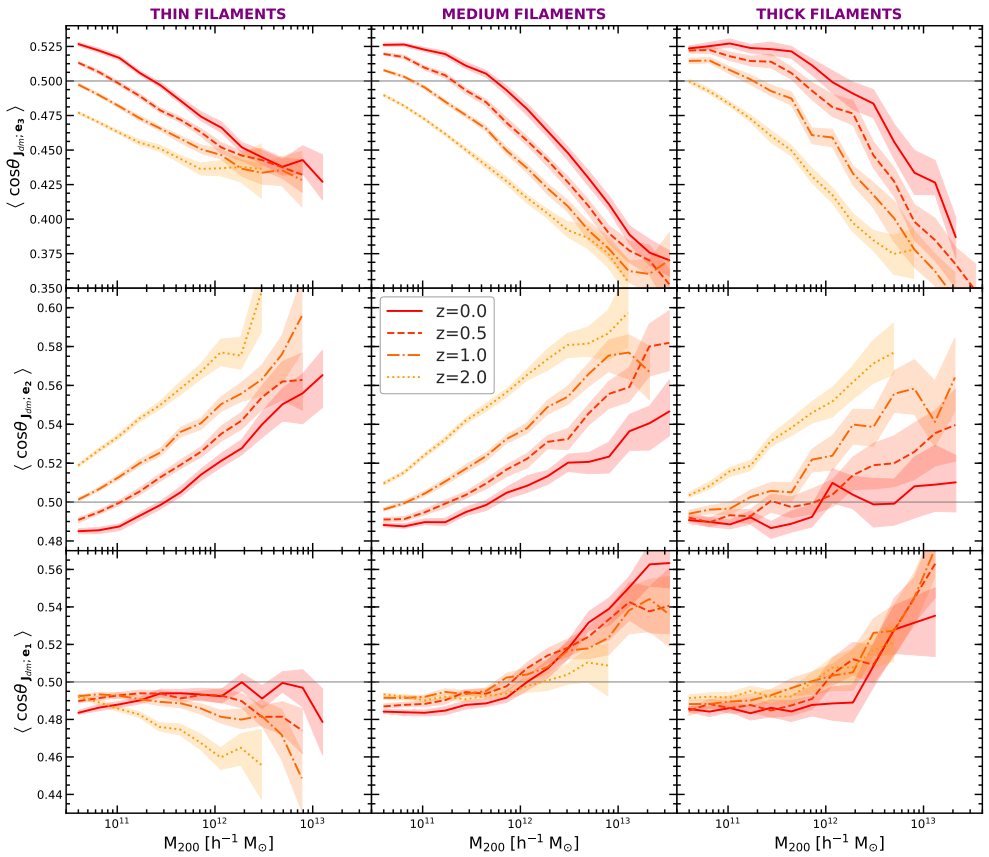

Figure 4.9 – ***Spin–filament alignment and its dependence on filament thickness:*** *The columns show the median alignment between halo spin and filament axes for three different filament subsamples: thin ($D_{\rm filament} < 2$ h^{-1} Mpc; left column), medium ($D_{\rm filament} \in [2, 4]$ h^{-1} Mpc; middle column), and thick ($D_{\rm filament} > 4$ h^{-1} Mpc; right column)). The rows show the alignment with the filament preferential axes (from top to bottom):* $\mathbf{e_3}$, $\mathbf{e_2}$, *and* $\mathbf{e_1}$. *This plot highlights that the spin-filament alignment and its redshift evolution depends on filament thickness.*

4.5 Filament thickness and spin alignments

The tidal field is responsible for the formation of the cosmic web and the growth of halo spin. Thus, the characteristics of the tidal field, such as its strength and degree of anisotropy, are expected to correlate with the properties of filaments and that of halo and galaxy spins. This correlation manifests itself as a dependence of spins on the nature of filaments, as pointed out by Ganeshaiah Veena et al. (2018) who have shown that spin alignments vary with filament thickness. Moreover, the environment of a halo affects the spin by determining the amount of matter and the anisotropic direction along which haloes and galaxies grow, thus potentially further enhancing the correlation between spins and the properties of the web element.

Here, we study the time dependence of spin alignments on the filament thickness in which the halo resides, which up to now has been studied only at $z = 0$ (Aragon-Calvo & Yang 2014; Ganeshaiah Veena et al. 2018). This begs the questions: Does the dependence of spin orientation on filament properties due to the recent non-linear spin growth or is it already imprinted in the initial conditions and thus predicted by TTT?

We calculate the filament thickness using the Cautun et al. (2014) approach, which represents a local estimate of the filament diameter, which we denote with $D_{\rm filament}$. The thickness is obtained by first determining the filament spine, and then by calculating the cross-section centred on the spine needed to enclose all the filament volume elements (i.e. grid cells used for determining the NEXUS+ web).

Following this, we define three sub-samples: **thick filaments** (with $D_{\rm filament} > 4\ h^{-1}$ Mpc), **medium filaments** (with $D_{\rm filament} \in [2, 4]\ h^{-1}$ Mpc) and **thin filaments** (with $D_{\rm filament} < 2\ h^{-1}$ Mpc). Properties of these three filament types, such as linear density and tangential mass profile are studied in detail in Cautun et al. (2014).

4.5.1 Halo distribution

In Figure 4.8 we show the physical distribution of haloes in the three filament sub-samples we just defined. The top-most panel shows haloes in thin filaments as blue dots and all the filament haloes of that slice as light green dots. Panels from left to right correspond to redshift 2, 1 and 0, respectively, and show the time evolution. In the central and lower panels, red and black dots show haloes in medium and thick filaments, respectively.

The three categories of haloes populate different regions of the filamentary network. Haloes in thin filaments are in the peripheral regions, bordering the main filamentary network. Some haloes are even located inside the much thinner

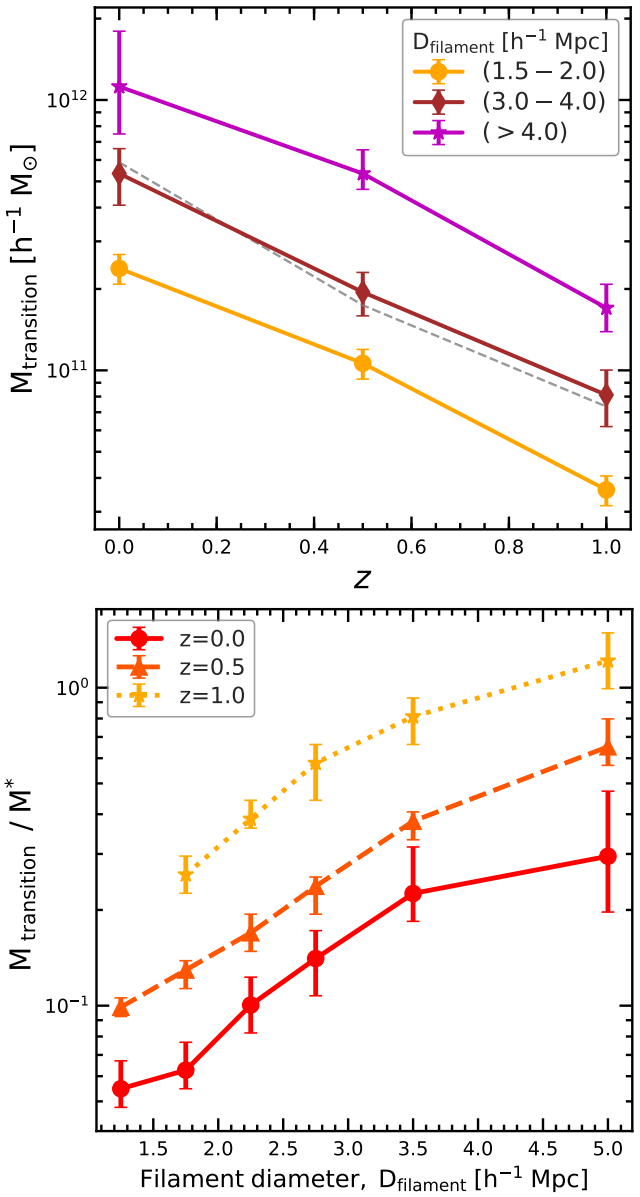

Figure 4.10 – ***Transition mass and filament diameter:*** *The top panel shows the redshift evolution of the spin alignment transition mass for filaments of different thickness (see plot legend). The grey dashed line shows the curve for* $(1+z)^{-3}$. *The bottom panel shows transition mass normalised by characteristic mass,* M^*, *as a function of filament diameter. Transition mass increases with filament diameter and also evolves with time.*

filamentary fabric within voids. Haloes in the medium filaments populate the main arteries of the filamentary network. Haloes in thick filaments shown in the lowest panel are usually closer to clusters, at the intersections of prominent filaments.

Since the haloes are located at distinct locations in the filamentary network, we expect them to have varied dynamical histories. For instance, haloes in the very thin filaments that are part of void regions are isolated from many dynamical processes such as major mergers. Hence, we expect them to retain the original tidal torque acquired during turn-around. At the intersections of the filamentary networks we expect the opposite, i.e, more mergers and accretion along many directions, whereas in the main arteries, we expect a more coherent transfer of mass and angular momentum onto the haloes. We expect these differences to manifest in their angular momentum growth, specifically in the eventual orientation of angular momentum.

4.5.2 Evolution of halo spin alignment and filament thickness

We now proceed to study the evolution of the spin-filament alignment for the three filament sub-samples we defined at the beginning of this section. The results are shown in Figure 4.9, where each row corresponds to the alignment with the preferential filament axes, $\mathbf{e_3}$, $\mathbf{e_2}$, and $\mathbf{e_1}$, and each column corresponds to thin, medium and thick filaments, respectively.

Figure 4.9 illustrates that the spin–filament alignment depends on the filament thickness and that this variation is seen at all redshifts. The size of the difference varies with halo mass and redshift. For example, for $\sim 10^{12}\ h^{-1}\mathrm{M}_{\odot}$ haloes at $z = 0$ we find that $\cos\theta_{\mathbf{J};\mathbf{e_3}}$ is lower for the thin filaments than for the thick ones. This means that haloes of that mass are more likely to have their spins perpendicular to the filament spine if they reside in thin filaments compared to if they would be in thick filaments. For the same $\sim 10^{12}\ h^{-1}\mathrm{M}_{\odot}$ haloes at $z = 0$ we also find that $\cos\theta_{\mathbf{J};\mathbf{e_2}}$ is larger for thin filaments than for thick ones, while $\cos\theta_{\mathbf{J};\mathbf{e_1}}$ shows very little variation with filament thickness.

In terms of redshift dependence, we see an evolution in the alignment with the $\mathbf{e_3}$ and $\mathbf{e_2}$ filaments axes, and a much weaker evolution in the alignment with the $\mathbf{e_1}$ axis. In thin filaments, at redshifts of 2 and 1, we do not find any spin transition from parallel to perpendicular as the majority of the haloes are spinning preferentially perpendicular with respect to $\mathbf{e_3}$. The spin transition is seen at later redshifts of 0.5 and 0. In medium and thick filaments, the transition is already seen at a redshift of 1. The fraction of preferentially parallel haloes increases with time and filament thickness at fixed halo mass. Similar observations can be made for the alignment with the $\mathbf{e_2}$ axis, but in this case the fraction of preferentially parallel haloes decreases with time at

Halo population (Filament type)	**Redshift** z	**Transition mass** M_{tr} [10^{11} $h^{-1}\mathrm{M}_{\odot}$]	**Cross-over mass** $M_{+}^{\perp \text{ vs. } \parallel}$ [10^{11} $h^{-1}\mathrm{M}_{\odot}$]	**Cross-over mass** $M_{+}^{\text{thick vs. thin}}$ [10^{11} $h^{-1}\mathrm{M}_{\odot}$]
All	0.0	3.8	2.3	3.1
	0.5	1.5	1.5	1.0
	1.0	0.6	0.7	0.7
Thin	0.0	2.3	1.8	–
	0.5	0.9	1.3	–
	1.0	–	0.6	–
Medium	0.0	5.4	2.3	–
	0.5	2.0	1.4	–
	1.0	0.8	0.7	–
Thick	0.0	10	7.0	–
	0.5	5.3	3.0	–
	1.0	1.7	1.1	–

Table 4.2 – *The values of transition and cross-over masses for various populations of filament haloes. Transition mass, M_{tr}, is the halo mass at which the halo spin–$\mathbf{e_3}$ alignment changes from preferentially parallel to preferentially perpendicular. The cross-over mass, which we discuss in subsection 4.5.4, describes our find that the median halo spin, $\langle\lambda\rangle$, is higher for massive haloes whose spin is perpendicular to their filaments than for those with parallel spins. However, for low-mass haloes the opposite is true, with the cross-over taking place at the mass, $M_{+}^{\perp \text{ vs. } \parallel}$. Similarly, high mass haloes in thick filaments have higher spins that those in thin filaments but the opposite is true for low-mass haloes, with the cross-over taking place at halo mass, $M_{+}^{\text{thick vs. thin}}$. We present results for all filament haloes and for haloes residing in filaments of different thickness: thin (with diameter, $D_f < 2\ h^{-1}$ Mpc), medium ($D_f = 2-4\ h^{-1}$ Mpc), and thick ($D_f > 4\ h^{-1}$ Mpc).*

fixed halo mass.

Compared to $\mathbf{e_3}$ and $\mathbf{e_2}$, evolution of the spin alignment with the $\mathbf{e_1}$ axis is not very prominent for all three filament sub-samples studied here. Especially at the low-mass end, there is hardly any time evolution with respect to $\mathbf{e_1}$. However, the high mass haloes in thin filaments do show a redshift evolution in their alignment with $\mathbf{e_1}$.

To summarise, we observe the dependence of spin–filament alignment on filament thickness at all redshifts studied here. This suggest that this trend, first pointed out in Ganeshaiah Veena et al. (2018), is not due to the recent and highly nonlinear process of spin growth. Instead, it suggests that this difference could have been in place since high redshift and potentially could indicate a systematic variation of the halo spin and its orientation on the local properties of the tidal field (the relevant properties are those that determine the filament thickness). In fact, for low mass haloes ($\lesssim 10^{11}\ h^{-1}\mathrm{M}_\odot$) we find that late time spin growth leads to less variation with filament thickness of the spin-filament alignment (see top and middle rows in Figure 4.9).

4.5.3 Transition mass: evolution and dependence on filament thickness

The mass at which the halo population goes from preferentially parallel to perpendicular is known as the transition mass, $M_{\mathrm{transition}}$. We plot in the left panel of Figure 4.10 the variation of this transition mass as a function of redshift for a selection of filament diameters. We study only the redshift range $z \leq 1$ since for $z = 2$, as we see in Figure 4.9, there is no transition from preferentially parallel to perpendicular alignments and hence, we cannot determine this mass (if it exits). This is likely due to the limited mass resolution of our simulation: we only resolve haloes with masses above $3 \times 10^{10}\ h^{-1}\mathrm{M}_\odot$. It remains to be studied using even higher resolution simulations whether $z = 2$ haloes show a spin alignment transition mass.

We find that the transition mass increases towards present-day and also with filament diameter. In particular, filaments of different thickness show the same qualitative behaviour of $M_{\mathrm{transition}}(z)$, with the only difference being the overall normalisation. It indicates that the evolution of $M_{\mathrm{transition}}$ is the same for all the three filament samples shown in the figure and that they are different only because they started from a different initial value.

This raises an important question: Is the evolution in the transition mass due to haloes growing in mass with time? To answer this, we study the transition mass normalised by the characteristic mass, $M^*(z)$, at each redshift, which is shown in the right panel of Figure 4.10. There, we show $M_{\mathrm{transition}}/M^*$ as

a function of filament thickness, with the three curves now corresponding to different redshifts. If the increase in transition mass was only because of halo growth, we would have expected the curves at different redshift to coincide when scaled by the characteristic mass. However, this is not the case since $M_{\rm transition}/M^*$ still changes with redshift. Interestingly, in this case we see a reversal of the trend, the normalized transition mass $M_{\rm transition}/M^*$ decreases with time. Therefore, the evolution of the transition mass is due to other secondary processes and not only halo mass growth.

4.5.4 Dependence of halo spin on filament thickness

We just have seen that the spin orientation of haloes depends on the filament thickness in which the haloes resides. Could the processes responsible for this trend also lead to systematic variations in the spin magnitude as a function of filament thickness? We explore this question in Figure 4.11, where we plot the median spin parameter (see section 4.3) as a function of mass, for haloes in thin and thick filaments. Note that in this section we are looking at the evolution of the median spin parameter, $\langle\lambda\rangle$, and not alignments.

At redshift 0 (left-most panel in Figure 4.11), we find that low-mass haloes in thin filaments have higher spins than their counterparts in thick filaments.

However, for massive haloes this trend is reversed and the spin is higher for haloes in thick filaments. The cross-over between the two regimes takes place at a mass of $3.1 \times 10^{11}\ h^{-1}{\rm M}_\odot$, which we refer to as the cross-over mass, $M_+^{\text{thick vs. thin}}$. The difference in $\langle\lambda\rangle$ between haloes in thin and thick filaments is small compared to the variance of the spin distribution (see Figure 4.5) but it is a robust result (i.e. difference is larger than the uncertainties due to the finite number of haloes; see shaded regions in the figure).

A similar dependence of median halo spin with filament thickness is seen at higher redshift too, as seen in the other three panels of Figure 4.11. The only difference is that the cross-over mass decreases with increasing redshift to the point that for $z = 2$ the cross-over, if any, is outside the mass range available in our simulation (the cross-over at $M{\sim}2 \times 10^{12}\ h^{-1}{\rm M}_\odot$ seen for $z = 2$ is consistent to noise and likely a spurious effect).

The values of the cross-over mass, $M_+^{\text{thick vs. thin}}$, at different redshifts are summarised in Table 4.2 and they indicate that this mass is roughly equal to the spin alignment transition mass at that redshift. This suggests that the same processes that are responsible for the transition in spin–filament orientation are likely to be the ones responsible for the dependence of halo spin magnitude on filament thickness. We will discuss some of these processes in our discussions section, section 4.6.

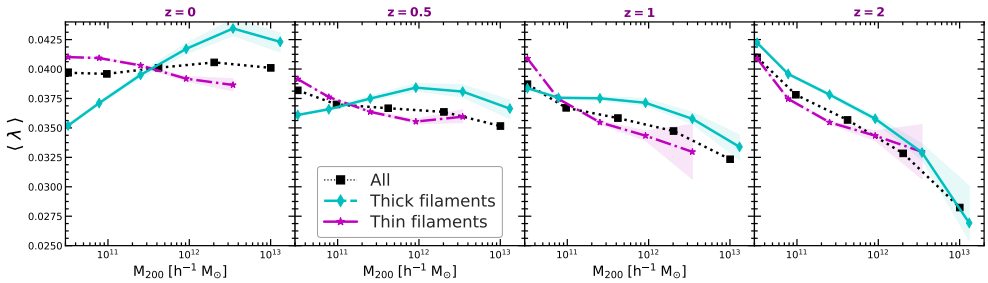

Figure 4.11 – ***The spin of haloes in thin and thick filaments.*** *The plot shows the median spin of haloes residing in thin and thick filaments as a function of halo mass. Each panel corresponds to a different redshift (from left to right): $z = 0, 0.5, 1,$ and 2. At high masses, haloes in thick filaments tend to have a higher median spin than those in thin filaments; for low-mass haloes the trend reverses.*

4

4.5.5 Dependence of halo spin on spin–filament orientation

We now address the final question of this paper: Do parallel and perpendicular haloes have different spin distributions? In otherwords, do haloes spinning preferentially perpendicular to the filament gain angular momentum differently compared to haloes spinning preferentially parallel? To explore this, we first classify the subsamples of parallel and perpendicular haloes. **Parallel haloes** are those whose spin is close to parallel to the spine of their host filaments, i.e. $\cos\theta_{\mathbf{J};\mathbf{e_3}} > 0.8$, which is equivalent to $\theta_{\mathbf{J};\mathbf{e_3}} < 36$. Similarly, **perpendicular haloes** are those with $\cos\theta_{\mathbf{J};\mathbf{e_3}} < 0.2$, which corresponds to $\theta_{\mathbf{J};\mathbf{e_3}} > 78$.

We plot the median spin parameter, $\langle\lambda\rangle$ for these two halo populations as a function of mass at different redshifts in Figure 4.12. At z=0, for haloes less massive than the cross-over mass, $M_+^{\perp \text{ vs. } \parallel} \sim 2 \times 10^{11} h^{-1}\mathrm{M}_\odot$, parallel haloes spin faster than perpendicular haloes, but above this mass, the trend reverses and perpendicular haloes spin faster than parallel haloes. The mass at which this trend reverses decreases as we go to higher redshifts and at z=2, we do not see this crossing over trend.

Interestingly, the cross-over mass seen in the parallel versus perpendicular subsamples and that for thin versus thick filament subsamples are very similar, as can be seen from Table 4.2. This could potentially mean one of the effects is a manifestation of the other one, however, this is not the case. Firstly, thin filaments contain slightly more perpendicular haloes than parallel ones (this can be inferred from the top row in Figure 4.9, where thin filaments have a larger fraction of perpendicular alignments than thicker ones), however, the dependence of $\langle\lambda\rangle$ in thin filaments is opposite to the dependence for perpen-

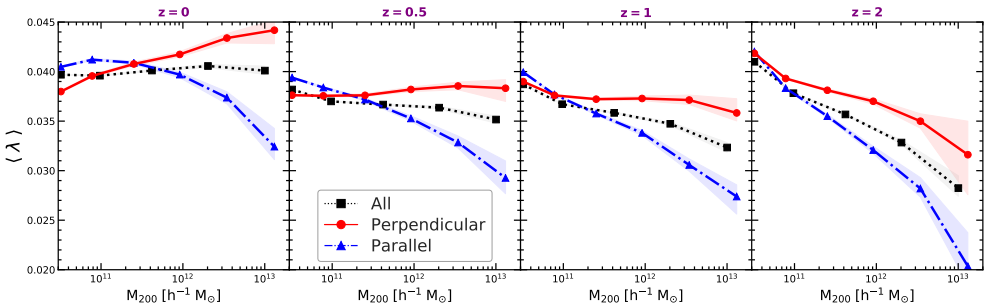

Figure 4.12 – ***The spins of parallel and perpendicular haloes.*** *We plot the median spin of haloes spinning parallel ($\cos\theta_{\mathbf{J};\mathbf{e_3}} > 0.8$) and perpendicular ($\cos\theta_{\mathbf{J};\mathbf{e_3}} < 0.2$) to the filament spine. As in Figure 4.11, the panels correspond to different redshifts. At high masses, perpendicular haloes have a higher spin than parallel haloes; the trend is reversed at low masses.*

dicular haloes. That is, the mass range where $\langle\lambda\rangle$ is larger in thin filaments is the same mass range where $\langle\lambda\rangle$ is larger for parallel, not for perpendicular, haloes. Secondly, when splitting the haloes in thin filaments into parallel and perpendicular subsamples we find the exact same trend as in Figure 4.12: at the high mass end, perpendicular haloes have a higher spin than parallel one, while the reverse is true for low mass haloes (the same holds true for medium and thick filaments too).

To summarise, the spin magnitude depends on both the thickness of the filament in which a halo resides and on the orientation of the spin with respect to the filament spine. These observations underline the multiple complex processes that are responsible for determining the halo spin and its orientation.

4.6 Discussion

In the following, we discuss the most important ramifications of our results and compare them with previous studies in the field.

4.6.1 The variation of halo spin magnitude with web environment

We have found a clear trend between the magnitude of halo spins and the web environment, with the median spin, $\langle\lambda\rangle$, being highest for filament haloes (that is $\langle\lambda\rangle_{\rm filament} > \langle\lambda\rangle_{\rm wall} > \langle\lambda\rangle_{\rm void}$). This trend is present for all the redshifts we have studied ($z \leq 2$) and it does not vary strongly with time. The dependence of halo spin on web environment is a rather small effect ($\sim$10% of the variance of the halo spin distribution) and our very large sample of haloes was essential for revealing this effect. A hint of this trend has been reported in Hahn et al.

(2007b) but that study lacked the large halo sample needed to robustly quantify the effect. The dependence of spin on web environment is another aspect of halo assembly bias, which describes the finding that haloes of the same mass but with different properties cluster differently (e.g. Gao & White 2007). In our case, more clustered haloes, such as those in nodes and filaments, have higher spins than their less clustered equal mass counterparts (Faltenbacher & White 2010).

The dependence of spin on environment can be ascribed to three potential stages in the growth of haloes. Firstly, it could be a manifestation of correlations present in the initial conditions. In the TTT framework, the spin is due to the misalignment between the shape of protohaloes and the initial tidal field. This misalignment can vary systematically from region to region (e.g. van de Weygaert & Bertschinger 1996b; Desjacques 2008; Rossi 2013; Codis, Pichon & Pogosyan 2015), and in particular can be different for the regions that will collapse to form filaments, sheets and voids. Secondly, the maximum expansion of a halo and thus the time available for halo spin to grow (within TTT most of the halo spin is acquired at or before maximum expansion of the halo) also depend on environment (e.g. Hahn et al. 2007a; López, Merchán & Paz 2019). Thirdly, the spin growth is affected by nonlinear processes, such as mergers, which can also imprint an environment dependence. For example, Hetznecker & Burkert (2006) have shown that the spin parameter increases considerably for haloes that have undergone major mergers, which are expected to be more common in crowded environments such as filaments. The late-time spin growth is affected by the degree of anisotropic accretion and, in particular, by highly anisotropic infall of satellites (Libeskind et al. 2014; González & Padilla 2016; Shao et al. 2017, see Tormen 1997 for a detailed study of this aspect in the case of clusters). Our finding that the dependence of spin magnitude on environment is roughly the same since at least redshift, $z = 2$, suggests that early time processes, such as the first two we discussed, are likely the most important ones.

4.6.2 Evolution of halo spin alignment with the cosmic web

We have studied the evolution of the alignment between halo spin and the preferential axes of the host filaments and walls. In general, we find that the alignment varies with halo mass and redshift (see also Aragón-Calvo et al. 2007b; Aragón Calvo 2007; Codis et al. 2012; Trowland, Lewis & Bland-Hawthorn 2013; Wang & Kang 2018b). For example, in present day filaments, the spins of low-mass haloes are preferentially parallel while those of high-mass haloes are preferentially perpendicular to the filament spine, $\mathbf{e_3}$. At fixed halo mass, a higher fraction of haloes have parallel spin–$\mathbf{e_3}$ alignment at later times, while the opposite is true for the spin–$\mathbf{e_2}$ alignment. For filaments, we find the

largest evolution in the spin alignment with the intermediate, $\mathbf{e_2}$, and last, $\mathbf{e_3}$, axes of collapse, and hardly any evolution with $\mathbf{e_1}$ (but nonetheless the spin–$\mathbf{e_1}$ alignment varies with halo mass).

To account for halo mass growth, we also have studied the evolution of the spin–filament alignment as a function of the normalized mass, M_{200}/M^*, i.e. the halo mass in units of the characteristic collapse mass $M^*(z)$ at redshift z. In this case, at fixed M_{200}/M^*, we find that a higher fraction of haloes have spins perpendicular to $\mathbf{e_3}$ at later times, while the opposite trend is seen for $\mathbf{e_1}$. The spin–$\mathbf{e_2}$ alignment hardly changes with time. This indicates that individual haloes, on average, tend to reorient their spins to be preferentially perpendicular to the filament spine, $\mathbf{e_3}$. One explanation for this is the anisotropic accretion of substructures along the host filament spine (e.g. Libeskind et al. 2014; Shao et al. 2017), which leads to the halo major axis being oriented along the filament spine and the spin perpendicular to the filament spine (van Haarlem & van de Weygaert 1993a; Libeskind et al. 2013; Ganeshaiah Veena et al. 2018).

In walls, we find that the most important spin alignments are with the $\mathbf{e_1}$ and $\mathbf{e_2}$ preferential axes, and only a weak alignment with $\mathbf{e_3}$. In particular, at all halo masses the spins are perpendicular to the normal to the wall, $\mathbf{e_1}$, indicating that the halo spins are preferentially pointing in the plane of the wall (Aragón-Calvo et al. 2007b; Aragón Calvo 2007; Aragon-Calvo & Yang 2014; Wang & Kang 2017; Codis et al. 2018). At fixed mass, the halo spins reorient such that fewer wall haloes have spins perpendicular to $\mathbf{e_1}$ at later times, more akin to filament haloes. This fits well with the picture of mass transport across the cosmic web environment in which wall haloes are expected to migrate to filaments (Cautun et al. 2014; Wang & Kang 2017).

4.6.3 Dependence of spin alignments on filament thickness

Motivated by the results of Ganeshaiah Veena et al. (2018), who have shown that at $z = 0$ the halo spin alignments vary with filament properties, we have studied the evolution of the spin–filament alignment for filaments of different thickness. The alignment shows a pronounced variation with filament diameter, with a higher fraction of equal mass haloes having perpendicular spins if they reside in thin filaments compared to thick filaments. This is present at all the redshifts we have studied (i.e. $z \leq 2$) and shows a mild growth with redshift, i.e. the difference is somewhat larger at earlier redshift. This indicates that the dependence of spin–filament alignment on filament properties is set at early times and it is not a late-time effect. One potential explanation is that the dependence on filament thickness is set in the initial condition, that is the misalignment between the moment of inertia of the protohalo and the

tidal field is correlated to the size of the $z{\sim}0$ filaments.

The dependence of the spin alignment on filament properties highlights that the tidal environment in which a halo is located influences halo growth and therefore its eventual angular momentum orientation (see e.g. Jain & Bertschinger 1994). The correlation between tidal field and halo spins has figured prominently in the theoretical studies of Lee, Libeskind & Ryu (2020) (also see Lee 2019) and Porciani, Dekel & Hoffman (2002a,b). In a recent study, Wang & Kang (2018b) showed that haloes in regions with low tidal anisotropy have spins orientated preferentially parallel to $\mathbf{e_3}$ (the last collapse axis) while haloes in regions with high tidal anisotropy have spins preferentially perpendicular to $\mathbf{e_3}$. The dependence of the spin orientation on filament thickness and the effect indicated by Wang & Kang (2018b) are potentially related, but it is unclear to what extent.

To get more insight into the question of the influence of the thickness of filaments, and its relation with the tidal force field, we need to identify the factors that determine the strength and thickness of filaments. The cosmic web theory of Bond, Kofman & Pogosyan (1996) points out three major influences that determine a filament's properties. For example, a strong tidal field translate into thicker and more massive filaments (van de Weygaert & Bertschinger 1996b; van de Weygaert & Bond 2008b). The most prominent filaments tend to form in between galaxy clusters because of the strongly anisotropic force field induced by such configurations. Stronger tides can be induced by more massive clusters and/or shorter mutual distances. Also, we know that filaments are not uniform structures, and tend to attain a considerably higher density and diameter at the location where they connect to the outskirts of clusters (Cautun et al. 2014). Indeed, in this study we have found that, in general, the haloes in thick filaments are those that are close to galaxy clusters (see lowest row in Figure 4.8, also see Figure 17 in Cautun et al. and Galárraga-espinosa et al. 2020). In conclusion, the dependence of spin on filament nature highlight the fact that the strength and the degree of anisotropy of the tidal field plays a crucial role in determining halo properties, such as spin magnitude and orientation (Bond & Myers 1996; Desjacques 2008; Codis, Pichon & Pogosyan 2015; Paranjape, Hahn & Sheth 2018).

4.6.4 The evolution of transition mass for spin alignment

As we discussed, the spin alignment with the filament spine, $\mathbf{e_3}$, changes from a propensity for parallel orientations for low-mass haloes to one of perpendicular configurations at high mass. The halo mass corresponding to this change, known as the transition mass, increases with both time and filament thickness. In particular, the variation with filament thickness is rather large, with more

than one order of magnitude variation between the thinnest and thickest filaments (Ganeshaiah Veena et al. 2018). Due to the multiscale nature of the method, NEXUS+ identifies many more thin filaments than the majority of other web finders (Libeskind et al. 2018) and thus determines a systematically lower transition mass than previous studies.

The transition mass of the full population of filament haloes decreases with redshift as $(1+z)^{-3}$, which in good agreement with the redshift trend found by Codis, Pichon & Pogosyan (2015) although our values are almost an order of magnitude lower than theirs. We have also studied the evolution of the transition mass for filaments of different thickness to find that the relative growth rate is the same in all cases. This is another indication that the dependence of spin alignment on filament thickness is not a late time process but actually is in place before redshift 2.

4.6.5 Dependence of spin magnitude on filament properties and spin–filament alignment

In subsection 4.6.1 we discussed how the magnitude of the halo spin depends on web environment, being highest in filaments. We have also found that the spin magnitude depends on filament properties, such as their thickness. Massive haloes have a slightly higher spin if they reside in thick filaments compared to thin filaments. For low-mass haloes, the opposite relation holds, with haloes in thin filaments having higher spin. The cross-over between the two regimes takes place at a halo mass that is roughly equal with the spin alignment transition mass at that redshift.

This highlights that the two phenomena, i.e. variation of spin magnitude with filament thickness and spin–filament alignment, are highly correlated and likely due to the same physical processes.

We have also found that the spin magnitude depends on whether a halo is oriented parallel or perpendicular to the spine of its host filament. Similarly to the dependence of spin magnitude on filament thickness, here we also have found a mass dependent trend. High mass haloes spin faster on average if their spins are oriented perpendicular to $\mathbf{e_3}$, while the opposite is true for low-mass haloes. The cross-over mass between the two regimes is the same as the cross-over mass for the dependence of the spin magnitude on filament thickness. This might suggest that the two effects are the same, however that is not the case, as we have discussed at length in subsection 4.5.5.

One possible explanation for the dependence of the spin magnitude on filament thickness and spin–filament alignment has to do with the collapse time of a halo. López, Merchán & Paz (2019) have shown that on average haloes that

collapse later (their W-sample) end up having higher spins than haloes which collapse early. The location of these late collapse haloes depends on their mass. High-mass haloes are more clustered (i.e. in our language they are found in thicker filaments), while low-mass haloes are less clustered (i.e. preferentially found in thin filaments). This offers an elegant explanation for the trend between spin and halo thickness found in this paper.

The López, Merchán & Paz (see also López & et al. 2020) results also offer an explanation for the trend between spin magnitude and spin–filament alignment. At all masses the late collapsing haloes have spins that are preferentially perpendicular on their host filaments, and explains why we find that massive haloes spin faster if they have perpendicular spin–filaments alignments.

However, the López, Merchán & Paz results do not explain the inverted trend we find for low-mass haloes, where the fastest spinning haloes are the ones with parallel spin–filament alignments. The discrepancy could be due to the fact that López, Merchán & Paz have used a different halo and filaments definition than ours and have studied all haloes while we have analysed only filament haloes. Filaments contain the majority of high-mass haloes (i.e. $M_{200} \in [1, 50] \times 10^{12}\ h^{-1}\mathrm{M}_{\odot}$) but only around half of the low-mass ones (i.e. $M_{200} \sim 1 \times 10^{11}\ h^{-1}\mathrm{M}_{\odot}$; see Figure 4.2), so we can only make qualitative comparisons but not draw an explicit connection between the halo sub-samples of the two studies.

The relation between the collapse time of a halo and filament thickness has been explored by Borzyszkowski et al. (2017). They have found that haloes in filaments that are thin compared to the halo size (i.e. their *accreting* sample) grow by accretion from the filaments surrounding them, which imparts them a tendency for spin orientations perpendicular to the filaments feeding them, and have on average late collapse times. In contrast, the mass distribution of haloes embedded in thick filaments for their size (i.e. *stalled* haloes in the Borzyszkowski et al. nomenclature) has been set in place since early redshift and recent accretion mostly takes place along directions perpendicular to the host filament spine in which the halo is located. In this case, the accreted mass brings in angular momentum that is preferentially parallel to the filament spine.

To summarise, haloes that have collapsed sooner are likely to have less spin compared to haloes that collapse later on, which have more time to grow their spin through tidal torques.

4.7 Conclusions

In this paper, we have studied the late time ($z \leq 2$) growth of the angular momentum of haloes and how this property is affected by the cosmic web en-

vironment in which a halo resides. We have identified the cosmic web elements using the NEXUS+ multi-scale algorithm that has been designed to capture the hierarchical and scale-free character of the large-scale web. Our study made use of a large volume and very high resolution N-body simulation, Planck-Millennium, that resolves the formation of dark matter haloes over several decades in halo mass. To ensure that our halo properties are well resolved and converged, we have studied only objects with at least 300 particles, corresponding to a halo mass above $3.2 \times 10^{10}\ h^{-1}\mathrm{M}_{\odot}$.

We have focused on two factors of halo spin growth: i) how the spin magnitude varies with web environment, and ii) the evolution of the orientation of halo spins with respect to the preferential axes of filaments and walls. The main conclusions of this study are as follows:

- The median spin parameter, $\langle\lambda\rangle$, is highest for haloes in filaments followed by haloes in walls and is least for void haloes. This trend is seen for all redshifts we have studied (the distribution of halo spin parameters hardly changes since $z = 2$).

- The spins of haloes show a preferential alignment with the spine of their host filaments that depends on halo mass and redshift. Massive haloes show a propensity for perpendicular alignments while low-mass haloes have an excess of parallel alignments. The spin transition from perpendicular to parallel orientations is seen for $z \leq 1$ but not at z=2, perhaps due to the limited mass resolution of our simulation.

- The mass at which the halo spin–filament alignment changes from preferentially parallel to perpendicular, known as the spin transition mass, evolves with time. It is highest at present and decreases towards higher redshifts.

- By scaling the halo mass by the characteristic collapse mass at each redshift, we have shown that the spin of individual haloes reorients such that, on average, it becomes more perpendicular to the filament spine at later times. When expressed in units of the characteristic collapse mass at each redshift, the spin transition mass decreases with time.

- The spin–filament alignment varies with host filament properties, such as filament thickness. At all redshifts, the fraction of halo spins with perpendicular orientations is largest in thin filaments and decreases in thicker filaments.

- Similarly, the transition mass grows rapidly with filament thickness (it varies by an order of magnitude between thin and thick filaments). The

values and the redshift evolution of the spin transition mass also depends on filament thickness.

- The dependence of the spin alignment on filament thickness may not be a late time effect but it is likely already set at high redshift (possibly in the initial conditions). This can be inferred from the fact that the relative growth rate of the spin transition mass is the same for filaments of different thickness.

- The magnitude of the halo spin, similarly to its orientation, depends on filament thickness. The spin of massive haloes is higher if they reside in thick filaments compared to thin filaments, while the opposite is true for low-mass haloes.

- Similarly, the magnitude of the halo spin depends on the halo spin–filament angle. Massive haloes in which the spin is perpendicular to the filament spine have higher spin than haloes in which the spin is along the filament spine, while the converse is true for low-mass haloes.

Our analysis highlights the complex relation between halo spin and the web element in which a halo resides. Both the magnitude and orientation of the halo spin depends on whether the halo is inside a node, filament, sheet or void, and for filaments, which host the majority of haloes, it also depends on filament properties, such as thickness. Understanding this problem is further complicated by the fact that the correlation between spin and web environment depends also on halo mass, with haloes of different masses showing distinct trends with redshift.

The implications of our results have been discussed at length in section 4.6. Here, we would like to highlight that many of the trends we have found, such as the dependence of halo spin magnitude on web environment or the dependence of the spin alignment angle on filament thickness, are mostly set either in the initial conditions or in the early stages ($z > 2$) of halo growth. This hypothesis can be investigated by tracing back in time all the dark matter particles associated to a late time halo and determining how the spin of that particle distribution changes in time. This is analogous to the TTT approach in which the spin of the present day halo is given by the integrated effect of the tidal field acting on the particle distribution that ends up collapsing to form the $z = 0$ halo. This approach will be applied in the upcoming study of López & et al. (2020), who will study the halo spin–filament alignments in the context of TTT. A recent study by Motloch et al. (2020) even attempted to follow this approach in an observational context, within the context of the (still limited) dataset of the SAMI or MaNGA IFU galaxy surveys.

Our study involved a statistical analysis of a large sample of haloes at different redshifts. This is useful for discovering and characterising correlations in the data, but it has the disadvantage of being difficult to isolate the physical processes responsible for these trends. A next step involves studying the evolution of individual haloes and identifying the non-linear processes that affect the halo spin evolution in the context of the cosmic web. Such a study is challenging due to at least two aspects: i) halo spin growth includes an intrinsic level of stochasticity due to the hierarchical and anisotropic nature of halo formation (e.g. see Contreras, Padilla & Lagos 2017), and ii) the correlation between halo spin and the web environment is rather weak and thus a large number of objects need to be studied to reliably identify the relevant processes. Nonetheless, despite these challenges, studying the formation history of individual haloes is key to understand halo spin acquisition and its relation to the cosmic web.

Acknowledgements

We are grateful to Bernard Jones, Enn Saar, Cristiano Porciani, Noam Libeskind and Joss Bland-Hawthorn for encouraging and insightful discussions. PGV and ET acknowledge Tartu Observatory and University of Tartu funds T1900, 1UT40-2, MOBTP36. MC acknowledges support by the EU Horizon 2020 research and innovation programme under a Marie Skłodowska-Curie grant agreement 794474 (DancingGalaxies) and by the ERC Advanced Investigator grant, DMIDAS [GA 786910]. This work used the DiRAC@Durham facility managed by the Institute for Computational Cosmology on behalf of the STFC DiRAC HPC Facility (www.dirac.ac.uk). The equipment was funded by BEIS capital funding via STFC capital grants ST/K00042X/1, ST/P002293/1, ST/R002371/1 and ST/S002502/1, Durham University and STFC operations grant ST/R000832/1. DiRAC is part of the National e-Infrastructure.

Bibliography

Abazajian K. et al., 2003, AJ, 126, 2081

Abel T., Hahn O., Kaehler R., 2012, MNRAS, 427, 61

Alpaslan M. et al., 2015, MNRAS, 451, 3249

—, 2016, MNRAS, 457, 2287

—, 2014a, MNRAS, 438, 177

—, 2014b, MNRAS, 440, L106

Altay G., Colberg J. M., Croft R. A. C., 2006, MNRAS, 370, 1422

Aragón Calvo M. A., 2007, PhD thesis, University of Groningen

Aragon-Calvo M. A., 2019, MNRAS, 484, 5771

Aragón-Calvo M. A., Jones B. J. T., van de Weygaert R., van der Hulst J. M., 2007a, A&A, 474, 315

Aragon Calvo M. A., Neyrinck M. C., Silk J., 2019, The Open Journal of Astrophysics, 2, 7

Aragón-Calvo M. A., van de Weygaert R., Jones B. J. T., 2010a, MNRAS, 408, 2163

Aragón-Calvo M. A., van de Weygaert R., Jones B. J. T., 2010b, MNRAS, 408, 2163

Aragón-Calvo M. A., van de Weygaert R., Jones B. J. T., van der Hulst J. M., 2007b, ApJ, 655, L5

Aragon-Calvo M. A., Yang L. F., 2014, MNRAS, 440, L46

Araya-Melo P. A., 2008, PhD thesis, University of Groningen

Aubert D., Pichon C., Colombi S., 2004, MNRAS, 352, 376

Bag S., Mondal R., Sarkar P., Bharadwaj S., Choudhury T. R., Sahni V., 2019, MNRAS, 485, 2235

Bagla J. S., Ray S., 2005, MNRAS, 358, 1076

Bailin J., Steinmetz M., 2005, ApJ, 627, 647

Baldry I. K., Balogh M. L., Bower R. G., Glazebrook K., Nichol R. C., Bamford S. P., Budavari T., 2006, MNRAS, 373, 469

Ball N. M., Loveday J., Brunner R. J., 2008, MNRAS, 383, 907

Bamford S. P. et al., 2009, MNRAS, 393, 1324

Bardeen J. M., Bond J. R., Kaiser N., Szalay A. S., 1986, ApJ, 304, 15

Bardeen J. M., Bond J. R., Kaiser N., Szalay A. S., 1986, ApJ, 304, 15

Barnes J., Efstathiou G., 1987, ApJ, 319, 575

Barrow J. D., Bhavsar S. P., Sonoda D. H., 1985, MNRAS, 216, 17

Batuski D. J., Burns J. O., 1985, ApJ, 299, 5

Baugh C. M. et al., 2019, MNRAS, 483, 4922

Baugh et al., 2018, in prep

Berti E. et al., 2015, Classical and Quantum Gravity, 32, 243001

Bertschinger E., 1985, ApJS, 58, 39

Bertschinger E., Jain B., 1994, ApJ, 431, 486

Bett P., Eke V., Frenk C. S., Jenkins A., Helly J., Navarro J., 2007, MNRAS, 376, 215

Bett P. E., Frenk C. S., 2012, MNRAS, 420, 3324

—, 2016, MNRAS, 461, 1338

Beygu B., Kreckel K., van der Hulst J. M., Jarrett T. H., Peletier R., van de Weygaert R., van Gorkom J. H., Aragon-Calvo M. A., 2016, Monthly Notices of the Royal Astronomical Society, 458, 394âĂŞ409

Bharadwaj S., Bhavsar S. P., Sheth J. V., 2004, ApJ, 606, 25

Blue Bird J. et al., 2020, MNRAS, 492, 153

Bocquet S., Saro A., Dolag K., Mohr J. J., 2016, MNRAS, 456, 2361

Bonamente M., Nevalainen J., Tilton E., Liivamägi J., Tempel E., Heinämäki P., Fang T., 2016, MNRAS, 457, 4236

Bond J. R., Cole S., Efstathiou G., Kaiser N., 1991, ApJ, 379, 440

Bond J. R., Kofman L., Pogosyan D., 1996, Nature, 380, 603

Bond J. R., Myers S. T., 1996, ApJS, 103, 1

Bond N. A., Strauss M. A., Cen R., 2010a, MNRAS, 406, 1609

—, 2010b, MNRAS, 409, 156

Bonnaire T., Aghanim N., Decelle A., Douspis M., 2019, arXiv e-prints, arXiv:1912.00732

Borzyszkowski M., Porciani C., Romano-Díaz E., Garaldi E., 2017, MNRAS, 469, 594

Bos E. G. P., van de Weygaert R., Dolag K., Pettorino V., 2012, MNRAS, 426, 440

Bos E. G. P., van de Weygaert R., Kitaura F., Cautun M., 2016, in IAU Symposium, Vol. 308, The Zeldovich Universe: Genesis and Growth of

the Cosmic Web, van de Weygaert R., Shandarin S., Saar E., Einasto J., eds., pp. 271–288

Bosma A., 1981, AJ, 86, 1791

Boylan-Kolchin M., Springel V., White S. D. M., Jenkins A., Lemson G., 2009, MNRAS, 398, 1150

Brunino R., Trujillo I., Pearce F. R., Thomas P. A., 2007, MNRAS, 375, 184

Bryan G. L., Norman M. L., 1998, ApJ, 495, 80

Buehlmann M., Hahn O., 2019, MNRAS, 487, 228

Bullock J. S., Dekel A., Kolatt T. S., Kravtsov A. V., Klypin A. A., Porciani C., Primack J. R., 2001, ApJ, 555, 240

Buncher B., Carrasco Kind M., 2019, arXiv e-prints, arXiv:1912.04412

Burchett J. N., Elek O., Tejos N., Prochaska J. X., Tripp T. M., Bordoloi R., Forbes A. G., 2020, ApJ, 891, L35

Calder L., Lahav O., 2010, Physics World, 23, 32

Catelan P., Theuns T., 1996, MNRAS, 282, 455

Cautun M., van de Weygaert R., Jones B. J. T., 2013, MNRAS, 429, 1286

Cautun M., van de Weygaert R., Jones B. J. T., Frenk C. S., 2014, MNRAS, 441, 2923

Cautun M. C., van de Weygaert R., 2011, The DTFE public software: The Delaunay Tessellation Field Estimator code. Astrophysics Source Code Library

Cervantes-Sodi B., Hernandez X., Park C., 2010, MNRAS, 402, 1807

Chen Y.-C., Ho S., Brinkmann J., Freeman P. E., Genovese C. R., Schneider D. P., Wasserman L., 2016, MNRAS, 461, 3896

Chira M., Plionis M., Corasaniti P.-S., 2018, A&A, 616, A137

Chisari N. E., Dunkley J., Miller L., Allison R., 2015, MNRAS, 453, 682

Chisari N. E. et al., 2017, MNRAS, 472, 1163

Clauwens B., Schaye J., Franx M., Bower R. G., 2018, MNRAS, 478, 3994

Codis S., Jindal A., Chisari N. E., Vibert D., Dubois Y., Pichon C., Devriendt J., 2018, MNRAS, 481, 4753

Codis S., Pichon C., Devriendt J., Slyz A., Pogosyan D., Dubois Y., Sousbie T., 2012, MNRAS, 427, 3320

Codis S., Pichon C., Pogosyan D., 2015, MNRAS, 452, 3369

Colberg J. M., Krughoff K. S., Connolly A. J., 2005, MNRAS, 359, 272

Colless M. et al., 2003, arXiv e-prints, astro

Contreras S., Padilla N., Lagos C. D. P., 2017, MNRAS, 472, 4992

Correa C. A., Schaye J., Clauwens B., Bower R. G., Crain R. A., Schaller M., Theuns T., Thob A. C. R., 2017, MNRAS, 472, L45

Crain R. A. et al., 2015, MNRAS, 450, 1937

Danovich M., Dekel A., Hahn O., Ceverino D., Primack J., 2015, MNRAS, 449, 2087

Darvish B., Sobral D., Mobasher B., Scoville N. Z., Best P., Sales L. V., Smail I., 2014, ApJ, 796, 51

Davis M., Efstathiou G., Frenk C. S., White S. D. M., 1985, ApJ, 292, 371

de Lapparent V., Geller M. J., Huchra J. P., 1986, ApJ, 302, L1

de Rossi M. E., Tissera P. B., De Lucia G., Kauffmann G., 2009, MNRAS, 395, 210

Dekel A., Birnboim Y., 2006, MNRAS, 368, 2

Desjacques V., 2008, MNRAS, 388, 638

D'Onghia E., Navarro J. F., 2007, MNRAS, 380, L58

Doroshkevich A. G., 1970a, Astrofizika, 6, 581

—, 1970b, Astrofizika, 6, 581

Dressler A., 1980, ApJ, 236, 351

Dubois Y. et al., 2014, MNRAS, 444, 1453

Dutton A. A., van den Bosch F. C., 2012, MNRAS, 421, 608

Eardley E. et al., 2015, MNRAS, 448, 3665

Efstathiou G., Jones B. J. T., 1979, MNRAS, 186, 133

Efstathiou G., Sutherland W. J., Maddox S. J., 1990, Nature, 348, 705

Einasto J., Kaasik A., Saar E., 1974, Nature, 250, 309

Einasto M., Einasto J., Tago E., Andernach H., Dalton G. B., Müller V., 2002, AJ, 123, 51

Fadda D., Biviano A., Marleau F. R., Storrie-Lombardi L. J., Durret F., 2008, ApJ, 672, L9

Falck B., Neyrinck M. C., 2015, MNRAS, 450, 3239

Falck B. L., Neyrinck M. C., Szalay A. S., 2012, ApJ, 754, 126

Faltenbacher A., White S. D. M., 2010, ApJ, 708, 469

Florack L. M. J., Romeny B. M. T. H., Koenderink J. J., Viergever M. A., 1992, Image and Vision Computing, 10, 376

Forero-Romero J. E., Contreras S., Padilla N., 2014, MNRAS, 443, 1090

Forero-Romero J. E., Hoffman Y., Gottlöber S., Klypin A., Yepes G., 2009, MNRAS, 396, 1815

Frenk C. S., White S. D. M., 2012, Annalen der Physik, 524, 507

Friedmann A., 1922, Zeitschrift fur Physik, 10, 377

Galárraga-espinosa D., Aghanim N., Langer M., Gouin C., Malavasi N., 2020, 1

Gamow G., 1946, Physical Review, 70, 572

Ganeshaiah Veena P., Cautun M., Tempel E., van de Weygaert R., Frenk C. S., 2019, MNRAS, 487, 1607

Ganeshaiah Veena P., Cautun M., van de Weygaert R., Tempel E., Jones B. J. T., Rieder S., Frenk C. S., 2018, ArXiv e-prints, arXiv:1805.00033

Gao L., White S. D. M., 2007, MNRAS, 377, L5

Garaldi E., Romano-Díaz E., Borzyszkowski M., Porciani C., 2018, MNRAS, 473, 2234

Geller M. J., Huchra J. P., 1983, ApJS, 52, 61

—, 1989, Science, 246, 897

González R. E., Padilla N. D., 2010, MNRAS, 407, 1449

—, 2016, ApJ, 829, 58

Gott, J. Richard I., Jurić M., Schlegel D., Hoyle F., Vogeley M., Tegmark M., Bahcall N., Brinkmann J., 2005, ApJ, 624, 463

Gunn J. E., Gott, J. Richard I., 1972, ApJ, 176, 1

Gurbatov S. N., Saichev A. I., Shandarin S. F., 1989, MNRAS, 236, 385

Guth A. H., 1981, Phys. Rev. D, 23, 347

Hahn O., Carollo C. M., Porciani C., Dekel A., 2007a, MNRAS, 375, 489

—, 2007b, MNRAS, 381, 41

Hahn O., Teyssier R., Carollo C. M., 2010, MNRAS, 405, 274

Haider M., Steinhauser D., Vogelsberger M., Genel S., Springel V., Torrey P., Hernquist L., 2016, MNRAS, 457, 3024

Haynes M. P., Giovanelli R., 1986, ApJ, 306, L55

Heavens A., Peacock J., 1988, MNRAS, 232, 339

Hellwing W. A., Frenk C. S., Cautun M., Bose S., Helly J., Jenkins A., Sawala T., Cytowski M., 2016, MNRAS, 457, 3492

Hetznecker H., Burkert A., 2006, MNRAS, 370, 1905

Hidding J., 2017, Jhidding/Adhesion-Example 1.0.0

Hidding J., van de Weygaert R., Vegter G., Jones B. J. T., Teillaud M., 2012, arXiv e-prints, arXiv:1205.1669

Hirv A., Pelt J., Saar E., Tago E., Tamm A., Tempel E., Einasto M., 2017, A&A, 599, A31

Hoffman Y., Metuki O., Yepes G., Gottlöber S., Forero-Romero J. E., Libeskind N. I., Knebe A., 2012, MNRAS, 425, 2049

Hoyle F., 1949, Central Air Documents Office, Dayton, 195

Hubble E., 1929, Proceedings of the National Academy of Science, 15, 168

Huchra J. et al., 2005, in IAU Symposium, Vol. 216, Maps of the Cosmos, Colless M., Staveley-Smith L., Stathakis R. A., eds., pp. 170–179

Huchra J. P., Geller M. J., 1982, ApJ, 257, 423

Huchra J. P. et al., 2012, ApJS, 199, 26

Icke V., 1973, A&A, 27, 1

Ishiyama T. et al., 2013, ApJ, 767, 146

Jain B., Bertschinger E., 1994, ApJ, 431, 495

Jain B., Khoury J., 2010, Annals of Physics, 325, 1479

Jenkins A., 2010, MNRAS, 403, 1859

Joachimi B. et al., 2015, Space Sci. Rev., 193, 1

Jones B., van de Weygaert R., 2009, Astrophysics and Space Science Proceedings, 8, 467

Jones B. J. T., 1976, Reviews of Modern Physics, 48, 107

Jones B. J. T., van de Weygaert R., Aragón-Calvo M. A., 2010, MNRAS, 408, 897

Kaiser N., 1984, ApJ, 284, L9

Kang X., Wang P., 2015, ApJ, 813, 6

Kauffmann G., White S. D. M., Heckman T. M., Ménard B., Brinchmann J., Charlot S., Tremonti C., Brinkmann J., 2004, MNRAS, 353, 713

Kiessling A. et al., 2015, Space Sci. Rev., 193, 67

Knebe A., Gill S. P. D., Gibson B. K., Lewis G. F., Ibata R. A., Dopita M. A., 2004, ApJ, 603, 7

Kofman L., Pogosian D., Shandarin S., 1990, MNRAS, 242, 200

Kofman L., Pogosyan D., Shandarin S. F., Melott A. L., 1992, ApJ, 393, 437

Koyama K., Sakstein J., 2015, Phys. Rev. D, 91, 124066

Kraan-Korteweg R. C., Cluver M. E., Bilicki M., Jarrett T. H., Colless M., Elagali A., Böhringer H., Chon G., 2017, MNRAS, 466, L29

Kraljic K., Davé R., Pichon C., 2020, MNRAS, 493, 362

Kreckel K., Platen E., Aragón-Calvo M. A., van Gorkom J. H., van de Weygaert R., van der Hulst J. M., Beygu B., 2012, AJ, 144, 16

Kreckel K. et al., 2011, AJ, 141, 4

Krolewski A., Ho S., Chen Y.-C., Chan P. F., Tenneti A., Bizyaev D., Kraljic K., 2019, ApJ, 876, 52

Kuutma T., Tamm A., Tempel E., 2017, A&A, 600, L6

Lacey C., Cole S., 1993, MNRAS, 262, 627

Lagos C. d. P. et al., 2015, MNRAS, 452, 3815

Lagos C. d. P. et al., 2018, MNRAS, 473, 4956

Laigle C. et al., 2015, MNRAS, 446, 2744

Lavaux G., Wandelt B. D., 2010, MNRAS, 403, 1392

—, 2012, in American Astronomical Society Meeting Abstracts, Vol. 219, American Astronomical Society Meeting Abstracts #219, p. 336.02

Lee J., 2004, ApJ, 614, L1

—, 2019, ApJ, 872, 37

Lee J., Erdogdu P., 2007, ApJ, 671, 1248

Lee J., Libeskind N. I., Ryu S., 2020, arXiv e-prints, arXiv:2004.02638

Lee J., Pen U.-L., 2000, ApJ, 532, L5

—, 2001, ApJ, 555, 106

Lemaître G., 1927, Annales de la Société Scientifique de Bruxelles, 47, 49

Lewis I. et al., 2002, MNRAS, 334, 673

Li Q., Sone S., Doi K., 2003, Medical Physics, 30, 2040

Libeskind N. I., Frenk C. S., Cole S., Helly J. C., Jenkins A., Navarro J. F., Power C., 2005, MNRAS, 363, 146

Libeskind N. I., Hoffman Y., Knebe A., Steinmetz M., Gottlöber S., Metuki O., Yepes G., 2012, MNRAS, 421, L137

Libeskind N. I., Hoffman Y., Steinmetz M., Gottlöber S., Knebe A., Hess S., 2013, ApJ, 766, L15

Libeskind N. I., Knebe A., Hoffman Y., Gottlöber S., 2014, MNRAS, 443, 1274

Libeskind N. I., Tempel E., Hoffman Y., Tully R. B., Courtois H., 2015, MNRAS, 453, L108

Libeskind N. I. et al., 2018, MNRAS, 473, 1195

Lietzen H. et al., 2016, A&A, 588, L4

Liivamägi L. J., Tempel E., Saar E., 2012, A&A, 539, A80

Lindeberg T., 1998, Int. J. Comput. Vision, 30, 79

López P., et al., 2020, in prep.

López P., Merchán M. E., Paz D. J., 2019, MNRAS, 485, 5244

Ludlow A. D., Borzyszkowski M., Porciani C., 2014, MNRAS, 445, 4110

Ludlow A. D. et al., 2013, MNRAS, 432, 1103

Lynden-Bell D., Faber S. M., Burstein D., Davies R. L., Dressler A., Terlevich R. J., Wegner G., 1988, ApJ, 326, 19

Malavasi N. et al., 2017, MNRAS, 465, 3817

Mandelbaum R., Hirata C. M., Ishak M., Seljak U., Brinkmann J., 2006, MNRAS, 367, 611

Martizzi D. et al., 2018, arXiv e-prints

McAlpine S. et al., 2016, Astronomy and Computing, 15, 72

McCullagh N., Norberg P., Cole S., Gonzalez-Perez V., Baugh C., Helly J., 2017, ArXiv e-prints

Mo H., van den Bosch F., White S., 2010, Formation and Structure of Dark Matter Halos, Cambridge University Press, p. 319âĂŞ365

Morse M., 1996, American Mathematical Society Colloquium Publications, Vol. 18, The calculus of variations in the large. American Mathematical Society, Providence, RI, pp. xii+368, reprint of the 1932 original

Motloch P., Yu H.-R., Pen U.-L., Xie Y., 2020, arXiv e-prints, arXiv:2003.04800

Navarro J. F., Frenk C. S., White S. D. M., 1997, ApJ, 490, 493

Neyrinck M. C., 2008, MNRAS, 386, 2101

Neyrinck M. C., Aragon-Calvo M. A., Falck B., Szalay A. S., Wang J., 2019, arXiv e-prints, arXiv:1904.03201

Oort J. H., 1983, ARA&A, 21, 373

Padmanabhan T., 1993, Structure Formation in the Universe. Cambridge University Press, p. 499

Pahwa I. et al., 2016, MNRAS, 457, 695

Pandey B., Sarkar S., 2017, MNRAS, 467, L6

Paranjape A., Hahn O., Sheth R. K., 2018, MNRAS, 476, 3631

Peebles P. J. E., 1969, ApJ, 155, 393

—, 1980, The large-scale structure of the universe. Princeton University Press

Peirani S., Mohayaee R., de Freitas Pacheco J. A., 2004, MNRAS, 348, 921

Penzias A. A., Wilson R. W., 1965, ApJ, 142, 419

Pereyra L. A., Sgró M. A., Merchán M. E., Stasyszyn F. A., Paz D. J., 2019, arXiv e-prints, arXiv:1911.06768

Perlmutter S. et al., 1999, ApJ, 517, 565

Pichon C., Pogosyan D., Kimm T., Slyz A., Devriendt J., Dubois Y., 2011, MNRAS, 418, 2493

Pillepich A. et al., 2018, MNRAS, 473, 4077

Pisani A., Sutter P. M., Hamaus N., Alizadeh E., Biswas R., Wandelt B. D., Hirata C. M., 2015, Phys. Rev. D, 92, 083531

Planck Collaboration et al., 2014, A&A, 571, A16

—, 2016, A&A, 594, A13

—, 2018, arXiv e-prints, arXiv:1807.06209

Platen E., van de Weygaert R., Jones B. J. T., 2007, MNRAS, 380, 551

—, 2008, MNRAS, 387, 128

Pomarède D., Hoffman Y., Courtois H. M., Tully R. B., 2017, ApJ, 845, 55

Porciani C., Dekel A., Hoffman Y., 2002a, MNRAS, 332, 325

—, 2002b, MNRAS, 332, 339

Press W. H., Schechter P., 1974, ApJ, 187, 425

Proust D. et al., 2006, A&A, 447, 133

Rahmati A., Schaye J., Bower R. G., Crain R. A., Furlong M., Schaller M., Theuns T., 2015, MNRAS, 452, 2034

Ramachandra N. S., Shandarin S. F., 2015, MNRAS, 452, 1643

Rieder S., van de Weygaert R., Cautun M., Beygu B., Portegies Zwart S., 2013, MNRAS, 435, 222

Rieder et al., 2018, in prep.

Riess A. G. et al., 1998, AJ, 116, 1009

Rodriguez-Gomez V. et al., 2017, MNRAS, 467, 3083

Romano-Díaz E., Garaldi E., Borzyszkowski M., Porciani C., 2017, MNRAS, 469, 1809

Romano-Díaz E., van de Weygaert R., 2007, MNRAS, 382, 2

Romano-Díaz E., van de Weygaert R., 2007, MNRAS, 382, 2

Rossi G., 2013, MNRAS, 430, 1486

Rubin V. C., Ford, W. K. J., Thonnard N., 1980, ApJ, 238, 471

Sahni V., Sathyaprakash B. S., Shandarin S. F., 1998, ApJ, 495, L5

Sales L. V., Navarro J. F., Theuns T., Schaye J., White S. D. M., Frenk C. S., Crain R. A., Dalla Vecchia C., 2012, MNRAS, 423, 1544

Salvador-Solé E., Solanes J. M., Manrique A., 1998, ApJ, 499, 542

Sancisi R., Fraternali F., Oosterloo T., van der Hulst T., 2008, A&A Rev., 15, 189

Sathyaprakash B. S., Sahni V., Shandarin S. F., 1996, ApJ, 462, L5

Sato Y., Nakajima S., Shiraga N., Atsumi H., Yoshida S., Koller T., Gerig G., Kikinis R., 1998, Medical Image Analysis, 2, 143

Schaap W. E., van de Weygaert R., 2000, A&A, 363, L29

Schäfer B. M., 2009, International Journal of Modern Physics D, 18, 173

Schaye J. et al., 2015, MNRAS, 446, 521

Schechter P., 1976, ApJ, 203, 297

Shandarin S. F., 2011, J. Cosmology Astropart. Phys., 2011, 015

Shandarin S. F., Sunyaev R. A., 2009, A&A, 500, 19

Shandarin S. F., Zeldovich Y. B., 1989, Reviews of Modern Physics, 61, 185

Shao S., Cautun M., Frenk C. S., Gao L., Crain R. A., Schaller M., Schaye J., Theuns T., 2016, MNRAS, 460, 3772

Shao S., Cautun M., Frenk C. S., Grand R. J. J., Gómez F. A., Marinacci F., 2017, ArXiv e-prints

Shapley H., 1930, Harvard College Observatory Bulletin, 874, 9

Sheth J. V., Sahni V., 2005, arXiv e-prints, astro

Sheth R. K., Mo H. J., Tormen G., 2001, MNRAS, 323, 1

Sheth R. K., Tormen G., 2002, MNRAS, 329, 61

Sheth R. K., van de Weygaert R., 2004, MNRAS, 350, 517

Sousbie T., 2011, MNRAS, 414, 350

Sousbie T., Pichon C., Kawahara H., 2011, MNRAS, 414, 384

Springel V., 2005, MNRAS, 364, 1105

Springel V., Frenk C. S., White S. D. M., 2006, Nature, 440, 1137

Springel V. et al., 2018, MNRAS, 475, 676

—, 2005, Nature, 435, 629

Springel V., White S. D. M., Tormen G., Kauffmann G., 2001, MNRAS, 328, 726

Stewart K. R. et al., 2017, ApJ, 843, 47

Stoica R. S., Martínez V. J., Mateu J., Saar E., 2005, A&A, 434, 423

Sutter P. M. et al., 2015, Astronomy and Computing, 9, 1

Tasitsiomi A., Kravtsov A. V., Gottlöber S., Klypin A. A., 2004, ApJ, 607, 125

Tempel E., 2014a, Nature, 513, 41

—, 2014b, Nature, 513, 41

Tempel E., Guo Q., Kipper R., Libeskind N. I., 2015, MNRAS, 450, 2727

Tempel E., Libeskind N. I., 2013a, ApJ, 775, L42

—, 2013b, ApJ, 775, L42

Tempel E., Libeskind N. I., Hoffman Y., Liivamägi L. J., Tamm A., 2014a, MNRAS, 437, L11

Tempel E., Saar E., Liivamägi L. J., Tamm A., Einasto J., Einasto M., Müller V., 2011, A&A, 529, A53

Tempel E., Stoica R. S., Kipper R., Saar E., 2016, Astronomy and Computing, 16, 17

Tempel E., Stoica R. S., Martínez V. J., Liivamägi L. J., Castellan G., Saar E., 2014b, MNRAS, 438, 3465

—, 2014c, MNRAS, 438, 3465

Tempel E., Stoica R. S., Saar E., 2013, MNRAS, 428, 1827

Tempel E., Tamm A., 2015, A&A, 576, L5

Tenneti A., Mandelbaum R., Di Matteo T., Feng Y., Khandai N., 2014, MNRAS, 441, 470

Tormen G., 1997, MNRAS, 290, 411

Trayford J. W. et al., 2017, MNRAS, 470, 771

—, 2015, MNRAS, 452, 2879

Trowland H. E., Lewis G. F., Bland-Hawthorn J., 2013, ApJ, 762, 72

Tully R. B., Courtois H., Hoffman Y., Pomarède D., 2014, Nature, 513, 71

van de Weygaert R., 2000, in Large Scale Structure in the X-ray Universe, Plionis M., Georgantopoulos I., eds., p. 135

—, 2002, in Astrophysics and Space Science Library, Vol. 276, Modern Theoretical and Observational Cosmology, Plionis M., Cotsakis S., eds., p. 119

—, 2016, in IAU Symposium, Vol. 308, The Zeldovich Universe: Genesis and Growth of the Cosmic Web, van de Weygaert R., Shandarin S., Saar E., Einasto J., eds., pp. 493–523

van de Weygaert R., Bertschinger E., 1996a, MNRAS, 281, 84

—, 1996b, MNRAS, 281, 84

van de Weygaert R., Bond J. R., 2008a, Clusters and the Theory of the Cosmic Web, Plionis M., López-Cruz O., Hughes D., eds., Vol. 740, Springer,Dordrecht, p. 335

—, 2008b, in Lecture Notes in Physics, Berlin Springer Verlag, Vol. 740, A Pan-Chromatic View of Clusters of Galaxies and the Large-Scale Structure, Plionis M., López-Cruz O., Hughes D., eds., p. 24

van de Weygaert R. et al., 2011, Astrophysics and Space Science Proceedings, 27, 17

van de Weygaert R. et al., 2011, Environment and the Formation of Galaxies: 30 years later, 17âĂŞ24

van Haarlem M., van de Weygaert R., 1993a, ApJ, 418, 544

—, 1993b, ApJ, 418, 544

van Uitert E. et al., 2017, MNRAS, 467, 4131

Velliscig M. et al., 2015, MNRAS, 453, 721

Vera-Ciro C. A., Sales L. V., Helmi A., Frenk C. S., Navarro J. F., Springel V., Vogelsberger M., White S. D. M., 2011, MNRAS, 416, 1377

Vitvitska M., Klypin A. A., Kravtsov A. V., Wechsler R. H., Primack J. R., Bullock J. S., 2002, ApJ, 581, 799

Vogelsberger M. et al., 2014, MNRAS, 444, 1518

Vogelsberger M., Marinacci F., Torrey P., Puchwein E., 2020, Nature Reviews Physics, 2, 42

Wang J. et al., 2011, MNRAS, 413, 1373

Wang P., Guo Q., Kang X., Libeskind N. I., 2018a, ApJ, 866, 138

—, 2018b, ApJ, 866, 138

Wang P., Kang X., 2017, MNRAS, 468, L123

—, 2018a, MNRAS, 473, 1562

—, 2018b, MNRAS, 473, 1562

Wechsler R. H., Bullock J. S., Primack J. R., Kravtsov A. V., Dekel A., 2002, ApJ, 568, 52

Welker C. et al., 2020, MNRAS, 491, 2864

Welker C., Devriendt J., Dubois Y., Pichon C., Peirani S., 2014, MNRAS, 445, L46

White S. D. M., 1984, ApJ, 286, 38

White S. D. M., Silk J., 1979, ApJ, 231, 1

Wu Y., Batuski D. J., Khalil A., 2009, ApJ, 707, 1160

Zavala J. et al., 2016, MNRAS, 460, 4466

Zeldovich I. B., Einasto J., Shandarin S. F., 1982, Nature, 300, 407

Zel'Dovich Y. B., 1970, A&A, 500, 13

Zhang Y., Yang X., Wang H., Wang L., Luo W., Mo H. J., van den Bosch F. C., 2015, ApJ, 798, 17

Zhang Y., Yang X., Wang H., Wang L., Mo H. J., van den Bosch F. C., 2013, ApJ, 779, 160

Zwicky F., 1933, Helvetica Physica Acta, 6, 110

Summary in English

Every celestial object in the Universe is rotating, from small asteroids and planets to large galaxies and even the long filaments of the cosmic web. The origin of rotation remains an intriguing question which is yet to be fully understood, especially in the context of galaxies and their dark matter haloes. The most popular theory is that in the early Universe, as matter began to clump together, the resulting anisotropic distribution of matter torqued up nascent matter clouds that eventually grow into galaxies. The tiny spin grew with time as the clouds collapsed and resulted in the distinctly rotating discs of galaxies.

Over the last two decades, there has been increasing evidence that because of the torquing in the early Universe, there is a correlation between the spin-axis of galaxies and the orientation of the large-scale structures that they are growing in. This thesis addresses the intricate relationship between the cosmic web and galaxy spins using large numerical data. We specifically explore spin transition from parallel to perpendicular as a function of the mass of a halo or galaxy with respect to the spine of the host cosmic filament. We also investigate the various factors that influence these trends, such as filament properties and redshift. The thesis uncovers the role of the cosmic web environment in establishing the rotation of haloes and galaxies, and hence possibly their overall morphology and nature.

Galaxy-alignment studies carried out in this thesis are important for various reasons. They not only hold information on the early Universe but also help in developing precise models to account for alignment effects on weak lensing measurements. This will enable us to make better interpretations of the data from future weak lensing surveys such as EUCLID, LSST and DESI. More recently, the notion of spin transition mass is being developed as a tool to probe cosmology.

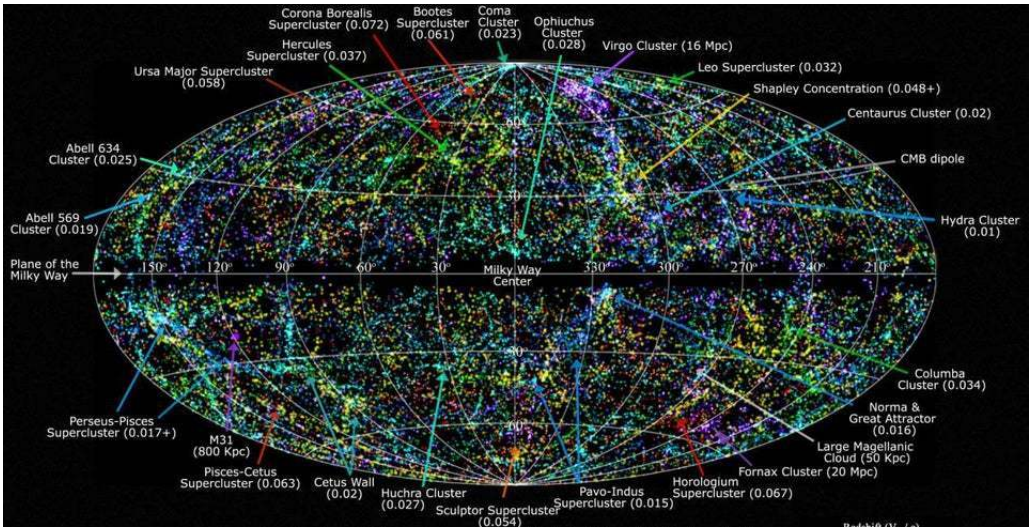

Figure 1 – *Map of the Universe showing galaxies from the 2MASS redshift survey. Colors represent redshift with blue being the closest to us and yellow, red farther away. Image made by T.Jarret(IPAC/Caltech) using galaxies from Huchra et al. (2012).*

Mapping the Universe

All through recorded history, humans have displayed an inexplicable urge to explore and map the world around them. This cartographic instinct extends far and beyond, even to the edge of our Universe. Throughout this grand quest, whenever the scale of observation has made a leap, the definitions and descriptions of the Universe have also undergone paradigm shifts. For a considerable period of time, our ancestors painted a picture of the Universe as consisting of a few planets, the Moon, the Sun and a few stars. Gradually, this description expanded to the horizons of our galaxy, the Milky Way, which is made up of billions of stars and was then thought to be the edge of the Universe. Further on, as many more galaxies were discovered, our description once again extended to encompass virialized local clusters. With the advent of deep spectroscopic sky surveys, it is now possible to map the skies to an even great extent. In Figure 6, a recent map of the local Universe is shown and we have now confirmed that the distribution of matter on very large scales (few to more than a 100 Megaparsecs) is not uniform, but in fact, forms an intriguing sponge-like or web-like pattern known as the Cosmic Web.

Galaxies, gas and all the matter in the Universe aggregate to form **filaments**, **walls** and **voids** over a wide range of scales that together constitute the cosmic web. This observation is a culmination of persistent efforts through the ages to

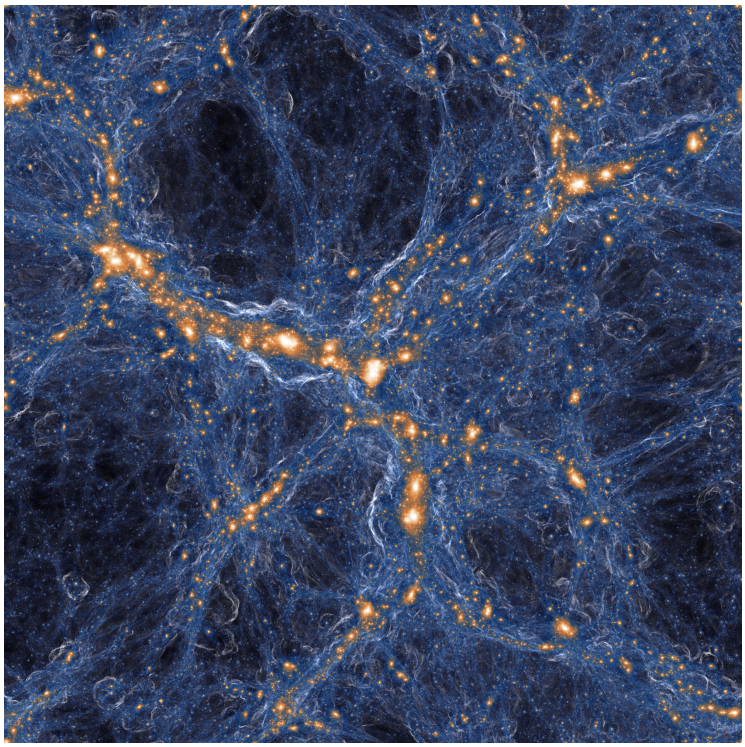

Figure 2 – *The image shows the dark matter density field in the Illustris simulation. The white and orange structures depict the gravitationally collapsed objects embedded within the cosmic network. Image courtesy: Illustris collaboration (Vogelsberger et al. 2014).*

explore the Universe around us. Large-scale patterns came out as a prominent characteristic of computer simulations as illustrated in Figure 7. The sky surveys and cosmological simulations together heralded a new beginning of the large-scale structure studies.

These rich structures emerged from tiny density fluctuations in the early Universe that were amplified due to gravity. The components of the cosmic web are a result of the anisotropic collapse of matter due to the action of gravity. Under the influence of self-gravity, the over-dense fluctuations collapse to form denser regions and the matter streams out of underdense regions making them further underdense. This increases the contrast between over and underdense regions. Eventually, regions that are denser collapse to form gravitationally bound objects such as haloes and galaxies and the underdense regions become the empty spaces of the universe. This process gives rise to an intricate network of high-density clusters, interlinked via elongated filaments that are encompassed within walls and voids, as can be seen in Figure 7.

This thesis

In this thesis, we have addressed the following main question: To what extent does the cosmic web influence the spins and shapes of haloes and galaxies? The multiscale nature and the complex connectivity of the web make it hard to pinpoint the large-scale processes that affect the formation of galaxies. To this end, we have addressed several open questions on the alignment of the spins of haloes and galaxies with the cosmic web, using state-of-the-art numerical simulations and cosmic web detection techniques.

The alignment signal is weak, so we need a large sample of objects to measure it robustly, and thus it is challenging to disentangle the contributions from various processes. To address this, we identified the cosmic web in a very large volume P-Millennium simulation and studied its connection to the distribution and properties of haloes over several orders of magnitude in halo mass. Similarly, we used the EAGLE hydrodynamical simulation to study galaxy spin alignments.

Cosmic web and spin magnitude of haloes

The anisotropic collapse of over-densities, due to the tidal fields that lead to the formation of the cosmic web, also torqued up dark matter protohaloes and protogalaxies. Therefore, we expect the imprints of web formation on galaxy and halo spins that are embedded within the cosmic network.

In chapter 2, we show that there is an explicit dependence of halo spin on the environment, as can be seen in Figure 8. The filament haloes are on average the fastest spinning, while the node haloes have the lowest spins. We also show in chapter 4 that this segregation between halo spins in different environments is seen even at higher redshifts (see bottom panel of Figure 8). This establishes a clear connection between halo growth and the large scale environment.

Spin transition of haloes and galaxies

In chapter 2 and chapter 4, we have calculated the spin–filament alignment signal (measured as the angle between the halo angular momentum and the axis of the filament in which the halo resides) and confirmed, using much better statistics, that low-mass haloes are preferentially aligned parallel to their host filament while the more massive haloes are spinning preferentially perpendicular to the filaments in which they reside. With this, we established, with a very high statistical significance, the existence of the spin transition of haloes with respect to the filaments of the cosmic web.

The time evolution of this trend is studied in chapter 4. At fixed halo mass, halo populations tend to be more perpendicular to the filament spine at high

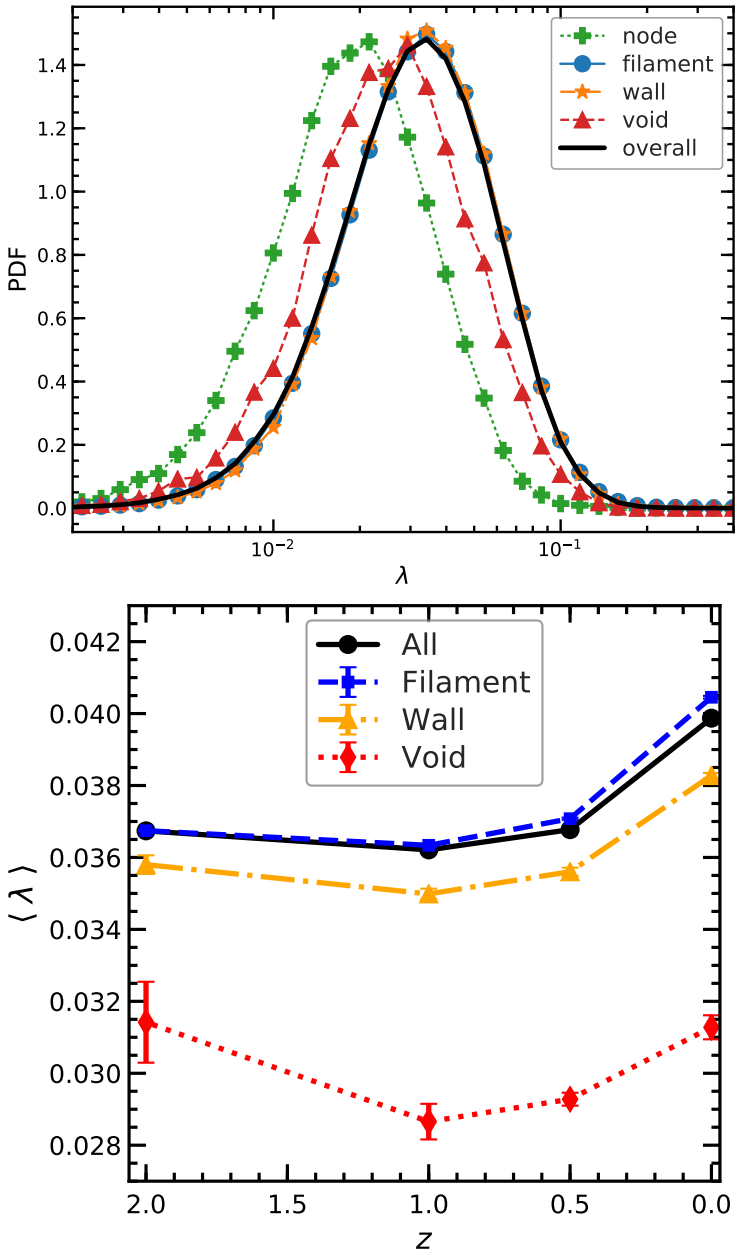

Figure 3 – *Top panel: The spin distribution of haloes is plotted for haloes in filaments, voids, nodes and walls. Bottom panel: Median halo spin at several redshifts. (reproduced from Ganeshaiah Veena et al. 2018, 2020).*

redshift compared to today. In contrast, the spins of individual haloes were more parallel to their filaments at high redshift.

In chapter 3, we explore the mass-dependent trend for galaxies in the EAGLE simulation. Although we found a mass-dependent spin orientation, we did not find a transition as in the case of haloes in the P-Millennium or the EAGLE simulations. EAGLE galaxies were found to be more perpendicular to the filament spine compared to the inner fractions of dark matter haloes, implying that processes responsible for galaxy angular momentum accretion are slightly different from that of haloes.

To further assess the cause of the spin transition in haloes, we also studied in chapter 2 the alignment of the inner fractions of haloes and showed that the inner parts retain the original tidal torque orientation with the tidal field better than the outer parts. This is because the outer regions are much more influenced by later secondary processes such as accretions and mergers.

This is a clear illustration of the complex interplay between haloes/galaxies and the dynamics of the cosmic web.

Filament properties, web finders and transition mass

The identification of filaments presents several challenges, such as the sparsity and bias of tracer populations and the availability of only redshift information, and not actual distances. This prompted us to compare the filamentary networks identified by different finders, such as filaments traced by the density versus the velocity field in chapter 2, and filaments identified in the dark matter versus the galaxy distribution in chapter 3.

In chapter 2, we compared NEXUS+, which classifies web features based on the geometric information of the density field, with NEXUS_VELOCITY_SHEAR, which classifies the web based on the dynamical signature contained in the velocity shear field. While both these methods identify the main arteries of the filamentary network, NEXUS+ also picks up the more tenuous filaments that pervade the low-density environments.

These differences manifest as different halo populations and therefore also in the value of the transition mass, which is the mass at which the halo population goes from a preferential parallel alignment to a preferential perpendicular orientation with the filament spine.

In chapter 3, we highlight the importance of filaments as cosmological probes for understanding galaxy formation. We show that filaments contain about 50% of all the matter and about 80% of all the galaxies in the Universe. We further compare spin and shape alignments for filaments traced by the dark

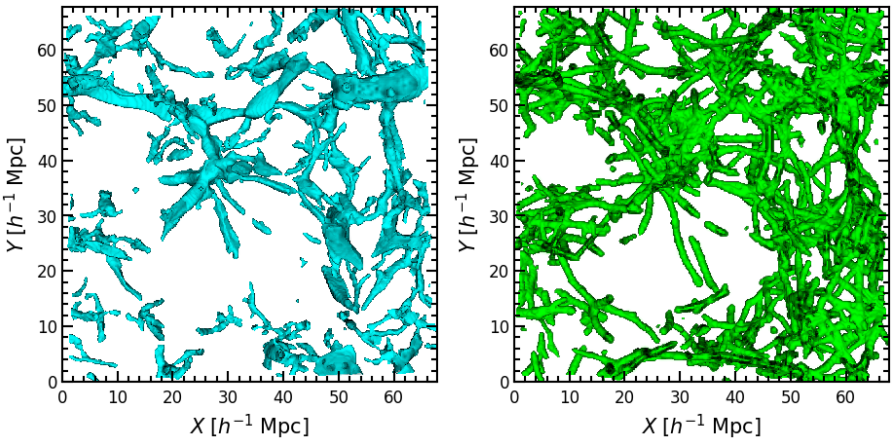

Figure 4 – *The two panels show NEXUS+ filaments (tracing the dark matter distribution) and Bisous filaments (tracing the galaxy distribution) in the same* 10 h^{-1}Mpc *thick slice of the EAGLE simulation. Image reproduced from Ganeshaiah Veena et al. 2019.*

matter (NEXUS+) versus filaments traced by galaxy distribution (Bisous). Although NEXUS can be applied to galaxy and gas distributions alike, for our study we chose to use the dark matter distribution. The comparison between these two is illustrated in Figure 9, which contrasts the NEXUS+ and Bisous filaments in the same volume of the EAGLE hydrodynamical simulation. Overall, we have found reasonable consistency between the two filamentary networks, with the differences being well understood and characterised in the case of spin alignment differences.

We also highlight in chapter 2 and chapter 4 that not all filaments are the same and that they can be classified based on properties such as thickness. The properties of haloes and galaxies are linked to the characteristics of their host filament. The transition mass strongly varies (by more than one order of magnitude) with filament thickness and it is highest in thick filaments.

Halo-galaxy connection

An interesting question to ask is if it would be possible to predict the angular momentum of a galaxy given the angular momentum of its dark matter halo, or vice-versa. We have addressed this question in chapter 3 via galaxy shape-filament alignments.

Using the EAGLE simulation, we studied to what extent the halo spin alignment with respect to the filament would affect its galaxy spin and shape align-

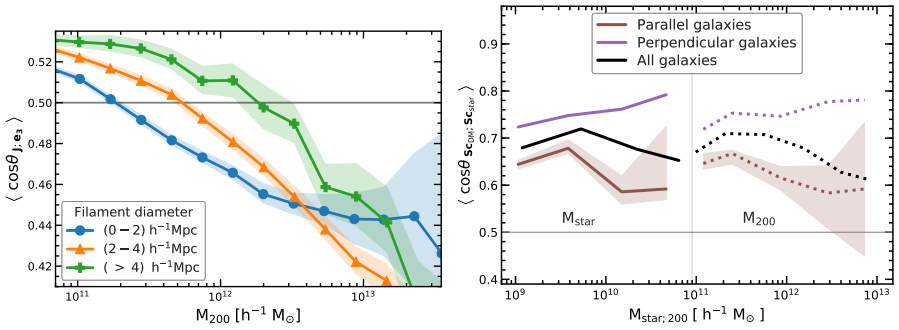

Figure 5 – *The first panel shows the median spin-filament alignment signal for haloes in thin, medium and thick filaments. The second panel shows median alignment between the minor axis of central galaxies and the minor axis of their host haloes. This is plotted separately for galaxies that spinning parallel and perpendicular to the filaments. Galaxies perpendicular to filaments are better aligned with their host haloes compared to the galaxies that are parallel to their filament. (reproduced from Ganeshaiah Veena et al. 2018, 2019).*

ments and vice-versa. In Figure 10, the alignment between halo minor axis and galaxy minor axis is shown for two populations: galaxies that have their minor axis perpendicular to the filaments and those that are parallel to the filaments. We found that the perpendicular galaxies are better aligned with their host dark matter haloes than the parallel galaxies.

Along the same lines, we studied the spin-filament alignments of haloes that host elliptical and spiral galaxies. Host haloes of ellipticals showed a preferential perpendicular alignment, while the host haloes of spirals showed a clear parallel spin alignment with respect to the filaments they reside in. Therefore, by looking at galaxy spin alignments with filaments, one can make predictions on their host halo spin and shape alignments with filaments.

This finding is key for designing new cosmological tests since it can statistically predict the shape and orientation of dark matter haloes.

Concluding remarks

To summarize, this thesis establishes the complex interplay between the processes on the large scale and properties of haloes and galaxies. We have shown that various processes are responsible for evolution of galaxy and halo spin with the web environment. In particular, the galaxy–filament alignment, which is of uttermost importance for predicting intrinsic alignment for weak lensing

cosmological studies, is strongly affected by non-linear late-time effects. Furthermore, we show that the alignment varies with the web nature, and in particular with the properties of filaments, which host the majority of bright galaxies. The next step in this field is to establish how these alignments affect weak-lensing measurements such that cosmological parameters are correctly determined. Spin-transition mass and its sensitivity to cosmology also needs to be explored so that it can be used as an additional probe for cosmology. Galaxy spin-filament alignments have to be studied in greater detail using high statistics in order to be able to develop models to predict their halo spins and shed light on the dark sector of the Universe.

Nederlandse samenvatting

Alle hemellichamen in het heelal roteren. Van de kleinste asteroïden en planetoïden tot aan grote sterrenstelsels en zelfs de lange filamenten van het kosmische web, ze roteren allemaal. Het is nog niet volledig duidelijk wat de oorsprong van deze rotatie is, vooral niet in sterrenstelsels en hun halo van donkere materie. De meest populaire theorie beschrijft de oorsprong van deze rotatie in het vroege heelal toen materie samen begon te klonteren. Deze onevenredige verdeling van materie zorgde voor getijdenkrachten op de omliggende gaswolken, waardoor deze licht zijn gaan roteren. Door de ineenstorting van deze wolken onder hun eigen zwaartekracht werd de in het begin kleine hoeveelheid rotatie met de tijd steeds groter. Dit resulteerde uiteindelijk in de kenmerkende roterende schijven van sterrenstelsels.

In de afgelopen twee decennia werden er steeds meer aanwijzingen gevonden dat er een relatie bestaat tussen de richting van de rotatie-as van de sterrenstelsels en de oriëntatie van de grote-schaal structuren waarin ze zich vormen als gevolg van de torsie in het vroege heelal. In dit proefschrift wordt deze samenhang tussen het kosmische web en de rotatie van sterrenstelsels bestudeerd door gebruik te maken van grote numerieke simulaties. De vergeleken eigenschappen zijn de rotatie van het sterrenstelsel of halo en de as van het kosmische filament. Deze gaan van loodrecht op tot evenwijdig aan elkaar, afhankelijk van de massa van het sterrenstelsel of halo. Bovendien bestuderen we de verschillende factoren die van invloed zijn op deze relatie, zoals de eigenschappen van de filamenten en de roodverschuiving. Dit proefschrift onthult de rol die de omgeving in het kosmische web speelt in het tot stand brengen van de rotatie van halo's en sterrenstelsels en daarmee mogelijk ook hun algehele aard en morfologie beïnvloed.

De studie van de uitlijning van sterrenstelsels, die in dit proefschrift is uitgevoerd, is belangrijk voor verscheidene redenen. Zo biedt het niet alleen

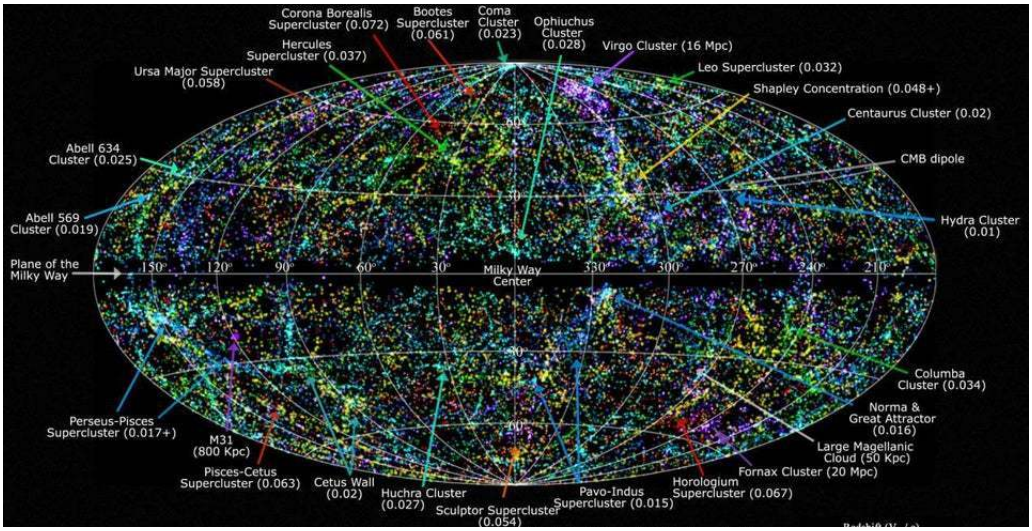

Figuur 6 – *Kaart van het universum die de sterrenstelsels van de 2MASS Redshift Survey. De kleuren geven de roodverschuiving van de sterrenstelsels aan, waarbij blauw dichtbij is en geel en rood verder weg. Deze afbeelding gemaakt door T.Jarret(IPAC/Caltech) en gebruikt sterrenstelsels van Huchra et al. (2012).*

informatie omtrent het vroege heelal, maar helpt het ook in het ontwikkelen van nauwkeurige modellen die kunnen corrigeren voor de effecten van de uitlijning op metingen van zwakke zwaartekracht lenswerking. Dit zal het mogelijk maken om toekomstige observaties van deze zwakke lenswerking, zoals met EUCLID, LSST en DESI gedaan zullen worden, beter te interpreteren. Daarnaast is er recentelijk begonnen om een kader te ontwikkelen om de massa van de rotatie-overgang te gebruiken om kosmologie te kunnen onderzoeken.

Het heelal in kaart brengen

Al vanaf de vroegste momenten in de geschreven historie toont de mensheid de drang om de wereld om zich heen te ontdekken en in kaart te brengen. Dit instinct beperkt zich niet slechts tot onze planeet, maar reikt veel verder: Tot aan het eind van ons heelal. Elk moment waarop de mens verder wist te komen met het ontdekken van de volgende, grotere fysieke schaal, ging dit gepaard met een verandering in de gebruikte definities en beschrijvingen van alles wat we zien. Zo heeft ook ons begrip van het heelal verscheidene paradigmaverschuivingen ondergaan. Onze voorouders dachten lange tijd dat het heelal bestond uit een klein aantal planeten, de maan en enkele sterren. Langzamerhand werd deze beschrijving uitgebreid naar de grenzen van ons sterrenstelsel, de Melkweg,

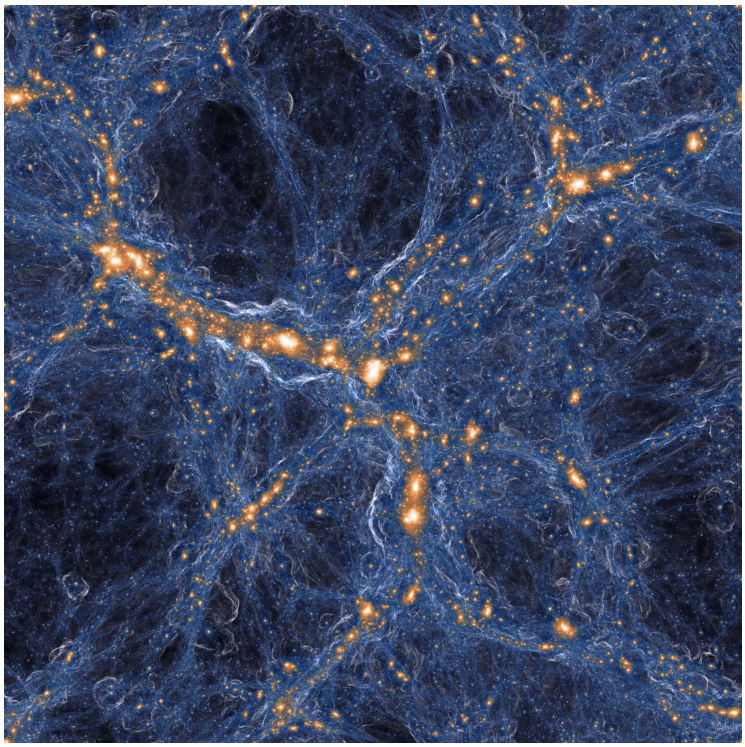

Figuur 7 – *Deze afbeelding laat de dichtheidsverdeling van donkere materie zien in de Illustris simulatie. Wit en oranje kleuren geven structuren aan in het kosmische web die ineengestort zijn door zwaartekracht. Referentie afbeelding: Illustris-collaboratie, (Vogelsberger et al. 2014).*

bestaande uit miljarden sterren. Men dacht destijds dat dit de rand van ons heelal is. Toen daarna steeds meer sterrenstelsels werden gevonden moest onze definitie van het heelal mee veranderen om de gevirialiseerde lokale clusters te omvatten. Door de opkomst van diepe spectroscopische observaties is het nu mogelijk geworden om de hemel zelfs nog verder in kaart te brengen. Figure 6 laat een recente kaart zien van het nabije heelal. Dit bevestigd dat materie op hele grote schaal (een paar tot meer dan 100 Megaparsecs) niet uniform verdeeld is. In werkelijkheid vormt het een intrigerend patroon dat doet denken aan een spons of een web en wordt daarom het kosmische web genoemd.

Sterrenstelsels, gas en alle materie in het heelal klonteren samen om filamenten, wanden en leegtes te vormen die zich manifesteren over een breed scala aan schalen en samen het kosmische web opmaken. Deze waarneming is het resultaat van de grote, eeuwenlange inspanningen om het heelal te verkennen. Zoals weergegeven in Figure 7, komen de karakteristieke patronen op grote schaal duidelijk naar voren in computersimulaties. De vele observaties samen met de opkomst van grote computersimulaties hebben een nieuwe fase ingeluid

van de studie van de grote-schaalstructuur.

De oorsprong van de structuren in het kosmische web is terug te leiden tot kleine fluctuaties in de dichtheid van het vroege heelal die door de zwaartekracht zijn uitvergroot. Onder invloed van hun eigen zwaartekracht groeien de gebieden met hogere dichtheid uit en worden steeds dichter terwijl materie juist uit de gebieden met lage dichtheid stroomt. Hierdoor wordt het contrast tussen de gebieden met hoge en lage dichtheid steeds groter. Uiteindelijk storten de dichtere gebieden ineen om objecten te vormen die zijn gebonden door de zwaartekracht, zoals halo's en sterrenstelsels. Daarentegen vormen de gebieden met lage dichtheid de leegtes in het heelal. Dit proces leidt tot het complexe netwerk van clusters met hoge dichtheid die worden verbonden via de lange filamenten die zijn ingenesteld in de wanden en leegtes. Dit is duidelijk te zien in Figure 7.

Dit proefschrift

In dit proefschrift hebben we de volgende hoofdvraag onderzocht: In welke mate beïnvloedt het kosmische web de rotatie (ook wel spin genoemd) en de vorm van halo's en sterrenstelsels?âĂĺOmdat het web zich manifesteert op meerdere schalen en door de ingewikkelde connectiviteit van het web is het moeilijk om precies vast te stellen welke processen op grote schaal invloed uitoefenen op de formatie van sterrenstelsels. Daarom hebben we ons gericht tot meerdere open vragen betreffende de uitlijning van de spins van halo's en sterrenstelsels in het kosmische web. Deze vragen pakken we aan door gebruik te maken van moderne numerieke simulaties en technieken om het kosmische web te detecteren.

Het signaal van de uitlijning is zwak en vereist daardoor een grote hoeveelheid objecten om het signaal duidelijk te kunnen meten. Het is daarbij een uitdaging om de bijdrage van de verscheidene relevante processen van elkaar te onderscheiden. Om dit aan te pakken hebben we het kosmische web geïdentificeerd in een P-Millennium simulatie met groot volume, met als doel om vervolgens de connectie tussen het web en de verdeling en eigenschappen van halo's te kunnen bestuderen over een groot bereik in halomassa. Op vergelijkbare wijze hebben we de uitlijning van de spin van sterrenstelsels bestudeerd door gebruik te maken van de hydrodynamische EAGLE-simulatie.

Het kosmische web en de grootte van de spin van halo's

Het anisotrope ineenstorten van gebieden met hoge dichtheid door het getijdenveld bij het ontstaan van het kosmische web heeft ook de eerste donkere materie halo's en de eerste sterrenstelsels aan het draaien gebracht. Derhalve kan worden verwacht dat de formatie van het web een afdruk heeft achtergelaten in de spins van de halo's en sterrenstelsels die zich in het kosmische netwerk bevinden.

In Hoofdstuk 2 laten we zien dat er een duidelijk verband bestaat tussen de omgeving van een halo en zijn spin (zie Figure 8). Halo's in filamenten roteren gemiddeld het snelst, terwijl halo's in knooppunten de kleinste spin hebben. Bovendien tonen we in Hoofdstuk 4 aan dat deze afscheiding tussen de spin van halo's in verschillende omgevingen zich zelfs op hogere roodverschuiving voordoet (zie onderste paneel in Figure 8). Dit stelt vast dat er overduidelijk een connectie bestaat tussen de groei van een halo en de omgeving op grote schaal.

Spin-transitie van halo's en sterrenstelsels

n Hoofdstuk 2 en Hoofdstuk 4 hebben we het signaal berekend van de uitlijning tussen de spin en filamenten. Dit wordt gemeten als de hoek tussen het impulsmoment van de halo en de as van het filament waarin de halo zich bevindt. Hiermee hebben we, met grotere waarschijnlijkheid dan voorheen, bevestigd dat halo's met lage massa voornamelijk parallel aan hun herbergende filament zijn uitgelijnd, maar dat de rotatie-as van massievere halo's voornamelijk loodrecht is uitgelijnd met de as van het filament. Dit geeft met hoge significantie aan dat er een transitie bestaat in de oriëntatie van de spin van halo's ten opzichte van de filamenten van het kosmische web.

De tijdsevolutie van deze trend is vervolgens bestudeerd in Hoofdstuk 4. Bij een vaste halomassa neigen de algehele halopopulaties om meer loodrecht aan de as van het filament te roteren op hoge roodverschuiving, vergeleken met halo's in het huidige heelal. Dit in tegenstelling tot de spin van individuele halo's, die op hoge roodverschuiving juist meer parallel is georiënteerd aan hun filament.

In Hoofdstuk 3 onderzoeken we de massa-afhankelijke trend voor sterrenstelsels in de EAGLE-simulatie. Hoewel we vonden dat de oriëntatie van de spin afhangt van de massa van het sterrenstelsel, ontdekten we geen overgang, zoals dat wel het geval was voor de halo's in de P-Millenium en EAGLE-simulaties. We ontdekten dat sterrenstelsels in EAGLE meer loodrecht roteren aan de

as van het filament vergeleken met het binnenste gedeelte van de donkere materie halo's. Dit impliceert dat de processen die verantwoordelijk zijn voor de accretie van impulsmoment licht verschillen van de processen bij halo's.

Om verder uit te zoeken waar de transitie in de spin van halo's vandaan komt hebben we in Hoofdstuk 2 ook de uitlijning van de binnenste gebieden van halo's bestudeerd. Dit werk toonde aan dat deze binnenste delen de oorspronkelijke oriëntatie van de getijdenkoppel met het getijdenveld beter behouden dan de buitenste delen. De buitenste gebieden worden veel meer beïnvloed door secundaire processen die zich later in de tijd voordoen, zoals accretie en samensmeltingen.

Dit laat duidelijk zien dat er een ingewikkelde wisselwerking plaatsvindt tussen de halo's en sterrenstelsels enerzijds en de dynamiek van het kosmische web anderzijds.

Eigenschappen van filamenten, web-identificatie en de transitiemassa

Om filamenten te identificeren moeten verscheidene uitdagingen worden overkomen. Zo is de verdeling van de geobserveerde objecten vaak schaars en is deze niet noodzakelijk representatief voor het onderliggende dichtheidsveld. Daarnaast meten observaties de roodverschuiving in plaats van de daadwerkelijke afstanden. Dit bracht ons ertoe om een vergelijking te maken tussen de netwerken die worden geïdentificeerd door verschillende methodes. We vergeleken het kosmische web gebaseerd op het dichtheidsveld met die van het snelheidsveld in Hoofdstuk 2. In Hoodfstuk 3 werd het verschil tussen filamenten geïdentificeerd in de donkere materie en filamenten uit de verdeling van sterrenstelsels onderzocht.

Hoofdstuk 2 vergelijkt de NEXUS+-code, waarin de kenmerken van het web worden geclassificeerd via de geometrische informatie van het dichtheidsveld, met de NEXUS_VELOCITY_SHEAR-code waarbij het web wordt geïdentificeerd op basis van de schuifspanningssnelheid. Hoewel beide methodes de hoofdkanalen van het netwerk weten te identificeren, is NEXUS+ ook in staat om de zwakkere filamenten die uitstrekken in de gebieden met lage dichtheid op te sporen.

Het verschil in de geïdentificeerde filamenten uit zich als verschillende populaties van halo's. Hierdoor verandert ook de transitiemassa waarop de spin van de halopopulatie overgaat van voornamelijk evenwijdig naar loodrecht op de oriëntatie van de as van het filament.

In Hoofdstuk 3 benadrukken we het belang van filamenten bij het begrip van

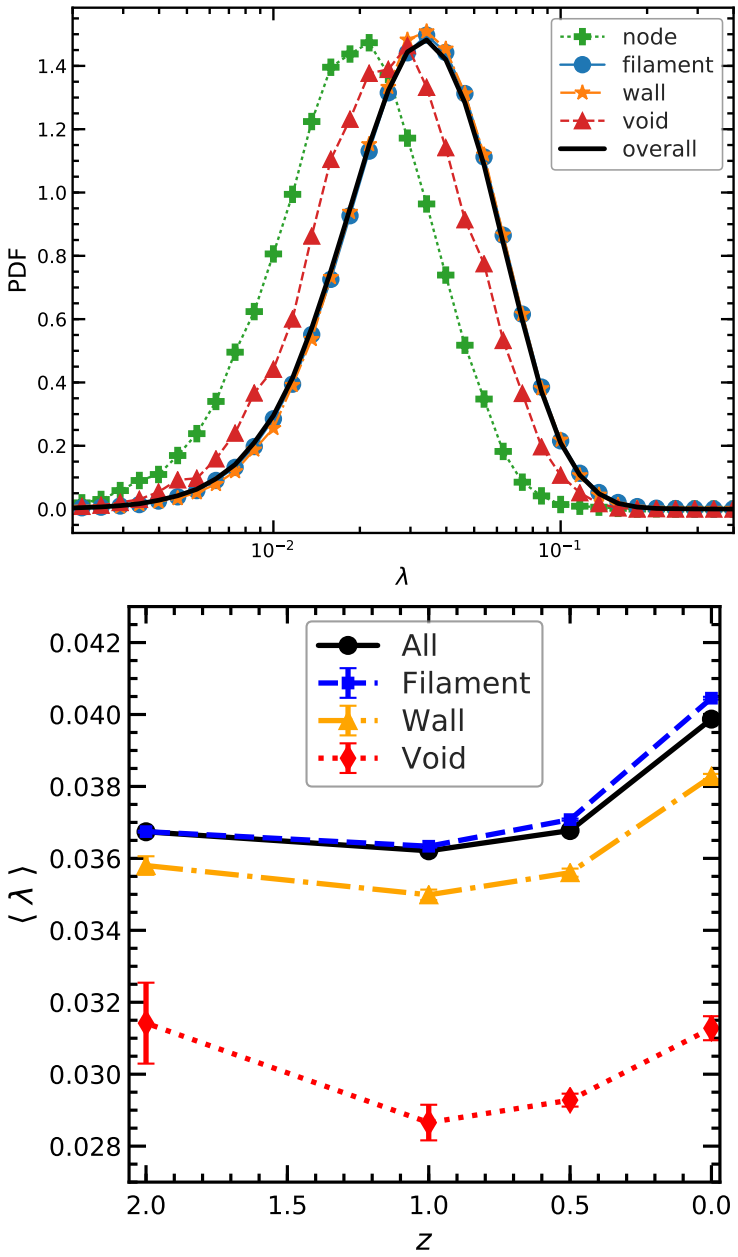

Figuur 8 – *bovenste paneel: De verdeling van de spin van halo's die zich bevinden in filamenten, leegtes, knooppunten of wanden. Onderste paneel: de mediaan van de spin van halo's als functie van de roodverschuiving. (Reproductie uit Ganeshaiah Veena et al. 2018,2020*

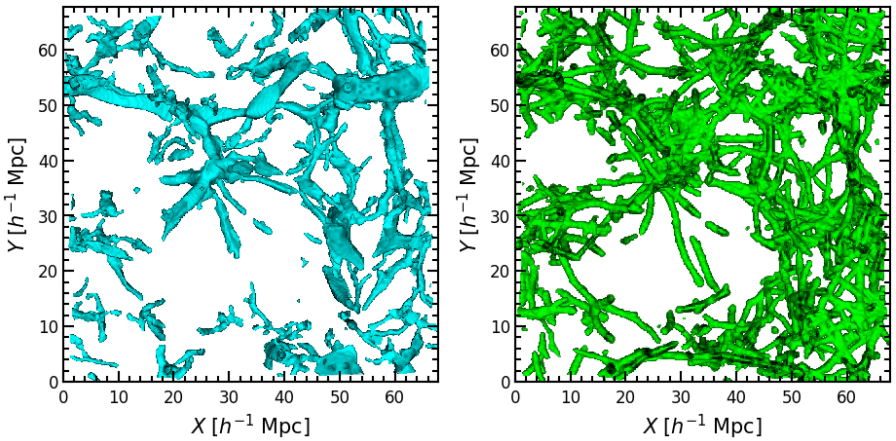

Figuur 9 – *De twee panelen laten respectievelijk* NEXUS+*-filamenten (die de verdeling van donkere materie volgen) en Bisous-filamenten (de verdeling van sterrenstelsels volgende) zien in hetzelfde deel van de EAGLE-simulatie met een dikte van* 10 h^{-1}Mpc*. De afbeelding is gereproduceerd uit Ganeshaiah Veena et al. 2019.*

de formatie van sterrenstelsels. We tonen aan dat zo'n 50% van alle materie en zo'n 80% van alle sterrenstelsels in het heelal zich in de filamenten bevindt. Tevens vergelijken we de uitlijning van de spin en de vorm van sterrenstelsels in filamenten getraceerd door de donkere materie (NEXUS+) met filamenten in de verdeling van sterrenstelsels (Bisous). Hoewel NEXUS ook kan werken met de verdeling van sterrenstelsels of gas, is voor dit onderzoek gekozen om het toe te passen op de verdeling van donkere materie. De vergelijking van de twee methodes wordt uitgebeeld in Figure 9. Hierin is het verschil te zien tussen filamenten van NEXUS+ en die van de Bisous-methode in hetzelfde volume van de hydrodynamische EAGLE-simulatie. Globaal gezien vonden we dat de netwerken van filamenten redelijk consistent met elkaar waren, waarbij de verschillen in de uitlijning van de spin goed te begrijpen en te karakteriseren zijn.

Bovendien laten we in Hoodstuk 2 en Hoofdstuk 4 zien dat er verschillen bestaan tussen filamenten en dat ze kunnen worden geclassificeerd op basis van hun eigenschappen, zoals dikte. De eigenschappen van halo's en sterrenstelsels zijn verbonden aan de eigenschappen van hun herbergende filament. De transitiemassa varieert sterk (meer dan een orde van grootte) met de dikte van de filamenten, waarbij deze massa het grootst is in de dikste filamenten.

Connectie tussen halo en sterrenstelsel

Een interessante vraag die gesteld kan worden, is of het mogelijk is om het impulsmoment van een sterrenstelsel te voorspellen voor een gegeven impulsmoment van de donkere materie halo, en omgekeerd. Deze vraag bespreken we in Hoofdstuk 3 met behulp van de uitlijning tussen de vorm van sterrenstelsels en filamenten.

Door gebruik te maken van de EAGLE-simulatie heb we bestudeerd in hoeverre de uitlijning van de spin van een halo ten opzichte van het filament invloed heeft op de spin en vorm van zijn sterrenstelsel en andersom. In Figure 10 wordt de uitlijning tussen de korte as van de halo en die van het sterrenstelsel weergegeven voor twee populaties: sterrenstelsels waarbij de korte as loodrecht staat op het filament en sterrenstelsels waar deze evenwijdig ligt aan het filament. We ontdekten dat de loodrechte sterrenstelsels beter zijn uitgelijnd met de donkere materie halo's waarin ze zich bevinden dan de evenwijdige sterrenstelsels.

Op vergelijkbare wijze hebben we de uitlijning tussen spin en filamenten bestudeerd voor halo's die een elliptisch sterrenstelsel bevatten en halo's met een spiraalstelsel. De halo's met een elliptisch stelsel tonen een voorkeur voor loodrechte uitlijning met het filament. Halo's met een spiraalstelsel daarentegen, roteren duidelijk evenwijdig aan de as van het filament waarin ze zich bevinden. Het is daarom mogelijk om een voorspelling te maken voor de uitlijning van de spin en vorm van een halo met een filament door te kijken naar de uitlijning van hun sterrenstelsels.

Dit is een cruciale ontdekking die belangrijk zal zijn voor nieuwe testen in de kosmologie omdat het hiermee mogelijk is om op een statistische manier voorspellingen te maken voor de vorm en oriëntatie van donkere materie halo's.

Afsluitende woorden

Kort samengevat onthult dit proefschrift de ingewikkelde wisselwerking tussen de mechanismen die zich voordoen op grote schaal en de eigenschappen van halo's en sterrenstelsels. We hebben laten zien dat er vanuit de omgeving in het kosmische web verscheidene processen verantwoordelijk zijn voor de evolutie van hun spin. Zo wordt de uitlijning tussen een sterrenstelsel en filament sterk beïnvloed door non-lineaire effecten die zich later voordoen in de tijd. Dit is van groot belang voor het voorspellen van de intrinsieke uitlijning bij kosmologische onderzoeken naar de zwakke zwaartekracht lenswerking. Bovendien tonen we aan dat de uitlijning verschilt, afhankelijk van de eigenschappen van de component van het web waarin de halo of het sterrenstelsel zich bevindt.

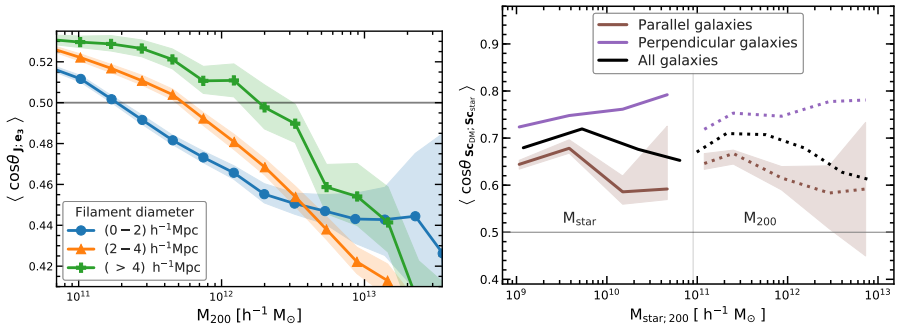

Figuur 10 – *Het linker paneel toont de mediaan van het signaal van de uitlijning tussen spin en filamenten voor halo's in dunne, gemiddelde en dikke filamenten. Het paneel rechts geeft de mediaan weer van de uitlijning tussen de korte as van centrale sterrenstelsels en de korte as van hun halo's. Dit is afzonderlijk geplot voor sterrenstelsels die evenwijdig en loodrecht aan de as van de filamenten roteren. Loodrechte sterrenstelsels zijn beter uitgelijnd met hun halo's dan sterrenstelsels die evenwijdig staan aan de as van het filament. (Verwerkt uit Ganeshaiah Veena et al. 2018, 2019).*

We laten dit met name zien voor de eigenschappen van filamenten, de component dat de meeste heldere sterrenstelsels herbergt. Bij de volgende stap in dit onderzoeksveld zal het noodzakelijk zijn om vast te stellen hoe precies deze uitlijning de metingen van de zwakke zwaartekracht lenswerking beïnvloeden om zo de juiste kosmologische parameters te kunnen bepalen. Daarnaast moet verder worden onderzocht hoe gevoelig de transitiemassa is voor de onderliggende kosmologie en of het zodanig kan worden gebruikt om de kosmologische parameters te meten. Als laatste zal er uitgebreider onderzoek naar de uitlijning tussen de spin van sterrenstelsels en de filamenten moeten plaatsvinden met behulp van grote simulaties om modellen te ontwikkelen waarmee de spin van hun halo's kan worden voorspeld. Dit alles zal helpen om meer licht te werpen op de donkere componenten van ons heelal.

Saaraamsha

ನಮ್ಮ ಸುತ್ತಲಿನ ಬ್ರಹ್ಮಾಂಡದಲ್ಲಿ ಎಲ್ಲಾ ವಸ್ತುಗಳು- ಸಣ್ಣ ಸಣ್ಣ ಉಲ್ಕೆಗಳಿಂದ ಬೃಹತ್ ಗ್ರಹಗಳವರೆಗೂ, ಕೋಟಿ ಕೋಟಿ ನಕ್ಷತ್ರಗಳನ್ನು ಒಡಲಲ್ಲಿ ಹೊಂದಿರುವ ನಕ್ಷತ್ರಪುಂಜಗಳಿಂದ, ದಶಕೋಟಿಗೂ ಹೆಚ್ಚಿನ ನಕ್ಷತ್ರಪುಂಜಗಳ ಸಾಲು 'ತಂತು' /'ಎಳೆ'ಗಳವರೆಗೂ, ತಮ್ಮದೇ ಕಕ್ಷೆಯ ಸುತ್ತ ನಿರಂತರವಾಗಿ ಸುತ್ತುತ್ತಲೇ ಇವೆ. ಈ ಸುತ್ತುವಿಕೆಯ ಮೂಲ ಚೇತನ, ವಿಶೇಷವಾಗಿ ನಕ್ಷತ್ರಪುಂಜಗಳ ಹಾಗೂ ಅವುಗಳ ನಿಶಾಭಾಗದ ನಿರ್ವಾತಗಳ (dark matter halo) ಭ್ರಮಣದ ಹಿಂದಿನ ಶಕ್ತಿ, ಇಂದಿಗೂ ಸಂಪೂರ್ಣವಾಗಿ ಬೇದಿಸಲಾಗದೆ ನಿಗೂಢವಾಗಿಯೇ ಉಳಿದಿದೆ. ಒಂದು ಪ್ರಸಿದ್ಧ ಸಿದ್ಧಾಂತದ ಪ್ರಕಾರ, ಈ ಸೃಷ್ಟಿಯ ಬ್ರೂಣಾವಸ್ಥೆಯಲ್ಲಿ, ಎಲ್ಲಾ ಘನಕಣಗಳ ಸಮೂಹವು ಕ್ರೋಡೀಕೃತಗೊಳ್ಳುತ್ತಿದ್ದಾಗ ಉಂಟಾದ ಅಸಮಾವರ್ತಕ ಘನವಿತರಣೆಯೇ ಪ್ರೋಟೊ-ನಕ್ಷತ್ರಪುಂಜ ಮೋಡಗಳ ಸುತ್ತುವಿಕೆಯ ಮೂಲ ಚೇತನಶಕ್ತಿ ಎಂದು ವಾದಿಸಲಾಗಿದೆ. ಹಾಗೆ ಸೂಕ್ಷ್ಮವಾಗಿ ಗಿರಕಿ ಹೊಡೆಯುವಂತೆ ಪ್ರಾರಂಭವಾದ ಕಣಸಮೂಹದ ಮೋಡಗಳು ಕಾಲಕ್ರಮೇಣ ಸ್ವ-ಗುರುತ್ವಾಕರ್ಷಣೆಗೆ ಕುಸಿದು, ತಿರ್ರನೆ ತಿರುಗುವ ಸುರುಳಿ ನಕ್ಷತ್ರಪುಂಜಗಳಾಗಿ ಬೆಳೆದವು.

ಕಳೆದ ಎರಡು ದಶಕಗಳಲ್ಲಿ ದೊರೆತಿರುವ ಆಧಾರಗಳ ಪ್ರಕಾರ, ನಕ್ಷತ್ರಪುಂಜಗಳು ತಿರುಗುತ್ತಿರುವ ಕಕ್ಷೆಗಳ ದಿಕ್ಕುಗಳಿಗೂ, ಮತ್ತು ಅದೇ ನಕ್ಷತ್ರ ಪುಂಜಗಳನ್ನೊಳಗೊಂಡಿರುವ, ಭ್ರಹ್ಮಾಂಡದ ಮಹಾರಚನೆಗಳ ಅಭಿಮುಖಕ್ಕೂ ಪರಸ್ಪರ ಸಂಬಂಧವಿದೆ ಎಂದು ವಿಧಿತವಾಗಿದೆ. ಪ್ರಸ್ತುತ ಈ ಸಂಶೋಧನಾ ಪ್ರಬಂಧದಲ್ಲಿ ಬೃಹತ್ ಸಂಖ್ಯಾಧ್ಮಕ ಮಾಹಿತಿಯನ್ನಾಧರಿಸಿ, ಭ್ರಹ್ಮಾಂಡದ ರಚನಾಜಾಲ ಮತ್ತು ನಕ್ಷತ್ರಪುಂಜಗಳ ಸುತ್ತುವಿಕೆಯ ನಡುವೆ ಇರಬಹುದಾದ ಸಂಕೀರ್ಣವಾದ ಸಹಸಂಬಧವನ್ನು ವಿಶ್ಲೇಸಿಸಲಾಗಿದೆ. ವಿಶೇಷವಾಗಿ, ನಕ್ಷತ್ರ ಪುಂಜಗಳ ಮತ್ತು ಅವುಗಳ ನಿಶಾಭಾಗಗಳು ತಿರುಗುವ ದಿಕ್ಕಿಗೂ, ಹಾಗೂ ಆ ನಕ್ಷತ್ರ ಪುಂಜಗಳ ಸಾಲುತಂತುಗಳ ಅಭಿಮುಖಕ್ಕೂ ಇರುವ ಸಹಸಂಬಂಧವು ಸಮನಾಂತರ ಸ್ಥಿತಿಯಿಂದ ಲಂಬಸ್ಥಿತಿಗೆ ಸಂಕ್ರಮಣವಾಗುವ ಪ್ರಕಾರವನ್ನು ಅಧ್ಯಯನ ಮಾಡುವುದರ ಜೊತೆಗೆ, ಅಂಥಹ ಸ್ಥಿತಿಪಲ್ಲಟಕ್ಕೆ ಕಾರಣವಾದ ಅಂಶಗಳನ್ನು ಗುರುತಿಸಲಾಗಿದೆ. ಉದಾಹರಣೆಗೆ ಅಂಥಹ ಸ್ಥಿತಿಪಲ್ಲಟದ ಸೂಚಕ-ಕೋನಗಳ ಮೇಲೆ, ತಂತುಗಳ ಗುಣಗಳು, ಕೆಂಪುವರ್ಣ ಪಲ್ಲಟಳ (redshift), ಮುಂತಾದ ಅಂಶಗಳು ಹೇಗೆ ಪ್ರಭಾವ ಬೀರುತ್ತವೆ ಎನ್ನುವುದನ್ನೂ ಪರಿಶೀಲಿಸುವತ್ತ ಈ ಅಧ್ಯಯನ ಗಮನ ಹರಿಸಿದೆ. ಅಂತೆಯೇ ನಕ್ಷತ್ರಪುಂಜಗಳ ಮತ್ತು ಅವುಗಳ ನಿಶಾಭಾಗಗಳ ಸುತ್ತುವಿಕೆಯ ಮೇಲೆ ಬ್ರಹ್ಮಾಂಡದ ರಚನಾಜಾಲದ ಪ್ರಭಾವ ಹೇಗಿರಬಹುದು ಎನ್ನುವುದರ ಬಗ್ಗೆಯೂ ಇಲ್ಲಿ ವಿಶ್ಲೇಶಿಸಲಾಗಿದೆ. ಆ ಮೂಲಕ ಸುರುಳಿ ಪುಂಜಗಳ ರಚನೆ ಮತ್ತು ರೂಪದ ಬಗ್ಗೆಯೂ ಅರಿಯುವ ಪ್ರಯತ್ನ ಮಾಡಲಾಗಿದೆ.

ನಕ್ಷತ್ರ ಪುಂಜಗಳ ಭ್ರಮಣ ತೋರುವ ನಿಯೋಜನೆಯ ಬಗೆಗಿನ ಅಧ್ಯಯನವು ಹಲವಾರು ರೀತಿಯಲ್ಲಿ ಪ್ರಮುಖ. ಅಂಥಹ ಅಧ್ಯಯನವು ಸೃಷ್ಟಿಯ ಪ್ರಾರಂಭದ ಸ್ಥಿತಿಯ ಬಗ್ಗೆ ಮಾಹಿತಿಯನ್ನು ಒದಗಿಸುತ್ತದೆ. ಜೊತೆಗೆ, ನಕ್ಷತ್ರ ಪುಂಜಗಳ ಅಭಿಮುಖ ನಿಯೋಜನೆಯು ಅವು ಸೃಷ್ಟಿಸುವ ದುರ್ಬಲ ರೂಪದ ಮಸೂರ ಕ್ರಿಯೆಯ ಮೇಲೆ ಉಂಟುಮಾಡಬಹುದಾದ ಪ್ರಭಾವವನ್ನು ಅರಿಯಲು ಸೂಕ್ತ ಮಾದರಿಯನ್ನೂ ರಚಿಸಲು ಸಹಕಾರಿಯಾಗುತ್ತದೆ. ಇದರಿಂದಾಗಿ EUCLID, LSST ಮತ್ತು DESI ಮುಂತಾದ ಮಸೂರ ಸಂವೀಕ್ಷ-

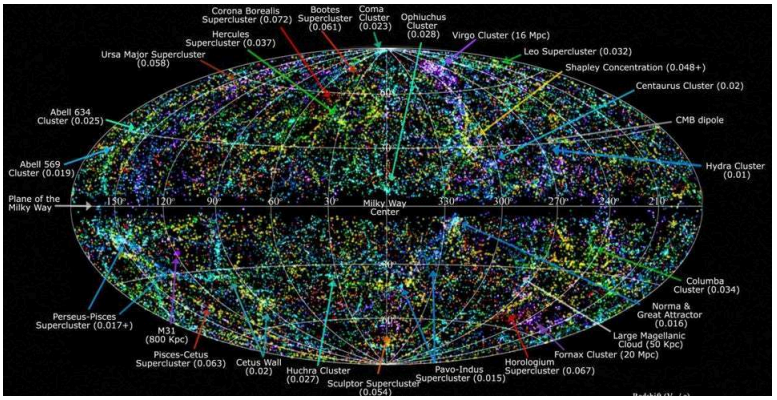

ಚಿತ್ರ 1 – ಬ್ರಹ್ಮಾಂಡದ ನಕ್ಷೆ. ಈ ನಕ್ಷೆಯಲ್ಲಿ *2MASS* ಕೆಂಪುವರ್ಣದ ಪಲ್ಲಟ ಸಂವೀಕ್ಷಣೆಯಿಂದ ಕಂಡ ನಕ್ಷತ್ರಪುಂಜಗಳನ್ನು (ಬಣ್ಣದ ಚುಕ್ಕೆಗಳು) ತೋರಿಸಲಾಗಿದೆ. ಹಸಿರು ಚುಕ್ಕೆಗಳು ನಮಗೆ ಅತೀ ಹತ್ತಿರದ ನಕ್ಷತ್ರ ಪುಂಜಗಳನ್ನೂ, ಹಳದಿ ಮತ್ತು ಕೆಂಪುಚುಕ್ಕೆಗಳು ಕ್ರಮೇಣ ನಮ್ಮಿಂದ ದೂರದಲ್ಲಿರುವ ನಕ್ಷತ್ರ ಪುಂಜಗಳನ್ನೂ ಸೂಚಿಸುತ್ತವೆ. ಚಿತ್ರ ಋಣ: *T.Jarret(IPAC/Caltech) using galaxies from Huchra et al. (2012).*

ಣೆಯ ಫಲಿತಾಂಶಗಳನ್ನು ಸೂಕ್ತ ರೀತಿಯಲ್ಲಿ ಅರ್ಥೈಸಲೂ ಸಾಧ್ಯವಾಗುತ್ತದೆ. ನಕ್ಷತ್ರ ಪುಂಜಗಳ ಸುತ್ತುವಿಕೆಯು ತೋರುವ ನಿಯೋಜನೆಯ ಅಧ್ಯಯನದ ಪರಿಣಾಮವಾಗಿ ಇತ್ತೀಚೆಗಂತೂ ಅವುಗಳ 'ಗಿರಕಿ ಸಂಕ್ರಮಣ ತೂಕ' ದ ಬಗೆಗಿನ ಪರಿಕಲ್ಪನೆಯು ಭ್ರಹ್ಮಾಂಡದ ಅಂತರ್ಯವನ್ನು ಅರಿಯುವಲ್ಲಿ ಒಂದು ಪ್ರಮುಖ ಸಾಧನವಾಗಿ ಹೊರಹೊಮ್ಮುತ್ತಿದೆ.

ಬ್ರಹ್ಮಾಂಡದ ನಕ್ಷೆ

ಕಾಣದ್ದನ್ನು ಹುಡುಕುವಲ್ಲಿ, ಕಂಡದ್ದನ್ನು ಅರಿತು ಚಿತ್ರಿಸುವುದರಲ್ಲಿ ಮಾನವನಿಗೆ ಎಂದಿಗೂ ತಣಿಯದ ಆಸಕ್ತಿ. ಚರಿತ್ರೆಯ ಉದ್ದಕ್ಕೂ, ಮಾನವ ತನ್ನ ಸುತ್ತಲಿನ ಪ್ರಪಂಚವನ್ನು ಅನ್ವೇಷಿಸಿ ಅದರ ನಕ್ಷೆಯನ್ನು ತಯಾರಿಸಲು ಸದಾ ಕಾತುರತೆ ತೋರಿದ್ದಾನೆ. ಈ ಕಾತುರತೆ ಅವನನ್ನು ಬ್ರಹ್ಮಾಂಡದ ಅಂಚಿಗೂ ಸೆಳೆದೊಯ್ದಿದೆ. ಆ ಮಹಾನ್ವೇಷಣೆಯಲ್ಲಿ, ತನ್ನ ವೀಕ್ಷಣೆಯ ವಿಸ್ತಾರದ ಮಿತಿ ಜಿಗಿದಂತೆಲ್ಲ, ಬ್ರಹ್ಮಾಂಡದ ವ್ಯಾಖ್ಯಾನ ಮತ್ತು ಅದರ ಚಿತ್ರಣದ ರೂಪ ರೇಷೆಗಳೂ ಕೂಡ ಅಭೂತಪೂರ್ವವಾಗಿ ಬದಲಾಗುತ್ತಲೆ ಇವೆ. ಬಹಳಷ್ಟು ಕಾಲ ಇಡೀ ಬ್ರಹ್ಮಾಂಡವು ಸೌರಮಂಡಲ, ಮತ್ತು ಇತರೆ ಕೆಲವು ನಕ್ಷತ್ರಗಳನ್ನು ಮಾತ್ರವೆ ಹೊಂದಿದೆ ಎಂಬ ಚಿತ್ರಣವನ್ನು ಕಟ್ಟಿಕೊಂಡಿದ್ದ. ಕ್ರಮೇಣ, ಬ್ರಹ್ಮಾಂಡದ ವ್ಯಾಪ್ತಿಯು ಶತ ಶತ ಕೋಟಿ ನಕ್ಷತ್ರಗಳಿಂದ ಕೂಡಿರುವ ನಮ್ಮದೆ ನಕ್ಷತ್ರ ಪುಂಜವಾದ ಕ್ಷೀರಪಥದ ದಿಗಂತದವರೆಗೂ ಹರಡಿ ಅದರ ಪರಿದಿಯನ್ನೆ ಈ ಬ್ರಹ್ಮಾಂಡದ ಗಡಿ ಎಂದು ಬಾವಿಸಲಾಗಿತ್ತು. ಆನಂತರ, ನಮ್ಮದೆ ನಕ್ಷತ್ರಪುಂಜದಂತಹ ನೂರಾರು, ಸಾವಿರಾರು ..ಅಷ್ಟೆ ಅಲ್ಲ ಕೋಟಿ ಕೋಟಿ ಸಂಖ್ಯೆಯಲ್ಲಿವೆ ಎಂದೂ, ಅವೆಲ್ಲವೂ ಅಲ್ಲಲ್ಲಿ ತಮ್ಮದೇ ಗುಂಪುಗಳಲ್ಲಿ, ಪರಸ್ಪರ ಗುರುತ್ವಾಕರ್ಷಣೆಯ ಸಮತೋಲನದ ಪರಿದಿಯೊಳಗೆ ಗುಚ್ಚಗಳಂತೆ ಹರಡಿಕೊಂಡಿವೆ ಎಂದೂ ತಿಳಿದುಬಂತು. ಬ್ರಹ್ಮಾಂಡದ ಆಳದೊಳಗಿನ ಬೆಳಕಿನ ಮೂಲಗಳನ್ನು ವಿಭಜಿಸಿ ಅವಲೋಕಿಸುವ ಸ್ಪೆಕ್ಟ್ರೋಸ್ಕೋಪ್ ಯಂತ್ರಗಳ ಅನ್ವೇಷಣೆಯ ಮೂಲಕ ನಡೆಸಿದ ಸಂವೀಕ್ಷಣೆಯ ಫಲವಾಗಿ, ನಾವಿಂದು ನಬೋಮಂಡಲದ ಬೃಹತ್ ವಿಸ್ತಾರದಲ್ಲಿನ ಬ್ರಹ್ಮಾಂಡದ ನಕ್ಷೆಯನ್ನು ರಚಿಸಲು ಸಾಧ್ಯವಾಗಿದೆ (Figure 1). ಈ ಮೂಲಕ, ನಬೋಮಂಡಲದಲ್ಲಿನ ೧೦೦ ಮೆಗಾಪಾರ್ಸೆಕ್ ಗಳ ವರೆಗಿನ ವಿಸ್ತಾರದಲ್ಲಿ ಹರಡಿಕೊಂಡಿರುವ ಘನ ಸಮೂಹದ ಹರಹುವಿನ ಸ್ಥಿತಿಯನ್ನು ಅವಲೋಕಿಸಿಲಾಯಿತು. ಆಗ ಕಂಡುಬಂದದ್ದು, ಬ್ರಹ್ಮಾಂಡದ ಘಟಕಗಳು ಎಲ್ಲೆಡೆಯೂ ಸಮನಾಗಿ ಅಥವ ಸಮವರ್ತಕ ಸ್ಥಿತಿಯಲ್ಲಿ ಹರಡಿಕೊಂಡಿಲ್ಲ, ಬದಲಿಗೆ ಸ್ಪಂಜಿನ ಹಾಗೆ ಅಲ್ಲಲ್ಲಿ ಟೊಳ್ಳುಗಳ ಸುತ್ತ, ಬಲೆಯಂತೆ ಅಥವ ಜಾಲದಂತೆ ಹರಡಿಕೊಂಡಿದೆ ಎಂದು.

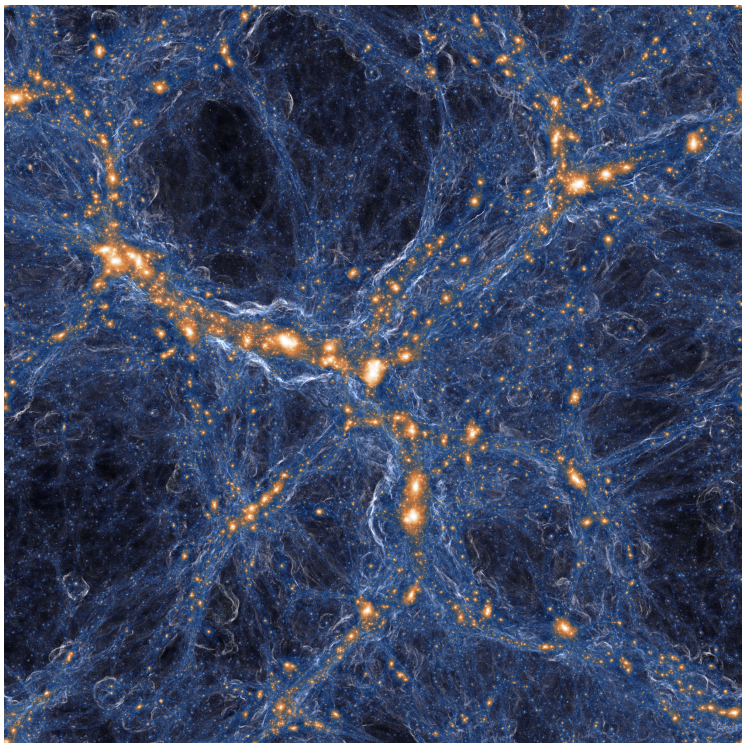

ಚಿತ್ರ 2 □ *Illustris*ನ ಮೂಲಕ ಪಡೆದ ನಿಶಾಭಾಗದ ಘನಸಾಂದ್ರತೆಯನ್ನು ಬಿಂಬಿಸುವ ಚಿತ್ರಣ. ಬಿಳಿ ಮತ್ತು ಕಿತ್ತಳೆ ಬಣ್ಣದ ಬಾಗಗಳು, ಬ್ರಹ್ಮಾಂಡದಲ್ಲಿ, ಸ್ವಗುರುತ್ವಾಕರ್ಷಣೆಯಿಂದ ಕುಸಿದ ಕೇಂದ್ರಗಳನ್ನು ತೋರಿಸುತ್ತದೆ. ಚಿತ್ರ ಋಣ: *Illustris collaboration (Vogelsberger et al. 2014)*.

ಬ್ರಹ್ಮಾಂಡದ ಈ ರಚನೆಯನ್ನು ಅರಿಯಲು ಮಾನವ ತೋರಿದ ಅವಿರತ ಪರಿಶ್ರಮದ ಫಲವಾಗಿ ಇಂದು ದೊರಕಿರುವ ಚಿತ್ರಣದ ಪ್ರಕಾರ, ನಕ್ಷತ್ರಪುಂಜಗಳು, ಎಲ್ಲೆಲ್ಲೂ ಆವರಿಸಿರುವ ಮೂಲ ಅನಿಲ, ಮತ್ತು ಘನಕಣ ಇವೆಲ್ಲವೂ ಅಲ್ಲಲ್ಲಿ **ಗುಚ್ಚ**ಗಳಾಗಿ, **ತಂತು/ಎಳೆ**ಗಳಾಗಿ, ಕೆಲವೆಡೆ **ಪದರು**ಗಳಂತೆ, ಮತ್ತು ಬಹುಪಾಲು **ನಿರ್ವಾತ**ಗಳ ರೂಪದಲ್ಲಿ ಸ್ಥಿತ್ಯವಾಗಿ ಬ್ರಹ್ಮಾಂಡವನ್ನು ರೂಪಿಸಿವೆ. ಹಾಗಾಗಿ ನಮ್ಮ ವೀಕ್ಷಣೆಯ ಪರಿದಿಯಲ್ಲಿ ನಾವು ಕಾಣುವುದು ನಕ್ಷತ್ರಪುಂಜಗಳ ಸಾಲು 'ತಂತು'ಗಳ, 'ಪದರು'ಗಳ, ಅದೇ ನಕ್ಷತ್ರಪುಂಜಗಳು ಕೇಂದ್ರೀಕೃತವಾಗಿವ 'ಗಂಟು/ಗುಚ್ಚ'ಗಳ, ಮತ್ತು ಮಹಾ ನಿರ್ವಾತಗಳ, **'ಬ್ರಹ್ಮಾಂಡ ಜಾಲ'**ವನ್ನು. ಬ್ರಹ್ಮಾಂಡದ ಉಗಮ ಮತ್ತು ಬೆಳವಣಿಗೆಯನ್ನು ಪ್ರತಿಬಿಂಬಿಸುವಂತೆ ಗಣಕಯಂತ್ರದಲ್ಲಿ ರೂಪಿಸಿದ ಚಿತ್ರಣವೂ ಇಂತದೆ ರಚನೆಯನ್ನು ಸೂಚಿಸಿದೆ (Figure 2). ಹೀಗೆ ಆಕಾಶ ವೀಕ್ಷಣೆಯಿಂದ ಮತ್ತು ಗಣಕಯಂತ್ರದಲ್ಲಿ ರೂಪಿಸಿದ ಚಿತ್ರಣಗಳ ನಡುವಿನ ಸಾದೃಶ ಹೋಲಿಕೆಯು ಬ್ರಹ್ಮಾಂಡದ ಉಚ್ಚರಚನೆಯ ಬಗೆಗಿನ ನಮ್ಮ ಅರಿವಿಗೆ ಹೊಸ ನಾಂದಿ ಹಾಡಿದೆ ಎನ್ನಬಹುದು.

ಬ್ರಹ್ಮಾಂಡದ ರಚನೆಯಲ್ಲಿ ನಾವು ಕಾಣುವ ಈ ಭಿನ್ನವಾದ ಹಾಗೂ ಸ್ಪಷ್ಟವಾದ ರಚನೆಗಳು (ತಂತುಗಳು, ಗೋಡೆಗಳು ಹಾಗೂ ನಿರ್ವಾತಗಳು) ಸೃಷ್ಟಿಯ ಉಗಮದ ಸಮಯದಲ್ಲಿ ಘನಕಣಗಳ ಸಾಂಧ್ರತೆಯಲ್ಲಿ ಉಂಟಾಗಿದ್ದ ಸಣ್ಣ ಸಣ್ಣ ಏರುಪೇರುಗಳನ್ನು ಗುರುತ್ವಾಕರ್ಷಣೆ ಶಕ್ತಿಯು ಉಲ್ಬಣಗೊಳಿಸಿದ್ದರ ಪರಿಣಾಮದಿಂದ. ಮೂಲದಲ್ಲಿ ಸಾಂಧ್ರತೆಯಲ್ಲಿ ತಾರುಮಾರಾಗಿ ಸೂಕ್ಷ್ಮ ಏರುಪೇರುಗಳಾದಾಗ, ಸಾಂಧ್ರತೆ ಹೆಚ್ಚಿದ್ದ ಕಡೆಯ ಘನಕಣಗಳ ಗುರುತ್ವಾಕರ್ಷಣೆಗೆ ಕಡಿಮೆ ಸಾಂಧ್ರತೆಯಲ್ಲಿರುವ ಕಣಗಳು ಆಕರ್ಶಿತಗೊಳ್ಳುತ್ತವೆ. ಇದರಿಂದಾಗಿ ಸಾಂಧ್ರತೆ ಹೆಚ್ಚಿದ್ದ ಕಡೆಯೆ ಮತ್ತಷ್ಟು ಕಣಗಳು ಸೇರಿ, ಸಾಂಧ್ರತೆ ಇನ್ನೂ ಹೆಚ್ಚಾಗುವುದರಿಂದ ಅವುಗಳ ಒಟ್ಟಾರೆ ಆಕರ್ಶಕ ಶಕ್ತಿ ವೃದ್ಧಿಯಾಗುತ್ತದೆ. ಆದರೆ, ಆಕರ್ಶಿತಗೊಂಡ ಜಾಗಗಳಲ್ಲಿನ ಕಣಗಳು ಕಡಿಮೆಯಾಗುವುದರಿಂದ, ಅವು ಇನ್ನೂ ದುರ್ಬಲವಾಗಿ ಮತ್ತಷ್ಟು ಆಕರ್ಶಿತಗೊಳ್ಳುತ್ತವೆ. ಗುರುತ್ವಾಕರ್ಶ-

ಣೆಯ ಈ ಅನನ್ಯ ಕ್ರಿಯೆಯ ಅವಿಚ್ಛಿನ್ನವಾದ ಪುನರಾವರ್ತನೆಯಿಂದಾಗಿ ಸೂಕ್ಷ್ಮವಾದ ಭಿನ್ನತೆಗಳಿಂದ ಪ್ರಾರಂಭವಾಗುವ ಬ್ರಹ್ಮಾಂಡವು ಕಾಲಕಳೆದಂತೆ ದಟ್ಟ ಹಾಗೂ ವಿರಳ ಬಾಗಗಳಾಗಿ ಬೇರ್ಪಡುತ್ತ ಸಾಗುತ್ತದೆ. ಕ್ರಮೇಣ ದಟ್ಟವಾದ ಬಾಗಗಳ ಕೇಂದ್ರದತ್ತ ಘನಕಣಗಳು ಕುಸಿದು ನಕ್ಷತ್ರ ಪುಂಜಗಳು ಉದಯಿಸಿದರೆ, ವಿರಳವಾದ ಬಾಗಗಳಿಂದ ಕಣಗಳು ಸಂಪೂರ್ಣವಾಗಿ ಕಾಲಿಯಾಗಿ ಅಲ್ಲಿ ಶೂನ್ಯತೆ ಸೃಷ್ಟಿಯಾಗುತ್ತದೆ. ಈ ಆಕರ್ಷಣಕ್ರಿಯೆಯ ಅಸಮಾನತೆ ಮುಂದುವರಿದಂತೆ, ಅತೀ ದಟ್ಟವಾದ ಬಾಗಗಳು ತಂತುಗಳಾಗಿ, ಪದರುಗಳಾಗಿ ನೆಲೆನಿಂತರೆ, ಶೂನ್ಯ ಸ್ಥಳಗಳು ವಿಶಾಲವಾದ ನಿರ್ವಾತಗಳಾಗಿ ರೂಪುಗೊಳ್ಳುತ್ತವೆ (Figure 2).

ಈ ಪ್ರಬಂಧ

ಪ್ರಸ್ತುತ ಪ್ರಬಂಧದಲ್ಲಿ ನಾವು ಹಲವು ಪ್ರಶ್ನೆಗಳನ್ನು ಉತ್ತರಿಸಲು ಪ್ರಯತ್ನಿಸಿದ್ದೇವೆ: ನಕ್ಷತ್ರ ಪುಂಜಗಳ ಮತ್ತು ಅವುಗಳ ಸುತ್ತ ಆವರಿಸಿಕೊಂಡಿರುವ ನಿಶಾಭಾಗಗಳ ಸುತ್ತುವಿಕೆ (ಗಿರಕಿ)ಯನ್ನು ಮತ್ತು ಆಕಾರಗಳನ್ನು ರೂಪಿಸುವಲ್ಲಿ ಬ್ರಹ್ಮಾಂಡಜಾಲದ ಪಾತ್ರವೇನು? ಬ್ರಹ್ಮಾಂಡ ಜಾಲದ ವಿವಿದ ರಚನಾಬಾಗಗಳು (ತಂತು, ಪದರ, ನಿರ್ವಾತ ಗಂಟು) ಹಲವು ಸ್ಥರಗಳಲ್ಲಿ ವ್ಯಕ್ತವಾಗುತ್ತವೆ ಹಾಗೂ, ಆ ಎಲ್ಲ ಸ್ಥರಗಳಲ್ಲೂ ಆ ಬಾಗಗಳ ನಡುವಿನ ನಂಟು ಅತೀ ನಿಕಟ ಮತ್ತು ಸಂಕೀರ್ಣವಾಗಿರುತ್ತದೆ. ಆದ್ದರಿಂದ ನಕ್ಷತ್ರ ಪುಂಜಗಳು ರೂಪಗೊಳ್ಳುವಾಗಿನ ಮಹಾ ಕ್ರಿಯೆಯಲ್ಲಿ ಜಾಲದ ಪ್ರಭಾವವನ್ನು ನಿರ್ದಿಷ್ಟವಾಗಿ ಸೂಚಿಸುವುದು ಸುಲಭಸಾಧ್ಯವಲ್ಲ. ಈ ನಿಟ್ಟಿನಲ್ಲಿ ನಕ್ಷತ್ರ ಪುಂಜಗಳ ಹಾಗೂ ನಿಶಾಭಾಗಗಳ ನಿಯೋಜನೆ ಮತ್ತು ಸುತ್ತುವಿಕೆಯ ಬಗ್ಗೆ ಇನ್ನೂ ಉತ್ತರ ಕಾಣದ ಹಲವು ಪ್ರಶ್ನೆಗಳನ್ನು ನಾವು ಅಧ್ಯಯನ ಮಾಡಲು ಪ್ರಯತ್ನಿಸಿದ್ದೇವೆ. ಅದಕ್ಕಾಗಿ, ಜಾಲದ ವಿವಿದ ರಚನಾಬಾಗಗಳನ್ನು ಗುರುತಿಸಲು ಪ್ರಸ್ತುತದಲ್ಲಿ ಮಾನ್ಯವೆನಿಸಿರುವ ಕೆಲವು ಗಣಕ ತಂತ್ರಗಳನ್ನು ಈ ಅಧ್ಯಯನದಲ್ಲಿ ಉಪಯೋಗಿಸಿಲಾಗಿದೆ. ನಕ್ಷತ್ರಪುಂಜದ ನಿಯೋಜನೆಯ ಸಂಕೇತಗಳು ಅತ್ಯಂತ ದುರ್ಬಲ. ಹಾಗಾಗಿ ಅವುಗಳ ಅಭಿಮುಖವನ್ನು ನಿಖರವಾಗಿ ಅಳೆಯಲು ಹೆಚ್ಚು ಹೆಚ್ಚು ಪುಂಜಗಳಿಂದ ಮಾಹಿತಿ ಪಡೆಯುವುದು ಅನಿವಾರ್ಯ. ಇನ್ನು ಆ ನಿಯೋಜನೆಯನ್ನು ರೂಪಿಸುವ ವಿವಿದ ಕ್ರಿಯೆಗಳ ಪಾತ್ರವನ್ನು ನಿರ್ಧರಿಸುವುದೂ ಕೂಡ ಒಂದು ಕ್ಲಿಷ್ಟವಾದ ಸವಾಲಾಗಿದೆ. ಈ ಸವಾಲನ್ನು ನೀಗಿಸಲು ನಾವು P-Millennium simulation ನ ದೊಡ್ಡ ಗಾತ್ರದ ಜಾಲದ ಘನಾಕೃತಿಯನ್ನು ಅಧ್ಯಯನಕ್ಕೆ ಪರಿಗಣಿಸಿದೆವು. ಹಾಗೂ ಆ ಬೃಹತ್ ಗಾತ್ರದ ಜಾಲದಲ್ಲಿ ಕಂಡ ಹಲವು ಪಟ್ಟು ತೂಕದ ವ್ಯಾಪ್ತಿಯ ಪುಂಜಗಳ ಹಾಗೂ ನಿಶಾಭಾಗಗಳ ನಿಯೋಜನೆಯ ವಿತರಣೆಯನ್ನು ಮತ್ತು ಅವುಗಳ ಗುಣಗಳನ್ನು ಪರಿಶೀಲಿಸಿದ್ದೇವೆ. ಅವು ಜಾಲದ ರಚನಾಬಾಗಗಳೊಂದಿಗೆ ಹೊಂದಿರಬಹುದಾದ ಸಂಬಂಧವನ್ನೂ ಅವಲೋಕಿಸಿದ್ದೇವೆ. ಜೊತೆಗೆ, EAGLE hydrodynamical simulation ನ ಮೂಲದಿಂದಲೂ ಮಾಹಿತಿ ಪಡೆದು ಅಂತದೆ ಅವಲೋಕನೆ ಕೈಗೊಂಡೆವು.

ಬ್ರಹ್ಮಾಂಡ ಜಾಲ ಮತ್ತು ನಿಶಾಭಾಗಗಳ ಗಿರಕಿಯ ಪ್ರಮಾಣ

ಅಸಮಾನವರ್ತಕ ಸ್ಥಿತಿಯಲ್ಲಿ ಅಧಿಕ ಸಾಂಧ್ರತೆಯತ್ತ ಆಕರ್ಶಿತಗೊಂಡ ಘನಕಣ ಸಮೂಹಗಳು ತರಂಗೋಪಾದಿಯಲ್ಲಿ ಹರಿಯುತ್ತ ಕೆಲವೆಡೆ ಕೇಂದ್ರೀಕೃತವಾಗುತ್ತ ಬ್ರಹ್ಮಾಂಡ ಜಾಲದ ಸೃಷ್ಟಿಯಾಗುತ್ತಿದ್ದಂತೆ ಅದರೊಂದಿಗೆ ನಿಶಾಭಾಗದ ಹಾಗೂ ಪುಂಜಗಳ ಆದಿರೂಪಗಳೂ ಕೂಡ ಉದ್ಭವವಾಗತೊಡಗಿದವು. ಹಾಗಾಗಿ ಬ್ರಹ್ಮಾಂಡ ಜಾಲಬಂಧದ ಈ ವಿಕಾಸಕ್ರಿಯೆಯ ಪಳೆಯುಳಿಕೆಗಳು ಪುಂಜಗಳ ಹಾಗೂ ನಿಶಾಭಾಗಗಳ ಸುತ್ತುವಿಕೆಯಲ್ಲಿ ಊರ್ಜಿತವಾಗಿರುವುದನ್ನು ನಿರೀಕ್ಷಿಸಬಹುದು. ೨ನೆ ಅಧ್ಯಾಯದಲ್ಲಿ ಯಾವುದೆ ನಿಶಾಭಾಗದ ಸುತ್ತಿವಿಕೆಯು ಅದರ ಸುತ್ತಲಿನ ಜಾಲದ ಸ್ತಿತಿಗತಿಗಳನ್ನು ನೇರವಾಗಿ ಅವಲಂಬಿಸಿರುತ್ತದೆ ಎಂದು ತೋರಿಸುತ್ತೇವೆ. ತಂತುಗಳಲ್ಲಿರುವ ನಿಶಾಭಾಗಗಳು ಗಂಟುಗಳಲ್ಲಿರುವ ನಿಶಾಭಾಗಗಳಿಗಿಂತ ಕ್ಷಿಪ್ರವಾಗಿ ಸುತ್ತುತ್ತಿವೆ ಎನ್ನವುದನ್ನು ತೋರಿಸಲಾಗಿದೆ. ಈ ವ್ಯತ್ಯಾಸವು ಕೆಂಪುವರ್ಣ ಪಲ್ಲಟ ಹೆಚ್ಚಿರುವ ಬ್ರಹ್ಮಾಂಡದ ಬಾಗಗಳಲ್ಲೂ, ಅಂದರೆ ಕಾಲಮಾನದಲ್ಲಿ ಹಿಂದಕ್ಕೆ ಹೋದಂತೆಯೂ, ಕಾಣಬಹುದು ಎನ್ನುವುದನ್ನು ಅಧ್ಯಾಯ ೪ರಲ್ಲಿ ತೋರಿಸುತ್ತೇವೆ (Figure 3ರ ಕೆಳಬಾಗ). ಇದೆಲ್ಲದರಿಂದ ನಿಶಾಭಾಗದ ವಿಕಾಸಕ್ಕು ಜಾಲದ ಬೃಹತ್ ರಚನಾಕ್ರಮಕ್ಕೂ ಇರುವ ಸಂಬಂಧವನ್ನು ದೃಡೀಕರಿಸಲಾಗಿದೆ.

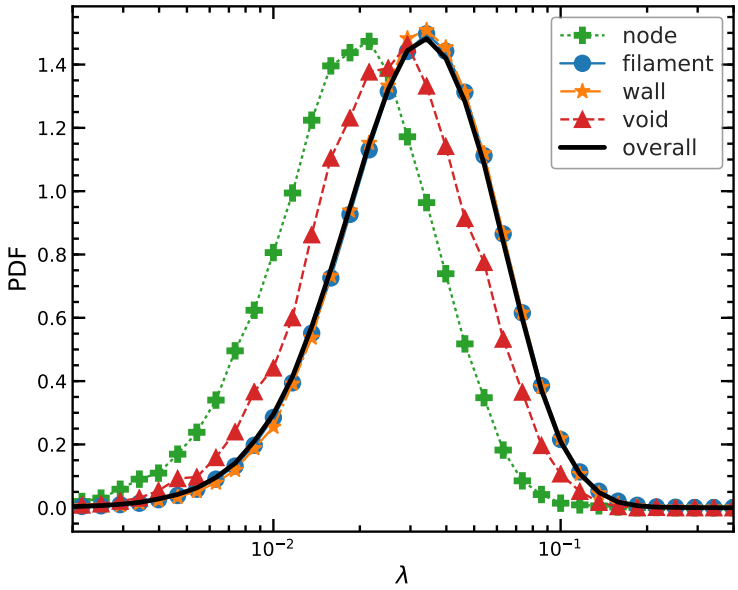

ಚಿತ್ರ 3 □ ಮೇಲಿನ ಚಿತ್ರ: ತಂತುಗಳಲ್ಲಿ, ನಿರ್ವಾತಗಳಲ್ಲಿ, ಗಂಟುಗಳಲ್ಲಿ ಮತ್ತು ಪದರುಗಳಲ್ಲಿರುವ ನಿಶಾ–ಭಾಗಗಳ ಭ್ರಮಣದ ಹರಹು. ಕೆಳಗಿನ ಚಿತ್ರ: ಹಲವು ಕೆಂಪು ಪಲ್ಲಟಗಳಲ್ಲಿ ನಿಶಾಭಾಗಗಳ ಭ್ರಮಣದ ಹರಹಿನ ನಡುವಣ. (ಚಿತ್ರ ಮೂಲ: *Ganeshaiah Veena et al. 2018, 2020*).

ಪುಂಜಗಳ ಮತ್ತು ನಿಶಾಭಾಗಗಳ ಭ್ರಮಣದ ಸಂಕ್ರಮಣ

ಅಧ್ಯಾಯ ೨ ಮತ್ತು ಅಧ್ಯಾಯ ೪ ರಲ್ಲಿ ನಿಶಾಭಾಗದ ಸುತ್ತುವಿಕೆಯ ಕೋನೀಯ ಆವೇಗಕ್ಕೂ (angular momentum) ಮತ್ತು ತಂತುಗಳ ಅಕ್ಷರೇಖೆಗೂ ಇರುವ ಕೋನವನ್ನು, ಅಂದರೆ 'ಗಿರಕಿ-ತಂತು ಸೂಚ್ಯಂಕ'ವನ್ನು ಅಳೆದು, ಆ ಕೋನವು ನಿಶಾಭಾಗಗಳ ತೂಕದೊಂದಿಗೆ ಹೇಗೆ ಬದಲಾಗುತ್ತದೆ ಎಂದು ಅವಲೋಕಿಸಿದ್ದೇವೆ. ಇದಕ್ಕಾಗಿ ನಮ್ಮ ಮಾಹಿತಿಯನ್ನು, ಲಭ್ಯವಿರುವ ಅತ್ಯುತ್ತಮ ಸಂಖ್ಯಾಶಾಸ್ತ್ರದ ವಿಧಾನಗಳಿಗೆ ಒಳಪಡಿಸಿ ಪರಿಶೀಲಿಸಿದ್ದೇವೆ. ಅದರಂತೆ, ಲಘುತೂಕದ ನಿಶಾಭಾಗಗಳು ತಾವಿರುವ ತಂತುಗಳಿಗೆ ಸಮನಾಂತರವಾಗಿಯೂ, ಬೃಹತ್ ತೂಕದ ನಿಶಾಭಾಗಗಳು ಲಂಬಕೋನದಲ್ಲಿಯೂ ನಿಯೋಜಿತಗೊಂಡಿರುತ್ತವೆ ಎಂದು ಕಂಡುಬಂದಿದೆ. ಈ ಮೂಲಕ ಜಾಲದ ತಂತುಗಳಲ್ಲಿ ನಿಶಾಭಾಗಗಳ ಗಿರಕಿಯು ಅವುಗಳ ತೂಕದೊಂದಿಗೆ ಸಂಕ್ರಮಣವಾಗುವ ಪ್ರಕ್ರಿಯೆಯನ್ನು ಅತೀ ಖಚಿತವಾಗಿ ಸಾಬೀತುಪಡಿಸಿದ್ದೇವೆ.

ಬ್ರಹ್ಮಾಂಡವು ವಿಕಾಸಗೊಂಡಂತೆ ನಿಶಾಭಾಗಗಳ ನಿಯೋಜನೆಯು ಹೇಗೆ ಬದಲಾಗುತ್ತದೆ ಎನ್ನುವುದರ ಚಿತ್ರಣವನ್ನು ಅಧ್ಯಾಯ ೪ರಲ್ಲಿ ತೋರಿಸಲಾಗಿದೆ. ಬ್ರಹ್ಮಾಂಡದ ವಿಕಾಸದ ಹಾದಿಯ ಗುಂಟ ಒಂದು ನಿಗದಿತ ತೂಕದ ನಿಶಾಭಾಗಗಳ ವರ್ತನೆಯನ್ನು ಪರಿಶೀಲಿಸಿದಾಗ ಕಂಡದ್ದೆಂದರೆ ಕಾಲದಲ್ಲಿ ಹಿಂದೆ ಹೋದಂತೆ, ನಿಶಾಭಾಗಗಳ ಒಟ್ಟಾರೆ ನಿಯೋಜನೆಯು ತಂತುಗಳ ಅಕ್ಷರೇಖೆಗೆ ಲಂಬಕೋನದಲ್ಲಿದ್ದು, ಕಾಲಕ್ರಮೇಣ ಸಮನಾಂತರವಾಗುತ್ತವೆ ಎನ್ನುವುದು. ಆದರೆ ಪ್ರತಿ ನಿಶಾಭಾಗವೂ ಆದಿಯಲ್ಲಿಯೂ ಸಮನಾಂತರವಾಗಿರುತ್ತವೆ ಎನ್ನುವುದು ವೈಚಿತ್ರ್ಯ.

ಅಧ್ಯಾಯ ೩ರಲ್ಲಿ EAGLE simulation ನ ಪುಂಜಗಳ ತೂಕದೊಂದಿಗೆ ಅವುಗಳ ಭ್ರಮಣದ ಬದಲಾವಣೆಯ ಕ್ರಮವನ್ನು ಅನ್ವೇಶಿಸಿದ್ದೇವೆ. ಪುಂಜಗಳ ನಿಯೋಜನೆಯೂ ಅವುಗಳ ತೂಕವನ್ನಾಧರಿಸಿರುವುದು ಸ್ಪಷ್ಟವಾಗಿ ಕಂಡಿತಾದರೂ, ನಿಶಾಭಾಗಗಳಲ್ಲಾದಂತೆ ಲಂಬಕೋನದಿಂದ ಸಮನಾಂತರಕ್ಕಾದ ಸಂಕ್ರಮಣ

(P-Millennium ಅಥವ EAGLE simulations ಗಳಲ್ಲಿ) ಕಾಣಲಿಲ್ಲ. EAGLE ನ ಪುಂಜಗಳು, ತಂತುವಿನ ಅಕ್ಷರೇಖೆಗೆ ನಿಶಾಭಾಗಗಳ ಒಳಾವರಣಗಳಿಗಿಂತಲು ಹೆಚ್ಚು ಲಂಬಕೋನದಲ್ಲಿದ್ದವು. ಪುಂಜಗಳ ಮತ್ತು ನಿಶಾಭಾಗಗಳ ನಡುವಿನ ಈ ಭಿನ್ನತೆಯು ಅವುಗಳ ಉಗಮ ಹಾಗೂ ವಿಕಾಸದಲ್ಲಿಯೂ ಭಿನ್ನವಾಗಿರುವ ಸಾಧ್ಯತೆಯನ್ನು ಸೂಚಿಸುತ್ತದೆ.

ವಿಕಾಸದ ಹಾದಿಯಗುಂಟ 'ನಿಶಾಭಾಗಗಳ ಗಿರಕಿ-ತಂತು ಸೂಚ್ಯಂಕ'ದಲ್ಲಿ ಕಾಣುವ ಬದಲಾವಣೆಯ ಬಗ್ಗೆ ಮತ್ತಷ್ಟು ಅರಿಯಲು ಆ ನಿಶಾಭಾಗಗಳ ಒಳಗಿನ ಮತ್ತು ಹೊರಗಿನ ಆವರಣಗಳ ನಿಯೋಜನೆಗಳನ್ನು ಹೋಲಿಸಿ ನೋಡಿದೆವು (ಅಧ್ಯಾಯ ೨). ಒಳಾವರಣವು ತಮ್ಮ ಮೂಲದ ತರಂಗ ತಿರುಗುಶಕ್ತಿಯ ಅಭಿಮುಖವನ್ನು ಹೊರಾವರಣಕ್ಕಿಂತ ಹೆಚ್ಚು ಸ್ಥಿರವಾಗಿ ಉಳಿಸಿಕೊಳ್ಳುತ್ತದೆ. ಹೊರಗಿನ ಆವರಣಗಳು ಸುತ್ತಲೂ ನಡೆಯುವ ಘನೀಕರಣ ಹಾಗೂ ವಿಲೀನ ಕ್ರಿಯೆಗಳಿಂದ ಹೆಚ್ಚು ಪ್ರಭಾವಿತವಾಗುವುದರಿಂದ ಈ ವ್ಯತ್ಯಾಸವನ್ನು ನಿರೀಕ್ಷಿಸಬಹುದು. ನಿಶಾಭಾಗಗಳ, ನಕ್ಷತ್ರಪುಂಜಗಳ ಹಾಗೂ ಬ್ರಹ್ಮಾಂಡ ಜಾಲಗಳ ನಡುವೆ ಸತತವಾಗಿ ಚಾಲನೆಯಲ್ಲಿರುವ ಕ್ರಿಯಾತ್ಮಕ ಪ್ರಭಾವಕ್ಕೆ ಇದೊಂದು ದೃಷ್ಟಾಂತ.

ತಂತುಗಳ ಗುಣಗಳು, ಜಾಲ–ಶೋಧನಾಕ್ರಮಗಳು ಮತ್ತು ಸಂಕ್ರಮಣ ತೂಕ

ತಂತುಗಳನ್ನು ಗುರುತಿಸುವ ಕ್ರಿಯೆ ಹಲವು ಸವಾಲುಗಳನ್ನು ಒಡ್ಡುತ್ತದೆ. ಉದಾಹರಣೆಗೆ, ಬ್ರಹ್ಮಾಂಡದೆಲ್ಲೆಡೆಯಿಂದ ನಮಗೆ ತಲುಪುವ ಬೆಳಕಿನ ಮೂಲಗಳು ಎಷ್ಟು ದೂರದಲ್ಲಿವೆ ಎನ್ನುವುದರ ಬಗ್ಗೆ, ಕೆಂಪುವರ್ಣ ಪಲ್ಲಟದ ಸೂಚ್ಯಂಕದಿಂದ ಪರೋಕ್ಷವಾಗಿ, ಮಾತ್ರವೆ ನಮಗೆ ತಿಳಿಯಲು ಸಾಧ್ಯವಿದ್ದು, ಅವುಗಳ ನಿಜವಾದ ದೂರದ ಮಾಹಿತಿ ಲಬ್ಯವಿಲ್ಲ. ಅಲ್ಲದೆ ಆ ಅನ್ವೇಷಕ ಸಮೂಹಗಳಲ್ಲಿನ ವಿರಳತೆ ಮತ್ತು ದೋಷತೆಯೂ ತಂತುಗಳನ್ನು ಗುರುತಿಸುವಲ್ಲಿ ಅಡ್ಡಿಯಾಗುತ್ತವೆ. ಈ ಕಾರಣದಿಂದಾಗಿ ನಾವು ಹಲವು ವಿದದ ತಂತು ಶೋಧಕ ಕ್ರಮಗಳನ್ನು ಉಪಯೋಗಿಸಿದೆವು. ಅಧ್ಯಾಯ ೨ ರಲ್ಲಿ ಸಾಂಧ್ರತೆ ಮತ್ತು ವೇಗವನ್ನಾಧರಿಸಿ ಗುರುತಿಸಿದ ತಂತುಗಳನ್ನೂ, ಅಧ್ಯಾಯ ೩ರಲ್ಲಿ ನಿಶಾಭಾಗಗಳ ಮತ್ತು ನಕ್ಷತ್ರ ಪುಂಜಗಳ ಹರಹುವಿನ ಮೂಲಕ ಗುರುತಿಸಿದ ತಂತುಗಳನ್ನೂ ಹೋಲಿಸಿದೆವು.

ಅಧ್ಯಾಯ ೨ ರಲ್ಲಿ, ಕ್ಷೇತ್ರ ಸಾಂಧ್ರತೆಯ ಜ್ಯಾಮಿತಿಯ ಮಾಹಿತಿಯನ್ನಾಧರಿಸಿ ಜಾಲದ ಲಕ್ಷಣಗಳನ್ನು ವರ್ಗೀಕರಿಸುವ NEXUS+ ಅನ್ನು, ಕ್ಷೇತ್ರದ ವೇಗ ಛೇದದಲ್ಲಿನ ಕ್ರಿಯಾತ್ಮಕ ಸಹಿಗಳನ್ನಾಧರಿಸಿ ಜಾಲಗಳನ್ನು ವರ್ಗೀಕರಿಸುವ NEXUS_VELOCITY_SHEAR ಜೊತೆಗೆ ಹೋಲಿಸಲಾಗಿದೆ. ಈ ಎರಡೂ ವಿಧಾನಗಳು ತಂತುಗಳ ಪ್ರಮುಖ ನಾಳಗಳನ್ನು ಗುರುತಿಸುತ್ತವೆಯಾದರೂ, NEXUS+, ಅತೀ ಕಡಿಮೆ ಸಾಂಧ್ರತೆಯಲ್ಲಿ ಹರಡಿರುವ ಸೂಕ್ಷ್ಮ ತಂತುಗಳನ್ನೂ ಹೆಕ್ಕಿತೋರುತ್ತದೆ.

ಈ ವ್ಯತ್ಯಾಸದ ಪರಿಣಾಮವಾಗಿ ಎರಡೂ ವಿಧಾನಗಳಿಂದ ದೊರಕುವ ನಿಶಾಭಾಗಗಳ ಸಮೂಹಗಳಲ್ಲಿ ಹಾಗೂ ಆ ಸಮೂಹಗಳ ತೂಕಾಧಾರಿತ ನಿಯೋಜನೆಯ ಪರಿವರ್ತನೆಯಲ್ಲಿಯೂ ವ್ಯತ್ಯಾಸವಿರುತ್ತದೆ, ಅಂದರೆ ನಿಶಾಭಾಗಗಳು ತಂತುವಿನ ಅಕ್ಷರೇಖೆಗೆ ಸಮಾನಾಂತರದಿಂದ ಲಂಬಾಭಿಮುಖವಾಗುವ ಪ್ರಕ್ರಿಯೆಯ ತೂಕಗಳನ್ನು ಗುರುತುಸುವಲ್ಲಿಯೂ ಅವೆರಡರ ಫಲಿತಾಂಶಗಳು ಭಿನ್ನವಾಗಿರುತ್ತವೆ.

ಅಧ್ಯಾಯ ೩ ರಲ್ಲಿ ನಕ್ಷತ್ರ ಪುಂಜಗಳು ರೂಪಗೊಳ್ಳುವುದನ್ನು ಅರಿಯುವ ನಿಟ್ಟಿನಲ್ಲಿ ತಂತುಗಳು ಬ್ರಹ್ಮಾಂಡದ ಶೋಧ ಸಾಧನಗಳಾಗಿ ಹೇಗೆ ಪ್ರಾಮುಖ್ಯತೆ ಪಡೆಯುತ್ತವೆ ಎನ್ನುವುದನ್ನು ಸ್ಪಷ್ಟಪಡಿಸಿದ್ದೇವೆ. ಇಡೀ ಬ್ರಹ್ಮಾಂಡದ ಶೇಕಡ ೫೦ ರಷ್ಟು ಘನವಸ್ತು, ಹಾಗೂ ಶೇಕಡ ೮೦ರಷ್ಟು ನಕ್ಷತ್ರಪುಂಜಗಳು ಜಾಲದ ತಂತುಗಳಲ್ಲಿವೆ ಎನ್ನುವುದನ್ನು ತೋರಿಸಿದ್ದೇವೆ. ನಂತರ ನಿಶಾಘನವಸ್ತುವಿನ ಮೂಲಕ (NEXUS+) ಪಡೆದ ತಂತುಗಳ, ಮತ್ತು ಪುಂಜಗಳ ಹರಹುವಿನ ಮೂಲಕ (Bisous) ಪಡೆದ ತಂತುಗಳ ಆಕಾರ ಮತ್ತು ಗಿರಕಿಗಳನ್ನು ಹೋಲಿಸಿ ಪರಿಶೀಲಿಸಿದ್ದೇವೆ. ಇವೆರಡರ ನಡುವಿನ ಹೋಲಿಕೆಯನ್ನು ಚಿತ್ರ -೯ ರಲ್ಲಿ ತೋರಿಸಲಾಗಿದೆ. EAGLE hydrodynamical simulation ನಲ್ಲಿ ಉಪಯೋಗಿಸಿದ ಘನಾಕೃತಿಯಿಂದ NEXUS+ ಮತ್ತು Bisous ಗಳ ಮೂಲಕ ಪಡೆದ ತಂತುಗಳನ್ನು, ಮುಖಾಮುಖಿಯಾಗಿ ಹೋಲಿಸಲಾಗಿದೆ. ಒಟ್ಟಾರೆ ಎರಡೂ ತಂತುಗಳ ಜಾಲಬಂಧಗಳಲ್ಲಿ ಸಾದೃಶ ಹೋಲಿಕೆ ಇದ್ದು, ಅವುಗಳ ಗಿರಕಿ ನಿಯೋಜನೆಯಲ್ಲಿ ಮಾತ್ರವೆ ವ್ಯ-

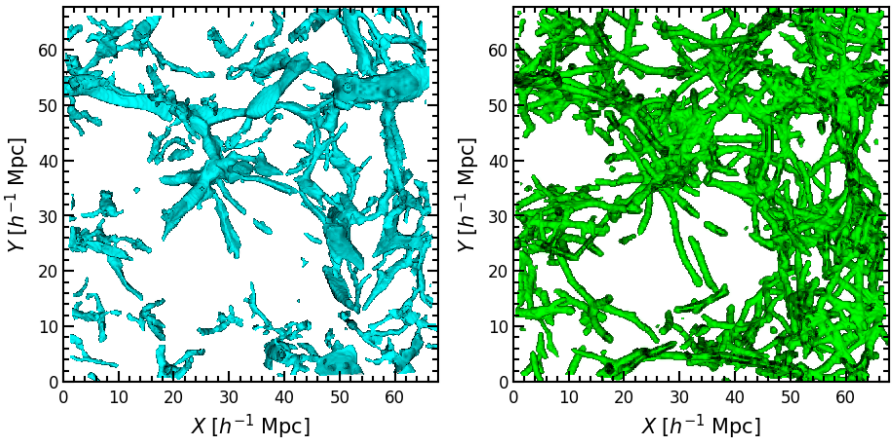

ಚಿತ್ರ 4 □ *EAGLE simulation* ನ ೧೦ *Mpc/h* ವ್ಯಾಪ್ತಿಯಲ್ಲಿನ ಬ್ರಹ್ಮಾಂಡದಲ್ಲಿ *NEXUS+* ಮೂಲಕ ಕಂಡ ತಂತುಗಳನ್ನು (ನಿಶಾ ಘನಕಣಗಳ ಹರಹು) ಮತ್ತು *Bisous* ಮೂಲಕ ಕಂಡ ತಂತುಗಳನ್ನು (ನಕ್ಷತ್ರ ಪುಂಜಗಳ ಹರಹು) ತೋರಿಸಲಾಗಿದೆ. (ಮೂಲ: *Ganeshaiah Veena et al. 2019*)

ತ್ಯಾಸ ಕಾಣಬಹುದು.

ನಿಶಾಭಾಗ ಹಾಗೂ ನಕ್ಷತ್ರ ಪುಂಜಗಳ ನಂಟು

ಇಲ್ಲಿ ಒಂದು ಕುತೂಹಲಕರ ಪ್ರಶ್ನೆಯನ್ನು ಪರಿಶೀಲಿಸಬಹುದು: ನಿಶಾಭಾಗದ ಕೋನೀಯ ಆವೇಗದ ಆಧಾರದ ಮೇಲೆ ನಕ್ಷತ್ರಪುಂಜದ ಕೋನೀಯ ಆವೇಗವನ್ನು ತಿಳಿಯಬಹುದೆ? ಅಂತೆಯೇ ನಕ್ಷತ್ರ ಪುಂಜದಿಂದ ನಿಶಾಭಾಗದ ಕೋನೀಯ ಆವೇಗವನ್ನು ಪಡೆಯಬಹುದೆ? ನಕ್ಷತ್ರ ಪುಂಜಗಳ ಮತ್ತು ತಂತುಗಳ ನಿಯೋಜನೆಯ ಅವಲೋಕನೆಯ ಮೂಲಕ ಈ ಪ್ರಶ್ನೆಗೆ ಅಧ್ಯಾಯ ೩ ರಲ್ಲಿ ಉತ್ತರಿಸಲು ಪ್ರಯತ್ನಿಸಿದ್ದೇವೆ.

EAGLE simulation ಉಪಯೋಗಿಸಿಕೊಂಡು, ತಂತುವಿನ ಅಭಿಮುಖಕ್ಕೆ ಸಂಭಂದಿಸಿದಂತೆ ನಿಶಾಭಾಗದ ಮತ್ತು ನಕ್ಷತ್ರ ಪುಂಜದ ಸುತ್ತುವಿಕೆಯ ನಿಯೋಜನೆಗಳ ನಡುವಿನ ಪರಸ್ಪರ ಸಂಬಂಧವನ್ನು ಅಧ್ಯಯನ ಮಾಡಿದೆವು. Figure 5 ರಲ್ಲಿ ನಿಶಾಭಾಗದ ಹಾಗೂ ಪುಂಜಗಳ ತೃಣ ಕಕ್ಷೆಗಳ ನಡುವಿನ ಸಂಬಂಧವನ್ನು ಎರಡು ಸಮೂಹಗಳಿಗೆ ತೋರಿಸಲಾಗಿದೆ: ಅವುಗಳಲ್ಲಿ ಒಂದು ಪುಂಜಗಳ ತೃಣ ಕಕ್ಷೆಯು ತಂತುಗೆ ಸಮಾನಾಂತರವಾಗಿರುವ ಸಮೂಹ, ಮತ್ತೊಂದು ಲಂಬವಾಗಿರುವ ಸಮೂಹ. ಇವುಗಳಲ್ಲಿ ಎರಡನೆಯದು, ಅಂದರೆ ತಾವಿರುವ ತಂತುಗೆ ಲಂಬವಾಗಿ ತೃಣ ಕಕ್ಷೆಯನು ಹೊಂದಿರುವ ಪುಂಜಗಳು ನಿಶಾಭಾಗದೊಂದಿಗೆ ಹೆಚ್ಚಿಗೆ ನಿಯೋಜಿತಗೊಂಡಿವೆ ಎಂದು ತಿಳಿಯುತ್ತದೆ.

ಇದೇ ನಿಟ್ಟಿನಲ್ಲಿ, ಸುರುಳಿ (disc) ಹಾಗೂ ಅಂಡಾಕಾರದ (spheroid) ಪುಂಜಗಳನ್ನು ಹೊಂದಿರುವ ನಿಶಾಭಾಗಗಳ ತಂತುಗಳೊಂದಿಗಿರುವ ಭ್ರಮಣದ ನಿಯೋಜನೆಯನ್ನು ಅಧ್ಯಯನ ಮಾಡಿದೆವು. ಅಂಡಾಕಾರದ ಪುಂಜಗಳಿರುವ ನಿಶಾಭಾಗಗಳು ಬಹುಪಾಲು ಲಂಬವಾಗಿಯೂ, ಸುರುಳಿಯಿರುವ ನಿಶಾಭಾಗಗಳು ತಂತುಗಳಿಗೆ ಸಮನಾಂತರವಾಗಿಯೂ ನಿಯೋಜಿತಗೊಂಡಿರುವುದು ಸ್ಪಷ್ಟವಾಗಿ ಕಂಡಿತು. ಹಾಗಾಗಿ ಪುಂಜಗಳ ತಿರುಗು ನಿಯೋಜನೆಯ ವೀಕ್ಷಣೆಯಿಂದಲೆ ನಿಶಾಭಾಗಗಳು ತಾವಿರುವ ತಂತುಗಳೊಂದಿಗೆ ತೋರುವ ಗಿರಕಿ ಮತ್ತು ಆಕಾರಗಳನ್ನು ಊಹಿಸಲು ಸಾಧ್ಯ. ಈ ಅವಿಷ್ಕಾರದಿಂದ ನಿಶಾಭಾಗಗಳ ಆಕಾರ ಮತ್ತು ಅಭಿಮುಖದ ಬಗ್ಗೆ ಮುನ್ಸೂಚಕವಾಗಿ ತಿಳಿಯುವ ಅವಕಾಶವಿರುವುದರಿಂದ, ಬ್ರಹ್ಮಾಂಡದ ಬಗೆಗಿನ ಪರಿಕಲ್ಪನೆಗಳನ್ನು ಪರೀಕ್ಷೆಗೆ ಒಡ್ಡಲು ಸಾಧ್ಯವಾಗುತ್ತದೆ.

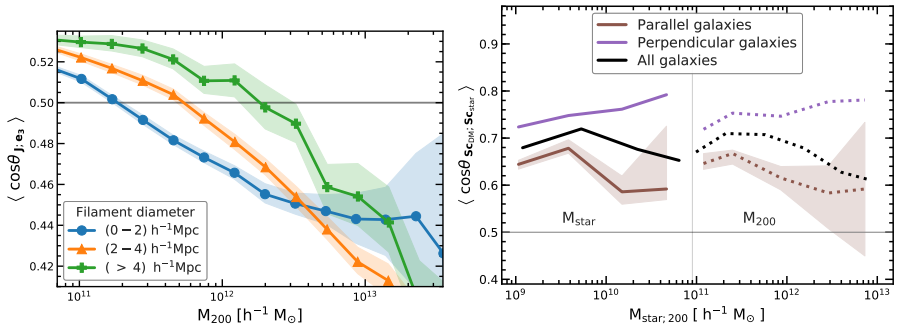

ಚಿತ್ರ 5 □ ಎಡಚಿತ್ರ: ಕ್ಷೀಣ, ಮಧ್ಯಮ ಮತ್ತು ದಪ್ಪ ತಂತುಗಳಲ್ಲಿನ ನಿಶಾಭಾಗಗಳ ನಿಯೋಜನೆಯ ಸೂಚ್ಯಂಕದ ಮಧ್ಯಾಂಕವನ್ನು ಸೂಚಿಸಲಾಗಿದೆ. ಬಲಚಿತ್ರ: ನಕ್ಷತ್ರ ಪುಂಜಗಳ ಹಾಗೂ ನಿಶಾಭಾಗಗಳ ತೃಣಕಕ್ಷೆಗಳು ಪರಸ್ಪರ ನಿಯೋಜನೆಗೊಂಡಿರುವ ಕ್ರಮವನ್ನು ತೋರಿಸಲಾಗಿದೆ. ಈ ಸಂಬಂಧವನ್ನು ತಮ್ಮ ಜಾಲಗಳೊಂದಿಗೆ ಸಮನಾಂತರವಾಗಿ ಹಾಗೂ ಲಂಬವಾಗಿ ನಿಯೋಜನೆಗೊಂಡಿರುವ ನಕ್ಷತ್ರಪುಂಜಗಳಿಗೆ ಬೇರೆಬೇರೆಯಾಗಿಯೇ ತೊರಿಸಲಾಗಿದೆ. ಲಂಬವಾಗಿ ನಿಯೋಜನೆಗೊಂಡಿರುವ ಪುಂಜಗಳು ಅವುಗಳ ಸುತ್ತಲ ನಿಶಾಭಾಗಗಳೊಂದಿಗೆ, ಸಮನಾಂತರವಾಗಿರುವ ಪುಂಜಗಳಿಗಿಂತ ಹೆಚ್ಚು ಹೋಲಿಕೆಯನ್ನು ತೋರುತ್ತಿರುವುದನ್ನು ಕಾಣಬಹುದು.(ಋಣ: *Ganeshaiah Veena et al. 2018, 2019*).

ಮುಕ್ತಾಯದ ಮಾತು

ಈ ಸಂಶೋಧನಾ ಪ್ರಬಂಧದಲ್ಲಿ ಬ್ರಹ್ಮಾಂಡದ ಬೃಹತ್ ಮಟ್ಟದ ಪ್ರಕ್ರಿಯೆಗಳ ಹಾಗೂ ಅದರಲ್ಲಿನ ನಕ್ಷತ್ರ-ಪುಂಜಗಳ ಮತ್ತು ನಿಶಾಭಾಗಗಳ ಗುಣವಿಶೇಷಗಳ ನಡೆಯುವ ಸಂಕೀರ್ಣ ಕ್ರಿಯಾಕ್ರಮಗಳನ್ನು ನಿರೂಪಿಸಲಾಗಿದೆ. ಬ್ರಹ್ಮಾಂಡ ಜಾಲದ ವಿವಿಧ ಸ್ಥಿತಿಗತಿಗಳ ಹಿನ್ನೆಲೆಯಲ್ಲಿ ನಕ್ಷತ್ರ ಪುಂಜಗಳು ಮತ್ತು ನಿಶಾಭಾಗಗಳ ವಿಕಾಸಕ್ಕೆ ಕಾರಣೀಭೂತವಾದ ಕ್ರಿಯೆಗಳನ್ನು ಇಲ್ಲಿ ಮಂಡಿಸಿದ್ದೇವೆ. ವಿಶೇಷವಾಗಿ, ತಂತುಗಳ ಅಕ್ಷರೇಖೆಗೆ ಪುಂಜಗಳ ಪರಿಭ್ರಮಣದ ನಿಯೋಜನೆಯು ಬ್ರಹ್ಮಾಂಡದ ಅಧ್ಯಯನಕ್ಕಾಗಿ ಬಳಸುವ ಸೂಕ್ಷ್ಮ ಮಸೂರ ಕ್ರಿಯೆಯನ್ನು ಪ್ರಭಾವಿತಗೊಳಿಸುವಲ್ಲಿ ಅತ್ಯಂತ ಪ್ರಮುಖವಾಗಿರುತ್ತದೆ. ಈ ಪ್ರಭಾವವು ಸೃಷ್ಟಿಯ ಉಗಮದಿಂದ ಇಲ್ಲಿಯವರೆಗಿನ ಕಾಲದ ಆಯಾಮದಲ್ಲಿ ರೇಖೀಯವಾಗಿರುವುದಿಲ್ಲ ಎಂದು ತೊರಿಸಿದ್ದೇವೆ. ಪುಂಜಗಳ ಹಾಗೂ ನಿಶಾಭಾಗಗಳ ನಿಯೋಜನೆಯು ಜಾಲದ ಸ್ಥಳೀಯ ಗುಣಗಳನ್ನವಲಂಬಿಸಿರುತ್ತದೆ ಎಂದೂ ತೋರಿಸಲಾಗಿದೆ; ಅದರಲ್ಲೂ ಪ್ರಕಾಶಮಾನವಾದ ಪುಂಜಗಳನ್ನು ಹೊಂದಿರುವ ತಂತುಗಳ ಗುಣಗಳಿಂದ ನಿಶಾಭಾಗಗಳ ನಿಯೋಜನೆಯು ಹೆಚ್ಚು ಪ್ರಭಾವಿತವಾಗುತ್ತದೆ ಎಂದು ದೃಢಪಡಿಸಿದ್ದೇವೆ. ಇನ್ನು ಮುಂದಿನ ಸವಾಲೆಂದರೆ ಈ ನಿಯೋಜನೆಗಳು ಪುಂಜಗಳು ಸೃಷ್ಟಿಸುವ ಸೂಕ್ಷ್ಮ ಮಸೂರ ಕ್ರಿಯೆಯಮೇಲೆ ಬೀರುವ ಪರಿಣಾಮವನ್ನು ಅಳೆಯಬೇಕಾಗಿರುವುದು. ಕಾರಣ ಆಗ ಬ್ರಹ್ಮಾಂಡದ ನಿಯತಾಂಕಗಳನ್ನು ನಿಖರವಾಗಿ ಅಳೆಯಲು ಸಾಧ್ಯ. ಜೊತೆಗೆ ಗಿರಕಿಯ ಪರಿವರ್ತನಾ ತೂಕವನ್ನು ಮತ್ತು ಬ್ರಹ್ಮಾಂಡದ ಜಾಲದ ಸ್ಥಿತಿಗತಿಗೆ ಅದರ ಸೂಕ್ಷ್ಮತೆಯನ್ನೂ ಅನ್ವೇಶಿಸಬೇಕಿದೆ. ಕಾರಣ ಅದು ಬ್ರಹ್ಮಾಂಡವನ್ನು ಬೇದಿಸುವಲ್ಲಿ ಮತ್ತೊಂದು ಉಪಯುಕ್ತ ಸಾಧನವಾಗುವ ಸಾಧ್ಯತೆಯಿದೆ. ವಿಶ್ವಮಂಡಲದ ಅಗೋಚರ ಘನಬಾಗಗಳ ಬಗ್ಗೆ ಹಾಗೂ ನಿಶಾಭಾಗಗಳ ಸುತ್ತುವಿಕೆಯ ಬಗ್ಗೆ ಹೆಚ್ಚಿನ ಬೆಳಕು ಚೆಲ್ಲಲು ನೂತನ ಪರಿಕಲ್ಪನೆಗಳನ್ನೂ ಮಾದರಿಗಳನ್ನೂ ಕಟ್ಟುವ ಸಲುವಾಗಿ ಪುಂಜಗಳ ಸುತ್ತುವಿಕೆಯ ನಿಯೋಜನೆಯನ್ನು ಇನ್ನೂ ಆಳವಾಗಿ ಅಧ್ಯಯನ ಮಾಡಬೇಕಿದೆ.

Acknowledgments

Firstly, many thanks to my supervisors, Rien, Elmo and Marius. Rien, the first few months of intense training I received from you on structure formation was very exciting. I enjoyed very much our discussions on various aspects of cosmology and structure formation. Your teaching style, courses on the cosmic web and talks are impeccable, especially the one you delivered at the Planetarium! Throughout the PhD, you always reminded me of the big picture and pushed me to explore deeper, think harder and write better. You supported me *unconditionally* during one of the hardest phases of my life and I will always be grateful for that. Thank you very much, Rien, for your support and guidance the past few years.

Elmo, the time with you in both Potsdam and Tartu were extremely enjoyable. While Rien encouraged me to dive deep, you encouraged me to swim fast and take charge, a combination that worked really well for this thesis. I am inspired by your work ethics, your pragmatism and clarity of thought. You very patiently listened to **all** of my problems - science and non-sciense alike, and always provided a fresh perspective to them. Working with you has given me a lot of optimism, confidence and joy. Although you managed to scare me about Estonian weather and saunas, I had a wonderful time at Tartu. Thank you for always encouraging me to attend conferences and give talks wherever and whenever possible. I hope that I can continue to be a part of Tartu Observatory and collaborate even after I leave. Special thanks to Lea for the numerous dinners and barbecues at your place and her delectable cakes!

Marius, you have been a *great* mentor and a dear friend to me. I admire the ease with which you always recognised the nature of help I needed and accordingly helped me at various stages of the PhD. You have played a crucial role in my PhD and the project gained enormous momentum, both in terms of mass and velocity, because of you. You helped me grow from an over-enthusiastic grad student to a more mature researcher :) I thoroughly enjoyed doing science with you and chatting with you. The visits to Durham and Leiden have been my most productive days. Thank you very much for the *Cautun hypothesis*, I wish that we prove this very soon! My heartfelt gratitude to you for the support I have been receiving on all other fronts associated with academia and life in general. I will very much miss the weekly meetings with all of you and wish that we can work together in the future.

Many thanks to Carlos, for hosting me at ICC, for several contributions to the project and for being very inclusive during my visits. I would like to express my gratitude to

the reading committee members, Nabila, Filippo and Joss for the detailed comments and assessment of the thesis work. To Bernard and Janet for the several stimulating conversations.

The land of tall people and rain

I realised that I am *very* short when I arrived in the Netherlands 4.5 years ago, and yes it was cold and raining that day. I was very happy to be given a desk in office 151 at the Kapteyn Institute in Groningen, which I shared with a few relatively *not-so-tall* people. Robin, Fabian, Nadine, Sander, Anais, Yanan and Mirjam (Mirjam is *very tall*!), our time in the office and road-trips together have been a highlight! Sander, for helping me find a Dutch bike that suits my height (an impossible feat!), for early morning Dutch lessons, and for giving me a *very warm* welcome, dank je wel! Fabian, within the short overlap we had in the office, you managed to give me a crash course on *'Surviving in Europe for Dummies'*, all of which proved very useful to know, wish I had made notes! I will cherish our friendship and your numerous photography lessons. Thank you for *always* taking care of your friends. Nadine, you have set an example and a high bar for how strong a woman can be. You are a great mom and little Linus is very lucky. Robin, thank you very much for your words of support during tough times and for painting a hopeful future every time I ask you for advice :) Most importantly, thanks a lot for translating the summary to Dutch. Yanan, it was great to have you as an office mate, you were very hardworking and focused. Anais, your optimism and zest for life is very uplifting, I am very glad to have known you.

To Avanti, for curing my homesickness; without you, I would've felt quite isolated. Suma, you came too late to Groningen, we could've spent so many more evenings arguing about everything! Thank you, Apu, for bringing in so much fun into the group. Thank you to Pooja, Bharat, Smaran and Sampath for the nice Indian evenings.

A big thank you to Lucia, Christa, Martine and Ramona. You are all very efficient, lovely and keep the institute running. To Lucia, Scott and Mariano for always helping me out and to Leon for all the help with computers.

Thanks to Patrick for sharing the thesis template, this is becoming one of the most popular templates at Kapteyn.

The land of silent people and snow

After being stuck in a "snowstorm" at Schipol airport for two days, I finally arrived in Tartu, which welcomed me with so much snow that the Dutch snowstorm felt like a breeze in comparison! People at Tartu Observatory immediately made me feel at home. Maarja, my deepest gratitude to you for integrating me into the group. Your confidence and charm is admirable, thanks for being my first sauna partner, driving me to work, teaching Estonian sarcasm and eastern European drinking, and for showing how Estonian mid-summer is really celebrated! Toni, for being a great flatmate, for the countless parties, the long lessons on whiskey and for introducing me to Western, Irish and metal music; good luck finding WHIM :) To Haruka, for the nice times together, to Teet, Nisa and Leo for the lovely dinners, to Daniel, for just

being Daniel! Moorits, all the best for your PhD, and best of luck to continue with the cookies journal club and other initiatives.

Rain, *rain or no rain*, you are very silent, yet very funny and inspiring. I have learnt a lot by working with you and have enjoyed our chats and scientific discussions- I wish our collaboration continues. Antti, I cannot think of a better person to lead the Observatory, you are very approachable, compassionate and inclusive. Juhan, thank you for the orienteering evenings and for showing me a bear, I have very much enjoyed all the outings together. Many thanks to Jaan Einasto, your presence at the observatory and frequent encouragement go a long way. To Maret, Peeter, Jukka, Taavi, Indrek, Jaan, Tõnis, Enn and Heidi, for making the cosmology team feel like a family. To Pekka, for the lovely times and for the Eha apartment. Many thanks to Priit, for showing me Estonian bogs and forests and for helping me see things from a different perspective. Thank you, Karl, for making my time in Tartu very enjoyable. To Ayush, for the amazing pizzas and parathas. To Sharvari, for your immense support; to Keerthana, Kapil and Ruby, although I got to know you all towards the end of my stay, you made the *corona-summer* delightful!

The land of *too many* people and sun

Many thanks to *Appaji* and *Amma*, you never stopped me from dreaming and gave me complete freedom to pursue whatever I wished for and provided a springboard that many don't get. Appaji, a special thank you for translating the thesis summary to *Kannada*. To all my relatives and my grandmother back in India, who always questioned the practical benefits of my PhD. To them, the most meaningful life is that which is spent with loved ones and saw no sense in me going away to a faraway land to study the heavens. Thank you for always keeping me connected and rooted during these last few years. To my parents-in-law, akka and bhava for your immense support, especially during times of crisis. To Belavadi uncle, your calm demeanour, encouraging talks and support helped me complete the thesis. Poornima, friendship with you is as Tagore says: like fluorescence, it shines better when everything has darkened- thank you for *always* being there for me. To Meghna, you have made my life so much happier and have always reminded me of what is truly important, especially during the last days of thesis writing, thank you for that! Thanks to Aditya, Kiran and VK, I know I can always rely on you :)

To Madhusudan sir, for teaching physics in an experiential way that got me interested at a very young age. To Varun Sahni, for encouraging me to embark on a PhD.

Finally, to my partner in crime, Suraj. You established an environment in which I could focus and write this thesis during the pandemic, while being in isolation with you at Tartu Observatory. Thank you for always standing by my side through bright and dark days alike and for inspiring me about the future.